UNIVERSIDAD DE CHILE
FACULTAD DE CIENCIAS FÍSICAS Y MATEMÁTICAS
DEPARTAMENTO DE FÍSICA

STUDY AND IMPLEMENTATION OF MODIFICATIONS TO THE PURE B-MODE PSEUDO-SPECTRUM OF THE POWER SPECTRUM ESTIMATOR FOR THE WIDE SKY PATCH ANALYSIS OF THE POLARBEAR-1 EXPERIMENT

TESIS PARA OPTAR AL GRADO DE
MAGÍSTER EN CIENCIAS, MENCIÓN FÍSICA

MARIO ANDRÉS OSVALDO AGUILAR FAÚNDEZ

PROFESOR GUÍA:
GONZALO PALMA QUILODRÁN

PROFESOR CO-GUÍA:
LUIS CAMPUSANO BROWN
DAVID BOETTGER

MIEMBROS DE LA COMISIÓN:
ROLANDO DÜNNER PLANELLA
DOMENICO SAPONE

Este trabajo ha sido parcialmente financiado por proyectos Fondecyt 1130777 y 1171811.

SANTIAGO DE CHILE
2021

Study and Implementation of Modifications to the Pure B-Mode Pseudo-Spectrum of the Power Spectrum Estimator for the Wide Sky Patch Analysis of the Polarbear-1 Experiment

Mario Andrés Osvaldo Aguilar Faúndez

Resumen

Esta tesis describe el trabajo que yo he realizado para contribuir al desarrollo de la tubería de análisis de datos para procesar las observaciones del experimento Polarbear. El proyecto observó el Fondo Cósmico de Microondas (CMB por sus siglas en inglés) durante tres años usando detectores sensitivos a polarización y una placa de media onda continuamente giratoria para modular la polarización del CMB. El experimento Polarbear está emplazado en el Telescopio Huan Tran (HTT por sus siglas en inglés) a 5190 metros de altitud en una ladera del Cerro Toco en el desierto de Atacama del norte de Chile. El propósito de este experimento es medir las ondas gravitacionales primordiales que han sido propuestas de haber sido creadas durante la expansión exponencial del universo temprano. Esta huella es una predicción única de un proceso denominado *Inflación Cósmica*, donde la amplitud total de esta señal r es un parámetro que requiere ser constreñido. La detección de esta señal de onda gravitacional representa un esfuerzo experimental desafiante.

Este manuscrito describe la tubería de análisis usada para transformar la secuencia de datos sin procesar a un espectro de potencia de polarización del CMB, con énfasis en la estimación del espectro de potencia. Doy una detallada descripción de mi contribución principal a esta tubería donde las modificaciones al pseudo-espectro del modo puro B son implementadas. El resultado principal de esta tesis es una resiliencia mejorada bajo variaciones del auto espectro de modo B de entrada para la estimación del contenedor de espectro multipolar más bajo. Cuantitativamente, 80% de las pruebas en el régimen perturbativo presentado en este trabajo tuvieron una diferencia significativa de entre 3σ y 4σ comparando el uso de las modificaciones implementadas en el estimador de espectro de potencia con el caso en que se prescinde de ellas. Estas modificaciones contribuyeron a la validación del espectro de potencia y a la detección de un moderado exceso de potencia por sobre las predicciones obtenidas del modelo ΛCDM con lente gravitacional en los dos contenedores de espectro multipolar más bajos de la campaña de observaciones de Polarbear. Por completitud, también describo brevemente el trabajo realizado por otros miembros de la colaboración Polarbear pero explícitamente menciono mis contribuciones a lo largo de este trabajo.

Study and Implementation of Modifications to the Pure B-Mode Pseudo-Spectrum of the Power Spectrum Estimator for the Wide Sky Patch Analysis of the Polarbear-1 Experiment

Mario Andrés Osvaldo Aguilar Faúndez

Abstract

This thesis describes the work that I performed to contribute to the development of the data analysis pipeline to process observations of the Polarbear experiment. The project observed the Cosmic Microwave Background (CMB) radiation for three years using polarization sensitive detectors and a continuously rotating half-wave plate to modulate the CMB polarization. The Polarbear experiment is placed on the Huan Tran Telescope (HTT) at 5,190 meters altitude on the side of Cerro Toco in the Atacama desert of northern Chile. The purpose of the experiment is to measure the primordial gravitational waves which are been proposed to have been created during the exponential expansion of the early universe. This signature is a unique prediction for a process dubbed *Cosmic inflation*, where the overall amplitude of this signal r is a parameter that needs to be constrained. The detection of this gravitational wave signal represents an extremely challenging experimental endeavor.

This manuscript describes the analysis pipeline used to transform the raw data streams into a CMB polarization power spectrum, with a focus on the power spectrum estimation. I give a detailed outline of my main contribution to this pipeline where modifications to the pure B-mode pseudo-spectrum are implemented. The main result of this thesis is an improved resilience under variations of the B-mode input auto spectrum for the estimation of the lowest multipole spectrum bin. Quantitatively, 80% of the tests in the perturbation regime reported in this work had a significant improvement between 3σ and 4σ, when comparing the use of the implemented modifications in the power spectrum estimator to the case where these changes were not applied. These modifications contributed to the validation of our power spectrum estimator and to the detection of a moderate excess of power above the predictions from the ΛCDM lensing model in the lowest two multipole bins of the Polarbear observations campaign. For completeness, I also briefly describe the work done by other members of the Polarbear collaboration but explicitly mention my contributions throughout this dissertation.

Dedicada a mis padres Magdalena Faúndez y Juan Carlos Aguilar

Agradecimientos

Estoy muy agradecido de muchas personas que de manera desinteresada me han apoyado durante el desarrollo de este trabajo y todo lo precedente, a pesar de mis numerosas falencias. Espero haber mencionado a varios, pero sin duda no podré mencionarlos a todos y me disculpo desde ya si he omitido a alguien.

No podría sino empezar por mi familia que ha sido pilar fundamental en este proceso. Agradezco a mis padres por brindarme toda la paciencia, ánimo y amor que es posible entregar. También a mi hermana que siempre ha mostrado su confianza y admiración en lo que hago.

A los integrantes del Departamento de Física y del Departamento de Astronomía, por la formación y el apoyo que me han brindado, no tan solo para la concreción de este grado, sino también por su orientación para lo que resta de mi vida profesional. No podría dejar de mencionar toda la confianza que ha depositado en mí el Profesor Gonzalo Palma, quien no dudó en guiar la realización de este trabajo, a pesar de desviarse de su primera línea de investigación. Espero haber contribuido en algo con esto a la integración de las diferentes disciplinas científicas en nuestra institución. Al Profesor Luis Campusano, por haberme puesto en contacto con proyectos de alcance internacional, como lo es Polarbear, y todo su apoyo y asesoramiento durante mi tiempo trabajando en este proyecto. Al Profesor Nelson Zamorano por su programa de Escuela de Verano para estudiantes de enseñanza media, que me animó a seguir una carrera en Física. A los Profesores Rolando Dünner y Domenico Sapone, por haber accedido a ser examinadores externos de este trabajo a pesar del poco tiempo de antelación con el que contaron.

A mis amigos de la Facultad de Ciencias Físicas y Matemáticas, a quienes les estoy muy agradecido por su apoyo y aliento durante mi tiempo en pregrado y postgrado: Paola Rojas, Sergio Liberman, Nicole Díaz, Javiera Figols, Alan Troncoso, Salvador López, Romina Arriaza, Alexander Hetz, entre muchos otros. En relación con este trabajo, doy mención especial para Natalia Díaz y Constanza Muñoz, a quienes torturé con prácticas del examen de grado, y cuyas observaciones fueron muy útiles.

A mis amigos de adolescencia, Camilo Alcaraz y Víctor Ortíz, por su amistad duradera.

También me siento extremadamente afortunado de haber trabajado con un fantástico grupo de personas en la colaboración Polarbear. Quiero agradecer especialmente a Dave Boettger por su asesoramiento experto, paciencia y explicaciones reflexivas, que han hecho posible este trabajo. Al Profesor Adrian Lee por haberme dado la oportunidad de trabajar en el proyecto. A Neil Goeckner-Wald, Satoru Takakura y Yuji Chinone por haberme ayudado en asegurar una correcta implementación de las mejoras al estimador del espectro de potencia que este trabajo contiene. A Nolberto Oyarce y José Cortes, por hacer mi tiempo en el sitio del telescopio más agradable de lo que habría sido de otra manera. Y podría seguir enumerando a muchos otros miembros de la colaboración que de una u otra manera hicieron

de mi participación en este proyecto la mejor de las experiencias.

No puedo terminar sin antes agradecer a mis compañeros de estudios de postgrado en la Universidad Johns Hopkins, quienes, aunque no tienen directa relación con el contexto en que se desarrolló esta tesis, han hecho de mi estadía en los Estados Unidos una experiencia muy enriquecedora. Sin más, agradezco a mis amigos Yasuo Oda, Zackary White, Enoch Leung, Alvin Modin, Gabriela Sato-Polito, Isu Ravi, Vicente Munizaga y tantos otros por ser tan acogedores y amigables. Mención especial nuevamente a Carolina Núñez, a quien también torturé con mis ensayos de la defensa de tesis y cuyas sugerencias han sido diligentemente adoptadas.

A Fondecyt, por el soporte económico brindado durante dos años y medio de realización de este trabajo de tesis.

Acknowledgements

I am indebted to many people who have selflessly supported me during the development of this work and everything that preceded it, despite my numerous imperfections. I hope that I have mentioned everyone, but I will certainly not be able to do so, and I apologize in advance if I have omitted anyone.

I can only start with my family, which has been a key support in this process. I give thanks to my parents for giving me all the patience, encouragement, and love that is possible to give. Also, to my sister, who has always shown her confidence and admiration in what I do.

To the members of the Department of Physics and the Department of Astronomy, for the training and support they have given me, not only for the completion of this degree, but also for their guidance for the rest of my professional life. I cannot omit all the confidence that Professor Gonzalo Palma has placed in me, who did not hesitate to advise in the realization of this work, despite it deviating from his primary research line. I hope I have contributed a bit to the integration of the different scientific disciplines in our institution. To Professor Luis Campusano, for including me in projects of international scope, such as Polarbear, and for all his support and advice during my time working on this project. To Professor Nelson Zamorano for his Summer School program for high school students, which encouraged me to pursue a degree in Physics. To Professors Rolando Dünner and Domenico Sapone, for having agreed to be external examiners of this work despite the short notice they had to perform their roles.

To my friends from the School of Physical and Mathematical Sciences, to whom I am very grateful for their support and encouragement over my time in undergraduate and graduate school: Paola Rojas, Sergio Liberman, Nicole Díaz, Javiera Figols, Alan Troncoso, Salvador López, Romina Arriaza, Alexander Hetz, among many others. In relation to this work, I give special mention to Natalia Díaz and Constanza Muñoz, whom I have tortured with thesis defense practices, and whose comments were very useful.

To my lifelong friends, Camilo Alcaraz and Víctor Ortíz, for their lasting friendship.

I also feel extremely fortunate to have worked with a fantastic group of people in the Polarbear collaboration. I specially would like to thank Dave Boettger for his expert guidance, patience, and thoughtful explanations, which have made this work possible. To Professor Adrian Lee for providing me with the opportunity to work on the project. To Neil Goeckner-Wald, Satoru Takakura, and Yuji Chinone who have helped me to ensure a successful implementation of the improvements to the power spectrum estimator that this work contains. To Nolberto Oyarce and José Cortes for making my time at the telescope site more enjoyable than it would have been otherwise. And to many other members of the collaboration who in one way or another made my involvement in this project a wonderful experience.

I cannot finish without also acknowledging my graduate fellows at Johns Hopkins Uni-

versity, who, although not directly connected with the context in which this thesis has been developed, have made my time spent in the United States a very enriching experience. Without further ado, I thank my friends Yasuo Oda, Zackary White, Enoch Leung, Alvin Modin, Gabriela Sato-Polito, Isu Ravi, Vicente Munizaga and so many others for being so welcoming and friendly. Special mention again to Carolina Núñez, whom I also tortured with my thesis defense practices and whose suggestions have been diligently adopted.

To Fondecyt, for the financial support provided during two and a half years of thesis work.

Contents

List of figures

List of tables

Units, notation and conventions

In this thesis, we use the convention of units $c = \hbar = M_P = 1$. c is the speed of light, $\hbar$ is the reduced Planck constant and $M_P = \sqrt{\hbar c/8\pi G}$ is the reduced Planck mass.

$g_{\mu\nu}$ is the spacetime metric.

Greek indices (α, β, ...) are assigned to spacetime components and latin indices (a, b, ...), to field-space components. An asterisk is used for the complex conjugate.

The Christoffel symbols are given by the expression,

$$\Gamma^a{}_{bc} = \frac{1}{2}\gamma^{ad}\left(\partial_b\gamma_{dc} + \partial_c\gamma_{db} - \partial_d\gamma_{bc}\right),$$

where ∂_a are partial derivatives with respect to the scalar fields and the Einstein summation convention is assumed. The Riemman tensor is given by,

$$R^a{}_{bcd} = \partial_c\Gamma^a{}_{bd} - \partial_d\Gamma^a{}_{bc} + \Gamma^a{}_{ce}\Gamma^e{}_{db} - \Gamma^a{}_{de}\Gamma^e{}_{cb},$$

with Ricci tensor and scalar defined as $R_{ab} = R^c{}_{acb}$ and $R = \gamma^{ab}R_{ab}$, respectively. The definitions for the spacetime metric are the same, indices used and context makes them distinguishable.

For noting a quantity as a vector, we interchangeably write in bold or put an arrow on top of the quantity, i.e., $\mathbf{a} \equiv \vec{a}$. We also use bold quantities for tensors and the indices distinguish them. The angular (auto/cross) power spectrum for CMB fields X, Y is interchangeably noted as $C_{XY}(\ell) \equiv C_\ell^{XY}$, where ℓ is the multipole moment. For this quantity, we also consider an interchangeable notation $l \equiv \ell$.

Chapter 1

Introduction

More than a century has elapsed since Einstein published the field equations that govern his theory of General Relativity (GR) [24]. This theory allows the possibility of an expanding universe. This option began to be considered with the observed relation of galaxies receding away with a velocity that is proportional to their distance, made by Edwin Hubble at the end of the thirties [25].

Later, in 1964, Penzias and Wilson were intrigued by an excess source of noise measurements of their radio antenna located at Bell Labs in Holmdel, New Jersey. After discarding a bunch of known interfering signals and cleaning the antenna from pigeons' droppings, the noise was still there, coming from every direction independently of time. Then they were told by a colleague about the search of this signal by another group. The signal was the Cosmic Microwave Background (CMB). It was in the context of early research into Big Bang nucleosynthesis (BBN), a cosmological stage of the Universe, that Gamow, Alpher, and Herman originally predicted the existence of the CMB in 1948 [26–29]. Nevertheless, they were focused on its energy density and did not realize its spectral shape or the fact that it could be measured.[30]

The year before Penzias and Wilson's discovery, the soviet physicists Doroshkevich and Novikov predicted a black body spectrum for the CMB and the possibility to detect it [31]. They even went farther and suggested that a specific Bell Laboratories antenna placed at Crawford Hill, NJ would be an ideal device for measuring it. Finally, this was the antenna used by Penzias and Wilson, unaware of this suggestion. This was reported by them [32], along with a second paper made by Dicke, Peebles, Roll and Wilkinson [33], where the CMB was proposed as a possible theoretical explanation for this measurement. This excess of radio noise, the CMB, would be a thermal artifact of the universe during its early expansion.

As the temperature of the universe dropped, photons were no longer scattered by electrons and protons, which recombined to become neutral hydrogen. In 1967, Partridge and Wilkinson shown that, over large portions of the sky, the temperature fractional difference was of order 0.1 per cent [34] , showing that the Universe was in thermal equilibrium during this decoupling stage.

Since then, several experiments have been deployed to study the universe through the CMB. In 1992, the Cosmic Microwave Background Explorer (COBE) satellite using its Far-InfraRed Absolute Spectrophotometer (FIRAS) instrument measured an almost perfect black body spectral radiation corresponding to a temperature of $T = 2.725 \pm 0.002K$, coming from all directions in the sky [35, 36]. To have in mind, Penzias and Wilson originally reported a temperature of $3.5 \pm 1K$, close to this value. COBE was also the first to observe the CMB anisotropies with an angular resolution of $\sim 7^{\circ}$ using the Differential Microwave Radiometer (DMR) instrument [37]. The extremely good approximation to a black body radiation allowed the possibility to perform precise tests of spectrum distortion through non-thermal energy injections before recombination, such as the existence of long-lived unstable particles.

After COBE, several advances in the field were achieved. The first peak (recombination) of the angular power spectrum of the CMB (defined in Eq.(1.22)) was first measured at the end of the nineties by the Mobile Anisotropy Telescope (MAT) experiment, located on Cerro Toco in the northern Chile [38]. The result was later confirmed by the balloon-based experiments BOOMERanG [39] and MAXIMA-1 [40] over the course of several flights. This proved the universe's flatness [41].

Several years later the Wilkinson Mapping Anisotropy Probe(WMAP) measured with unprecedented precision the first and second acoustic peaks in the CMB temperature anisotropies and further tightened constraints on the Universe's properties, in many cases at the percent levels [42]. This has been progressing to what are now few percent-level measurements. This has set the Standard Cosmological Model as the unrivaled model to explain the physics of the Universe.

One of the prominent breakthroughs in cosmology came in 1998 with the Supernova Cosmology Project, and the High-Z Supernova Search Team [43]. By then, the accepted idea was that the gravitational interaction of matter in the Universe would slow down the recession velocity of objects in the universe and a positive deceleration (negative acceleration) rate was expected. Using type Ia supernovae they measured this rate and contrary to this belief, they found the opposite: objects in the Universe are moving away from each other with a positive accelerated rate. This is known as the accelerating expansion of the universe. This was confirmed with the location of the first CMB acoustic peak described above, and analyses of the clustering of galaxies. This show us that generally accepted "facts" or preconceived notions should always be contrasted with well performed measurements of nature.

In the theoretical side, the theory of cosmic inflation, first proposed in the early eighties independently by Guth [44], Sato [45], Linde [46], Starobinsky [47], Albrecht and Steinhardt [48] to explain the homogeneity and the flatness of our Universe; has as bonus the machinery to generate density fluctuations that seeded the anisotropies in the CMB and subsequent growth of galaxy clusters. The measurements reported by WMAP underpinned the notion

that structures in the Universe emerged from gravitational instability to overdensities, as was thought two decades before these findings. With a similar timing as with Gamow, again, the theory successfully forecasted the measurements made by the WMAP experiment and recently, Planck, long time before.

These observations have provided strong evidence to support the currently leading cosmological model: the concordance or ΛCDM model. The acronym gives us the big picture of the composition of the Universe. The first letter, Λ, refers to the hypothetical source that drives the late expansion of the Universe, the dark energy. The remaining part, CDM, refers to the cold dark matter, which supplies enough gravitational attraction needed to form galaxies and source their observed rotation curves. Its nature and lack of interaction with ordinary matter are still a matter of debate. From the latest measurements our Universe consists of roughly 68.5% of dark energy, 26.6% of cold dark matter and 4.9% of baryonic matter [3], the ordinary matter of the Universe with which we are more familiar. The latter refers to the constituents of ourselves, what surrounds us, the planets, the stars, the interstellar and intergalactic medium. This model consists of a set of six free parameters that characterize the physics, content and geometry of the entire universe. As we mentioned above, some of the components are still modeled only from a phenomenological perspective. We still do not understand the microphysics that governs the nature of the dark matter and the dark energy. This is the reason why many particle physicists have turned into cosmologists to find the required evidence to fill the gaps in their Standard Model.

New, exciting, and unexpected results are going on in Observational Cosmology. Several methods have been developed to determine the rate of the expansion of the Universe with increasing accuracy and precision, but a recent tension has arisen between probes from the early and late universe. Unrecognized systematic uncertainties among several independent tests with the same amplitude and redshift pattern seems extremely unlikely, giving room for the development of new physics that could explain the evolution of the Universe from early to late times.

One of the parameters that it is possible to measure is the current rate of the expansion of the Universe, the Hubble constant, denoted by H_0. There are several independent methods to constrain the value of H_0 using data from the early and late Universe. From the former, we have the CMB power spectrum that contains a wealth of information about the distribution of dark matter, baryons, and radiation at the surface of last scattering. With the knowledge of the temporal evolution of those components and the use of additional assumptions like the spatial flatness of the Universe, it is possible to make precise predictions about the statistical properties of the modern-day universe, including its expansion rate. From the latter, we have methods such as the distance ladder. This method relates distance to redshift using objects with a known (or approximately known) intrinsic luminosity, like the Type Ia Supernovae (SNe Ia). The Cepheid variable stars are used as an intermediate step to help calibrate the supernova absolute luminosity because the rate of SNe Ia is too low in nearby galaxies where we have good direct distances.

Inference from early-Universe probes such the CMB is in an increasing statistical discrepancy with late-Universe determinations of the Hubble constant. For instance, the CMB Planck Mission reports a measurement of $H_0 = 67.4 \pm 0.5\ \mathrm{km\,s^{-1}\,Mpc^{-1}}$ assuming a ΛCDM model [49]. On the other hand, independent local determinations like the ones based on Cepheids/Type SNe Ia yields $H_0 = 74.03 \pm 1.42\ \mathrm{km\,s^{-1}\,Mpc^{-1}}$ [3]. Local measurements seem to be converging to a compatible value that is approximately at a 5σ level away from the Planck Mission.

This issue, known as the Hubble tension, has attracted increasing attention in the cosmological community. This could be the consequence of unaccounted for systematics in one or more experiments, or potential deviations from ΛCDM. The variety and independence of late-universe measurements based on probes like Cepheids/ Type SNe Ia, water megamasers and time-delay cosmography of lensed quasars, makes the existence of such systematics across all these experiments in the same direction, magnitude, and redshift pattern very unlikely [50, 51]. Also, the exclusion of one or more CMB experiments does not help reconcile the two regimes when galaxy clustering data are included [52]. This motivates the consideration of models beyond the ΛCDM concordance model that might contain new physics between the early and late Universe.

Another pending problem in the standard cosmology is the Lithium (^7Li) primordial abundance, known as the Lithium problem [53, 54]. It is theorized that in the first minutes after the Big Bang, nuclear reactions generated light elements such as ^4He, D, ^3He and ^7Li. The standard predictions of the abundance of these elements can be estimated and agree pretty well with the measurements, with the exception of ^7Li abundance by roughly a factor of three. The discrepancy between the predicted and observed Lithium primordial abundance has not been solved neither by new measurements nor by nuclear physics. Therefore, the ancient Lithium problem threatens either the success of BBN or the accepted thermal history of the universe.

Coming back to what bring us in this manuscript, another quest is to detect the primordial gravitational waves which were assumed to have been produced during the primordial stage of superluminal expansion of the universe. These gravitational waves generate unique imprints on the polarized CMB known as the tensor B-modes. Despite several experiments developed to measure them the primordial tensor B-modes remain elusive. If detected, this will be another compelling evidence for the theory of Cosmic inflation that proposes an initial period of exponential expansion of the Universe. The detection will also tell us about the energy scales in which inflation took place. With the increasing number of detectors, its sensitivity and the better control over systematics, in the next years we will be able to constrain this signal with substantially improved statistical power. This thesis shows honest efforts in this direction. Let us review this from the beginning.

1.1 The Standard ΛCDM Model

General Relativity is the theoretical framework that enables our understanding of the expanding universe. The Big Bang theory proposes that the universe we observe now was hotter and denser in earlier times due to its spatial expansion and promoted Cosmology as a precision science. The following review of this framework will be based on many standard books in the field such as [4, 55–58] and also [21, 22].

1.1.1 The Metric in General Relativity

The spatial and time intervals can be formulated for a system of coordinates with the four-dimensional metric tensor $g_{\mu\nu}$. Then we have for a line element ds:

$$ds^2 = g_{\mu\nu} dx^\mu dx^\nu \tag{1.1}$$

This tensor allows us to compute physical distances and time intervals integrating the line elements along some path of interest for the corresponding coordinate system. This is how GR describes the nature of space-time.

In GR, the metric $g_{\mu\nu}$ can be obtained from the Einstein field equations provided with a energy distribution and at the same time the energy moves along geodesics dictated by the metric. In other words, matter and energy dictate space how to curve, and the deformation of space dictates matter and energy how to move [59].

The Einstein field equations are ten coupled and non-linear differential equations which do not admit analytic solutions in general. However, we will simplify this given the experimental facts of the large scale geometry of the universe.

1.1.2 The Cosmological Principle

The Cosmological Principle is an example of a simplified geometry and requires that the distribution of energy be homogeneous and isotropic. This requierement is patently broken in the late universe, although it is thought to hold almost perfectly in the early universe and to a greater extent today at the largest scale. The metric that describes this scenario in the most general expression is the Friedmann-Robertson-Walker(FRW) metric. The line-element follows as [60]

$$\mathrm{d}s^2 = -\mathrm{d}t^2 + a^2(t) \frac{(\mathrm{d}x^2 + \mathrm{d}y^2 + \mathrm{d}z^2)}{\left[1 + \frac{\kappa}{4a^2}\left(x^2 + y^2 + z^2\right)\right]} \tag{1.2}$$

The parameter κ dictates the spatial curvature kind, where κ is 0 for flat space; 1 for positive curvature space and -1 for negative ones. For flat space, this metric case is equivalent to the Minkowski metric case of special relativity, except for the scale factor $a(t)$ that describes the scaling of spatial distances at different times. Hence the physical distances between two points in the x, y, z coordinate system can expand or contract with time, that corresponds to an expansion or contraction of space.

In cosmology, it is convenient to index time with the redshift z that relates the observed wavelength of a signal λ_{obs} to its emitted wavelength λ_{emit}:

$$1 + z = \frac{\lambda_{obs}}{\lambda_{emit}} = \frac{a(t_{obs})}{a(t_{emit})} \tag{1.3}$$

Then if $a(t)$ increases with time, same with the wavelength, and the frequency shifts to the infrared, that corresponds to the redshift today, by a factor $a(t_{emit})/a(t_{obs})$ and z is strictly positive. We define the Hubble parameter as the expansion rate of the universe,

$$H(t) = \frac{\dot{a}(t)}{a(t)} \tag{1.4}$$

For a universe in expansion, $H > 0$, and for a universe in contraction, the converse is true. By convenience and convention, we set $a(t_0) = 1$ and recognize $H(t_0) = H_0$ as the expansion rate of the universe today or the Hubble constant. Then we define a comoving or coordinate distance as the distance traveled by light from an object at time t and redshift z in the coordinate grid to us,

$$\chi(t) = \int_t^{t_0} \frac{dt'}{a(t')} = \int_{a(t)}^1 \frac{da'}{a'^2 H(a')} = \int_0^z \frac{dz'}{H(z')} \equiv \chi(z) \tag{1.5}$$

There are a couple of ways to compute distances that are important in cosmology. First, we have the *angular diameter distance*, the ratio of an object's known physical size l to the angle subtended by l at emission time as observed on Earth. Assuming absence of curvature, it is

$$d_A(z) = a(z)\chi(z) = \frac{\chi(z)}{1 + z} \tag{1.6}$$

The second is the *luminosity distance*. This describes the distance at which an object would locate based on its measured luminosity. This considers two attenuating factors: relativistic redshift and the Doppler shift of emission, with a contribution $1 + z$ of attenuation from each of them. Again, assuming $\kappa = 0$, we have:

$$d_L(z) = \frac{\chi(z)}{a(z)} = (1 + z)\chi(z) \tag{1.7}$$

All these three distance measures will differ at large redshifts, say $z > 0.1$, given the effects of the universe's expansion or contraction encoded in z, that will allow us to distinguish between these two states and their rate.

1.1.3 The Einstein-Friedmann equations

The motion equations of a test particle in the ΛCDM universe are obtained from the Einstein field equations,

$$\mathbf{G}_{\mu\nu} \equiv \mathbf{R}_{\mu\nu} - \frac{1}{2}\mathbf{R}\,\mathbf{g}_{\mu\nu} = \frac{8\pi G}{c^4}\mathbf{T}_{\mu\nu} \tag{1.8}$$

where $G_{\mu\nu}$ is the Einstein tensor, $R_{\mu\nu}$ and R are Ricci tensor and scalar, $g_{\mu\nu}$ is the metric discussed in Section 1.1.1, G is the Newton's gravitation constant, $T_{\mu\nu}$ is the stress-energy tensor, and c is the speed of light. Without anisotropic stresses or bulk flow, the stress-energy tensor can be written as:

$$\mathbf{T}_{\mu\nu} = \begin{pmatrix} \rho(t) & 0 & 0 & 0 \\ 0 & -p(t) & 0 & 0 \\ 0 & 0 & -p(t) & 0 \\ 0 & 0 & 0 & -p(t) \end{pmatrix} \tag{1.9}$$

where ρ represents the density and p the pressure of a perfect fluid with all the symmetries discussed previously. Obtaining the FLRW metric above was based on symmetry arguments and not on GR. It is matter of GR to obtain the scale factor $a(t)$ provided by a physical distribution of matter and energy following the Cosmological Principle described above. We can obtain the Friedmann equation, which dictates the evolution of the scale factor $a(t)$, by evaluating Eq.(1.8):

$$H^2(t) + \frac{\kappa}{a^2(t)} = \frac{8\pi G}{3}\rho(t), \quad \frac{\ddot{a}(t)}{a(t)} = \dot{H}(t) + H^2(t) = -\frac{4\pi G}{3}\left[\rho(t) + 3p(t)\right] \tag{1.10}$$

Here we have set $c = 1$. Using the conservation of the stress-energy tensor $T^{0\mu}{}_{;\nu}$, we have:

$$\dot{\rho}(t) + 3H(t)\left[\rho(t) + p(t)\right] = 0 \tag{1.11}$$

Cosmology often deals with low density gases, for which the equation of state is simple. For fluids of cosmological interest, the equation of state can be reduced to a simple linear relation:

$$p(t) = \omega\rho(t) \tag{1.12}$$

The, we can rearrange Eq.(1.11) as:

$$\frac{d\rho}{\rho} = -3(1+\omega)\frac{da}{a} \tag{1.13}$$

Assuming ω as a constant, then we have,

$$\rho(a) = \rho_0 a^{-3(1+\omega)} \tag{1.14}$$

That allows as to consider $a \sim \rho^{\frac{1}{-3(1+\omega)}}$ for $\omega \neq -1$. With the proper normalization, the scale factor in a spatially flat, single-component universe is:

$$a(t) = \begin{cases} \left(\frac{t}{t_0}\right)^{\frac{2}{3+3\omega}} & \text{for } \omega \neq -1 \\ e^{H(t-t_0)} & \text{for } \omega = -1 \end{cases} \tag{1.15}$$

Where t_0 is such that $a(t_0) = 1$. We see that the evolution of the scale factor $a(t)$ and the Hubble parameter $H(t)$ will depend on the fluid component under consideration. We know that our universe contains a mix of different fluid components, so we will sort them by their contribution to the pressure. The most remarkable cases are:

- **Cold Matter**. Also known just as *matter*, is used to denote *nonrelativistic matter* and corresponds to any kind of substance which contributes with negligible pressure, $p = 0$. A pressureless Universe is the simplest supposition that we can consider, where mass is the main component of the energy density. This describes pretty well the baryons in the Universe after the temperature has decreased significantly, as they are enough apart and without interact, and also applies to clusters of galaxies in the Universe, as the gravitational interaction is the only one they experience with each other. This includes dark matter. The concept *dust* is also used to refer to *matter* in some contexts. Setting $w = 0$, we obtain $\rho \propto a^{-3}$. This energy density's decrement is just the consequence of the expansion of a volume $V \propto a^3$.

- **Hot Matter**. Or better know as *radiation* or *relativistic matter*. Light particles travel, as we can guess, at the speed of light. Their dominant kinetic energy conducts to a pressure force, the radiation pressure, which can be proven to be $p = \rho/3$ with the aid of the standard theory of radiation. More broadly, any gas of particles traveling at relativistic speeds carry this equation of state. Photons, neutrinos, and gravitons being an obvious example. Setting $w = 1/3$, we obtain $\rho \propto a^{-4}$. Three of those powers we have already recognized as the expansion in volume, causing a dilution in the density. The remaining power is caused by the stretching of the wavelength of the photons. Since the stretching is proportional to the scale factor, and the energy of photons is proportional to their frequency $E = hf$, this ends in an extra decrease in energy density by the remaining power of a. This drop of energy is the same redshifting phenomena that we account to measure distances.

- **Dark Energy**. Contrasting with dark matter, this is a form of nonclustered energy density with negative pressure. It may be either a cosmological constant with $p = -\rho$ or a scalar field (quintessence) with $p = \omega\rho$ and $\omega < -1/3$ today. This is the hypothetical source for the late expansion of the universe. In the case of a cosmological constant it is also known as *vacuum energy* where a constant energy density $\rho \propto a^0$ is obtained. As we can see in this case, there is not dilution in the energy density, generating energy with the universe's expansion.

- **Curvature**. The curvature of spacetime can be thought as a fluid with $\omega = -1/3$ and an energy density $\rho \propto a^{-2}$.

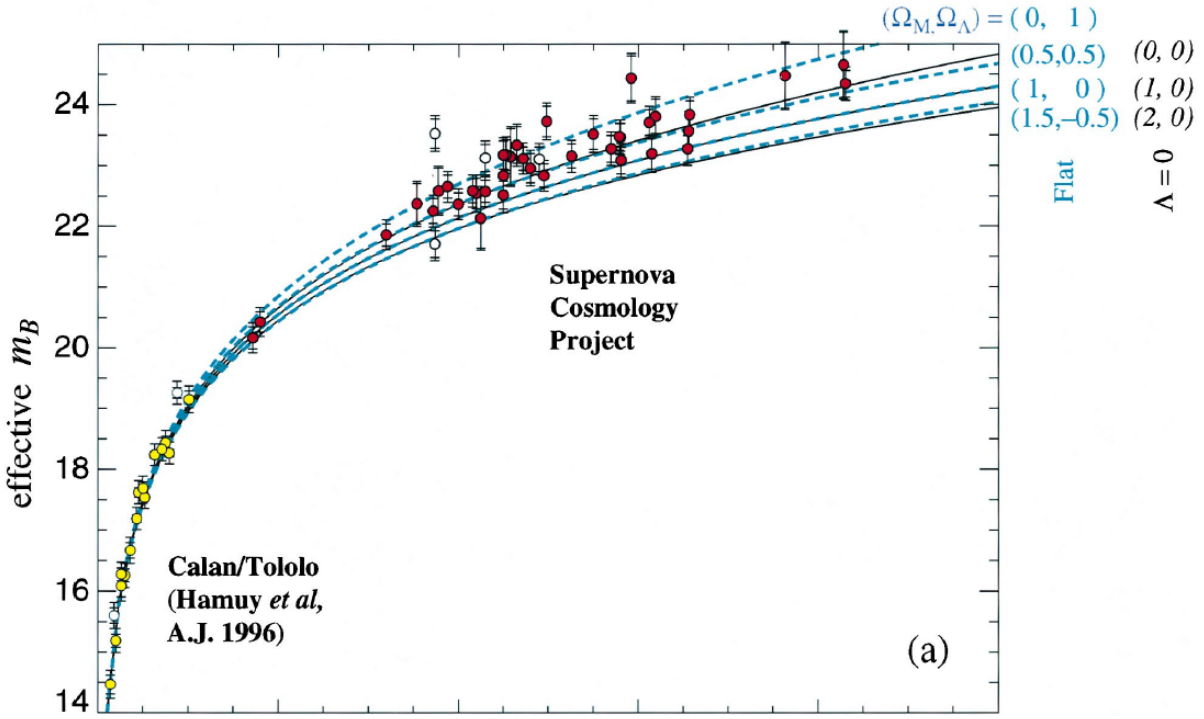

Figure 1.1: Discovery of an accelerating universe. The supernovae magnitude-redshift data for the Supernova Cosmology Project, at $0.18 < z < 0.83$, are fitted together with a set of supernovae from the Calán/Tololo Supernova Survey, at $z < 0.1$, for cosmological parameter inference. This was one of the attestations found at the end of the 1990's for dark energy. Figure from [1]. © AAS. Reproduced with permission.

From Eq.(1.10) we can denote the critical density of the universe ρ_c which is the density needed for the universe to be spatially flat with $\kappa = 0$,

$$\rho_{c,0} = \frac{3H_0^2}{8\pi G} \tag{1.16}$$

Where '0' stands to specify that these are today's values. It is customary to normalize the energy densities with respect to the ρ_c as the *density parameters*,

$$\Omega_{X,0} = \frac{\rho_{X,0}}{\rho_{c,0}} \tag{1.17}$$

Where X stands for any constituent of the universe: cold-dark matter (c), baryons (b), radiation (r), cosmological constant or dark energy (Λ) and m for the total non-relativistic matter $\Omega_{m,0} = \Omega_{c,0} + \Omega_{b,0}$. We can also define the curvature density parameter,

$$\Omega_{\kappa,0}(a) = -\frac{\kappa}{a^2 H_0^2} \tag{1.18}$$

Then inserting these definitions in Eq.(1.10), it becomes

$$H(a) = H_0\sqrt{\Omega_{r,0}a^{-4} + (\Omega_{c,0} + \Omega_{b,0})a^{-3} + \Omega_{\kappa,0}a^{-2} + \Omega_\Lambda} \tag{1.19}$$

The measurements are consistent with a flat universe with the density value equal to the current value of critical density $\mathcal{O}(10^{-27})$ kg m^{-3}, so we will omit it for the rest of this manuscript.

1.1.4 The concordance model of cosmology

The concordance or ΛCDM model consists of a set of six free parameters that characterize the content and geometry of the entire universe. It is built on well-proved physical postulates, which includes general relativity that characterizes the dynamics of the expansion of the universe, the quantum mechanical principles that rule the production of particle species during the early universe, and the Boltzmann equation which let us to analyze the evolution of each of these species.

Nevertheless, nearly all the parameters in this model carry information about still non-completely understood physics. The relative ratios of baryons, dark matter and dark energy in the universe are ruled by elemental processes that are still beyond the scope of the present-day Standard Model of particle physics, and might prolong up to the TeV, GUT or even Planck energy scales. There are several ways to define the set of parameters depending in the availability of data required to measure specific combinations of observables and our understanding of the underlying physics behind each of these parameter combinations.

Parameter	Planck TT,TE,EE+lowE+lensing
$\Omega_b h^2$	0.02237 ± 0.00015
$\Omega_c h^2$	0.1200 ± 0.0012
$100\theta_{MC}$	1.04092 ± 0.00031
τ	0.0544 ± 0.0073
$\ln(10^{10} A_s)$	3.044 ± 0.014
n_s	0.9649 ± 0.0042

Table 1.1: Baseline results for the six main parameters 68% confidence levels for the base-ΛCDM cosmology computed from the Planck CMB power spectra, in combination with CMB lensing reconstruction. Results extracted from [3].

Table 1.1 shows the six base parameter values inferred for the concordance model reported by [3]. From Table 1.1 we can extract with the appropriate parameter combinations that a flat universe is favored with a composition lead by 68.5% of dark energy, 26.6% of cold dark matter and 4.9% of baryonic matter. This configuration of the parameters contains information related to the primordial conditions needed to generate the CMB power spectrum. Under the supposition of a primordial universe permeated with small adiabatic curvature perturbations characterized with the following power spectrum term (which explanation will be more clear in Section 2.2.2):

$$\mathcal{P}_{\mathcal{R}} \propto A_s k^{n_s - 1} \tag{1.20}$$

Data from Table 1.1 constrains Eq.(1.20) to an approximated scale invariant power spectrum.

1.1.5 Brief thermal history

In Section 1.1.4 we examined the current content of the universe. The concordance model depicts the way dark energy is the main component of the universe, and how it is constituted

of a specific number of species. Inasmuch as dark energy keeps constant in time, at some point before, matter and radiation should have been the main components.

In the early epochs of our universe, it was hotter and denser than ever, experiencing an exponential expansion. This implies that they were featured by high energies, where some specific violated symmetries of fundamental physics were recovered, and by the important function that $H(t)$ performs as a time scale. Interaction among species freeze out or decouple as the interaction rate decreases below the expansion rate. Table 1.2 outlines phase transitions linked to events where symmetry is broken. We will give a brief summary of the most important events in the evolution of the Universe. This is heavily based on [57]:

	Time	Energy	Redshift
Electroweak phase transition	$2 \cdot 10^{-11}$ s	100 GeV	10^{15}
QCD phase transition	$2 \cdot 10^{-5}$ s	150 MeV	10^{12}
Neutrino decoupling	1 s	1 MeV	$6 \cdot 10^{9}$
Electron-positron annihilation	6 s	500 keV	$2 \cdot 10^{9}$
Big Bang nucleosynthesis	180 s	100 keV	$4 \cdot 10^{8}$
Matter-radiation equality	60 kyr	0.75 eV	3400
Recombination	$260 - 380$ kyr	$0.26 - 0.33$ eV	$1100 - 1400$
CMB decoupling	380 kyr	$0.23 - 0.28$ eV	$1000 - 1200$
Reionization	$100 - 400$ Myr	$2.6 - 7.0$ meV	$11 - 30$
Dark energy-matter equality	9 Gyr	0.33 meV	0.4
Today	13.8 Gyr	0.24 meV	0

Table 1.2: Some events of the termal history of the universe. Based on [21, 22].

- $\sim \mathbf{10^{-43}}$s ($T \sim 10^{19}$ GeV) We are in the Planckian scale regime and nonperturbative quantum gravity governs the dynamics, relegating General Relativity. The main problems of spacetime structure at the Planckian scale such as the question of cosmic singularities are still without a convincing explanation. An expected nonperturbative string/quantum gravity theory is awaiting to be discovered here to explain these mysteries.

- $\sim \mathbf{10^{-43} - 10^{-14}}$s ($T \sim 10^{19}$ GeV-10 TeV) These energy scales are outside the reach of current and planned accelerators. Nonperturbative quantum gravity would lose its predominance and General Relativity would be restored to explain the dynamics of the universe. The big question here is what the matter content of the Universe is. There are big chances of more particle species than what is observed today. Supersymmetry predicts that we should have twice the number of particles species. This theory also offers us interesting weakly interacting massive particle options for dark matter.

  Cosmic inflation, a plausible explanation for the accelerated universe's expansion, is expected to have took place close to the Grand Unification energy scales. Fortunately, the main predictions of inflation are not greatly dependent on undiscovered particle physics. Thus, is expected that we will be able to contrast their predictions with observations somewhen in the future.

The creation of baryon asymmetry in our universe is also linked to physics beyond the Standard Model. A *Grand Unification* of the electroweak and strong interactions are expected to dominate at energy scales of order 10^{16} GeV. Maybe cosmic strings, monopoles and other topological defects produced in unified theories were present in the early universe but current measurements of the CMB anisotropy rules out any significant role for large scale structure.

- $\sim \mathbf{10^{-14} - 10^{-10}}$s ($T \sim$ 10 TeV$-$100 GeV) We enter to the regime of energy scales achievable by accelerators. We can start to consider the application of the Standard Model of electroweak and strong interactions rules here. We expect that at temperatures below this regime the electroweak symmetry is broken, and the gauge bosons become massive. Fermion and baryon numbers become mostly conserved below these symmetry breaking temperatures.

- $\sim \mathbf{10^{-5}}$s ($T \sim$ 200 MeV) This is the quark–gluon transition energy scale: free quarks and gluons ends within baryons and mesons. The mechanism of such transition remains a mystery, although it is not believed that this event has left any relevant cosmological signature.

- $\sim \mathbf{0.2}$s ($T \sim 1 - 2$ MeV) With the drop in temperature, some weak interaction mechanisms fall out of equilibrium. To begin, the decoupling of primordial neutrinos from the rest of the matter takes place and they stream freely. Also, the ratio of neutrons to protons becomes constant as they are not chemically in equilibrium anymore due to the inefficiency of such interactions. The number of neutrons left after this proportion freezing will dictate the abundances of primordial elements.

- $\sim \mathbf{1}$s ($T \sim$ 0.5 MeV) This is the energy scale of the electron mass. Electrons and positrons start to annihilate in pairs as the temperature decreases below their rest mass and only a small fraction of electrons over positrons, approximately one per billion photons, are left after annihilation. The photons generated by these annihilations are in thermal equilibrium and their associated temperature rises with respect to the temperature of neutrinos, which have been decoupled before.

- $\sim \mathbf{200 - 300}$s ($T \sim$ 0.05 MeV) The temperature decreases enough for nuclear reactions to be efficient. Consequently, free protons and neutrons can combine into helium, lithium, and beryllium. The abundances of such elements predicted by primordial nucleosynthesis coincides in greatly extent to the measurements performed up to date and confirms our notions of the history of the universe since the first second of this plot.

- $\sim \mathbf{10^{11}}$s ($T \sim$ eV) During this period, the matter–radiation equality occurs which divides the radiation-dominated epoch from the matter-dominated epoch. The precise cosmological time at which equality took place is depended on the components of the dark matter and, thus, its current value is known with a multiplicative numerical factor of order unity.

- $\sim \mathbf{10^{11}}$s ($T \sim$ eV) During this period, the matter–radiation equality occurs which divides the radiation-dominated epoch from the matter-dominated epoch. The precise cosmological time at which equality took place is depended on the components of the dark matter and, thus, its current value is known with a multiplicative numerical factor of order unity.

Photons and charged matter particles are highly coupled in the plasma and density fluctuations disseminate as cosmic sound waves. About 0.1 eV (380. 000 yrs) electrons and protons merge into neutral hydrogen atoms. This period, when the the atoms starts to produce neutral hydrogen is known as recombination (a misnomer because electrons and nuclei were never combined before).

When the universe was at temperatures slightly above than 3000K it was formed of an ionized plasma of mainly electrons, protons and photons, with mostly helium and vestiges of lithium. The most important characteristic of this plasma was its opaqueness, this is to say, the mean free path of a light particle was shorter than the Hubble length. With the universe decreasing its temperature and expanding, the plasma recombines into neutral atoms, starting with helium and a bit later the hydrogen.

Following recombination, as we mentioned above, the plasma became neutral and finally the mean free path for light surpassed the Hubble length, because radiation decoupled from matter. The universe become filled of a background of free streaming photons with a nearly perfect black body radiation spectra during the recombination epoch. The initial temperature of this background radiation was of $T = 3000$K. The photons gets redshifted due to the expansion of the universe, causing its temperature to decrease with the growth of the scale factor as $T \propto a^{-1}$. It is possible for us to measure this background radiation today coming isotopically from all directions in the sky as seen from the Earth, with a temperature that averages $T_0 = 2.73$K. This is known as the cosmic microwave background (CMB). As we look to objects at higher redshifts, we are looking more to the past in time, so we observe the CMB photons as originated at a uniform surface of last scattering located at redshift 1100.

To the degree that recombination occurs at the same moment and in the same manner in all places, the CMB will be characterized of a precise uniform temperature. Although the observed CMB is highly isotropic, it is not totally isotropic. The most important contribution to CMB's anisotropy as observed from the Earth is merely Doppler shift produced by our planet's motion through space. The CMB photons experience a slight blue shifting in the same direction of our motion and a slight red shifting in the opposite direction of our motion. This motion changes the temperature of the CMB producing a distinctive shape of a dipole temperature anisotropy. However, it is a local feature that can be averaged out. Furthermore, any locally uniform perturbation will add to the effective temperature background, effect that would not be noticeable for us. Because of the mentioned reasons, we conclude that $\ell = 0, 1$ that corresponds to the monopole and dipole moments, are gauge dependent in a part in a one hundred thousand, so there is no reason to care too much about their precise values.

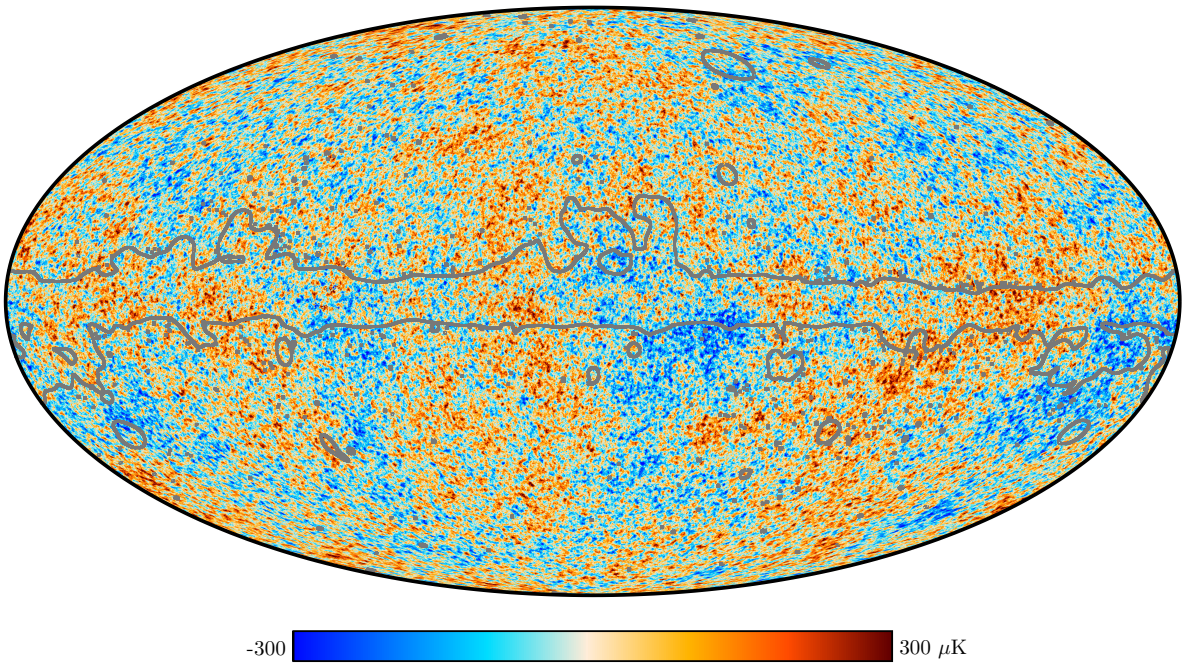

Figure 1.2: Temperature fluctuations in the CMB, as observed by Planck satellite. This map has been masked and inpainted in zones where residuals from foreground emission are believed to be important. This mask, mainly around the Galactic plane, is depicted by a grey line in the map. Figure from [2]. Reproduced with permission © ESO.

A primordial anisotropy of the CMB would be of much more interest for cosmological purposes. For characterization of the CMB anisotropy, we use the fact that the surface of last scattering is observed by us as a spherical surface at a redshift of $z = 1100$. Then a natural parametrization to describe the anisotropy of the CMB seen in the sky is an expansion in a series of spherical harmonics $Y_{\ell m}(\theta, \phi)$. Despite what was mentioned above about $\ell = 0, 1$, the rest of multipoles $l > 1$ are truly gauge invariant and well-defined quantities [61]:

$$\Theta(\theta, \phi) \equiv \frac{\Delta T(\theta, \phi)}{T_0} = \sum_{\ell=0}^{\infty} \sum_{m=-\ell}^{\ell} a_{\ell m}^T Y_{\ell m}(\theta, \phi) \ , \tag{1.21}$$

Assuming statistical isotropy, there are not special directions in the universe. Then the statistical properties of $\Delta T/T_0$ should not dependent on the index m. Under this assumption, it is customary to represent the CMB angular power spectrum as C_ℓ^{TT} which is the variance of the $a_{\ell m}$. The mean value of $a_{\ell m}$ is zero. Hence,

$$\begin{aligned} C_\ell^{TT} \delta_{\ell \ell'} \delta_{m m'} &= \langle a_{\ell m}^{T*} a_{\ell m}^T \rangle \\ C_\ell^{TT} &= \frac{1}{2\ell + 1} \sum_m \langle a_{\ell m}^{T*} a_{\ell m}^T \rangle \end{aligned} \tag{1.22}$$

Formally denoted as the rotationally invariant temperature angular power spectrum. Mathematically speaking, it is the variance of the probability distribution for the multipole moments $a_{\ell m}$. This quantity makes much simpler a big portion of the information hold in a CMB map pixel, and therefore is used in the CMB analysis.

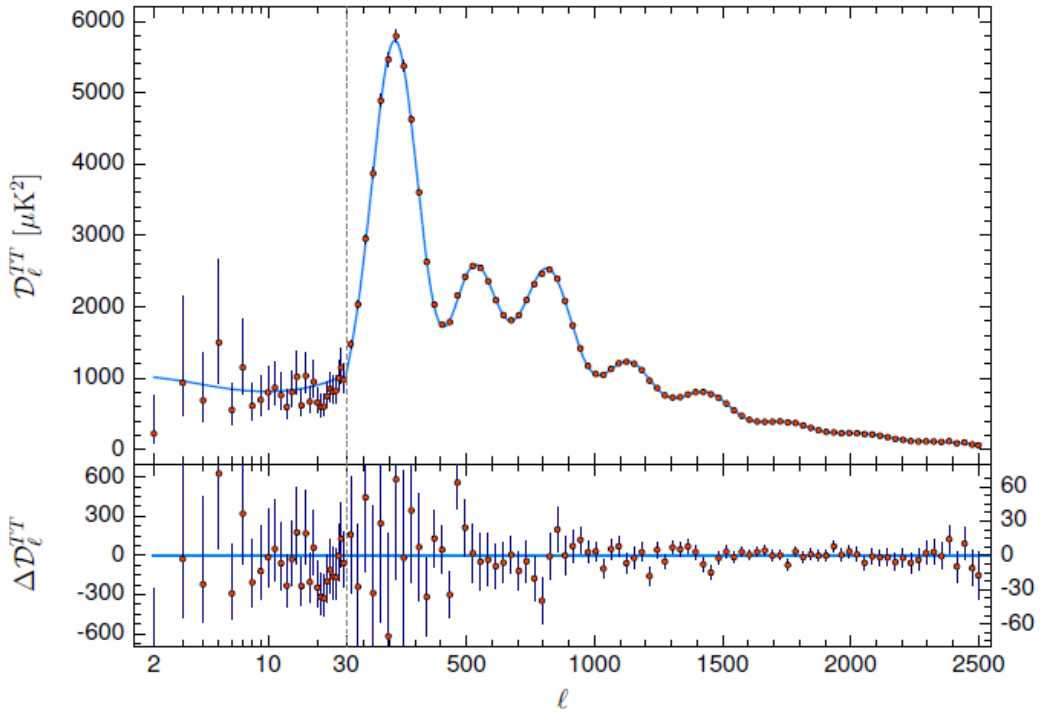

Figure 1.3: The angular power spectrum of temperature fluctuations according to the results of the PLANCK experiment reported in 2018. The base ΛCDM theoretical spectrum best fit to the Planck TT,TE,EE+lowE+lensing likelihoods with fit parameters shown in Table 1.1 is plotted in light blue in the upper panel. The mismatches with this model are reported in the lower panel. The measurements are well modeled by the six parameters ΛCDM model. The error bars include cosmic variance and not uncertainties in the foreground model at $\ell \geq 30$. The horizontal axis is logarithmic up to $\ell = 30$, and linear beyond. The shape of peaks and troughs is a manifestation of the coherence of primordial fluctuation. The vertical axis is $D_\ell^{TT} \equiv \ell(\ell+1)C_{TT}(\ell)T_0^2/2\pi$, where $C_{TT}(\ell)$ is the temperature angular power spectrum. Figure from [3]. Reproduced with permission © ESO.

The $\ell = 1$ moment is simply the dipole temperature anisotropy discussed above,

$$\left(\frac{\Delta T}{T_0}\right)_{\ell=1} \sim 10^{-3} \tag{1.23}$$

The first anisotropy found was the dipole which was first detected in the 1970's by several collaborations. More than a decade later, the first observation of the anisotropy was made for $\ell > 1$ by COBE satellite [37]. COBE's measurements indicates

$$\left(\frac{\Delta T}{T_0}\right)_{\ell>1} \approx 10^{-5} \tag{1.24}$$

This anisotropy shows the authentic fluctuations contained in the CMB induced by the existence of small primordial density fluctuations in the matter component of the universe at the recombination epoch.

These tiny density perturbations increase due to gravitational instability to create the large-scale distribution of the universe at late times. The struggle between the background pressure and the gravitational attraction delineates the particularities of the formation of the large-scale structure. In the radiation domination epoch, the overdensities are increasing at a small pace $\delta\rho \propto \ln a$. We must wait until the matter domination epoch for the overdensities to cluster at a higher rate, $\delta\rho \propto a$. As the small scales grow, they remain linear until $\rho \sim 1$ [55], and then start to collapse in more compact objects that are left behind the large-scale expansion and leave us an image of stratified structure configuration with small-scale structures, such as stars and galaxies, emerging and then clustering in larger structures, such as clusters and superclusters of galaxies.

At approximately redshift $z \sim 25$, high energized photons coming from the earliest stars start to ionize the hydrogen in the surrounding intergalactic medium. This epoch is known as reionization and ends at $z \sim 6$. In the meantime, the stars with highest mass exhausted their nuclear supplies and explode as supernovae. These explosions create the heavy elements (C, O, etc.) that are needed for the emergence of life. After $z \sim 1$ dark energy with its negative pressure become dominant in the expansion of the universe, counteracting the gravitational clustering, discontinuing the growth of structure, $\delta\rho \approx$ constant.

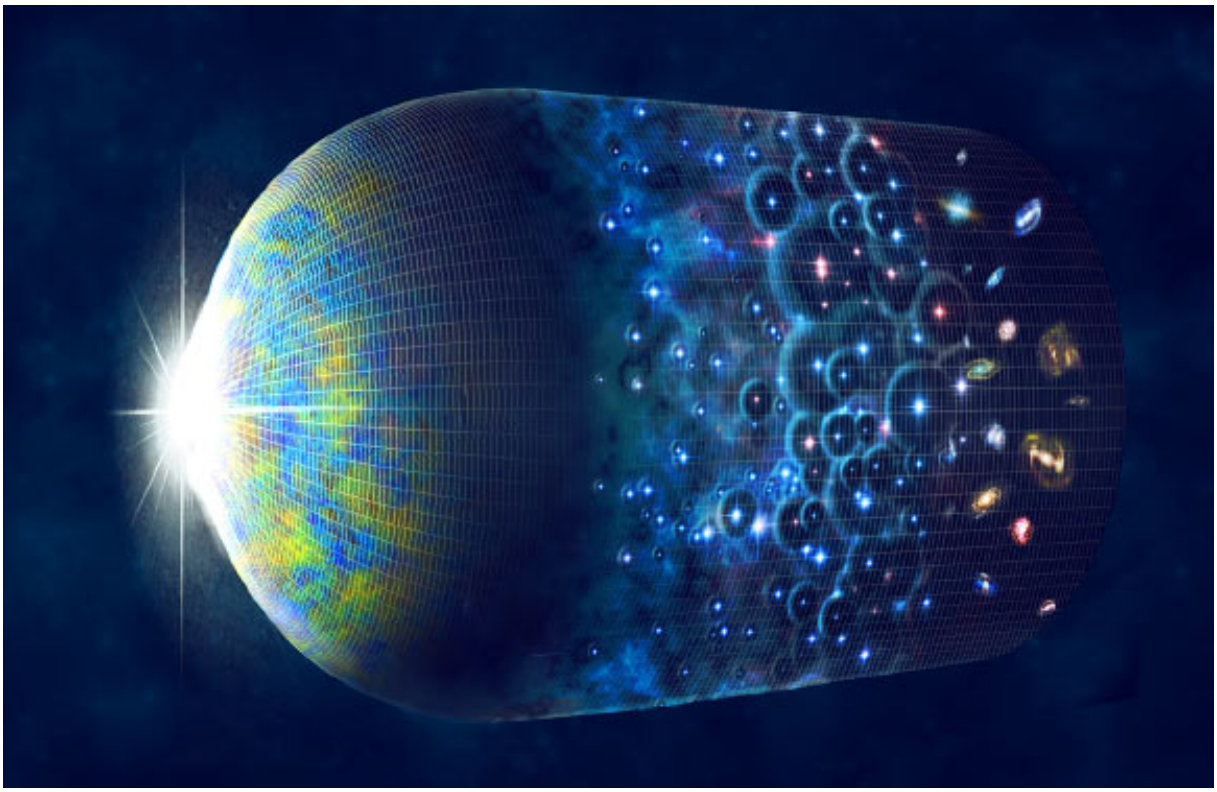

Figure 1.4: An artist's representation depicting the evolution of the Universe. It starts with the Big Bang on the left end of the figure. Moving to the right, we have the emergence of the CMB. Next, the formation of the earliest stars puts an end to the cosmic dark ages. Finally, to the right end of the picture, the plot ends with the formation of galaxies. Image credit: M. Weiss / Harvard-Smithsonian Center for Astrophysics.

Currently, there are several experiments such as Polarbear [6], CLASS [62], BICEP2 and KECK Array [14], ACTPol [15], SPTpol [11], SPIDER [63] and QUIJOTE [64], and also forthcoming experiments such as Simons Observatory [65], LiteBIRD [66] and PIPER [67], in the challenging quest of primordial gravitational waves (PGW) by the detection their unique imprints – the tensor B-modes – on the polarized CMB radiation. The PGW were produced during the first times of the universe when the universe expanded exponentially by a mechanism known as cosmic inflation. The fundamental importance of the primordial B-modes lies in the fact that they should be a product of quantum gravity phenomena. Moreover, we would be able to discover the energy scale of cosmic inflation. The quantum physics of inflation tell us that its signal should be there because it must excite light degree of freedom, but we do not have a clue of its energy. The solely detection of this signal will tell us by its own something about its energy, regardless of the inflationary model. If quantum fluctuations can justify the properties of primordial fluctuations that are somehow encoded in the distribution of our current universe, this would mean that quantum gravity effects are observable. This would imply that CMB polarization measurements can test physics at the grand unification energy scale, unachievable to any other current experimental technique. Such claims encourage our efforts to push the experimental frontiers to reveal the secrets of this elusive treasure.

The objective of the present thesis is to show my efforts in the validation of the power spectrum estimator of the polarized CMB within the context of one of the abovementioned projects, the Polarbear experiment.

1.2 Outline of this thesis

The outline of this thesis is the following: In Chapter 1, I sketch the most remarkable features of the standard cosmological model ΛCDM. In Chapter 2, I give a quick review of the standard paradigm of inflation. In Chapter 3, I discuss the mechanisms that shape the CMB polarization spectra, analyzing piece by piece the main features for the polarized signal, and its relation to inflationary physics. In Chapter 4, I introduce the Polarbear experiment, giving a quick summary of the different stages of the data analysis pipeline, with a focus on those that are applied earlier in the pipeline than the power spectrum estimator to the data. In Chapter 5, I present the background of the power spectrum estimator, the motivation of the present work and the study and implementation of prospective changes of such estimator. In Chapter 6, I show the implementation and results of different tests performed to test solely the performance of the implemented modifications, along with the coupling of such changes to the main data analysis pipeline and the final power spectrum validation of the entire data analysis framework, for which the products of this work constitute an integral part. In Chapter 7, I give a brief summary of the science results of the fiducial data analysis pipeline applied to real data, that uses the modifications described in this thesis. Finally, Chapter 8 presents some conclusions.

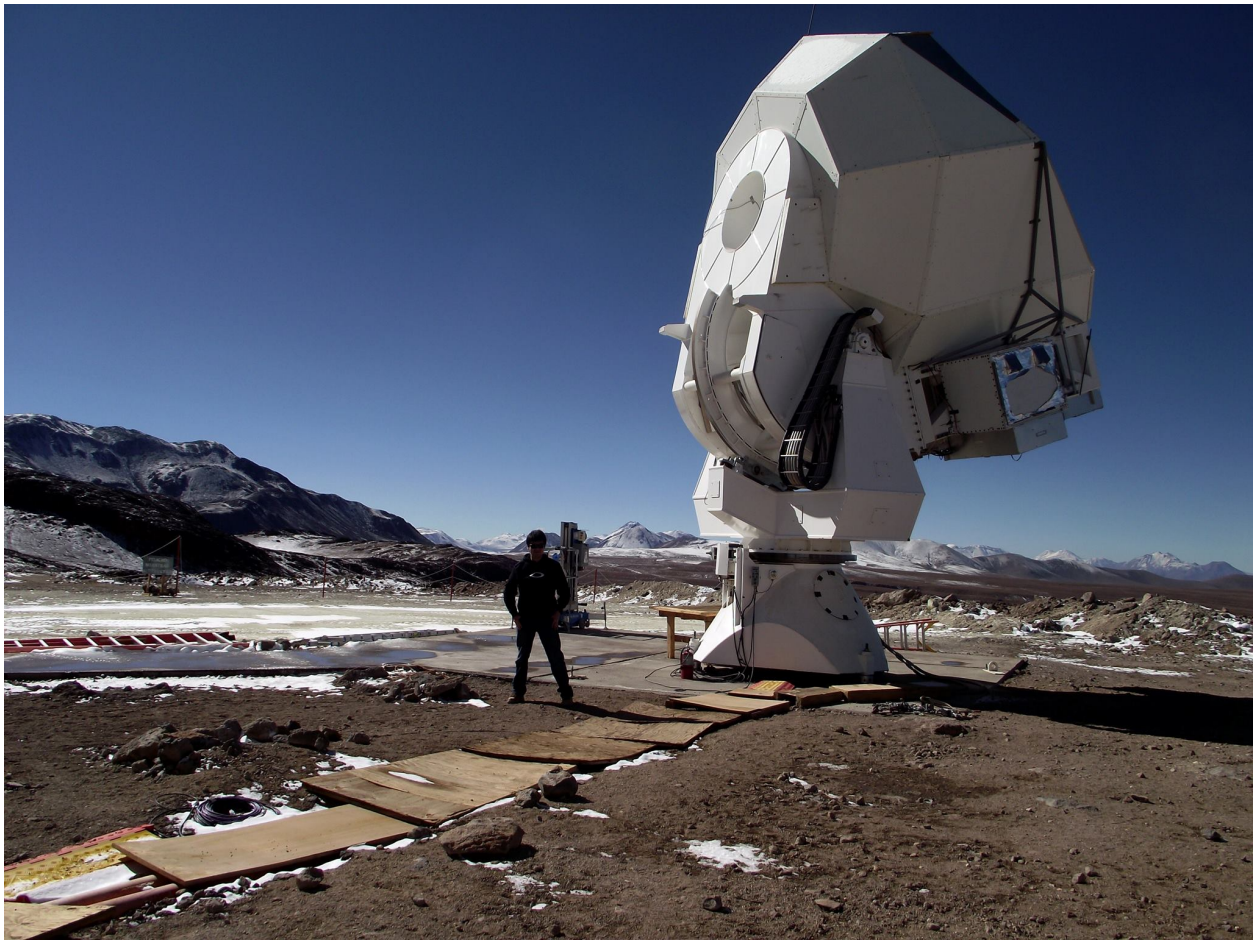

Figure 1.5: Me at the James Ax Observatory of the Polarbear experiment, located in the Chajnantor scientific reserve (Northern Chile) at an altitude of nearly 5200 m.

Chapter 2

Cosmic Inflation

The cosmic inflation or merely inflation is an early stage of our universe. During this epoch, the universe experiments a considerable exponential spatial expansion. This period can solve the issues associated with the universe flatness and why it is so homogeneous and isotropic on large scales. Soon, it was also noticed as a mechanism to generate the largescale structure (LSS) of the universe, producing quantum fluctuations of tiny regions of the space that grew exponentially by the inflationary expansion of the universe to form the LSS that we see today [44, 68].

The study of this mechanism will give us the initial conditions for the treatment of the Boltzmann and Einstein equations. As we have mentioned in Chapter 1, a direct experimental test of inflation requires energy scales that are largely out of the reach of present-day accelerators. However, it is the most promising explanation for the formation of the LSS and will have to confront the scrutiny of the forthcoming generation of CMB and LSS survey experiments, characterized by a dramatic increase in sensitivity.

A common set of predictions derived from the inflationary models have already been confirmed: the characterization of the primordial perturbations as Gaussian, adiabatic and described by a roughly scale-invariant power spectrum with a spectral index marginally below the unity. We will explore this in this chapter. We will begin with a brief review about some cosmic problems that motivated the idea of inflation and how it solves them. Then, the inflation-driven dynamics of the homogeneous and isotropic background for a single scalar field is introduced, and the simplest case of slow-roll is presented within this framework. Finally, the theory of primordial perturbations generated during the epoch of inflation is reviewed including their potential ability to tell us about the energy scales that drive inflation.

This chapter is in part based on [4, 21, 22, 56]. The content and structure of this chapter is greatly influenced by [69, 70].

2.1 Causal structure

The most sacred principle of physics refers to Causality. As the word suggests, it rules the relation between causes and effects. An effect cannot depend on a cause in the future. This tenet dictates the forms of both already discovered and hypothetical interactions of particle physics. In the context of General Relativity, it fundamentally defines the boundaries between regions of space time where events can influence each other with regions were this is not possible depending on their spatial and time coordinates. For a specific spacetime, this information is contained in the metric as we already have discussed in section 1.1.1 and will tell us if two events are able to make causal contact or not. For example, if we have enough time, two events can influence each other no matter how far from each other they are given the Minkowski metric case of special relativity. In contrast, no matter how much time passes, an object inside a Black Hole's event horizon will not be able to contact an object outside it. This introduces our task in this section. Whether or not two entities in an FWR universe can contact each other, and how it defines the causal structure of such universe.

This structure is defined by the propagation of photons in the universe given an FRW metric. Any massless particle like photons will move along null geodesics, mathematically $\mathrm{d}s^2 = 0$ in Eq.(1.2). For convenience, regarding these trajectories, we can define the conformal time,

$$\tau \equiv \int \frac{\mathrm{d}t}{a(t)} \tag{2.1}$$

for which the FRW metric becomes a Minkowski metric $\eta_{\mu\nu}$ rescaled by a time-dependent conformal factor $a(\tau)$

$$\mathrm{d}s^2 = a(\tau)^2 \eta_{\mu\nu} dx^\mu dx^\nu, \tag{2.2}$$

By isotropy we can just consider the radial propagation of photons, therefore, neglecting the angular term of the line element above,

$$\mathrm{d}s^2 = a(\tau)^2 \left[-\mathrm{d}\tau^2 + \mathrm{d}r^2\right], \tag{2.3}$$

Then, null geodesics written in conformal time are sketched as straight lines at 45° in the $\tau - r$ plane

$$r(\tau) = \pm\tau + \text{const.}, \tag{2.4}$$

The upper limit for the distance that photons can travel in the time interval $[t_\mathrm{i}, t]$ with $t > t_\mathrm{i}$ is

$$\Delta r(t, t_i) = \tau - \tau_\mathrm{i} = \int_{t_\mathrm{i}}^{t} \frac{\mathrm{d}t'}{a(t')}. \tag{2.5}$$

From Eq.(2.1) we recognize that this distance is equivalent to the amount of conformal time elapsed during the time interval $[t_\mathrm{i}, t]$. We can define the maximum distance traveled from the origin of the universe $t_\mathrm{i} = 0$ up to a later time t as the (comoving) particle horizon at that specific time t,

$$\Delta r_{max}(t) = \tau(t) - \tau(t_\mathrm{i}) = \int_0^t \frac{\mathrm{d}t'}{a(t')}. \tag{2.6}$$

Rearranging Eq.(2.1), including the definitions from Eqs.(1.3) and (1.4), we have,

$$\tau = \int \frac{\mathrm{d}a}{a^2 H(a)} = \int \frac{\mathrm{d}z}{H(z)} = \int \frac{\mathrm{d}\ln a}{aH(a)} \tag{2.7}$$

This means that the conformal time for a given period lean on the evolution of the comoving Hubble radius $(aH)^{-1}$ during that period. For instance, if we fill the universe with a fluid characterized by an equation of state $\omega = p/\rho$, the evolution is dictated by,

$$(aH)^{-1} \approx a^{\frac{1}{2}(1+3\omega)} \tag{2.8}$$

So, it is a power law with exponent depending on the factor $1 + 3\omega$. The strong energy dominance condition (SEC) $1 + 3\omega > 0$ is obeyed for all the known fluids. This implies the growth of the comoving Hubble radius with the expansion of the universe. Inserting Eq.(2.8) in Eq.(2.1) reduces to

$$\tau \approx \frac{2}{(1+3\omega)} a^{\frac{1}{2}(1+3\omega)} \tag{2.9}$$

The primordial singularity is at $\tau_i = 0$. For familiar sources, this implies

$$\tau_i \propto a_i^{\frac{1}{2}(1+3\omega)} \tag{2.10}$$

And the initial singularity means $a_i = 0$. The SEC avoids an undefinition of this contribution and the comoving horizon in Eq.(2.6) becomes finite

$$\Delta r_{max}(t) \propto a(t)^{\frac{1}{2}(1+3\omega)} \tag{2.11}$$

2.1.1 Flatness Problem

The evolution of the density parameter for the curvature given a FRW metric can be inferred from Eq.(1.18)

$$\Omega_\kappa(a) = -\frac{\kappa}{a^2 H^2} \tag{2.12}$$

To have rough idea, let's assume that the expansion is driven by a generic barotropic fluid with $\omega \neq 0$. Then, from Eq.(1.15) we can compute the evolution,

$$\dot{\Omega}_\kappa = \Omega_\kappa H \left(1 + 3\omega\right) \tag{2.13}$$

If we define N, "the total number of e-folds of inflationary expansion" (we will see what it means later)

$$\mathrm{d}N = \mathrm{d}\ln a = H\mathrm{d}t \tag{2.14}$$

Then we can insert this in Eq.(2.13)

$$\frac{\mathrm{d}\Omega_\kappa}{\mathrm{d}N} = \Omega_\kappa \left(1 + 3\omega\right) \tag{2.15}$$

It turns out that the assumption of the SEC $\omega > -1/3$ makes $\Omega_\kappa = 0$ an unstable solution. For any perturbation around this solution, Ω_κ will quickly move away, increasing consistently up to $\Omega_\kappa = 1$ for a perturbation towards a positive value of Ω_κ and decreasing consistently

down to $\Omega_\kappa = -1$ for the opposite case, given the restriction by definition for any of the density parameters, $|\Omega_\kappa| \leq 1$. When Ω_κ reach the extreme values, ω takes the value $-1/3$ for $\kappa < 0$, or we have the collapse of the universe for $\kappa > 0$.

To be more specific, let us assume a standard Universe (matter or radiation dominated) where the ordinary matter is prevalent over the curvature or dark energy. Then we can ignore the curvature contribution, and using Eqs.(1.4) and (1.15), we find

$$a^2H^2 \propto \begin{cases} t^{-1} & \text{radiation domination} \\ t^{-2/3} & \text{matter domination} \end{cases} \tag{2.16}$$

This implies from Eq.(2.12),

$$|\Omega_\kappa(t)| \propto \begin{cases} t & \text{radiation domination} \\ t^{2/3} & \text{matter domination} \end{cases} \tag{2.17}$$

In both cases, $|\Omega_\kappa|$ is a growing function of time given the restricted range of values already mentioned in the paragraph above. This is an explicit example of how flatness is an unstable solution for the Universe; any deviation from a flat geometry of the Universe will make that geometry rapidly more and more curved. In consequence, for the Universe to be so flat even at current times ($\Omega_\kappa = 0.001 \pm 0.002$ according to [3]) means that at ancient times its curvature must have been extremely close to zero.

Another way to visualize this is to recall that the matter and radiation densities dilutes as the universe expands with a dependence $1/a^3$ and $1/a^4$ respectively. Both drops are much quicker than the curvature density dilution term $1/a^2$. Consequently, if curvature is not the dominant component of the universe today, it must have started much smaller than the other components.

The equations for $|\Omega_\kappa|$ computed above are not valid anymore when curvature or dark energy terms become relevant contributions, due to our evaluation of $a(t)$ solutions for flatness to obtain them. But they give us a rough idea of the scale of the problem. Going further in this simplification, let us consider an always radiation-filled Universe. Using Eq.(2.17), we can estimated how close to zero the curvature density parameter must have been at some specific early times, given the measurements for our current universe ($t_0 \simeq 4 \times 10^{17}$ sec).

- At decoupling ($t \simeq 10^{13}$ s), we estimate $|\Omega_\kappa| \leq 10^{-5}$.
- At matter-radiation equality ($t \simeq 10^{12}$ s), we estimate $|\Omega_\kappa| \leq 10^{-6}$.
- At BBN ($t \simeq 1$ s), we estimate $|\Omega_\kappa| \leq 10^{-18}$.
- At electroweak phase transition ($t \simeq 10^{-12}$ s), we estimate $|\Omega_\kappa| \leq 10^{-30}$.
- At the Planck scale ($t \simeq 10^{-43}$ s), we estimate $|\Omega_\kappa| \leq 10^{-63}$.

We emphasize for example the BBN era, an epoch we are supposed to know very well within the standard model. Then, the curvature density parameter must have lain within a very narrow range, considering all the feasible values that it could have had. Any other value

would have ended with a universe extremely different to the one we are living in.

A possible solution could be that the Universe must have precisely the critical density. However, on the face of it there seems no reason for this fine tuning. An explanation for such, at first glance, arbitrary choice would solve this problem. A second possible explanation, can be that at some point of the existence of the universe, it would have been dominated by some exotic matter component that violates the SEC.

Despite our ability or inability to justify the physical generation of such values, we can confirm them by observations. Furthermore, having a universe extremely flat at decoupling and at BBN, has the nice advantage to let us set $\kappa = 0$ as a good approximation in the Friedmann equations when describing the physics governing those cosmological periods.

2.1.2 Horizon Problem

To introduce the problem, we will make a straightforward computation. Given that the universe appears to be extremely homogeneous at large scales, a legitimate inquiry to pose is if we can track back this to the origin of the universe. Let us start estimating the angle subtended by the comoving horizon at recombination. This is the proportion of the comoving particle horizon at recombination and the comoving angular diameter distance from the Earth (at redshift $z = 0$) to recombination ($z \approx 1100$).

$$\theta_{hor} = \frac{d_{hor}}{d_A} \tag{2.18}$$

From Eqs. (2.5) and (2.1), we can express the comoving distance between redshifts z_1 and z_2,

$$\tau_2 - \tau_1 = \int_{z_1}^{z_2} \frac{\mathrm{d}z}{H(z)} \equiv \mathcal{I}(z_1, z_2) \tag{2.19}$$

Let us evaluate the comoving particle horizon at recombination,

$$d_{hor} = \tau_{rec} - \tau_i \approx \mathcal{I}(z_{rec}, \infty) \tag{2.20}$$

In the same way, recalling the remarkable spatial flatness of our universe from Section 2.1.1, we express the comoving angular diameter distance from us to recombination as,

$$d_A = \tau_0 - \tau_{rec} = \mathcal{I}(0, z_{rec}) \tag{2.21}$$

So, we have all what we need. Evaluating both Eqs.(2.20) and (2.21) in Eq.(2.18), we obtain the angle subtended by the comoving horizon at recombination,

$$\theta_{hor} \approx \frac{\mathcal{I}(z_{rec}, \infty)}{\mathcal{I}(0, z_{rec})} \tag{2.22}$$

Evaluating the Hubble parameter as a function of redshift from Eq.(1.4), we have

$$H(z) = H_0 \sqrt{\Omega_{r,0}(1+z)^4 + \Omega_{m,0}(1+z)^3 + \Omega_\Lambda} \tag{2.23}$$

Inserting this in Eq.(2.23), we numerically evaluated this with the current parameter values as,

$$\theta_{hor} \approx 1.16^{\circ} \tag{2.24}$$

So, even regions which seem to be relatively close to each other on the sky ($\theta > \theta_c = 2\theta_{hor} = 2.3^{\circ}$) would not have been able to influence each other before decoupling to achieve thermal equilibrium. This largely contradicts the near perfect isotropy at large angular scales observed from the CMB measurements. This remarkable evidence shows us that even at the time of last scattering, the largest scales were well outside the comoving particle horizon. This is known as the *Horizon Problem*.

2.1.3 The LSS Seeding Problem

The near scale-invariant primordial scalar power spectrum of the matter overdensities that seeded the large-scale structure (LSS) of our universe needs a mechanism for the production of such perturbations.

2.1.4 Relic Particle Abundances Problem

Another riddle emerges from bringing together the Hot Big Bang model and modern concepts of particle physics. An inquisitive aspect concerning the Universe is that it remained radiation dominated for such a long time, roughly a thousand of years of the existence of the universe. This would not be expected considering that radiation density dilutes as $1/a^4$, the fastest drop rate among the known components of the universe. Even with a very small portion of non-relativistic matter, then its slower density dilution will quickly promote it as the main component of the universe.

The particles in the Standard Model do not prompt any issues since they actively couple with radiation and thermalization prevents them getting excessively dominant. Nevertheless, modern particle physics brings up other exotic particles. The kind of particles that mostly influenced the emergence of inflation are the magnetic monopole. Such particles are an inescapable outcome of theories of unification of fundamental interactions, referred as the Grand Unified Theories, which predict them with an enormous massiveness at the beginning of the universe. They are theorized to have a large mass; the Grand Unified Scale is believed to be roughly 10^{16} GeV in contrast with the proton's tiny ~ 1 GeV. Such particles would be non-relativistic for practically all the Universe's evolution, allowing them to easily become the most important component of the universe. The fact that we have not been able to detect any of these particles yet rules out any current dominance from this component and arises an unavoidable incompatibility between the standard Hot Big Bang model and such theories.

By the time inflation was proposed, magnetic monopoles were the most relevant relic particles. Nevertheless, new theories predict the existence of several types of relic particles with similar consequences, such as gravitinos and moduli fields.

2.2 A solution

The problems themselves can hint us about what such a solution requires. Eq.(1.5) show us that the comoving horizon τ is a logarithmic integral $d\ln a$ of the *comoving Hubble radius* $(aH)^{-1}$. The comoving Hubble radius is the estimated distance needed to be covered by light for the scale factor to be amplified by one Napier's constant. This definition serves as a ruler to determine if objects can at a specific time make contact during one e-fold expansion. In the matter or radiation domination epochs, the universe's expansion is characterized by a Hubble parameter with a scale factor dependence of $a^{-3/2}$ or a^{-2}, respectively, as can be derived from Eqs.(1.4) and (1.15), with a persistent growth of the comoving Hubble radius with the expansion of the universe. This means that the largest integrated amounts of τ correspond to the last epochs.

This sheds light to a solution. The existence of an early era characterized by a shrinking of the comoving Hubble radius would imply that the comoving horizon τ have received the most relevant contributions at very early times given a much larger Hubble radius. In other words, a larger portion of the universe would have been able to reach thermal equilibrium than what we naively anticipated on Eq.(2.24), and even much larger than our comoving horizon today. Given this early period, the uniformity observed in the CMB is no longer a problem. In such a case, a decreasing $(aH)^{-1} = \dot{a}^{-1}$ implies an increasing $\dot{a}^{-1}$, or $\ddot{a} > 0$, or in words, an accelerated expansion of the universe. In conclusion, a period of early acceleration would elucidate the apparent dissensions raised by the *Horizon Problem* in Section 2.1.2. This proposed period is what we call **inflation**.

There is a relation on the Hubble parameter that is imposed by inflation. It is

$$\frac{d}{dt}(aH)^{-1} = -\frac{\dot{a}H + a\dot{H}}{(aH)^{-2}} = -\frac{1}{a}(1-\varepsilon)\,, \quad \text{where} \quad \varepsilon \equiv -\frac{\dot{H}}{H^2}\,. \tag{2.25}$$

We realize that a shrinking comoving Hubble radius is equivalent to,

$$\varepsilon = -\frac{\dot{H}}{H^2} = -\frac{d\ln H}{dN} < 1 \tag{2.26}$$

Here, we have used N defined in Eq.(2.14). From there, Eq.(2.26) means that the fractional variation of the Hubble parameter per e-fold is small. Furthermore, ε should be imposed to remain less than one a sufficiently long time to solve the horizon problem. The fractional change of ε per e-fold is, then,

$$\eta \equiv \frac{\dot{\varepsilon}}{\varepsilon H} = \frac{d\ln\varepsilon}{dN} \tag{2.27}$$

We enforce $\eta << 1$ to allow inflation persists. Now we need to elucidate what kind of stress-energy tensor sourced this accelerated expansion. Let us assume a perfect fluid with pressure p and density ρ, Eqs.(1.10) and (1.11). Furthermore, we neglect curvature given our

conclusions from Section 2.1.1. Then, we have,

$$\begin{aligned}
\dot{H} + H^2 &= -\frac{4\pi G\rho}{3}\left(1 + 3\frac{p}{\rho}\right) \\
\dot{H} + H^2 &= -\frac{H^2}{2}\left(1 + 3\omega\right) \\
\frac{\dot{H}}{H^2} + 1 &= -\frac{1}{2}\left(1 + 3\omega\right) \\
\frac{\dot{H}}{H^2} + 1 &= -\frac{1}{2} - \frac{3\omega}{2} \\
-\frac{\dot{H}}{H^2} &= \frac{3}{2} + \frac{3\omega}{2} \\
\varepsilon = -\frac{\dot{H}}{H^2} &= \frac{3}{2}\left(1 + \omega\right)
\end{aligned} \tag{2.28}$$

The condition in Eq.(2.26) implies

$$\omega < -\frac{1}{3} \tag{2.29}$$

So this solution violates the SEC, and a solution for the *Flatness Problem* in Section 2.1.1 is also obtained.

The sudden expansion of the inflationary epoch dilutes away any luckless relic particles because their density is diminished by the expansion faster than the mysterious fluid that drives inflation, solving the *Monopole Problem* mentioned in Section 2.1.4. With the required amount of expansion, this dilution can easily account for the fact that the particles are not seen nowadays. Rather even less expansion is required to solve this than the other problems.

Nevertheless, the decay of this exotic matter which ends the inflationary expansion must not regenerate the problematic particles again. In consequence, the universe after the end of inflation must have cooled down sufficiently to suppress any new thermal production.

Our challenge now is how we can implement inflation on a theoretical context. To do this we have several alternatives. This is a big issue in inflation, as there is not a single model that is able to account for all the predictions of inflation. Rather, a myriad of models has been developed since the first proposition of inflation at the beginning of the eighties. Here, we will introduce the most basic and hackneyed example.

2.2.1 Single field slow-roll inflation

The simplest mechanism to source this transient period of accelerated expansion is by the existence of the potential energy of a scalar field (also used in the so-called *quintessence* dark energy models), dubbed the inflaton. We should keep in mind that there is still not confirmed scalar field that can do this. Moreover, the only scalar field that has been observed in nature

is the Higgs boson, and the measurements of its observables have rule it out as a candidate for inflation. As well, most of the possible model candidates from particle physics, like string theory models, contain several scalar fields. We will abandon any pretentious attempt to connect this generic scalar field to known physics, but we warn that the source of inflation could be something different than a scalar field.

Our first mission is to derive the stress-energy tensor for this scalar field. For that purpose, we begin with the Lagrangian for a canonical scalar field ϕ with a potential $V(\phi)$,

$$\mathcal{L}_\phi = -\frac{1}{2} g^{\mu\nu} \frac{\partial \phi}{\partial x^\mu} \frac{\partial \phi}{\partial x^\nu} - V(\phi) \tag{2.30}$$

It should be noticed that the Lagrangian is obtained by the subtraction of the potential energy from the kinetic energy and due to the negative value of g^{00}, we must impose a negative sign for the kinetic energy. The stress-energy tensor is given by,

$$T_{\mu\nu} = \frac{\partial \mathcal{L}_\phi}{\partial g^{\mu\nu}} + g_{\mu\nu} \mathcal{L}_\phi \tag{2.31}$$

Then, inserting Eq.(2.30) in Eq.(2.31) yields,

$$T^\alpha{}_\beta = g^{\alpha\nu} \frac{\partial \phi}{\partial x^\nu} \frac{\partial \phi}{\partial x^\beta} - \delta^\alpha{}_\beta \left[\frac{1}{2} g^{\mu\nu} \frac{\partial \phi}{\partial x^\mu} \frac{\partial \phi}{\partial x^\nu} - V(\phi) \right] \tag{2.32}$$

Considering the homogeneous background field $\phi(t)$ implies that solely the time derivatives of the field do not vanish. This means that the indices ν, β in the first part of Eq.(2.32) and μ, ν in the second must be set to 0. Then this is reduced to,

$$T^\alpha{}_\beta = -\delta^\alpha{}_0 \delta^0{}_\beta \dot{\phi}^2 + \delta^\alpha{}_\beta \left[\frac{1}{2} \dot{\phi}^2 - V(\phi) \right] \tag{2.33}$$

Comparing this to Eq.(1.9), we have,

$$\begin{aligned} \rho &= \frac{1}{2} \dot{\phi}^2 + V(\phi) \\ \mathcal{P} &= \frac{1}{2} \dot{\phi}^2 - V(\phi) \end{aligned} \tag{2.34}$$

Thus if there is more potential energy than kinetic (subdominant but not negligible), then we will have a negative pressure component. Furthermore, from Eqs.(1.12) and (2.34), this means that

$$\omega_\phi = \frac{\mathcal{P}}{\rho} = \frac{\frac{1}{2}\dot{\phi}^2 - V(\phi)}{\frac{1}{2}\dot{\phi}^2 + V(\phi)} \tag{2.35}$$

is roughly -1 and we easily fulfill the condition (2.29). To obtain the time evolution of the field for an arbitrary potential, we need to make use of the conservation of the stress-energy tensor:

$$\nabla_\mu T^\mu{}_\nu = \frac{\partial T^\mu{}_\nu}{\partial x^\mu} + \Gamma^\mu{}_{\alpha\mu} T^\alpha{}_\nu - \Gamma^\alpha{}_{\nu\mu} T^\mu{}_\alpha = 0. \tag{2.36}$$

The energy-momentum tensor for the homogeneous part of the field is of the same kind as Eq.(1.9). Then, we can make use of Eq.(1.10), along with Eq.(2.34), to obtain,

$$\ddot{\phi} + 3H\dot{\phi} + V_{,\phi}(\phi) = 0 \tag{2.37}$$

Where we have defined $V_{,\phi}(\phi) \equiv dV/d\phi$. Again, from Eq.(1.10) neglecting curvarture and inserting the energy density from Eq.(2.34), we have,

$$H^2 = \frac{8\pi G}{3}\left[\frac{1}{2}\dot{\phi}^2 + V(\phi)\right] \tag{2.38}$$

From Eqs.(2.37) and (2.38) we obtain the continuity equation,

$$\dot{H} = -4\pi G\dot{\phi}^2 \tag{2.39}$$

Now we are in conditions to rewrite the kinetic energy sub dominance condition obtained above in terms of the slow-roll parameter ε, inserting Eq.(2.39) in Eq.(2.26):

$$\varepsilon = -\frac{\dot{H}}{H^2} = 4\pi G\frac{\dot{\phi}^2}{H^2} \ll 1 \tag{2.40}$$

Also, we recognize that Eq.(2.37) is the same that describes the dynamics of a particle rolling down a potential, experiencing a frictional force mediated by the term $3H\dot{\phi}$. In the same way as for the particle dynamics, $\dot{\phi} \approx -V_{,\phi}/3H$ should be a slow-roll attractor solution for a sufficient large friction component. We can express this in terms of a slow roll parameter δ,

$$\delta \equiv \frac{\ddot{\phi}}{H\dot{\phi}} = \frac{d\ln\dot{\phi}}{dN} = \varepsilon - \frac{1}{2\varepsilon}\frac{d\varepsilon}{dN} = \varepsilon - \frac{\eta}{2} \ll 1 \tag{2.41}$$

where we have used Eq.(2.14) and Eq.(2.27). We also notice that $\{\varepsilon, |\delta|\} \ll 1 \Rightarrow \{\varepsilon, |\eta|\} \ll 1$. Then for inflation to occur and persist the two slow-roll parameters must be much smaller than 1. Specifically, the condition on the parameter ε tell us that we are on a background solution and the condition on the fractional change of $\dot{\phi}$ per Hubble time η tell us that we are on an attractor solution, and furthermore that this epoch of accelerated expansion ($\omega \approx -1$, $a \propto e^{Ht}$) will remain for a long time. The above conditions $\varepsilon \sim |\eta| \ll 1$ will allow us to simplify the equations of motion. This is what we call "slow-roll approximation". Expressing the parameters in terms of the potential, we find that,

$$\begin{aligned} \varepsilon &\approx \frac{1}{2}\left(\frac{V'}{V}\right)^2 \\ \eta &\approx \left(\frac{V''}{V}\right)^2 - \frac{1}{2}\left(\frac{V'}{V}\right)^2 \end{aligned} \tag{2.42}$$

These conditions allow us to rewrite the inflation equations in a simpler way. From Eq.(2.38),

$$H^2 = \frac{8\pi G}{3}\left[\cancelto{0}{\frac{1}{2}\dot{\phi}^2} + V(\phi)\right] \tag{2.43}$$

And then, the inflation equations reduces to,

$$\dot{\phi} = \frac{V'}{3H}, \quad H^2 = \frac{8\pi G V}{3}, \quad a \propto e^{Ht} \tag{2.44}$$

Inflation will stop to take place when the condition $\omega \approx -1$ does not hold anymore, which is equivalent to,

$$\varepsilon \sim \eta \sim 1 \tag{2.45}$$

At the beginning, the field starts on top of its potential and slowly rolls down. As the Hubble parameter decreases, there is less friction. Eventually, the slope of the potential becomes too pronounced and the field arrives to the minimum of the potential as sketched in Fig.2.1 In such location, the slow-roll configuration is not valid anymore as expressed in Eq.(2.45), and there is significant kinetic energy. The field oscillates around the bottom of the potential. At that time, the equation of state Eq.(2.35) is not -1 anymore. Instead, it is roughly zero, and the universe is expanding with a decreasing acceleration. Next, ϕ breaks down into lighter particles. Ultimately, maybe after a long concatenation of decays, the universe becomes a nearly homogeneous and radiation-filled universe. The details concerning this transition, dubbed *reheating*, are still not completely understood, but the perturbations of cosmological interest are not affected by them as they are well outside the horizon by the end of inflation. They keep frozen during this period.

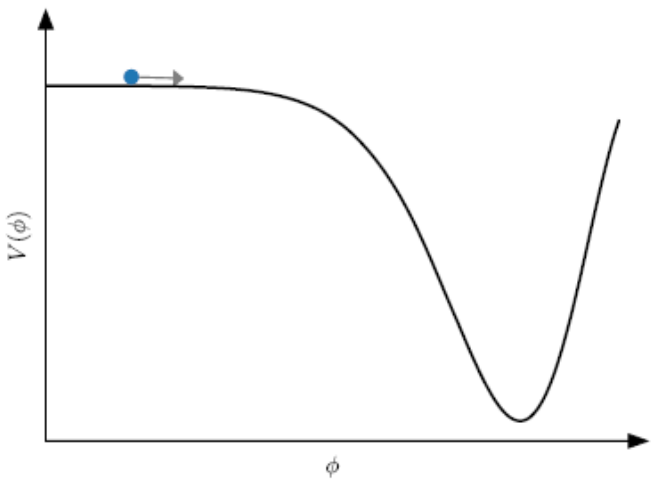

Figure 2.1: A scalar field is slowly rolling down a potential $V(\phi)$. As it is rolling slowly, the kinetic energy that it possesses is small. Nevertheless, the potential energy does not vanish. In consequence, there is a negative pressure associated with this scalar field. Inflation comes to an end when the field has arrived at the bottom of the potential. Figure from [4]. Reproduced with permission from Elsevier.

The degree of inflation needed to reconcile the observations with the theoretical predictions is much easy to express in number of e-folds as defined in Eq.(2.14). We can integrate such relation to obtain this quantity, using the fact that $a \propto e^{Ht}$ along with the slow roll approximations,

$$N(\phi) = \ln\left(\frac{a_{end}}{a}\right) = \int_a^{a_{end}} d\ln a = \int_t^{t_{end}} H dt = \int_\phi^{\phi_{end}} \frac{H}{\dot{\phi}} \approx \int_{\phi_{end}}^{\phi} \frac{V}{V'} d\phi, \tag{2.46}$$

In the CMB, the largest scales that can be seen were generated about 60-efolds before the culmination of inflation,

$$N_{CMB} \approx \int_{\phi_{end}}^{\phi} \frac{V}{V'} d\phi \approx 60 \tag{2.47}$$

2.2.2 Primordial Scalar and Tensor Perturbations

The need to explain the observed temperature uniformity of initially, supposed to be, uncorrelated scales push us into the theory of inflation. Not only inflation explains the persistent fine-tuning problems of the ΛCDM model such as the horizon, flatness and monopole problems as we have already discussed in the previous sections, but also serves as a mechanism for seeding the primordial perturbations around the uniform cosmic background, a problem already raised in Section 2.1.3.

During inflation, the universe is composed mainly of a uniform scalar field and a uniform background metric. From this background, the fields fluctuate quantum-mechanically,

$$\phi(\mathbf{x}, t) = \overline{\phi}(t) + \delta\phi(\mathbf{x}, t) \tag{2.48}$$

where we denoted the background field with an overbar. At any specific time, the average fluctuation vanishes, with patches of the universe with a little larger than its average value of the field and others in which it is smaller. Nevertheless, the variance, the mean of the square of the fluctuations, does not vanish. From this variance, we can draw from a distribution with this variance to impose the primordial conditions for the evolution of the large-scale structure.

One of the predictions of inflation is that quantum perturbations in the very initial universe are created when the scales of interest are in causal contact. Then, the wavelength of these modes is stretched by this dramatic expansion, while the comoving horizon remains roughly constant. These fluctuations are then quickly redshifted by the expansion until their wavelength becomes larger than the horizon, only to come back inside it much later to seed the initial conditions for the formation of the LSS in the universe. Fourier decomposition is the best way to describe these perturbations. The mean of a given Fourier mode, for instance for the gravitational potential, vanishes:

$$\langle \Phi(\mathbf{k}) \rangle = 0. \tag{2.49}$$

In addition, Fourier modes are not correlated with others. Nevertheless, a specific mode has a strictly positive variance, so

$$\langle \Phi(\mathbf{k}) \Phi^*(\mathbf{k}') \rangle = P_\Phi(k)(2\pi)^3 \delta_D^{(3)}(\mathbf{k} - \mathbf{k}'), \tag{2.50}$$

Furthermore, a remarkable result in relativity, the *decomposition theorem*, imposes an independent evolution of the different types of perturbations, such as scalar, vector, and tensor, when they are in a linear regime. For instance, for a given physical phenomena in the primordial universe that creates tensor perturbations, then they do not couple to scalar perturbations in their evolution. In the other hand, the evolution of scalar perturbations is not

affected by possible vector or tensor perturbations. The main justification for the validity of the decomposition theorem lies in the spatial isotropy of the background FLRW metric.

In the case of **scalar perturbations** to the metric, these couple to the density of matter and radiation, sourcing the density fluctuations at the same time as they are sourced by them, finally seeding the large structure we see nowadays. For these perturbations, one of the main predictions of single-field inflation is that it produces *adiabatic perturbations*: different regions of the universe have different overdensities, but the fractional density perturbations are uniform for all species:

$$\frac{\delta\rho_X}{\rho_X} = \frac{\delta\rho}{\rho} \tag{2.51}$$

with the same relations for their velocities. The fact that inflation is sourced by a single field is the main justification for this, whose value defines when inflation ceases. For that reason, any specific region in the epoch of inflation is totally defined by the value of the quantum field $\phi(\mathbf{x}, t)$. The adiabaticity of perturbations has been ratified to great extent by the CMB, which reduces the fact that each specie has their own primordial density perturbations (dubbed as *isocurvature* perturbations) to no more than a percent-level fraction of the adiabatic perturbations. Then it is enough to derive $\delta\rho$. In the same way, through the Einstein equations, we can determine the primordial conditions by Φ, because specifying one initial field is enough.

We will start with an FLRW metric that is slightly perturbed,

$$\begin{aligned} g_{00}(t,\mathbf{x}) &= -1 + h_{00}(t,\mathbf{x}) \\ g_{0i}(t,\mathbf{x}) &= a(t)h_{0i}(t,\mathbf{x}) = a(t)h_{i0}(t,\mathbf{x}) \\ g_{ij}(t,\mathbf{x}) &= a^2(t)[\delta_{ij} + h_{ij}(t,\mathbf{x})]. \end{aligned} \tag{2.52}$$

For scalar perturbations, we will begin in the conformal-Newtonian gauge, so that our metric becomes,

$$\begin{aligned} g_{00}(\mathbf{x},t) &= -1 - 2\Psi(\mathbf{x},t) \\ g_{0i}(\mathbf{x},t) &= 0 \\ g_{ij}(\mathbf{x},t) &= a^2(t)\delta_{ij}[1 + 2\Phi(\mathbf{x},t)]. \end{aligned} \tag{2.53}$$

Where we have introduced Ψ, the perturbation to the spatial curvature. When the wavelength of the perturbation is much smaller than the horizon, we can neglect the metric perturbations. Then, it is possible to derive the equation for perturbations to $\delta\phi$ considered in Eq.(2.48) in terms of conformal time η,

$$\delta\phi'' + 2aH\delta\phi' + k^2\delta\phi = 0 \tag{2.54}$$

Then $\delta\phi$ follows the equation of a massless field under the expansion of the universe just like the one of the massless gravitons as we will see below. It can be shown that the power spectrum of fluctuations in $\delta\phi$ is equal to

$$P_{\delta\phi} = \frac{H^2}{2k^3} \tag{2.55}$$

By the end of inflation, the metric perturbation becomes relevant. So, despite that the perturbations begin as only $\delta\phi$, they finish as a linear combination of Ψ and $\delta\phi$ or more broadly as a linear combination of Ψ and perturbations to the stress-energy tensor. The strategy consists to come up with a linear combination that is preserved outside the horizon. The value of this preserved quantity is defined by $\delta\phi$ when the perturbation crosses the horizon.In this way, the post-inflation power spectrum of Φ can be shown to be

$$P_\Psi(k) = P_\Phi(k) = \frac{8\pi G}{9k^3}\frac{H^2}{\varepsilon}\bigg|_{aH=1} \tag{2.56}$$

The first equality holds because we are neglecting anisotropic stresses and then we have $\Psi = -\Phi$ from the Einstein and Boltzmann Equations. We notice that the scalar spectrum has a dependence on the slow-roll parameter ε, that we have defined in Eq.(2.26), directly proportional to the derivative of the Hubble parameter. Considering that the Hubble parameter is mostly constant in the inflationary epoch, due to the potential energy dominance, then ε is usually tiny.

The scalar perturbations produced during inflation are currently most parametrized by the power spectrum of the gauge-invariant curvature perturbation $\mathcal{R}$. This quantity is a linear combination of Ψ and $\delta\phi$, as mentioned above. Hence, having as a benefit being preserved on super-horizon scales, without regard to if it is matter or radiation what dominates, and hence is a univocal reference point. This power spectrum is given by,

$$P_\mathcal{R}(k) = \frac{2\pi}{k^3}\frac{H^2}{m_{Pl}^2\varepsilon}\bigg|_{aH=k} \equiv 2\pi^2\mathcal{A}_s k^{-3}\left(\frac{k}{k_p}\right)^{n_s-1} \tag{2.57}$$

where we have defined $\mathcal{A}_s$ as the variance of curvature perturbations in a logarithmic wavenumber interval that has its center around the pivot wavenumber k_p, and n_s is the scalar spectral index. The pivot wavenumber is a convention choice, generally adopted as the scale that is best estimated by a specific survey (for instance, for the CMB anisotropies the Planck experiment chose $k_p = 0.05\,\mathrm{Mpc}^{-1}$, and we will adopt the same choice). For our fiducial cosmology,

$$\mathcal{A}_s = \frac{k_p^3}{2\pi^2}P_\mathcal{R}(k_p) \simeq 2.1\times 10^{-9} \tag{2.58}$$

Hence, the usual amplitude of curvature perturbations on the wavenumber k_p is $\sqrt{\mathcal{A}_s} \simeq 4.6\times 10^{-5}$ which is roughly of the same order, although slightly above, than the CMB temperature fluctuations. This is not an accidental coincidence, as can be reviewed in [4].

Along with scalar perturbations, inflation also produced **tensor perturbations** in the metric; this means gravitational waves. In a parallel track to cosmology, gravitational waves have become as a remarkable test of multiple astrophysical processes in the lights of their pioneering detection by the LIGO experiment [71]. The LIGO experiment is aimed to detect wavelengths in the order of hundreds of kilometers, but in the context of cosmology we will be analyzing wavelengths of thousands of megaparsecs. Nevertheless, the generation and streaming of the waves in both regimes are rule by the same master equation.

These perturbations are not coupled to the density and so are not the source for the LSS of the universe. However, the most auspicious method for the quest of cosmological gravitational waves is by their large-scale induced distortions in the CMB. These anisotropies become a singular imprint of inflation and represents the best window to inflation energy scales.

The generation of tensor perturbations are simpler than scalar perturbations: they are gauge invariant, meaning that they preserve their value regardless of the coordinate system that we chose to represent them. In addition, we can obviate the mixing of tensor modes with other types of perturbations in the metric or matter. Scalar perturbations are affected by both issues: they do not resemble the same depending on which coordinates we choose and the perturbations of the scalar field couples with the perturbations in the metric.

Tensor perturbations can be expressed by a metric perturbation Eq.(2.52) with the substitutions $h_{00} = -1$, $h_{0i} = 0$, $\delta g_{ij}(t, \mathbf{x}) = a^2(t) h_{ij}^{TT}(t, \mathbf{x})$, and

$$h_{ij}^{TT} = \begin{pmatrix} h_+ & h_\times & 0 \\ h_\times & -h_+ & 0 \\ 0 & 0 & 0 \end{pmatrix} \tag{2.59}$$

This means that the perturbations to the metric are characterized by two functions, h_+ and $h_\times$, that we suppose small. For definiteness, the perturbations are fixed in the x–y plane. There is an underlying coordinate choice: the one where the z-axis is in the direction of the perturbation wavevector, $\hat{\mathbf{k}} = \hat{\mathbf{e}}_z$. Broadly speaking, h_+ and $h_\times$ are the pair of components of a divergenceless, traceless, symmetric tensor. Divergenceless is expressed as $k^i h_{ij}^{TT} = k^j h_{ij}^{TT} = 0$, condition satisfied by Eq.(2.59) since there are no components with directions along the z-axis. Tracelessness means that the sum of the components along the diagonal is zero, condition that is also accomplished. It can be shown that both h_+ and $h_\times$ are governed by the same equation. Then, the tensor modes obey the equation

$$h_t'' + 2\frac{a'}{a} h_t' + k^2 h_t = 0 \tag{2.60}$$

With $t = +, \times$. Eq.(2.60) is a wave equation, with solutions as the so-called gravitational waves. For instance, if we ignore the expansion of the universe neglecting the damping term in Eq.(2.60), then the two solutions are $h_t \propto e^{\pm ik\eta}$. The perturbation to the metric written in real space is, then

$$h_t(\mathbf{x}, t) = \int \frac{d^3k}{(2\pi)^3} e^{i\mathbf{k}\cdot\mathbf{x}} \left[A(\mathbf{k}) e^{ik\eta} + B(\mathbf{k}) e^{-ik\eta} \right] \quad \text{(without expansion)} \tag{2.61}$$

The two modes in this solution represent waves propagating in the $\pm z$ direction at the speed of light. The spacetime induced deformations by these modes are sketched in the bottom panel of Fig. 2.2. There is an evident elliptical shape in the plane normal to the wavevector (bottom panel). This asymmetry is a characteristic difference between tensor and

scalar perturbations; the spacetime deformation produced by scalar perturbations is totally symmetric around the azimuthal direction of the perturbation wavevector.

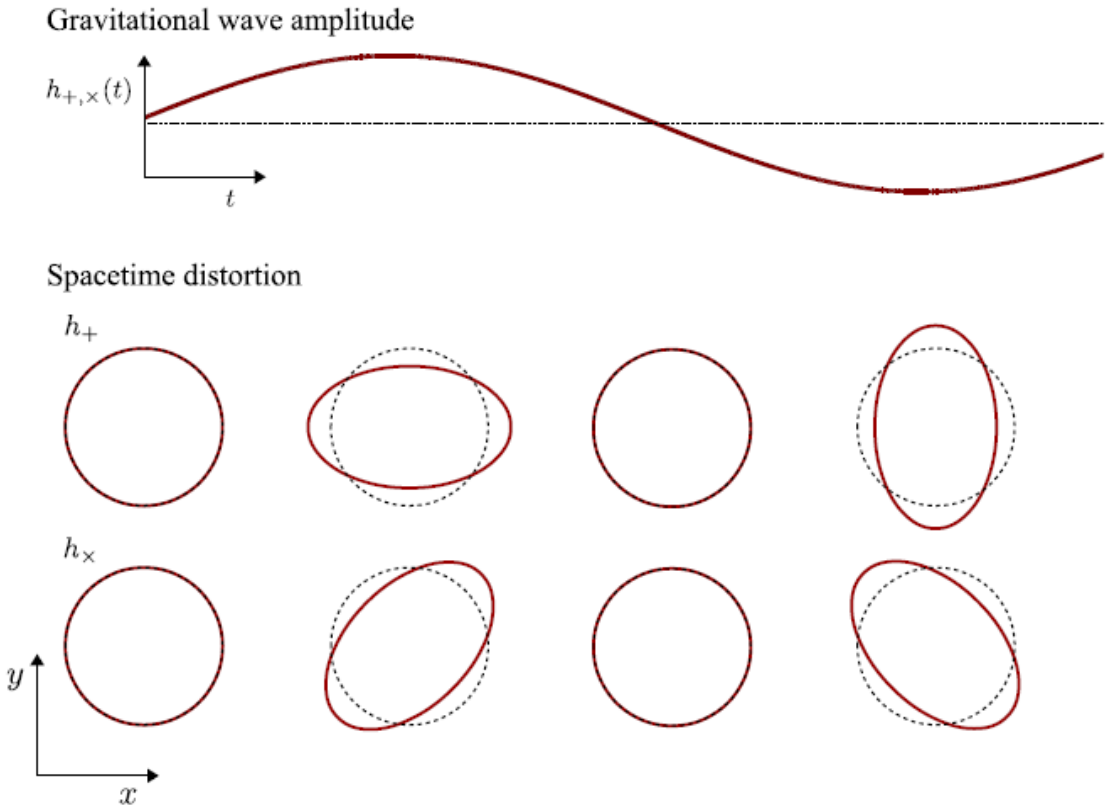

Figure 2.2: Sketch of spacetime distortions induced by a traveling gravitational wave (tensor mode). The wavenumber vector of the perturbation lies in the z axis as in Eq.(2.59), coming out of the page. The top panel illustrates the evolution of the mode amplitude as a function of time (ignoring the decay produced by the expanding universe within one oscillation cycle). The bottom illustrates the distension and squeezing of spacetime in the plane normal to the mode's direction of propagation at different times within one oscillation period. Figure from [4]. Reproduced with permission from Elsevier.

Eq.(2.60) is the expanding universe gravitational-wave equation. For a universe that is filled with only radiation or matter this equation can be solved analytically. The corresponding solutions are oscillations, such as the ones in Eq.(2.61), but damped in time. The evolution of h_t for four solutions of different wavelengths are shown in Fig. 2.3 During early times. when the wavelength of these modes is larger than the horizon, $k\eta < 1$, the mode remains constant in time. In fact, this can be seen if we take the limit $k \to 0$ in Eq.(2.60). Then we will see that $h_t =$ constant is a solution of that equation. When the wavelength of the mode is roughly of the same size as the horizon, its amplitude fluctuates with frequency $k/2\pi$ and starts to decrease. Specifically, the drop is such ($\propto 1/a$) that the energy density in gravitational waves redshifts as a^{-4}, the same that we obtain for radiation. A given mode with wavelength k crosses the horizon when $k\eta = 1$. The fact that the small-scale modes, like the one $k/H_0 = 1000$ plotted in Fig. 2.3, enter the horizon before than the large-scale tensor modes, makes the former more damped than the later.

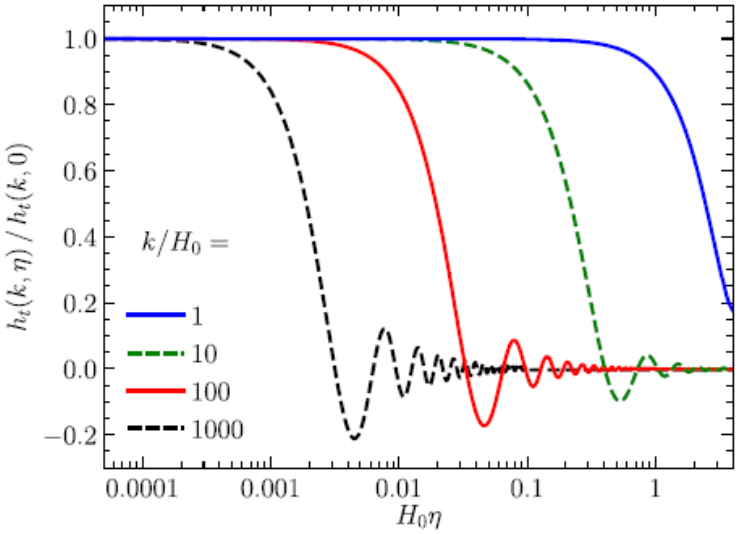

Figure 2.3: Gravitational waves for four different wavenumbers as a function of conformal time, normalized to their initial amplitude. After some time, each mode starts to oscillate and decrease as it enters the horizon, which corresponds to the epoch $k\eta = 1$. The small-scale modes (with large k) starts to decay before than the large-scale modes. Figure from [4]. Reproduced with permission from Elsevier.

Akin to scalar perturbations, perturbations to the tensor part of the metric are also Gaussian with mean zero. The power spectrum of a single polarization P_h in can be derived as,

$$P_h(k) = \frac{16\pi G}{a^2}\frac{1}{2k^3\eta^2} = \frac{8\pi G H^2}{k^3}\bigg|_{k|\eta|=1} \tag{2.62}$$

By convention, primordial tensor modes are characterized by their total power spectrum $P_T(k)$, outside the horizon, defined by

$$\left\langle h_{ij}^{TT}(\mathbf{k})\left(h_{ij}^{TT}\right)^*(\mathbf{k}')\right\rangle\bigg|_{\eta=0} = (2\pi)^3\delta_D^{(3)}(\mathbf{k}-\mathbf{k}')P_T(k), \tag{2.63}$$

Using Eq.(2.59) the left-hand side of Eq.(2.63). is reduced to $2\langle h_+ h_+^*\rangle + 2\langle h_\times h_\times^*\rangle$. Then, we have,

$$P_T(k) = 4P_h(k) = \frac{32\pi}{k^3}\frac{H^2}{m_{Pl}^2}\bigg|_{aH=k} \equiv 2\pi^2\mathcal{A}_T k^{-3}\left(\frac{k}{k_p}\right)^{n_T} \tag{2.64}$$

Where we have defined the tensor amplitude $\mathcal{A}_T$ and spectral index n_T.A spectrum in which $k^3P_(k)$ is constant on k is known as a a scale invariant or scale-free spectrum. Leaving out tiny divergences contained in the slow-roll parameters, the scale-invariance is followed by both the scalar and the tensor perturbations. Furthermore, inasmuch as the field is slowly rolling down a potential during the inflationary epoch such that the Hubble parameter is gradually decreasing, then is also commonly predicted that the potential is marginally red-tilted, that means that the larger-scale perturbations, the ones which have exited the horizon earlier, are characterized by a marginally larger amplitude than the smaller-scale perturbations that exited the horizon later. A spectrum with a small red tilt has been strongly confirmed by the CMB observations.

The well spread convention for the tensor parameter above fixes a scale-free scalar spectrum to $n_s = 1$ and at the same time for the tensor modes this is true for $n_T = 0$. It is more common to refer, in place of $\mathcal{A}_T$, to the tensor-to-scalar ratio r,

$$r(k) \equiv \frac{P_T(k)}{P_{\mathcal{R}}(k)} \overset{k=k_p}{=} \frac{\mathcal{A}_T}{\mathcal{A}_s}. \tag{2.65}$$

From Eqs.(2.57) and (2.64) we can obtain

$$r(k) = 16\varepsilon\Big|_{aH=k} \tag{2.66}$$

Technically r should depend on k for the sake of the different spectral index of scalar and tensor modes, but in practice this dependence is negligible. We can express the primordial spectral indices ns and nT in terms of the slow-roll parameters ε and δ:

$$\begin{aligned} n_T &= -2\varepsilon \\ n_s &= 1 - 4\varepsilon - 2\delta \end{aligned} \tag{2.67}$$

The prediction about a tensor index n_T proportional to ε is one of the most powerful that are derived from inflation. Several models of inflation with a multiplicity of prediction for the slow-roll parameters have been proposed. The common feature of most of these models though preserves the following relationship,

$$n_T = -\frac{r}{8} \tag{2.68}$$

The slow-roll parameters provide a suitable framework to encapsulate the predictions of an inflationary model. Nevertheless, at the end we are looking for the physics behind, so we are looking of the way these parameters link to the physical foundations of inflation, such as the potential V for the scalar field that drives inflation. These relations are summarized in Eq.(2.42). Hence, an estimation of the slow-roll parameters from cosmological observations is equivalent to testing the potential of the scalar field that sources inflation. Considering that the energy scale of this potential is estimated to be around 10^{15} GeV, 11 orders of magnitude beyond the reach of contemporary accelerators, this is a mesmerizing window to the high energy physics. However, we cannot assure that gravitational waves generated during the inflationary epoch will be inside the reach of cosmological experiments. In fact, given Eq.(2.62) and considering that $H^2 \propto \rho/m_{Pl}^2$, where $m_{Pl}^2 = 1/G$, the power spectrum is proportional to ρ/m_{Pl}^4, the energy density at the inflationary epoch in units of the Planck mass. If inflation occurs at energy scales well below the Planck scale, then primordial gravitational waves may be outside the reach of CMB experiments.

The fluctuations in h are highly Gaussian. The high degree of Gaussianity that characterizes the perturbations is another robust prediction of the theory of inflation, that has been ratified in the CMB and large-scale structure surveys, imposing more and more constricted upper bounds on the level of primordial non-Gaussianity. Anyway, some degree of non-Gaussianity, mainly of scalar perturbations, is theorized, including from theories of inflation. Its detection

would be another striking probe of the physics that drives inflation.

Finally, the third type of perturbations, the **vector perturbations**, are less appealing, because they are not generated in a relevant amount for most of the cosmological cases and, if produced, they decay quickly after their generation.

Chapter 3

Polarized CMB

During the recombination epoch, Compton scattering produced polarization anisotropies in the CMB. Polarization opens new gates in the analysis of the CMB. First, it duplicates the already available information that we can find regarding scalar perturbations in the temperature anisotropies. Nevertheless, more important for us will be the chance for polarization to reveal a singular pattern that only can be produced by the elusive and much-desired gravitational waves, or tensor perturbations, as opposed to scalar perturbations, which are unable to reproduce such imprints on large scales. Hence, polarization provide us an exceptional approach for the quest of the inflationary gravitational waves.

Most of the CMB polarization treatment resembles some aspects of the temperature manipulation. For the reasons mentioned above, and furthermore, due to the framework of this thesis, we will focus on the analysis of the polarization. We want to motivate and pave our way to the power spectrum estimation developed in the context of the Polarbear experiment. As we will see in Chapter 4, for the low multipole analysis of the experiment, where the present work is framed, the temperature maps are not considered, and we restrict our analysis to the polarization maps [18]. The goal of the experiment is to measure both the E and, above all, the B polarization modes, and the temperature anisotropies are not considered a data product of the project. Then, we will use some of the known results and facts of the CMB temperature analysis, but, apart from the brief introduction provided in Section 1.1.5, a detailed explanation and derivation of them is beyond the scope of this work and I refer the reader to look into the standard books of cosmology for the temperature treatment [4, 61].

Anyway, the polarization treatment is quite more complex than the temperature one in technical terms due to a pair of difficulties. One of the complexities comes from the fact that the characterization of the polarization pattern on the celestial sphere is not a straightforward function of the position on the celestial sphere as the temperature. Rather, the function becomes a "headless vector." We will make some simplifications under the flat-sky approximation (Section 3.1), restricting the reach of our results to small angular scales. This cost is small compared to the large degree of simplification that we will achieve in the derivations without losing any of the relevant physics involved. Moreover, this will be consistent with the size of the patch observed in the involved experiment, that allow us to consider such approximation in the data analysis, although with some unwanted consequences that, in fact,

we try to mitigate as an objective of this work. Other complexity lies in the consideration of the geometry involved in the Compton scattering of polarized emission. We will review this in a two-step approach in the corresponding Sections 3.1 and 3.2. The importance of this geometry is essential to realize the implication of polarization in the detection of the gravitational waves 3.6.

Sections 3.1 to 3.6 are heavily based on Chapter 10 of [4]. Section 3.8 takes from [8] and Section 3.9 is mostly based on [18].

3.1 Polarization of radiation

The easiest way to measure the polarization of a light wave is to place a polarizer in front of the detector, so that only a field pattern aligned in a specific direction of the transverse wave, ergo perpendicular to the direction of propagation, is not obstructed. The intensity measured by the detector can be plotted as a function of the polarizer angle to extract the polarization. Under a half-turn of the polarizer around its axis of rotation, we will quantify the same polarization, so it acts as a headless vector. Let us define the unit vector along the direction of the polarizer as $\hat{\mathbf{m}}$, so that $\hat{\mathbf{m}} \cdot \hat{\mathbf{p}} = 0$, with $\hat{\mathbf{p}}$ the wavevector of the light wave. Then, the intensity measured by the detector should be independent of the sign of $\hat{\mathbf{m}}$. Hence, the intensity should be quadratic in $\hat{\mathbf{m}}$. We can express it as,

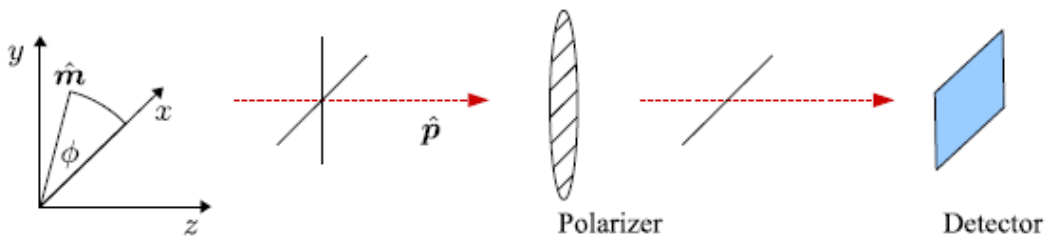

Figure 3.1: Detecting polarized radiation. Light particles coming with direction $\hat{\mathbf{p}}$ (in this case, $\hat{\mathbf{p}} = \hat{\mathbf{e}}_z$) have polarization in the plane normal to the direction of propagation $\hat{\mathbf{p}}$. The inference of polarization can be performed placing a polarizer in the path of the light wave, obstructing the pass of light that is not aligned with a given linear polarization. This is done rotating the polarizer around its axis, that is coincident with $\hat{\mathbf{e}}_z$ in the figure, allowing to quantify the amount and direction of polarization that characterize the signal. This measured polarization is described as a headless vector with azimuthal angle ϕ as measured from the x-axis in the $x - y$ plane that is normal to the direction of propagation $\hat{\mathbf{p}}$. Figure from [4]. Reproduced with permission from Elsevier.

$$I_{det}(\hat{\mathbf{m}}) = I_{ij}\hat{\mathbf{m}}^i\hat{\mathbf{m}}^j \tag{3.1}$$

where I_{ij} denotes the light polarization, also called the polarization tensor. We highlight that this is a two-dimensional square matrix, because $\hat{\mathbf{m}}$ is fixed to the plane normal to $\hat{\mathbf{p}}$. Evidently, I_{ij} can be considered a symmetric matrix [1]. Furthermore, in the case of unpolarized

[1]Technically, I_{ij} is Hermitian; but we will ignore circular polarization because it is not produced by cosmological perturbations and Polarbear is not aimed to measure it. In this scenario, I_{ij} can be considered

radiation, the measured intensity $I_{det}(\hat{\mathbf{m}})$ is the same in the $\hat{\mathbf{m}}_x-$ and $\hat{\mathbf{m}}_y-$directions, then I_{ij} is proportional to δ_{ij}. That allows to write,

$$I_{ij} = \begin{pmatrix} I+Q & U \\ U & I-Q \end{pmatrix} \tag{3.2}$$

The terms in the diagonal I are the intensity, which represents the temperature T, with a uniform part and a perturbation. The terms Q and U characterize the polarization as sketched in Figure 3.2. These elements I, Q, and U are three of the four Stokes parameters used in the context of electricity and magnetism to characterize polarization. The fourth parameter, V, is not present because we are neglecting circular polarization, by the same reason as the discussed in footnote 1. Then, in place of make use of a single distribution function $f(\mathbf{x}, \hat{\mathbf{p}}, \eta)$ as with the temperature treatment, we deal with two added distribution functions f_Q and f_U to account for. Furthermore, we will find that a somewhat different formalism is more convenient than the Q and U parametrization. In terms of the electromagnetic fields, we can express them as,

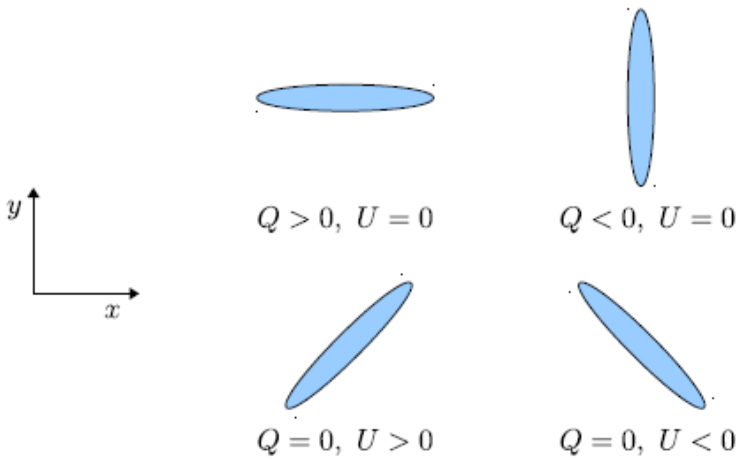

Figure 3.2: Definition of the Stokes parameters Q and U in the plane normal to the incident light wave. Radiation that is not polarized is characterized by $Q = U = 0$. Figure from [4]. Reproduced with permission from Elsevier.

$$\begin{aligned} I &= \langle E_x^2 \rangle + \langle E_y^2 \rangle \\ Q &= \langle E_x^2 \rangle - \langle E_y^2 \rangle \\ U &= 2\,\mathfrak{Re}(\langle E_x E_y^* \rangle) \\ V &= -2\,\mathfrak{Im}(\langle E_x E_y^* \rangle) \end{aligned} \tag{3.3}$$

The orientation of the polarization ellipse relative to the $x-$axis is given via the polarization angle,

$$m = \frac{1}{2} \tan^{-1} \frac{U}{Q} \tag{3.4}$$

as a real and symmetric matrix.

The polarization amplitude is given by,

$$\vec{P} = \sqrt{Q^2 + U^2}\hat{m} \tag{3.5}$$

Now our goal is to obtain the statistics for Q and U that we predict in the CMB. The statistics of the temperature are simple to obtain due to the invariant nature of temperature under coordinate transformations. However, this is different for polarization: if we detect polarization lying in the x-axis, that is coincident with Ixx, and we perform a rotation of the coordinate system, then the quantity Ixx is changed. The Stokes parameters Q and U change in the same way as well. They transform like a spin-2 object. That means that if a coordinate system $(\hat{\mathbf{x}}, \hat{\mathbf{y}})$ is rotated by an angle ϕ around $\hat{\mathbf{z}}$, then Q and U rotate to Q' and U' by an angle 2ψ. We have,

$$(Q \pm iU)'(\hat{\mathbf{z}}) = e^{\mp 2i\psi}(Q \pm iU)(\hat{\mathbf{z}}) \tag{3.6}$$

The polarization field of the CMB can be represented by the Stokes parameters U and Q. Inspired by Eq.(3.6), we can combine Eqs.(3.4) and (3.5) into a single complex object (a spin 2 and spin -2 field) describing the polarization in the direction $\hat{\mathbf{n}}$ on the celestial sphere,

$$P_{\pm 2}(\hat{\mathbf{n}}) = (Q \pm iU)(\hat{\mathbf{n}}) \tag{3.7}$$

This will be very useful when we introduce the E and B mode formalism in Section 3.7. For now, we will develop our derivations in the flat-sky approximation. This greatly facilitate the computations without losing any part of the physics. Thus, we can manipulate the position on the celestial sphere as a two-dimensional vector on the x–y plane, that we denote by θ. In the same way, rather than dealing with multipole moments ℓ, m as in Eq.(1.21), we denote a two-dimensional vector $\boldsymbol{l}$ as the Fourier counterpart of θ. For instance, for the temperature field, defined as proportional to the intensity I, has the following Fourier counterpart,

$$T(\boldsymbol{l}) = \int d^2\theta \, T(\vec{\theta}) \, e^{i\boldsymbol{l}\vec{\theta}} \tag{3.8}$$

Let us write Eq.(3.2) as,

$$I_{ij} = I\delta_{ij} + I^T_{ij} \tag{3.9}$$

where I^T_{ij} is traceless and encloses the information associated with the two polarization states. Rather than in Q and U, however, we want to describe those two states by their action when they are rotated. In the same way as we decomposed the components of the spatial metric perturbation h_{ij} in Section 2.2.2 into scalar, vector, and tensor perturbations, we want to do with I^T_{ij}. In fact, it is slightly easier in two dimensions: I_{ij} consist of three independent elements. Hence, its traceless part I^T_{ij} consists of only two independent components. One of these is a scalar which we can obtain by the contraction $l^i l^j I^T_{ij}/l^2$. We will denote this as $E(l)$. The remaining one, which we will call I^T_{ij} $(\boldsymbol{l})$, is a transverse and traceless tensor (that means $l^i I^{TT}_{ij}(\boldsymbol{l}) = 0$). Then, we can set the following decomposition:

$$I^T_{ij}(\boldsymbol{l}) = 2\left(\frac{l_i l_j}{l^2} - \frac{1}{2}\delta_{ij}\right) E(\boldsymbol{l}) + I^{TT}_{ij}(\boldsymbol{l}) \tag{3.10}$$

We will see that the scalar term E mixes to both scalar and tensor metric perturbations. In the other hand, the transverse and traceless term I_{ij}^{TT} is coupled only to tensor metric perturbations. This is an additional justification of the relevance of the decomposition. Now we have to find the relationships between this new base and the original Q/U decomposition. We can perform the contraction $l^i l^j I_{ij}^T/l^2$ to obtain the scalar part:

$$\begin{aligned} E(\boldsymbol{l}) &= \frac{l^i l^j}{l^2} + I_{ij}^T \\ &= (\cos^2\phi_l - \sin^2\phi_l)Q(\boldsymbol{l}) + 2\cos\phi_l \sin\phi_l U(\boldsymbol{l}) \end{aligned} \tag{3.11}$$

where in the last line we have expressed in terms of components using the azimuthal angle ϕ_l of the two dimensional wavevector: $\boldsymbol{l} = (l_x, l_y) = (\cos\phi_l, \cos\phi_l)l$. With the double angle trigonometric formulas, we can reduce it as

$$E(\boldsymbol{l}) = \cos 2\phi_l Q(\boldsymbol{l}) + \sin 2\phi_l U(\boldsymbol{l}) \tag{3.12}$$

Now, using Eq.(3.10) for I^{TT}, we write

$$\begin{aligned} I_{12}^{TT}(\boldsymbol{l}) &= I_{12}^T - 2\frac{l_1 l_2}{l^2} E(\boldsymbol{l}) \\ &= U(\boldsymbol{l}) - \sin 2\phi_l(\cos 2\phi_l Q(\boldsymbol{l}) + \sin 2\phi_l U(\boldsymbol{l})) \\ &= (1 - sin2\phi_l)U(\boldsymbol{l}) - \sin 2\phi_l \cos 2\phi_l Q(\boldsymbol{l}) \\ &= \cos 2\phi_l B(\boldsymbol{l}) \end{aligned} \tag{3.13}$$

Where we have defined,

$$B(\boldsymbol{l}) = -\sin 2\phi_l Q(\boldsymbol{l}) + cos2\phi_l U(\boldsymbol{l}) \tag{3.14}$$

In the same way, the rest of terms in I_{ij}^{TT} are also expressed in terms of B:

$$\frac{1}{2}\left(I_{11}^{TT} - I_{22}^{TT}\right)(\boldsymbol{l}) = -\sin 2\phi_l B(\boldsymbol{l}) \tag{3.15}$$

We have broken down the polarization tensor I_{ij}^T, which before we were able to express in terms of two independent parts Q and U, into the scalar component $E(\boldsymbol{l})$ and the tensor component $B(\boldsymbol{l})$. Finally, we can decompose the polarization tensor as [72]:

$$I_{ij}^T(\boldsymbol{l}) = \begin{pmatrix} \cos 2\phi_l & \sin 2\phi_l \\ \sin 2\phi_l & -\cos 2\phi_l \end{pmatrix} E(\boldsymbol{l}) + \begin{pmatrix} -\sin 2\phi_l & \cos 2\phi_l \\ \cos 2\phi_l & \sin 2\phi_l \end{pmatrix} B(\boldsymbol{l}) \tag{3.16}$$

For instance, we can focus on a single mode with a wavevector $\boldsymbol{l} = l_0\hat{\mathbf{e}}_x$ lying in the $x-$axis (so $\phi_l = 0$). The polarization pattern of this single mode as seen in real space is,

$$I_{ij}^T\left(\vec{\theta}\right) = \begin{pmatrix} 1 & 0 \\ 0 & -1 \end{pmatrix} e^{il_0\theta_x} E_0 + \begin{pmatrix} 0 & 1 \\ 1 & 0 \end{pmatrix} e^{il_0\theta_x} B_0 \tag{3.17}$$

This pattern is depicted in Fig. 3.3 The E-mode changes in amplitude along the same direction as, or perpendicular to, its orientation. This is the analogy of an electric field. An electric field produced from a point source $\mathbf{E} = q\hat{\mathbf{r}}/r^2$, changes in amplitude as one goes farther from the point source, but always has the same orientation: radially out of the source.

Moving in the same orientation of the field causes the amplitude of the field to decay. On the other hand, the B-mode changes in amplitude in a different direction from that in which it is oriented (that is to say, by 45°), evoking a magnetic field. We realize that the B-mode pattern can be obtained from the E-mode pattern if we turn around each of the polarization orientations by 45°.

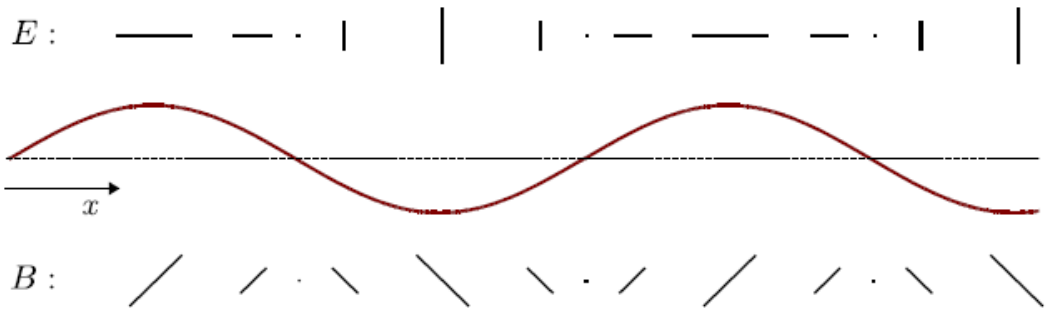

Figure 3.3: Polarization produced by a single plane wave of perturbation in the x-direction (so $\boldsymbol{k} = k\hat{\mathbf{e}}_x$), for an E-mode (upper panel) and a B-mode (lower panel). The size of each headless vector shows the polarization amplitude. These patterns are discernible by observing the way the polarization angle orientates with respect to the mode wavevector (the direction in which the polarization varies). As in Fig. 3.4, the light that corresponds to this polarization pattern propagates out of the page (in the z-direction). Figure from [4]. Reproduced with permission from Elsevier.

Inspired by this analogy, we can consider a superposition of plane waves in the x–y plane that have the same wavelength and phase at the origin, along with the amplitude. We only allow to vary the azimuthal angle ϕ_l. The produced polarization patterns for E- and B-modes are plotted in Fig. 3.4. These patterns are clearly noticeable, with the B-modes showing the distinctive "swirly" shape. We can extract from the plot that E- and B-modes show dissimilar parity: E have even parity, that is, it remains unchanged if we flip the figure, while B have odd parity, that is, it flips sign. So, it is possible to recognize the E- and B-components in an observed polarization map.

In short, E modes are scalar quantities with resembling properties of the divergence of the electric field, while B modes are pseudo-scalars with similar properties as those of the curl of the magnetic field. This observation does not apply for Q and U. Then, the computation of power spectra for E and B becomes unambiguously simple. Eq.(3.16) also tell us that we always can choose a smart coordinate system to realize if a specific physical phenomenon generates E- or B-modes. Based on Eq.(3.17), a mode with a wavevector $\boldsymbol{l}$ lying in the x-axis that is expressed only in terms of Q and not U, is a pure E-mode. By the invariance of the $E - B$ decomposition under coordinate transformations, this can be extrapolated to any orientation of the wavevector.

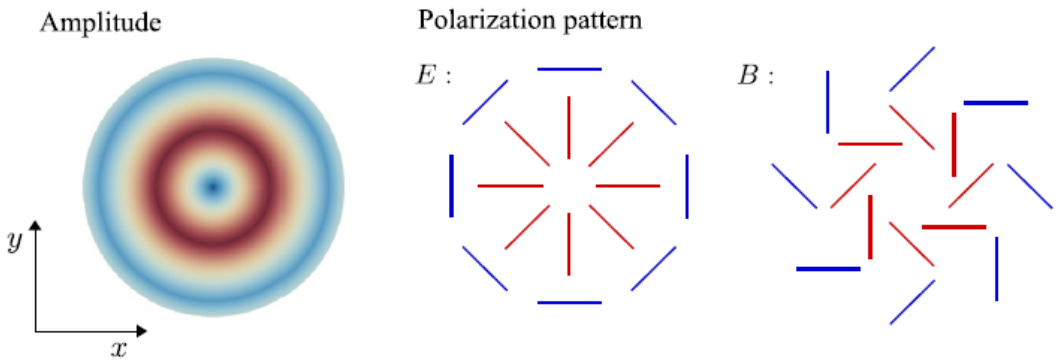

Figure 3.4: The same as Fig. 3.3, but now the polarization produced by a radial wave in the x–y plane is plotted (left panel), that is, a superposition of plane waves with identical phase and amplitude but varying azimuthal angle ϕ_l. The disposition of this plane waves shows the distinction between E- and B-mode patterns very evidently (middle and right panels, respectively; again, for radiation coming out of the page). For each case, the peak of the radial wave is depicted with inner red lines and the trough of the same wave is sketched outer blue lines. Figure from [4]. Reproduced with permission from Elsevier.

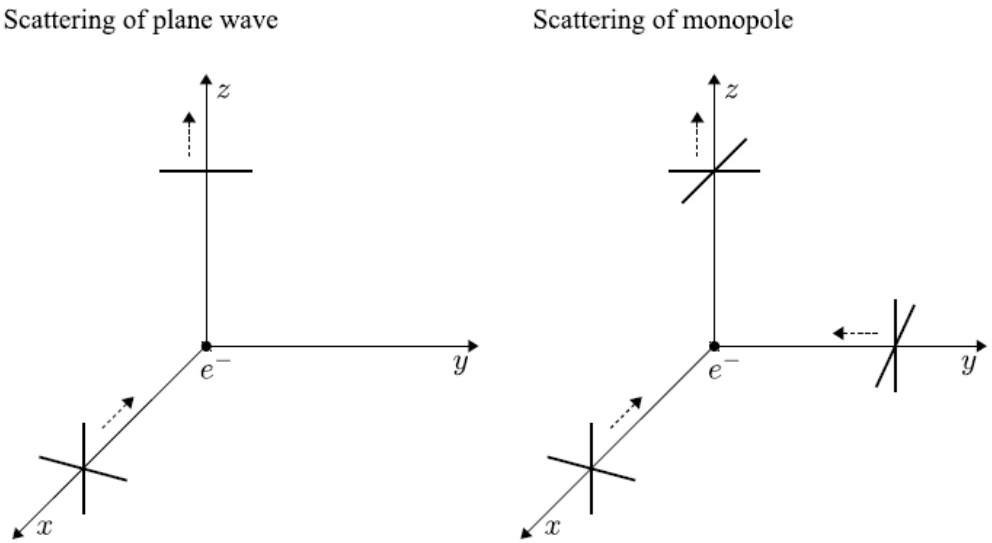

Figure 3.5: Left panel: unpolarized light ray propagating to the origin along the x-axis gets deflected by an electron into the $+z$-direction. Only the intensity along the y-axis is transmitted after scattering. Due to the absence of incident intensity along the x-direction, the outgoing light ray is polarized along the y-direction. Right panel: incident isotropic (i.e. monopole) radiation does not source polarization. In this case, because the incident intensities along the x- and y-axis are identical, the outgoing amplitudes along both of these directions are also the same, and polarization is not generated (another good explanation can be found in [5]). Figure from [4]. Reproduced with permission from Elsevier.

3.2 Polarization production from Compton scattering

Photons propagating in the z-direction have their corresponding electric and magnetic fields oscillating in the plane perpendicular to the direction of propagation, the x–y plane. If both transverse directions have the same intensity, we are talking about unpolarized radiation. It is time to analyze when this condition does not hold, i.e. the intensities along the two transverse directions are not the same and light is polarized.

Compton scattering can produce polarized light[2]. To conceptualize this, left panel of Fig. 3.5 illustrates a light ray coming from the $+x$-direction. This unpolarized light ray is characterized by the same intensity in the transverse y- and z-directions. Photons scatter off an electron at the origin and deviates to the $+z$-direction (the observer line of sight). Since the outgoing direction is coincident with the z-axis, no incoming intensity lying in this axis is transmitted. In opposition, the intensity associated with the y-axis (perpendicular to both the incoming and the outgoing ray directions) gets all transmitted. As outcome, the outgoing radiation is polarized, meaning that the discrepancy between the outgoing intensities in the two transverse directions (y: total transmission; x: no transmission) is maximized.

Now, let us consider incoming light from every possible direction towards an electron. Then the simplistic situation picture in the left panel of Fig. 3.5 will not hold anymore. Let us consider a situation a bit less oversimplified of isotropic incoming radiation from all directions to the electron in the right panel of the same figure. We still say it is oversimplified because we are considering incident rays from only two directions, the $+x$- and $+y$-directions, but this will be enough for our analysis. The I_{xx} projection of the intensity of the outgoing wave corresponds to the incoming light ray from the y-axis, while the outgoing I_{yy} comes from the incoming radiation from the $x-$direction. Due to the isotropy, the intensities of the incident light coming from both directions are the same. Then, the intensities associated with the two axes of the outgoing light wave are identical, $I_{xx} = I_{yy}$, so the outgoing radiation is not polarized.

We already have checked that isotropic radiation can only produce unpolarized emission. But what about anisotropic radiation? The most elemental case is when we are dealing with dipole radiation, as exemplified in the left panel of Fig. 3.6. In this example, the outbound intensity associated with the x-direction comes from the $\pm y$-incoming light rays, characterized by the average temperature (that are not shown in the figure). The outbound intensity associated with the y-direction has also the average temperature because it is a superposition of a cold spot (located in the $-x$-direction) and a hot spot (located in the $+x$-direction). Then, the dipole pattern cannot produce polarized emission.

To emit polarized light, the incident radiation must have a nonvanishing quadrupole radi-

[2]We are focusing on elastic scattering of light particles off electrons, a particular case of Compton scattering, the well-known Thomson scattering.

ation contribution. This is drawn in the right panel of Fig. 3.6. The hotter (colder) incoming light from the x- (y-) direction generates more (less) intensity than average, associated with the y- (x-) axis for the outgoing light ray. Thus, there is more intensity along the y-axis of the outgoing light ray than along the x-axis: the outbound radiation is polarized. Fig. 3.6 sketches polarization in the x–y plane, more specifically in the y-axis. We recall from Fig. 3.2 that this configuration corresponds to $Q < 0$ and $U = 0$. Rather, if we turn around the z axis the incident rays by 45°, the outbound polarization would have been along the axis 45° from the x and y-axes, generating only U polarization.

The implication that Compton scattering sources polarization only when the incident field has a nonzero quadrupole moment leads to relevant consequences for cosmology. Electrons and photons are strongly coupled before recombination, leading to a tiny quadrupole for the radiation field. Hence, we predict a smaller CMB polarization as compared to the temperature anisotropies.

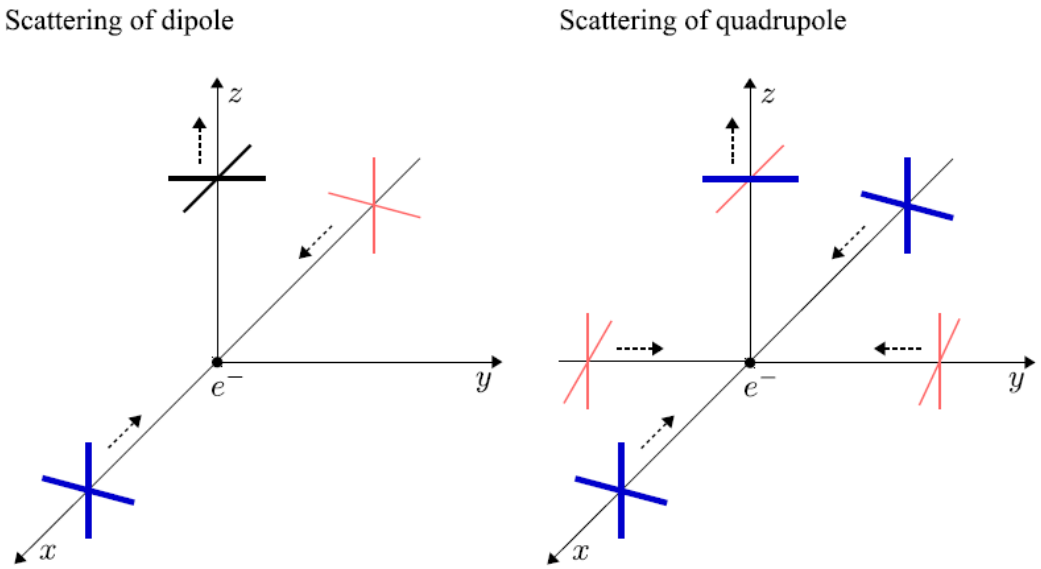

Figure 3.6: Left panel: incident radiation with a dipolar pattern is not able to emit polarized light. Hotter (colder) radiation is shown as thick blue (thin red) lines. In this example, the incident radiation is hotter than average (medium black lines denotes average) along the $+x$-axis, and colder than average along the $-x$-axis (the incident radiation from the $\pm y$-direction is characterized by the average intensity, as in the right panel of Fig. 3.5). The two light waves along the x-axis hence leads to the average temperature for the outgoing light wave along the y-axis. The outbound temperature associated with the $x-$axis is generated by the incoming light waves from the $\pm y$-directions. The outgoing temperature associated with the x-direction is also average because both incident rays share the same temperature. This leads to unpolarized outgoing light waves. Right panel: incident light with a quadrupolar pattern generates outgoing polarized radiation. The outgoing light ray has more intensity along the y-direction than in the x-axis. This is consequence of the incoming hotter light from the $\pm x$-direction than the radiation from the $\pm y$-direction. Figure from [4]. Reproduced with permission from Elsevier.

3.3 Polarization from a single plane wave

The examples of the previous subsection are relevant to acquire a qualitative comprehension of the mechanism responsible to source polarization in the CMB within the context of Compton scattering. To analyze the physical process quantitatively, we must account for the Boltzmann equation, considering the two photon polarization states and the polarization dependence of Compton scattering in the collision term. We start with the simplest case of a single plane-wave perturbation to the photon distribution.

In first place we set the polarization axes in the most generic situation when the incident light ray comes from direction $\hat{\mathbf{n}}'$ (Fig. 3.7). In the case of the incoming direction $\hat{\mathbf{e}}_x$, was obvious that polarization was expressed as the difference in the intensity associated with the two perpendicular directions, y and z. We generalize this to two axes perpendicular to this direction, spanning the plane in which incident waves are polarized, as $\hat{\epsilon}_1'$ and $\hat{\epsilon}_2'$. We are still focused on outbound rays along the z-axis, so we can set the two outgoing polarization axes as $\hat{\epsilon}_1 = \hat{\mathbf{e}}_x$ and $\hat{\epsilon}_2 = \hat{\mathbf{e}}_y$. In brief, the incident polarization vectors are $\hat{\epsilon}_i'$, the outgoing are $\hat{\epsilon}_i$.

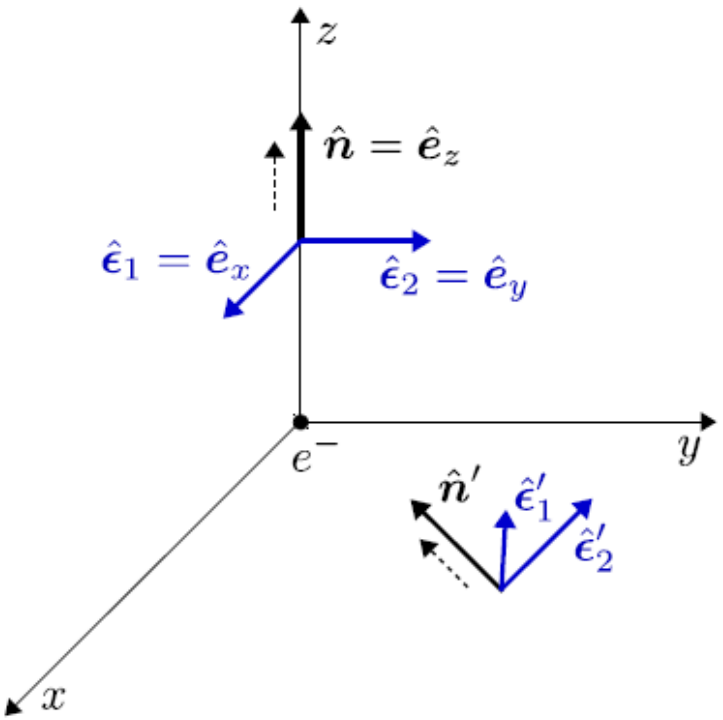

Figure 3.7: Incident light ray from direction $\hat{\mathbf{n}}'$ gets deviated by an electron at the origin generating an outbound ray along the direction $\hat{\mathbf{n}} = \hat{\mathbf{e}}_z$. The plane perpendicular to the incident direction is defined by the two polarization vectors, $\hat{\epsilon}_1' = \hat{\mathbf{e}}_\theta'$ and $\hat{\epsilon}_2' = \hat{\mathbf{e}}_\phi'$. The outbound ray is along the $\hat{\mathbf{e}}_z$-direction, leading to polarization vectors $\hat{\epsilon}_1 = \hat{\mathbf{e}}_x$ and $\hat{\epsilon}_2 = \hat{\mathbf{e}}_y$. Figure from [4]. Reproduced with permission from Elsevier.

Compton scattering has a polarization dependence, previously analyzed from a qualitative point of view, that is cleanly captured by a multiplicative factor in the amplitude squared for outbound light rays polarized along the $\hat{\epsilon}_i$-direction. Summing over the two (not rele-

vant) electron spins along with the incident light polarization, the usual unpolarized squared amplitude for the Thomson cross-section, considering each outgoing polarization $i = 1, 2$ individually, acquires an extra multiplicative contribution,

$$\sum_{3 \text{ spins}} |\mathcal{M}|^2 \propto \sum_{j=1}^{2} |\hat{\epsilon}_i(\hat{\mathbf{n}}) \cdot \hat{\epsilon}_j^{'}(\hat{\mathbf{n}}')|^2 \tag{3.18}$$

For the Q polarization that, according to Eq.(3.2), is produced by the difference between this cross-section for $i = 1$ and $i = 2$, that is to say, the difference between the field amplitude squared in the $\hat{\mathbf{e}}_x$- and $\hat{\mathbf{e}}_y$-directions, we have:

$$\sum_{j=1}^{2} |\hat{\epsilon}_1(\hat{\mathbf{n}}) \cdot \hat{\epsilon}_j^{'}(\hat{\mathbf{n}}')|^2 - \sum_{j=1}^{2} |\hat{\epsilon}_2(\hat{\mathbf{n}}) \cdot \hat{\epsilon}_j^{'}(\hat{\mathbf{n}}')|^2 = \sum_{j=1}^{2} \left(|\hat{\mathbf{e}}_x(\hat{\mathbf{n}}) \cdot \hat{\epsilon}_j^{'}(\hat{\mathbf{n}}') - |\hat{\mathbf{e}}_y(\hat{\mathbf{n}}) \cdot \hat{\epsilon}_j^{'}(\hat{\mathbf{n}}')|^2 \right) \tag{3.19}$$

We perform the integral over all incident $\hat{\mathbf{n}}'$-directions, resulting in

$$Q(\hat{\mathbf{e}}_z) = A \int d\Omega' f(\hat{\mathbf{n}}') \sum_{j=1}^{2} \left(|\hat{\mathbf{e}}_x(\hat{\mathbf{n}}) \cdot \hat{\epsilon}_j^{'}(\hat{\mathbf{n}}') - |\hat{\mathbf{e}}_y(\hat{\mathbf{n}}) \cdot \hat{\epsilon}_j^{'}(\hat{\mathbf{n}}')|^2 \right) \tag{3.20}$$

Where we have introducing A as a normalization factor fixed by the Boltzmann solution, and $f(\hat{\mathbf{n}}')$ is the amplitude of the incident light from the $\hat{\mathbf{n}}'$-direction, and we are performing the integral over all those directions. It is worthy to mention that f is a function of $\hat{\mathbf{n}}'$ solely and not on j: this is due to the supposition that the incoming light is not polarized.The dot products in Eq.(3.20) can be computed using Cartesian coordinates for $\hat{\epsilon}_1^{'}$ and $\hat{\epsilon}_2^{'}$. These unit vectors are prescribed to be orthogonal to $\hat{\mathbf{n}}'$, with components

$$\hat{\mathbf{n}}' = (\sin\theta' \cos\phi', \sin\theta' \sin\phi', \cos\theta') \tag{3.21}$$

We define $\hat{\epsilon}_2^{'}$ to be on the x-y plane, which ends with

$$\hat{\epsilon}_2^{'}(\theta', \phi') = (-\sin\phi', \cos\phi', 0) \tag{3.22}$$

Hence, $\hat{\epsilon}_1^{'}$ is totally fixed by the vector product of $\hat{\mathbf{n}}'$ and $\hat{\epsilon}_2^{'}$:

$$\hat{\epsilon}_1^{'}(\theta', \phi') = (\cos\theta' \cos\phi', \cos\theta' \sin\phi', -\sin\theta') \tag{3.23}$$

Inserting Eq.(3.23) in Eq.(3.20), we have

$$\begin{aligned} Q(\hat{\mathbf{e}}_z) &= A \int d\Omega' f(\hat{\mathbf{n}}') \left[\cos^2\theta' \cos^2\phi' + \sin^2\phi' - \cos^2\theta' \sin^2\phi' - \cos^2\phi' \right] \\ &= A \int d\Omega' f(\hat{\mathbf{n}}') \sin^2\theta' \cos 2\phi' \end{aligned} \tag{3.24}$$

We realize that the angular contribution is proportional to a superposition of the spherical harmonics: $Y_{2,2} + Y_{2,-2}$. Given the orthogonality of the spherical harmonics, the only nonzero terms in the integral corresponds to the $\ell = 2$, $m = \pm 2$ modes projected out of the intensity distribution f. So, a non-vanishing Q-component of polarization will be sourced only if the

incoming radiation has a quadrupole pattern. This is the quantitative verification of the understanding gained by plots of the previous section. The U part of the polarization can be obtained in a similar fashion and it is,

$$U(\hat{\mathbf{e}}_z) = A \int d\Omega' f(\hat{\mathbf{n}}') \sin^2\theta' \sin 2\phi' \tag{3.25}$$

For this case we realize that the angular contribution is proportional to a superposition of the spherical harmonics: $Y_{2,2} - Y_{2,-2}$. We arrive to the same conclusion, now for U polarization: it only can be sourced if the incoming radiation has a quadrupole moment.

Now we are in conditions to show how the outgoing Q and U fields are coupled to the moments of the incoming unpolarized intensity distribution. To study it, a first step might be considering the k-vector lying in the x-direction. The next step would be to let $\mathbf{k}$ lie in the x-z plane. The final step, a generalization to an arbitrary orientation of $\mathbf{k}$. Nevertheless, the first part will elucidate the most remarkable aspects of the general relationship.

The complication here lies in the fact that the orientation of the quadrupole pattern in the radiation intensity distribution $f(\hat{\mathbf{n}}')$ is dictated by the orientation of the wavevector. The photon distribution can be expressed as the sum of a zeroth-order part, a uniform distribution dictated by the Planck's law, and a perturbation as expressed in Eq.(1.21), here described by $\Theta(k, \mu)$ where μ is the dot product of the wave vector $\hat{\mathbf{k}}$ and the photon momentum vector. So, we need to pay attention to three orientations: the wavevector $\hat{\mathbf{k}}$; the incident direction $\hat{\mathbf{n}}'$; and the outbound photon direction $\hat{\mathbf{n}}$. Without loss of generality we can set $\hat{\mathbf{n}} = \hat{\mathbf{e}}_z$. In this situation, we have $\mu = \hat{\mathbf{k}} \cdot \hat{\mathbf{n}}'$. Hence, $f(\hat{\mathbf{n}}')$ in Eq.(3.24) can be expanded in terms of Legendre polynomials with argument $\hat{\mathbf{k}} \cdot \hat{\mathbf{n}}'$, that should not be confused with the $\cos\theta'$, because θ' is the angle from the z-axis to the incoming direction $\hat{\mathbf{n}}'$. Therefore, is not straightforward to connect the parameter μ with the angles θ' and ϕ'.Let us start with the first step we mentioned above. Then,

$$\mu \equiv \hat{\mathbf{k}} \cdot \hat{\mathbf{n}}' = (\hat{\mathbf{n}}')_x = \sin\theta' \cos\phi' \tag{3.26}$$

Where we have used Eq.(3.21). We expand the perturbation Θ of Eq.(1.21) in terms of Legendre polynomials,

$$\begin{aligned} \Theta(k, \hat{\mathbf{k}} \cdot \hat{\mathbf{n}}') &= \sum_l (-i)^l (2l+1) \Theta_l(k) \mathcal{P}_l(\hat{\mathbf{k}} \cdot \hat{\mathbf{n}}') \\ &\to -5\Theta_2(k) \mathcal{P}_2(\sin\theta' \cos\phi') \end{aligned} \tag{3.27}$$

Where we have inserted Eq.(3.26), and projected out the only relevant contribution for the integral in Eq.(3.24), that is the quadrupole term. Recall that we are concentrating our attention to scalar perturbations. Following the recipe described above to obtain the relationships of the outgoing Q and U fields with the moments of the incoming unpolarized intensity distribution Θ_l, after some derivations, we obtain for $\mathbf{k}$ lying in the x-z plane:

$$Q(\hat{\mathbf{e}}_z, \mathbf{k} \perp \hat{\mathbf{e}}_y) = 4\pi A \sin^2\theta_k \Theta_2(k) \tag{3.28}$$

And no U polarization is sourced. So, we only generate Q polarization for this case. Recalling the flat sky approximation, the plane in the sky is the x–y plane (because it is perpendicular to the line of sight, the z direction). Hence, a $\mathbf{k}$ vector lying in the x–z plane is projected along the x-axis on the sky plane. Due to the fact that the polarization is only Q in this case, we thus conclude from the polarization E/B-decomposition in Eqs.(3.16)-(3.17), that only the E polarization is sourced from scalar perturbations. For an arbitrary direction of $\mathbf{k}$, it can be shown that the polarization also obeys the pure E-mode expectation from Eq.(3.16):

$$\begin{aligned} Q(\hat{\mathbf{e}}_z, \mathbf{k}) &= 4\pi A \sin^2\theta_k \cos(2\theta_k)\Theta_2(k) \\ U(\hat{\mathbf{e}}_z, \mathbf{k}) &= 4\pi A \sin^2\theta_k \sin(2\theta_k)\Theta_2(k) \end{aligned} \tag{3.29}$$

Finally, we generalize these relations to an outgoing light ray, i.e. the line of sight, that has not to be along the z-direction. Instead, it is represented by a generic unit vector $\hat{\mathbf{n}}$. For that purpose, we remember the fact that the polarization is totally characterized by the scalar E-component on the sky, invariant under a rotation of $\hat{\mathbf{n}}$. Hence, we only need to insert $\hat{\mathbf{n}}\cdot\hat{\mathbf{k}}$ in place of $\cos\theta_k$. Then,

$$E(\hat{\mathbf{n}}, \mathbf{k}) = 4\pi A \left(1 - [\hat{\mathbf{n}}\cdot\hat{\mathbf{k}}]^2\right)\Theta_2(k) \tag{3.30}$$

These are results obtained under the umbrella of the flat-sky approximation. The full sky results are slightly more complicated, without a substantive gain in the physical understanding of the phenomenon.

Essentially, scalar perturbations can source only E-polarization because of their symmetry, as illustrated in Fig. 3.8. There we consider a configuration with a single plane-wave scalar perturbation lying in the x-axis. If we rotate the wave perturbation around this axis, it does not change. For this example the quadrupole pattern is seen as the hotter radiation along the $\pm\hat{\mathbf{e}}_x$-directions, and colder in the direction orthogonal to x-direction (consistent with the sum of $Y_{2,\pm2}$ that we found before). As the Fig. 3.8 illustrates, the polarization pattern sourced by Compton scattering is restricted to be lined up with the x-direction by the described rotational symmetry, case shown in Fig. 3.4, corresponding to a pure E-mode. This will have interesting consequences. A full-sky explanation of this phenomenon is also illustrated in [5].

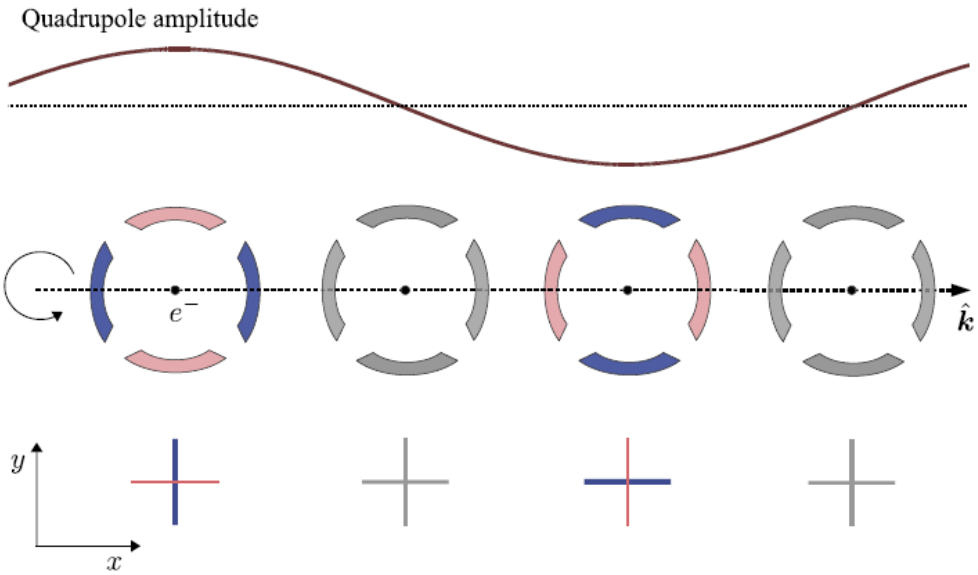

Figure 3.8: In the upper panel a polarization pattern produced by a single plane-wave scalar perturbation lying in the x-axis is illustrated. The perturbation produces a temperature quadrupole pattern that changes in space as observed by electrons, drawn as dots. In three-dimensional space, with the z-axis directed out of the page, this pattern is invariant under rotations around the wave vector $\hat{\mathbf{k}}$, say, the x-direction, as pointed out by the round arrow on the left. As a mental exercise, we can see the photons deviated by the electrons in the z-axis, directed out of the page. Recalling Section 3.2, the polarization pattern is seen as the one drawn in the lower panel. If we contrast this picture with Fig. 3.3, we realize that this should be a pure E-mode. Figure from [4]. Reproduced with permission from Elsevier.

3.4 Boltzmann solution

In the previous section, we realized that the polarization field $\Theta_P(k,\mu,\eta)$ coincides with the Q polarization for a wavevector k lying in the x-axis. Broadly speaking, $\Theta_P = \Theta_E$ tells the amplitude of the E-mode polarization. Since the scalar perturbations are rotationally symmetric around the $\hat{\mathbf{k}}$-direction, the polarization is solely specified by a single function $\Theta_P(k,\mu,\eta)$. We will need to introduce the Boltzmann equation to keep track of Θ_P in order to derive the predicted E-mode.

The LHS of the equation is specified by the free-streaming, i.e. the same as for the temperature field $\Theta(k,\mu,\eta)$. The RHS consists of the source and loss terms. From Eq.(3.28) we know that $(1-\mu^2)\Theta_2$, with μ the cosine of the angle subtended from $\hat{\mathbf{k}}$ to $\hat{\mathbf{n}}$, is a multiplicative factor of the outbound polarization, for $\hat{\mathbf{k}}$ lying in the x-z plane. The multiplicative factor must include the number of scattering events per η interval, then $A \propto -\tau'$, where we define the *Compton-scattering optical depth*:

$$\tau(\eta) \equiv \int_{\eta}^{\eta_0} d\eta' n_e \sigma_T a \tag{3.31}$$

where σ_T is the Thomson cross-section and n_e is the electron density. Then, the minus sign in

A comes from the convention of the optical depth being measured in reverse direction in time. Combining the two factors, we estimate a source term for Θ_P with a multiplicative factor $-\tau'(1-\mu^2)\Theta_2$. Also, another worthy consideration is that, if polarization is not produced, the photons reduce their polarization progressively due to the action of the Compton scattering. Therefore, we can conjecture a loss term proportional to Θ_P, say, $\tau'\Theta_P$. Combining everything, we are left with the following equation,

$$\Theta_P^{'} + ik\mu\Theta_P = -\tau'[b(1-\mu^2)\Theta_2 - \Theta_P] \tag{3.32}$$

with b a constant estimated to be of order one. We are almost set. A pair of missing terms here are needed to consider the polarization of the incident radiation, which we have supposed without polarization in our expressions. From [73], the complete equation is,

$$\Theta_P^{'} + ik\mu\Theta_P = -\tau' \left[-\Theta_P + \frac{3}{4}(1-\mu^2)\Pi\right] \tag{3.33}$$

With

$$\Pi(k,\eta) \equiv \Theta_2 + \Theta_{P2} + \Theta_{P0} \tag{3.34}$$

After some computations and approximations, the solution of Eq.(3.33) is given by:

$$\Theta_P(k,\mu) \simeq \frac{3}{4}\Pi(k,\eta_*)\left(1 + \frac{\partial^2}{\partial(k\eta_0)^2}\right) e^{-ik\eta_0\mu} \tag{3.35}$$

Where η_* is the conformal time at the peak of the visibility function, $g(\eta) \equiv -\tau'(\eta)e^{-\tau(\eta)}$. To obtain the moments $\Theta_{P,\ell}$, we take the product of Eq.(3.35) with $\mathcal{P}_\ell(\mu)$ and then, we take the integral spanning all the values of μ. It leads to,

$$E_\ell(k) = \Theta_{P,\ell}(k) \simeq \frac{3}{4}\Pi(k,\eta_*)\left(1 + \frac{\partial^2}{\partial(k\eta_0)^2}\right) j_\ell(k\eta_0) \tag{3.36}$$

Where we have replaced $\Theta_{P,\ell}$ with E_ℓ since scalar perturbations produce pure E-mode polarization. In the tight-coupling regime, we can relate Π in terms of the quadrupole,

$$\Pi = \frac{5\Theta_2}{2} \tag{3.37}$$

Using Eq.(3.37) and other approximations, we can write Eq.(3.36) as

$$E_\ell(k) \simeq \frac{15}{8}\Theta_2(k,\eta_*)\frac{\ell^2}{(k\eta_0)^2} j_\ell(k\eta_0) \tag{3.38}$$

Furthermore, in the tight-coupling regime, we can express the quadrupole in terms of the dipole,

$$\Theta_2 = -\frac{4k}{9\tau'}\Theta_1 \tag{3.39}$$

Inserting Eq.(3.39) in Eq.(3.38), we have,

$$E_\ell(k) \simeq \frac{5k}{6\tau'(\eta_*)}\Theta_1(k,\eta_*)\frac{\ell^2}{(k\eta_0)^2} j_\ell(k\eta_0) \tag{3.40}$$

This is the equation for the polarization moments as seen nowadays sourced by a single plane-wave scalar perturbation in the tightly coupled regime. There are three important points to highlight. To begin, we realize that the spectrum of the polarization is expected to be roughly k/τ' times smaller than the temperature anisotropy during the decoupling era. This is due to the dual fact that polarization is sourced by a quadrupole moment while the same quadrupole is damped before recombination by the action of Compton scattering. Another point to remark is that we conjecture an oscillatory pattern for the spectrum of polarization due to the relationship $E_\ell \propto \Theta_1$, which exhibits acoustic oscillations. More concretely, we estimate the polarization oscillations, in the same way as the dipole, evaluated out of phase with respect to the monopole Θ_0. The maxima and minima in the temperature anisotropy power spectrum, driven mainly by the oscillations in the monopole, should then be out of phase with the maxima and minima in the polarization spectrum. To finalize this highlighting, there is no such an integrated Sachs–Wolfe effect equivalent which affects the temperature anisotropy power spectrum. Polarization is not produced or affected by light particles moving across varying (small) gravitational fields. Hence, the polarization spectrum nowadays is to say a more uncorrupted evidence of the early universe, unaffected by its late evolution.

3.5 Polarization power spectra

The polarization moments originated from a single plane wave are expressed in Eq.(3.40), but the universe exhibits a combination of several of such waves, with different amplitudes $\Theta_P(\mathbf{k}, \hat{\mathbf{n}})$. The E_ℓ angular power spectrum from a sum of plane waves can be obtained in a similar fashion as how is usually derived the power spectrum of the temperature anisotropies. Following the conventional way, we introduce

$$\mathcal{T}_\ell^E(k) \equiv \frac{E_\ell(k)}{\mathcal{R}(\mathbf{k})} \tag{3.41}$$

And the power spectrum of polarization can be obtained in that way as,

$$C_{EE}(\ell) = \frac{2}{\pi}\int_0^\infty dk\, k^2 |\mathcal{T}_\ell^E(k)|^2 P_\mathcal{R}(k) \tag{3.42}$$

Another result we have in advance for scalar perturbations is,

$$C_{BB}(\ell) = 0 \tag{3.43}$$

The polarization power spectrum $C_{EE}(\ell)$ obtained numerically, along with is $C_{TT}(\ell)$ for reference (line of dots; decreased by a factor of 50), are plotted in Fig. 3.9. As we anticipated in the tight-coupling regime, the acoustic oscillations are boosted in $C_{EE}(\ell)$ and plotted out of phase with respect to $C_{TT}(\ell)$. This pair of observations have their cause in $C_{EE}(\ell)$ being dependent only in the dipole of the radiation distribution, remembering the proportionality of the quadrupole with the dipole distribution in the tight-coupling regime, at the same time as $C_{TT}(\ell)$ depends on both the monopole and dipole, with a predominance on the monopole. Furthermore, the dipole is more unchanged by photon diffusion, deriving in a less suppressed angular polarization spectrum toward small scales. This deduction can be checked in the

plot.

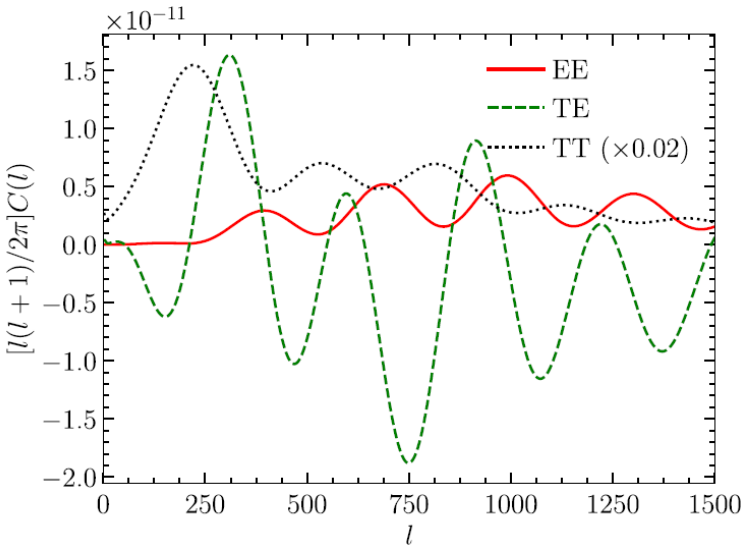

Figure 3.9: Angular power spectra of temperature anisotropies and E-mode polarization anisotropies, along with their cross-correlation, given a fiducial concordance cosmology. The polarization anisotropies power spectra are of lower amplitude than those of the temperature anisotropies by a factor of order 1/50, but less suppressed in smaller scales. Figure from [4]. Reproduced with permission from Elsevier.

In addition, the cross-correlation between temperature and polarization anisotropies is plotted in Fig. 3.9, from the following expression depending on both the temperature and $E-$mode moments:

$$C_{TE}(\ell) = \frac{2}{\pi}\int_0^\infty dk\, k^2 |\mathcal{T}_\ell(k)\mathcal{T}_\ell^E(k)| P_{\mathcal{R}}(k) \tag{3.44}$$

There is a predicted significant anticorrelation of T and E in the multipole range $\ell \lesssim 200$, that is evidenced as negative value for the cross-spectrum: it is a straight outcome of the evidence that the primordial conditions were configured beyond the horizon causing only the cosine mode of the acoustic oscillations to be produced. In the case that both sine and cosine modes were produced, the successive coherent maxima and minima measured in both the temperature and polarization anisotropies power spectrum would not be there [74]. Indeed, the acoustic oscillations are well-measured in the temperature anisotropies power spectrum. The first acoustic peak is approximately at multipole 200, corresponding to physical scales that were inside the horizon at the recombination era. It is plausible to find a model to produce perturbations at the recombination epoch suitable to produce solely the cosine mode. Anyway, the depression found in the TE cross-spectrum starts at a multipole around 30, coincident with scales that have not entered the horizon yet during the recombination era. Thus, for any suitable model for sub-horizon perturbation production, it would be impossible to it, by construction, to explain a non-vanishing TE signal on these super-horizon scales. The detection of this feature provides a compelling proof of an even earlier setup of the primordial perturbations, mechanism already addressed by the theory of inflation. A highly significant detection of this imprint in the measured CMB is shown in Fig. 3.10.

From $C_{EE}(\ell)$ and $C_{TE}(\ell)$ we can extract information about cosmological parameters, as discussed in Section 1.1.4. In particular, the A_s-τ_{rei} degeneracy generated by the scattering of CMB photons after reionization is broken by the polarization data. On scales within the horizon at the reionization epoch (when electrons start to scatter again), roughly speaking, $\ell \gtrsim 100$, the temperature anisotropies are suppressed by a factor $e^{-\tau_{rei}}$, at the same time as they remain the same on the very largest scales. Looking through the polarization window, nevertheless, this late era of scattering in practice sources anisotropies. Once more, the temperature quadrupole pattern left by the end of reionization and observed by the free electrons is transformed into polarized radiation due to the action of Compton scattering. As it is the same mechanism, we can still use Eq.(3.38), with the following substitutions: $\eta_* \to \eta_{rei}$, and $\eta_0 \to \eta_0 - \eta_{rei}$, with η_{rei} as the conformal time when reionization takes place. Due to the photons free streaming from recombination to reionization, the quadrupole $\Theta_2(k, \eta_{rei})$ at reionization is damped if the wavelength of the perturbation is smaller than the horizon at that time, this is, for $k \gg aH(\eta_{rei})$. Due to this fact, the polarization emission generated by reionization has a considerable significance only on very large angular scales. This is appreciable as the bump located in the multipole range $\ell < 10$ in Fig. 3.10, with a more noticeability in $C_{EE}(\ell)$. The amplitude of this bump in $C_{EE}(\ell)$ depends on a multiplicative factor τ_{rei}^2. Then, τ_{rei} is being able to be estimated in an independent way from the temperature anisotropies spectrum.

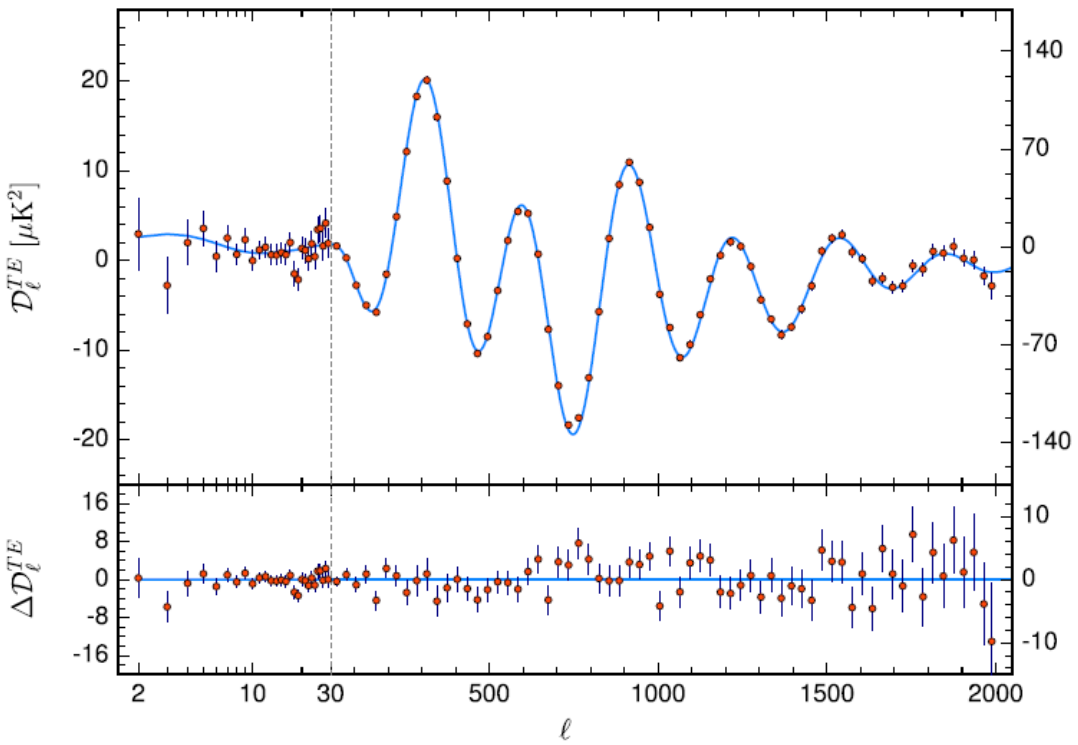

Figure 3.10: Top panel: Angular cross power spectrum of temperature and E-mode polarization anisotropies as observed by the Planck experiment (drawn with points; $D_\ell^{TE} \equiv \ell(\ell+1)C_{TE}(\ell)T_0^2/2\pi$, as plotted in Fig. 1.3). We must be aware that the scales of both the multipole and spectrum axes changes at $l = 30$. The solid line illustrates the forecast for the fiducial concordance cosmology. It is remarkable the values below zero in the multipole range $30 \lesssim \ell \lesssim 200$. Bottom panel: discrepancy of the theory with the measurements. Figure from [3]. Reproduced with permission © ESO.

3.6 Gravitational waves detection

Exists a key distinction between the scalar perturbations we have discussed in the previous sections and tensor perturbations. There is only one direction that photons need to use as a reference when dealing with a scalar plane-wave perturbation, the orientation of the wavevector $\mathbf{k}$. After fixing this orientation, the photon moments are expressed solely in terms of the angle subtended from the photon momentum vector to the wavevector. After fixing this angle, the photon moments are rotationally symmetric around the wavevector. From Fig. 3.8, this is the cause of scalar perturbations to generate only E-modes. For the polarization field we have two directions to keep track: the direction of the polarization and the direction that makes to vary the polarization amplitude. In the case of scalar perturbations, from Fig. 3.3, we noticed that these orientations should be in parallel or orthogonal one with respect to the other one. Naturally, each direction seeks the only direction available for orientation, the wavevector. This configuration is the conspicuous aspect that defines the pure E-modes.

The azimuthal symmetry around the wavevector we had in the photon distribution produced by scalar perturbations is broken by tensor perturbations. This lack of symmetry is caused by the salient pattern of the tensor metric perturbation sketched in Fig. 2.2. This pattern leads a rotational dependence around the wavevector to the photon distribution. This anisotropy in the photon distribution induced by a tensor perturbation given by Eq.(2.59) can be shown to be,

$$\begin{aligned}\Theta^T(k,\mu,\phi) &= \Theta^T_+(k,\mu)(1-\mu^2)\cos(2\phi) + \Theta^T_\times(k,\mu)(1-\mu^2)\sin(2\phi) \\ &= \Theta^T_+(k,\mu)\sin^2\theta\cos(2\phi) + \Theta^T_\times(k,\mu)\sin^2\theta\sin(2\phi)\end{aligned} \tag{3.45}$$

where ϕ is the azimuthal angle around the wavevector that points along the z-axis. In the process of generation of the polarization field, the additional dependence on this azimuthal angle with respect to the scalar case implies an extra direction to be specified. This suggests that the direction of the polarization is not constrained to be parallel or perpendicular to the orientation that makes the polarization amplitude to vary. It follows that gravitational waves can generate B-modes [75, 76], along with the E-mode polarization.

The relevance of the B-modes generated by tensor perturbations lies in the complication of measuring the tensor imprints in the temperature anisotropies or the E-mode polarization. They receive a mixed contribution from scalar and tensor perturbations, so in order to separate their contributions we need to consider the distinctive multipole dependence of their imprints in the spectrum. Anyway, even in the utopian presence of a completely accurate and precise (impossible by cosmic variance) measurement of the primordial temperature anisotropies or the E-modes, the overlapping effects in the spectrum of many combinations of the cosmological parameters lead to degeneracies in the parameter estimation, and so, in the fitted cosmological contributions that makes impossible a definite estimation of the tensor part. In contrast, B-modes do not have any coupling to scalar perturbations. That means, any B-mode detection should be an indication of gravitational waves. In theory, this method would not have any limitation in the detection of the inflationary tensor signal, since there should not be any other signal fluctuation to which compare the relative size of the

H_{inf}/m_{Pl} contribution. In reality, we have other sources of B-mode signal alteration during its propagation from the last scattering surface, such as the foreground contamination caused by dust and synchrotron emission from the Milky Way, or effects outside the linear regime such as gravitational lensing (Section 3.8). However, CMB B-modes are the most precise tool for the quest of inflationary gravitational waves for the next years or decades.

The polarization pattern calculation treatment from a single plane-wave of a tensor perturbation is the same used for the scalar case in Section 3.3. We must integrate over the incident radiation distribution to predict the outbound polarization pattern in the proximities of the z-axis. We want to evidence that tensor perturbations source B-modes. We recall that Eq.(3.17) tell us that for any k which projected into the sky plane lies in the x-axis, solely the B-component produces the U-polarization contribution. Then, we are only left with the goal of proving that tensor modes generate U polarization under this setup using Eq.(3.25). We consider the wavevector,

$$\hat{\mathbf{k}} = \cos\alpha\,\hat{\mathbf{e}}_z + \sin\alpha\,\hat{\mathbf{e}}_x \tag{3.46}$$

with α as the angle subtended from the wavevector to the line of sight vector $\hat{\mathbf{n}}$. Let us concentrate on the $h_\times$ part in Eq.(3.45). For our argument, it suffices for one of these components to produce the U-polarization contribution. To begin, we can write the angular part as a function of the unit vector $\hat{\mathbf{n}}'$ that represents the orientation of the incoming photon:

$$\begin{aligned}\Theta^T(\hat{\mathbf{n}}') &\propto \sin^2\theta'\cos(2\phi') \\ &= 2\hat{n}_x^{'}\hat{n}_y^{'}\end{aligned} \tag{3.47}$$

with $\hat{n}_{x,y,z}^{'}$ symbolizing the components of the incident photon direction. The next task is to express this for a wavevector of the form Eq.(3.46). This can be achieved by a rotation of the coordinate system about the y-axis by an angle $-\alpha$. This keeps $\hat{n}_y^{'}$ untouched, but $\hat{n}_x^{'}$ becomes

$$\hat{n}_x^{'} \to \cos\alpha\,\hat{n}_x^{'} - \sin\alpha\,\hat{n}_z^{'} \tag{3.48}$$

Next, we insert the Eq.(3.45), with the angular dependence given in Eq.(3.46), in Eq.(3.25). There is a cancellation of the angular integrals in the second term of Eq.(3.48). We are left with the first term, that end to be of the same angular dependence as previous to the rotation: $\propto \hat{n}_x^{'}\hat{n}_y^{'} = \sin^2\theta'\cos(2\phi')$. The equation is expressed now as,

$$\begin{aligned}U(\hat{\mathbf{e}}_z) &\propto h_\times\cos\alpha\int_1^{-1} d\cos\theta'\sin^4\theta'\int_0^{2\pi} d\phi'\sin^2(2\phi') \\ &= h_\times\cos\alpha\left(\frac{16}{15}\right)\left(\frac{\pi}{2}\right)\end{aligned} \tag{3.49}$$

We just have shown that for a tensor mode projected on the sky as parallel to the x-axis, it induces a non-zero U-polarization, sourcing in this way B-modes. Middle panel of Fig. 3.8 can illustrate this if we extrapolate the diagram a little bit: the tensor mode induces a quadrupole pattern that is in the same way as in the figure for scalar perturbations but with a rotation of $\pi/4$ around the z-axis , which is directed out of the page. We remember

that Fig. 2.2 for $h_\times$ (that is basically of the form expressed in Eq.(3.45)) shows precisely a configuration that is consistent with this rotated pattern. We note that Fig. 2.2 has $\hat{\mathbf{k}}$ along the z-axis, and so this pattern only arises if $\hat{\mathbf{k}}$ has a component in this direction, i.e. it is not totally contained in the $x-y$ sky plane ($\alpha \neq 90°$). This is precisely what is coded in the $\cos\alpha$ factor present in Eq.(3.49). This temperature quadrupole pattern has as an outcome that the polarization pattern illustrated in the lower panel of Fig. 3.8 is similarly rotated by $\pi/4$. The crosscheck with Fig. 3.3 makes evident that we are in the presence of a B-mode.

An illustration of the inflationary B-mode angular power spectrum for a pair of scalar-to-tensor ratio r values, defined in Eq.(2.65), is displayed in Fig. 3.11. From the same equation, it is evident that once A_s is fixed, $C_{BB}(\ell)$ has a linear proportionality with r). The bump at about $\ell = 100$ is generated from recombination. Also, another signal is visible on very large scales, reaching its maximum at $l < 10$, which is sourced by the scattering off electrons after the reionization epoch. A similar pattern, but induced by scalar perturbations, is visible in the polarization E-mode angular power spectrum, as we have anticipated, letting us estimate independently τ_{rei}. Recent observations set upper limits of approximately $r < 0.05$, limiting the B-mode angular power spectrum to take values well below the $C_{EE}(\ell)$ magnitudes. The inexistence of cosmic variance under the null hypothesis for inflationary B-modes let the upper limits to be driven by the experimental precision along with the effectiveness of the foreground subtraction methods. In the foreseen future, it is expected that the improvement in experimental sensitivity and better understanding of foregrounds will set tighter constrains to the inflationary B-modes.

There are other considerations we need to be aware. In Section 3.8, we will see that gravitational lensing alters the CMB, by remapping the apparent locations of CMB anisotropies. Remapping the locations of a pure E-mode polarization pattern also produces B-modes [77,78]. These expected "lensing B-mode" has already been confirmed in the measurements. Auspiciously, Fig. 3.11 tell us that the power spectrum of these B-modes are both of lower magnitude than the expected of the CMB anisotropies induced by scalar perturbations in the linear regime and also exhibits a different pattern from that of the inflationary primordial B-modes induced by tensor perturbations. This open a window of opportunity for the quest of this primordial signal on large scales.

3.7 E- and B- modes Formalism

We realized in Eq.(3.7), that the complex combination $Q + iU$ acts as a spin-2 field. Thus, contrasted to a scalar (spin-0) function, polarization cannot be expanded in a spherical harmonic basis on the surface of a sphere as we did in Eq.(1.22) with the temperature field. The mathematical instruments needed to represent the angular distribution of the polarization of the CMB on the sky are the spin-weighted harmonics ${}_sY_{\ell m}$. The full-sky treatment can be found in [79] using the full spin spherical harmonic formalism. As we have already mentioned, in this work we have been focusing on the easier and more intuitive flat sky formalism. A handy introduction that contains the link between the spherical and flat sky formalisms can be found in [80]. The flat-sky approximation can be adopted as a proxy

of the full spherical harmonic expansion only in consideration of small patches in the sky, that is the case for Polarbear. In this section, for completeness, we give a brief review of the most fundamental definitions of both formalisms and refer the reader to the abovementioned references for a deeper and more complete analysis of them along with the physics involved that we have already analyzed only in the context of the flat-sky formalism.

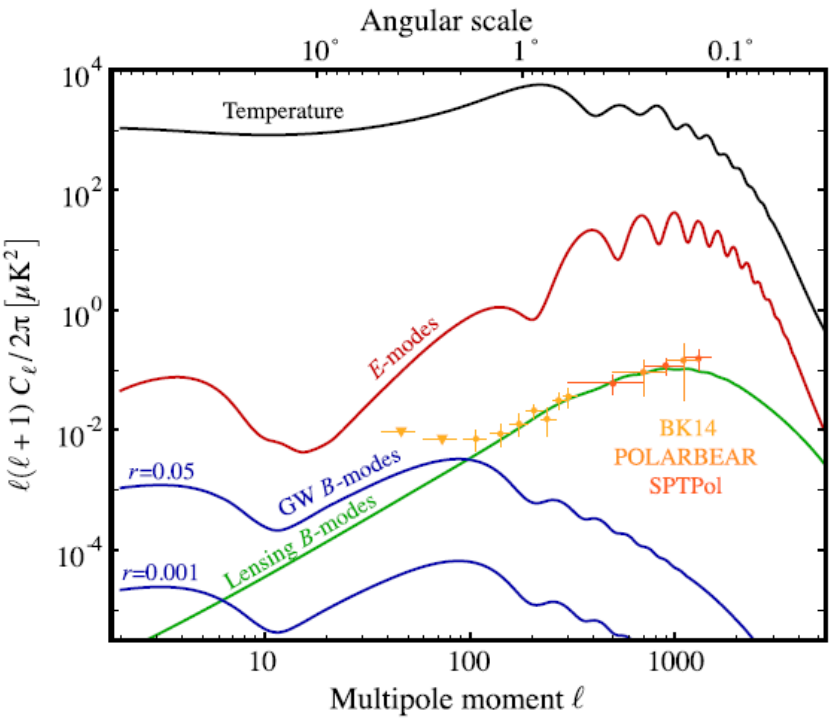

Figure 3.11: Inflationary B-mode CMB polarization anisotropy angular spectrum induced by tensor modes or gravitational waves, for a pair of the tensor-to-scalar ratio values $r = 0.001$, and $r = 0.05$, as indicated. From recent constrains on the r value, the B-mode power spectrum amplitudes are well below those of the E-mode polarization. On small scales, the B-mode signal is produced by the gravitational lensing of the photons caused by the intervening large-scale structure altering the primordial CMB E-mode polarization. The experimental data, drawn as points with error bars, have unequivocally confirmed the presence of this expected lensed emission. A signal surplus is also detected on large scales produced by polarized galactic emission. This work presents a new measurement of the B-mode CMB polarization anisotropy angular spectrum at large scales [6]. Figure from [4, 7]. Reproduced with permission from Elsevier.

From Eq.(3.6), we need a weighting term that considers their spins as follows,

$$[Q \pm iU](\hat{\mathbf{n}}) = \sum_{\ell=0}^{\infty} \sum_{m=-\ell}^{\ell} {}_{\pm 2}a_{\ell m}\, {}_{\pm 2}Y_{\ell m}(\hat{\mathbf{n}}) \tag{3.50}$$

Eq.(3.7) can also be expressed as,

$$[Q \pm iU](\hat{\mathbf{n}}) = \sum_{\ell=0}^{\infty} \sum_{m=-\ell}^{\ell} [E_{\ell m} \pm iB_{\ell m}]\, {}_{\pm 2}Y_{\ell m}(\hat{\mathbf{n}}) \tag{3.51}$$

where the real and imaginary components of the expansion have been separated since Q and U are real quantities. The E- and B-modes can be derived as

$$\begin{aligned} E_{\ell m} &= -\frac{{}_2a_{\ell m} + {}_{-2}a_{\ell m}}{2} \\ B_{\ell m} &= -\frac{{}_2a_{\ell m} - {}_{-2}a_{\ell m}}{2i} \end{aligned} \tag{3.52}$$

This let us define the E- and B-modes fields in real space,

$$\begin{aligned} E(\hat{\mathbf{n}}) &= \sum_{\ell=0}^{\infty} \sum_{m=-\ell}^{\ell} E_{\ell m} Y_{\ell m}(\hat{\mathbf{n}}) \\ B(\hat{\mathbf{n}}) &= \sum_{\ell=0}^{\infty} \sum_{m=-\ell}^{\ell} B_{\ell m} Y_{\ell m}(\hat{\mathbf{n}}) \end{aligned} \tag{3.53}$$

These have the same properties of the flat-sky equivalents that we have already derived: under transformation of parity the pattern of $E(\hat{\mathbf{n}})$ stay the same. In contrast, $B(\hat{\mathbf{n}})$ flips sign under the same transformation. Hence, E- and B-modes can be considered as the electric (i.e. "gradient") and magnetic (i.e. "curl') modes of the polarization function Eq.(3.7), whose patterns are shown Fig. 3.4.

In the case of the flat-sky approximation [81], the CMB anisotropy is characterized by the distribution in two dimensions in terms of $\mathbf{x} \equiv (\theta\cos\phi, \theta\sin\phi)$, with

$$\hat{\mathbf{n}} \equiv (\sin\theta\cos\phi, \sin\theta\sin\phi, \cos\theta) \tag{3.54}$$

And the $z-$axis is chosen to be along the direction from the observer to the patch middle point. Any vector field in two dimensions can be expressed in terms of a divergent and a rotational part. Then, the linear polarization distribution characterized by the Stokes parameters $Q(x)$ and $U(x)$ can be expressed in terms of two modes that are not dependent between them. As a spin-2 field, linear polarization can be decomposed into derivatives of second order applied to two scalar fields, the already introduced $E-$ and $B-$modes, as

$$\begin{aligned} [Q \pm iU](\mathbf{x}) &= (\bar{\partial}_x + i\bar{\partial}_y)^2 [E \pm iB](\mathbf{x}) \\ &= (\bar{\partial}_x^2 - \bar{\partial}_y^2)E(\mathbf{x}) - 2\bar{\partial}_x\bar{\partial}_y B(\mathbf{x}) + i[(\bar{\partial}_x^2 + \bar{\partial}_y^2)B(\mathbf{x}) + 2\bar{\partial}_x\bar{\partial}_y E(\mathbf{x})] \end{aligned} \tag{3.55}$$

Where we have defined a differential operator applied on a scalar function $f(\mathbf{x})$ as

$$\bar{\partial}_i f(\mathbf{x}) = \int \frac{d\vec{\ell}}{2\pi} f(\vec{\ell}) \frac{l_i}{l} e^{i\vec{\ell}\mathbf{x}} \tag{3.56}$$

For $i = \{x, y\}$, $f(\vec{\ell})$ the Fourier transform of $f(\mathbf{x})$ and $\ell = |\vec{\ell}|$.

From Eq.(1.21) and (3.53), we have three equations that fully characterize the temperature and polarization fields of the CMB. It is viable to compute six unique spectra from

temperature, E-mode and B-mode polarization. Such combinations are: TT, TE, TB, EE, EB and BB. From these combinations, the pair of even-odd parity fields are in most cases supposed to vanish because of parity arguments: if the universe is mirrored under a spatial reflection, then the spectra combinations are invariant with the exceptions $EB \to -EB$ and $TB \to -TB$. If these two exceptions are non-vanishing spectra, then the global parity of the universe will be broken. Subsequently, the three unique auto correlations are

$$\begin{aligned} C_\ell^{TT} &= \frac{1}{2\ell+1}\sum_m \langle a_{\ell m}^{T*} a_{\ell m}^{T} \rangle \\ C_\ell^{EE} &= \frac{1}{2\ell+1}\sum_m \langle a_{\ell m}^{E*} a_{\ell m}^{E} \rangle \\ C_\ell^{BB} &= \frac{1}{2\ell+1}\sum_m \langle a_{\ell m}^{B*} a_{\ell m}^{B} \rangle \end{aligned} \tag{3.57}$$

and the only cross spectrum,

$$C_\ell^{TE} = \frac{1}{2\ell+1}\sum_m \langle a_{\ell m}^{T*} a_{\ell m}^{E} \rangle \tag{3.58}$$

It is customary to use the flattened spectrum:

$$D_\ell = \frac{\ell(\ell+1)}{2\pi} C_\ell \tag{3.59}$$

The maximum precision that a measurement of a power spectrum can achieve is statistically given by the *sample variance* and it is a consequence of the finite number of modes that can be sampled. The *sample variance* is given by

$$\Delta C_{\ell,\text{sample}} = C_\ell \sqrt{\frac{2}{(2\ell+1)\Delta\ell f_{sky}}} \tag{3.60}$$

where $\Delta\ell$ is the multipole width and f_{sky} is the fractional area of the sky observed (or not masked) and where we have high confidence in the measurement of the signal. f_{sky} is generally below 1 because of Galactic foregrounds. The sample variance is also proportional to the power spectrum itself.

3.8 Gravitational lensing

Massive intervening large-scale structures in the propagation of the CMB photons from the last-scattering surface to us deflect their paths. This induces alterations in both the temperature and polarization anisotropies. We are mostly interested in the alterations on polarization. Under the weak lensing regime, observed polarization on the celestial sphere represented by $Q(\hat{\mathbf{n}})$ and $U(\hat{\mathbf{n}})$ from a specific direction $\hat{\mathbf{n}}$ can be linked to the polarized signal at last scattering surface ($\tilde{Q}$ and $\tilde{U}$) with the following expression [78],

$$[Q \pm iU](\hat{\mathbf{n}}) = [\tilde{Q} \pm \tilde{U}](\hat{\mathbf{n}} + \mathbf{d}(\hat{\mathbf{n}})) \tag{3.61}$$

where $\mathbf{d}(\hat{\mathbf{n}})$ denotes the angle deviation of light coming from direction $\hat{\mathbf{n}}$, dubbed the *lensing deflection field*. The deflection field keeps track of the successive deflections for each position on the sky, that is linked to the integral along the line of sight over the gravitational potential $\Psi(D\hat{\mathbf{n}})$ by means of $\mathbf{d}(\hat{\mathbf{n}}) = \nabla\phi(\hat{\mathbf{n}})$:

$$\phi(\hat{\mathbf{n}}) = -2\int dD \frac{D_s - D}{DD_s}\Psi(D\hat{\mathbf{n}}) \tag{3.62}$$

where D is the comoving distance in the direction of the line of sight and D_s is the distance to the last-scattering surface along the line of sight [78]. From Eq.(3.61), we can see that these slight deviations shuffle polarization on the celestial sphere but do not rotate it. In practice, the interpretation of this phenomenon would be the redirection of a mode wavevector without changing its polarization, which qualitatively indicates the reason for gravitational lensing to produce B-mode polarization from early E-mode polarization.

Concretely, for a single primordial pure E-mode, the lensing E- and B- modes generated are,

$$\begin{aligned} \Delta E(\vec{\ell}) &= \frac{\cos(2\phi_{\vec{\ell}\vec{\ell}'})}{(2\pi)^2} W(\vec{\ell}, \vec{\ell} - \vec{\ell}') \\ \Delta B(\vec{\ell}) &= \frac{\sin(2\phi_{\vec{\ell}\vec{\ell}'})}{(2\pi)^2} W(\vec{\ell}, \vec{\ell} - \vec{\ell}') \end{aligned} \tag{3.63}$$

where we have defined $\phi_{\vec{\ell}\vec{\ell}'} \equiv \phi_{\vec{\ell}'} - \phi_{\vec{\ell}}$ and,

$$W(\vec{\ell}, \vec{\ell} - \vec{\ell}') \equiv -[\vec{\ell}' \cdot (\vec{\ell} - \vec{\ell}')]\phi(\vec{\ell} - \vec{\ell}') \tag{3.64}$$

Hence, broadly speaking, lensing will produce B-modes along with modified E-modes from a single primordial pure E-mode, but with other distinctive patterns in Fourier space. We can integrate over several primordial E-modes via Eq.(3.63) to produce the changes ΔE and ΔB that we observe. These modifications to E-modes and B-modes induced by gravitational lensing correlate E-modes and B-modes over different regions of Fourier space, generating non-Gaussianities. These non-Gaussianities greatly differences the B-modes induced by gravitational lensing from the B-modes induced by gravitational waves, mostly Gaussian.

The prediction for $C_\ell^{\phi\phi} = \left\langle \phi(\vec{\ell})\phi(\vec{\ell}) \right\rangle_{\phi_{\vec{\ell}}}$ can be done theoretically via numerical methods akin to those used to compute the predicted CMB power spectra, but we also need to consider non-linear modifications for effects in later times [82]. $\phi(\vec{\ell})$ is predicted to be drawn from a Gaussian distribution in like manner the other CMB fields. $C_\ell^{\phi\phi}$ depends on the sum of neutrino masses at the percent level. This enables the chance for highly sensitive measurements of $C_\ell^{\phi\phi}$ to set tight limits in the sum of neutrino masses [83].

The predicted lensing potential estimates the angle deflections $\mathbf{d}(\hat{\mathbf{n}})$ to be in the order of a few arcminutes, although correlations of the deflection field are expected to be in the order

of several degrees. In Fig. 3.12, a theoretical computation for the correlations between the amplitude of the deflections $C_L^{dd} = [L(L+1)]^2 C_\ell^{\phi\phi}/2\pi$ over different angular scales $|\vec{L}|$, where $\vec{L} = \vec{l} + \vec{l}'$, is plotted.

Using $C_\ell^{\phi\phi}$ and C_ℓ^{EE} as inputs, the generated C_ℓ^{BB} power spectrum can be estimated. In Fig. 3.13, the concordance model computation for the C_ℓ^{BB} spectrum generated from the gravitational lensing of pure E-modes is plotted. The detection of this signal was the main goal of the first observation campaign of Polarbear.

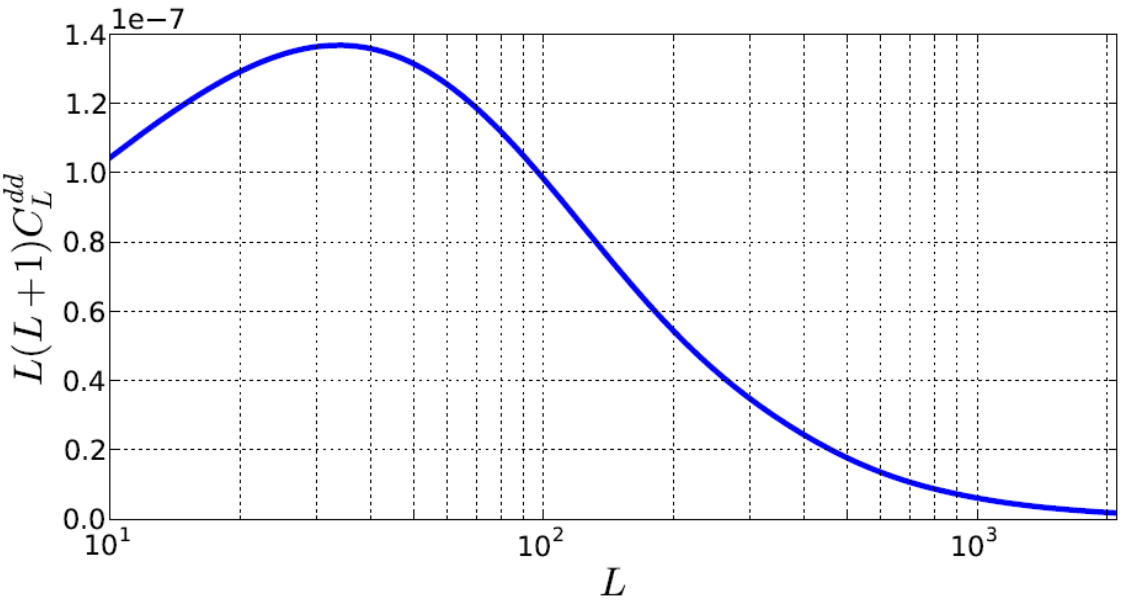

Figure 3.12: The concordance model theoretical prediction for C_L^{dd} angular power spectrum, where d is in units of radians, sourced by the LSS of the universe. Figure from [8].

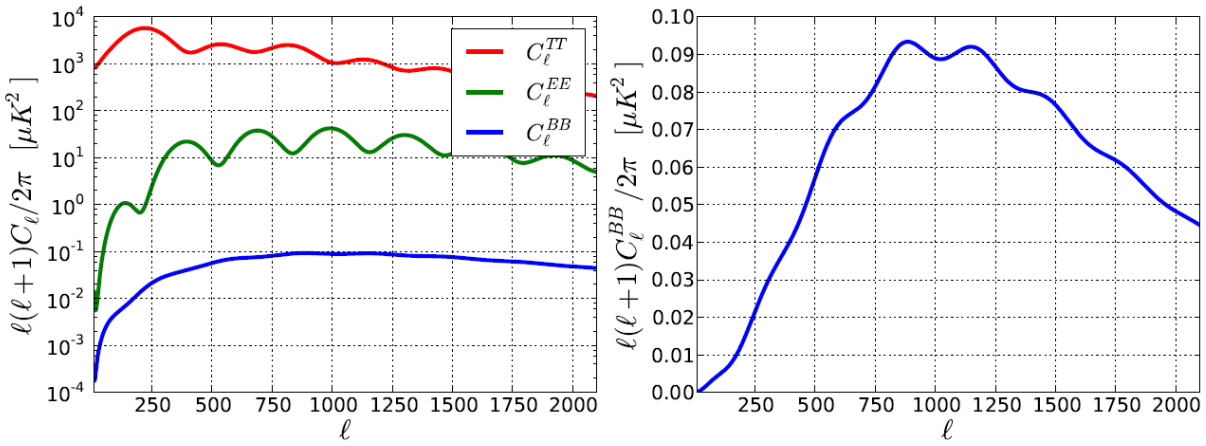

Figure 3.13: The ΛCDM theoretical prediction for the C_ℓ^{BB} angular power spectrum produced by gravitational lensing of pure E-mode polarization. Left panel: C_ℓ^{BB} on a logarithmic scale to compare it to C_ℓ^{TT} and C_ℓ^{EE}. Right panel: C_ℓ^{BB} on a linear scale. Figure from [8].

From Fig. 3.13, we note, again, that the emissions which Polarbear is intended to detect, C_ℓ^{BB}, have magnitudes that are some orders below those that had been experimentally characterized when the experiment started, C_ℓ^{TT} and C_ℓ^{EE}. This sets high standards for an instrument that must be both precise and effective in mitigation of systematic errors.

3.9 The current status of CMB experiments

A snapshot for some of the most recent measurements for the four non-vanishing CMB spectra is shown in Fig. 3.14.

The CMB E-mode polarization angular power spectrum was pioneer measured by the DASI experiment [84] placed at the South Pole. The present best constraints on the E-mode polarization angular power spectrum are given by the Planck collaboration at large scales [2]. The best constraints on the E-mode spectrum at small scales are reported by ACT [15] and SPT [10].

The B-mode polarization signal has been characterized in various independent ways. Various ancillary strategies have been applied, where a template for the gravitational lensing is provided from a tracer that does not rely directly or uniquely on the CMB polarization, like the cosmic infrared background (CIB) [23] or employing the corresponding CMB anisotropies [85]. Then, the B-mode angular power spectrum can be inferred in an independent way or in cross correlation with CMB polarization maps.

A detection of the B-mode angular power spectrum from only the CMB polarization was pioneer announced by the Polarbear collaboration in [23]. Successive direct characterizations of B-mode polarization have been published by Polarbear [17], BICEP2 [86], Keck Array [87], SPTpol [11], and ACTPol [15].

To obtain tighter upper limits in the tensor to scalar ratio r is necessary to cross correlate CMB observations with higher and lower frequencies for galactic foreground mitigation. That kind of cross-correlation studies have been reported by the BICEP2 and KECK Array collaboration [14, 88] and the ABS collaboration [89]. The Polarbear collaboration also performed such study using three seasons of data that is published along with the results obtained using the implemented modifications presented in this thesis [6].

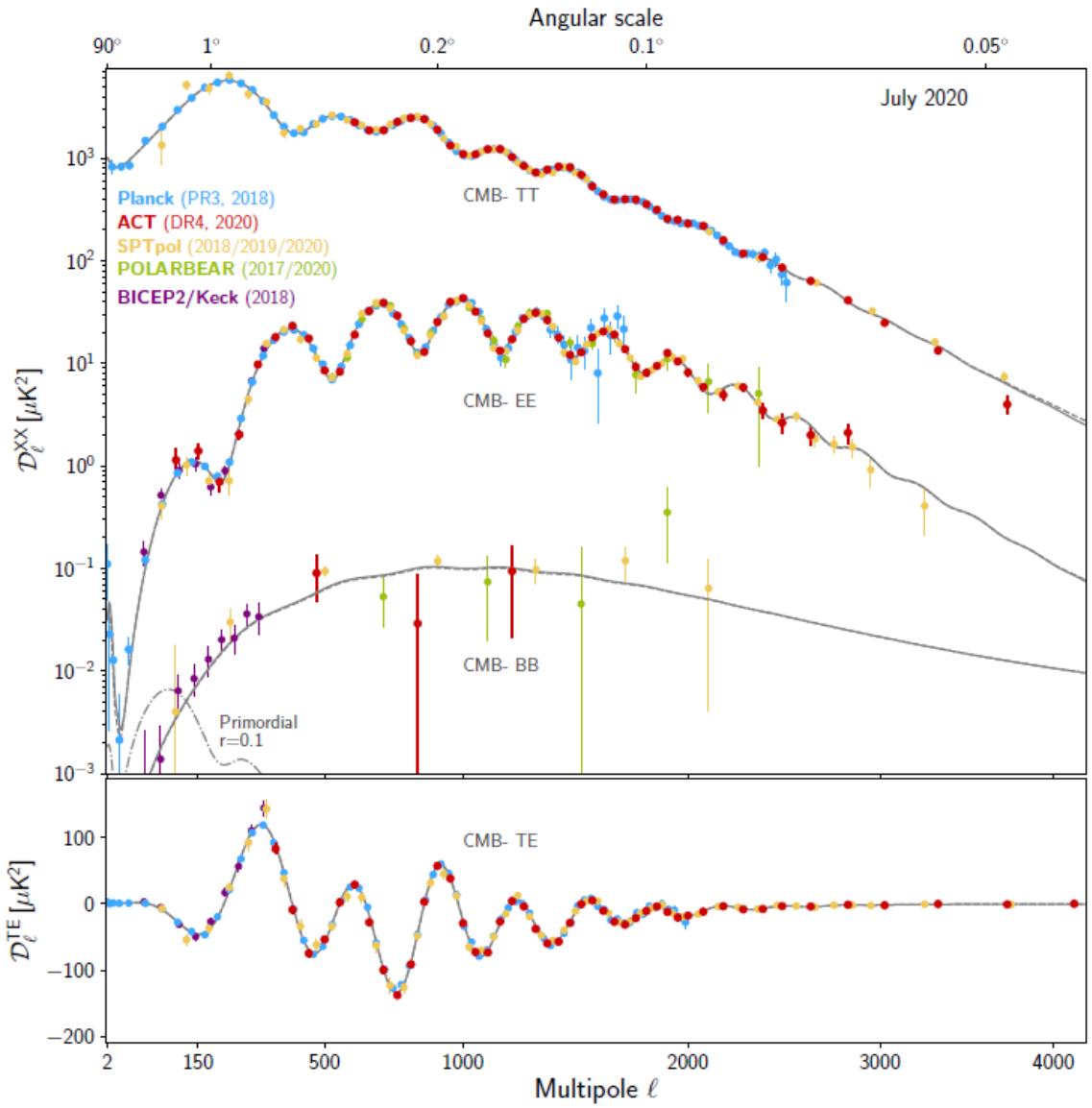

Figure 3.14: Current measurements of the CMB temperature anisotropy and polarization. The pair of models, the fine almost overlapping grey lines, comes from Planck (dashed line) and from ACT+WMAP (derived from [9], solid line). Additionally, the primordial B-modes auto spectrum with $r = 0.1$ is plotted with the dot-dashed line. For the Planck measurements, the 2018 results are shown [3]. For SPT the measurements performed in the 150 GHz band for TT $\ell < 2000$, TE and EE spectra are shown [10], and from [11] for BB spectrum. For the range $\ell > 2000$ the SPT spectrum from [12] which has been revised for point source contamination is shown. In practice, it is almost identical from the more precise but not revised spectrum in [13]. For BICEP2/KECK Array data from [14] are shown. For ACT, preliminary EE spectrum results for $\ell = [103, 150.5, 200.5, 250.5, 300.5]$, $D_\ell^{EE} = [1.14 \pm 0.32, 1.40 \pm 0.22, 0.70 \pm 0.14, 2.02 \pm 0.20, 9.74 \pm 0.39](\mu K)^2$ reported but not used in their analysis in [15] are shown. For Polarbear, EE spectrum from [16] and BB spectrum processed by pipeline A in [17] are shown. This work presents a new measurement of the B-mode CMB polarization anisotropy angular spectrum for Polarbear at large scales [6]. Each error bar is 1σ and data points which lack bottom bounds in TT and EE spectra are not shown at small scales. More data for each survey have been omitted here, for instance, data contained in other frequencies. Figure from [15].

Chapter 4

The Polarbear Experiment

B-mode polarization at angular scales of degrees is virtually a distinctive prediction of inflation. The detection and subsequent analysis of this signal will allow us to address more precisely the energy scale at which inflation happened and more about the extraordinarly high-energy physics that caused it. With its high angular resolution, Polarbear is very well placed to make a complete delineation of this signal.

The CMB photons are radiated at a redshift of $z \sim 1100$ and are gravitationally lensed as they travel along the intervening structure of the universe in direction to our telescopes; this lensing is another cause of B-mode polarization which contaminates the inflationary B-mode signal. If we want to analyse inflationary B-modes with high precision the removal of the lensing signal becomes necessary; that can best be achieved with data from projects with high angular resolution like Polarbear.

The POLARization of Background microwave Radiation (Polarbear) Experiment uses a telescope with a primary mirror with its size optimized to cover the range of angular scales indispensable to address both inflationary $B-$modes and lensing $B-$modes, and with optics which are conceived to give a focal plane with large area and angle of view that permit the utilization of a large number of detectors and reduce the observation noise.

The focus of this thesis is the improvement of the power spectrum estimator employed by the collaboration to characterize the CMB polarization signal. Nevertheless, the polarization maps do not spontaneously appear at the doors of our estimator. Contrary to these punishable beliefs, a large amount of time, manpower and funding is devoted to all the previous steps, including of course the instrument designing, construction and maintenance, along with the process of data acquisition and processing, and it is my duty to acknowledge those efforts in this section.

This section is organized in the following way. In Section 4.1, I give a brief description of the Polarbear Experiment and the data set employed in this work, focusing on the introduction of a continuously rotating half-wave plate (HWP) to the optical path for sky polarization

modulation. In Section 4.2, I mention the pre-processing and low-level calibrations that the data undergo. Finally, in Section 4.3, I summarize the process to transform raw bolometer data stream of observations or time-ordered data (TOD) into polarization maps Q and U. As mentioned before, my work focused primarily on the power spectra estimator discussed in Chapters 5, and I did not make relevant contributions to this part of the project. However, I present this section for completeness. Furthermore, also for completeness and documentation, in Section 4.3.2 I give a brief description of a parallel study carried out by me about the glitch flagging statistics of the data selection pipeline as a revision of at that moment available database, without any relevant or unexpected findings. Hence this study does not form part of the final publication [6].

This chapter is mainly based on [6].

4.1 Experiment and Data Set

4.1.1 The Polarbear Instrument

Polarbear is a CMB experiment that uses a 2.5 m aperture telescope, dubbed Huan Tran Telescope, which first light took place on 10 January 2012. The telescope is placed at the James Ax Observatory. The place is located at an elevation of 5190 m in the Atacama Desert, Northern Chile. The Polarbear receiver contains seven wafers that consist of 1274 transition-edge sensor bolometers across all the wafers, which temperature is kept to 0.3 K while scans the sky by way of lenslet-coupled double-slot dipole antennas. The field of view of the focal plane at any time is roughly $1^\circ.2$ in radius. A schematic diagram of the receiver is shown in Fig. 4.1. For a deeper description of the receiver and the telescope I refer the reader to [90] and [91].

During February 2014, the collaboration inserted a continuously rotating half-wave plate (HWP) in the focus of the primary mirror for low-frequency noise control [92]. The HWP is composed of an antireflective-coated birefringent single crystal sapphire plate spinning at two hertz. For a detailed description of the insertion of the HWP in the optical path of the telescope and the evaluation of its operation in a sequence of trial observation I refer the reader to [93].

4.1.2 Observation Strategy and Wide Sky Patch Observations

The maps considered in this study aim a 670 effective square degree patch of the sky whose center is located on $(RA, Dec) = (+0^h12^m0^s, -59^\circ18')$. This region of the sky overlaps in great extent with the patches covered by the South Pole telescopes such as BICEP, the Keck Array, and SPTPol. The map coverage is shown in Fig. 4.2. Routine CMB patch scans with the HWP started on July 25, 2014 and were performed until December 30, 2016. The collected data is divided in three seasons, as specified in Table 4.1.

Season Number	Beginning Date	End Date
HWP commissioning	2014 May 4	2014 Jul 24
Third season	2014 Jul 25	2015 Mar 1
Fourth season	2015 Mar 2	2015 Dec 31
Fifth season	2016 Jan 1	2016 Dec 30

Table 4.1: List of observing seasons for the data set considered in this study. The seasons are divided by interval periods of hardware maintenance. The first two seasons are detailed in [17, 23] and are not part of this study. Table from [6]. ©AAS. Reproduced with permission.

This map coverage differs from the one corresponding to the first two seasons of operations, where three $3° \times 3°$ patches of sky were observed targeting the sub-degree scale B-mode polarization angular power spectrum and gravitational lensing imprints. The change of this configuration will have unwanted consequences in the performance of the power spectrum estimator due to the flat sky approximation adopted and will be the main motivation for the changes in the estimator studied and implemented in the context of this work.

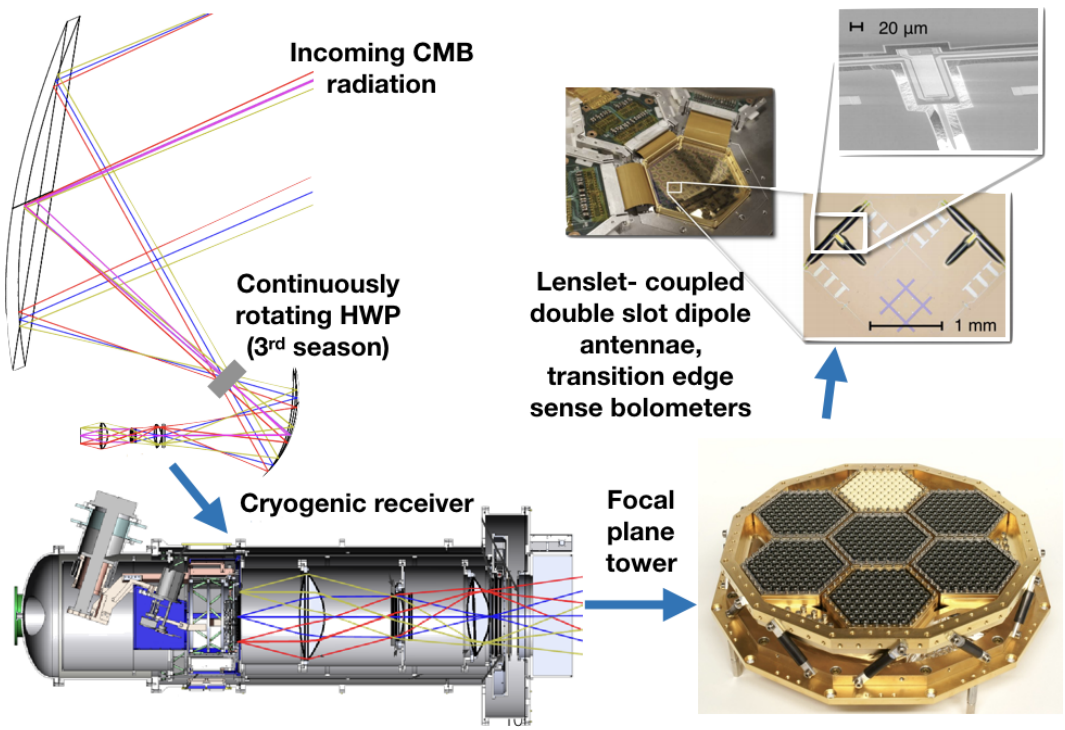

Figure 4.1: Sketch of the Polarbear receiver that illustrates the optical path, focal plant tower and microfabricated antennae and TES bolometers. Figure from [18].

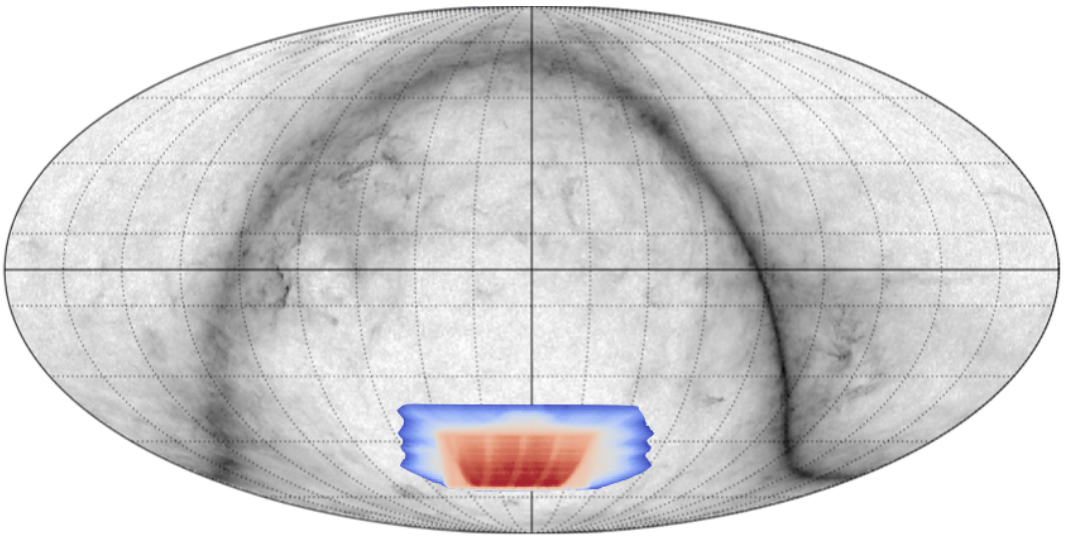

Figure 4.2: Patch coverage centered at $(RA, Dec) = (+0^h12^m0^s, -59°18')$. The scan pattern illustrates with red the nethermost center and with blue the poor weighted boundaries. The nethermost region of the patch has a map depth as low as $16\mu K$-arcmin and the average of the effective map depth is 32 μ K-arcmin, both quantities in polarization. The vertical lines correspond to an artifact of breaks in the low elevation observations to regularly tune the detectors and execute the relative gain calibration. The horizontal lines correspond to an artifact of the elevation offsets performed in the transit scan. The Polarbear depth map is superimposed on the Planck 353 GHz temperature map to illustrate the Galactic contamination pattern. Figure from [18].

The observation planning is composed by three series of observations done over each sidereal day. The telescope observes for a 4 hr 45 minute interval as the region ascends above the horizon, a 3 hr 53 minute interval at high elevation as the region transits, and a 4 hr 45 minute interval as the region descends. The ascending and descending observations happen at a boresight elevation of 30° and 35°.2, respectively. The elevation of the high-elevation observations is stepped across ten offsets from 45°.5 to 65°.5 to assure uniform coverage of the region with one offset picked each day. Each scan interval is separated into observations of one hour denoted as "constant elevation scans" (CESs). Right after that, the detectors are retuned. The calibration steps will be briefly reviewed in Section 4.2. The telescope is repointed from one four-hour long interval to the next one but not from one CES to the next one.

In the course of the observations, the telescope scans at a constant speed of $0°.4s^{-1}$ subtending 20° and 35° on the sky for the low elevation and high elevation observations, respectively. The outcome is roughly 70 subscans (determined as one left-going or right-going scan of the telescope) for every CES.

The total data set ended made up of 429 days. The ten high-elevation observation offsets allowed a complete map to be generated only once each ten days of observations. An important number of these ten-day scan subsets have been coadded in post-processing because of

a low yield or incomplete coverage after the data is selected. The resulting splits serve as the base for the cross-spectra implemented in the power spectrum estimation.

4.2 Calibration and Pre-processing

This section gives a brief overview of the steps performed to produce the inputs that are fed into the data analysis pipelines. The lost data packets are afterward marked in the data selection.

4.2.1 Reconstruction of HWP Angle

The HWP angle is recovered and interpolated to be equal to the bolometer readout time records. The associated errors are subdominant to the total statistical error.

4.2.2 Pointing

The telescope pointing reconstruction uses exclusively assigned raster scans of bright point sources chosen from PCCS [94] and ATCA [95] catalogs before every CMB observation. The measured locations estimated from the azimuth and elevation encoder values of the telescope are contrasted to the predicted locations. The azimuth and elevation offsets obtained $\Delta Az(Az, El)$, $\Delta El(Az, El)$ are modeled by an eight-parameter model that incorporates terms for non-uniform heating of the instrument produced by the insolation [96]. The errors associated with the degrees of freedom of this calibration procedure are negligible for the multipole range considered in this work.

The detector beam offsets are generated from detector array raster observations across Jupiter. The reconstructed offsets are compatible with earlier measurements at the order of several tens of arcseconds. Bolometers whose average modeled beam offset are discrepant with previous analysis in [17] exceeding $1'$, are not considered in subsequent analysis steps. This cut does not have a significant repercussion in the total efficiency of the data selection.

4.2.3 Beam Profiles

The instrumental beam and the corresponding window function B_ℓ are obtained using exclusively assigned raster scans across Jupiter. These are performed with the HWP spinning nominally at two revolutions per second and at a scan speed of $0^\circ.2 s^{-1}$ on the sky. The HWP synchronous structure induced by the instrumental polarization of the primary and differential transmission and emissivity of the HWP is subtracted. Then, the data stream is mapped into $0'.5$ pixels on the sky. The beam window function is the average of the 2D Fourier transformed maps that are averaged in azimuth, after we have divided out the Jupiter disk for every observation and corrected for the pixel window function in an analytical way. The generated beam window function is plotted in Fig. 4.3, with a median Gaussian $3'.6$ full width at half maximum (FWHM).

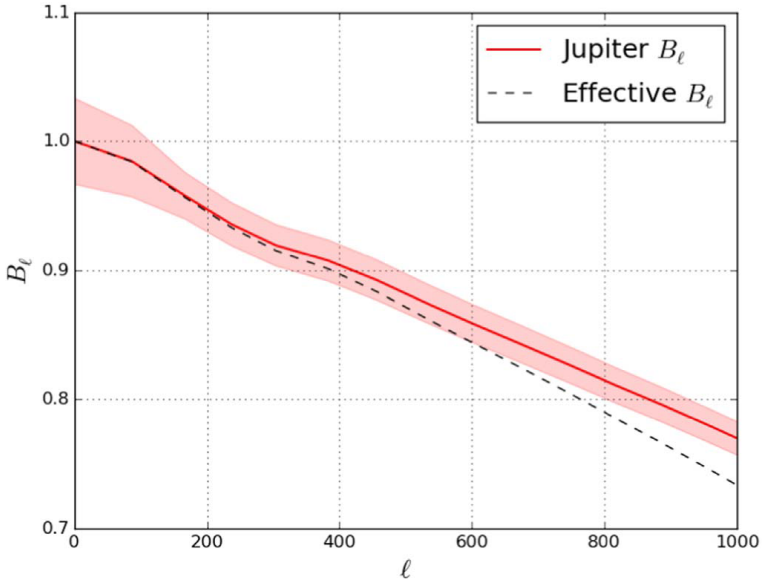

Figure 4.3: Generated beam window function from Jupiter raster scans. The statistical uncertainty in the pointing model suppressed more power at small scales, as illustrated by the dashed effective beam curve. The statistical uncertainty in the Jupiter beam window function corresponds to the shaded area. Figure from [6]. ©AAS. Reproduced with permission.

Boresight and detector statistical pointing error suppress more power at small scales of the maps. The pointing model estimates residual pointing uncertainties of 50″ rms. A multipole dependence is fitted to the overall gain amplitude, in line with the broaden of the effective beam induced by pointing error, and an extra broaden of the effective beam induced by pointing uncertainty is not statistically preferred. Thus, a Gaussian associated with the best-fit pointing model error generated from the $E-$mode polarization angular power spectrum is convolved with the beam window function, and the effective beam width uncertainty is considered in the multiplicative error budget.

The detector beam window function is generated from temperature measurements but used to estimate polarization angular power spectra. An effective beam discrepancy induced by the detector crosstalk behaving dissimilarly in temperature and polarization and also dissimilarly with the addition of a continuous HWP [97], is found to be statistically subdominant. Also, a scalar component extracted from the polarization response to Jupiter is subtracted to mitigate temperature-to-polarization leakage and higher order components are found to be negligible.

4.2.4 Time Constants and Detector Gains

A three-step gain calibration procedure was adopted to convert the data stream into physical temperature with an extra correction for polarization efficiency. A detector relative time-dependent gain calibration is measured by the operation of a chopped thermal calibration source before and after every block of four CESs. To obtain the time dependence of the gain, these measurements are linearly interpolated in between. From that time these values are converted to temperature on the sky by the use of the same Jupiter data employed to

estimate the beam window function. The simulated systematic error in the CMB spectra originated in the error of the measured gain are found to be statistically subdominant in all the CMB fields.

The measurement of the detector time constants is obtained by stepping the frequency of the chopped thermal source from four to forty-four revolutions per second. The source amplitude as a function of chopper frequency is fit to a single pole low pass filter model. The estimated time constants are interpolated linearly between the measurements and deconvolved in the following data stream processing.

4.2.5 Angle of Polarization

The polarization angles of detectors and polarization efficiencies are measured from exclusively assigned raster observations of Tau A. The raster observations are performed at $0^\circ.2s^{-1}$ scan speed on the sky with the HWP spinning nominally. The detector time constants obtained from a chopped thermal source calibration right before and after the Tau A raster observation is deconvolved. This is needed because a phase difference between the detector data stream and the reconstructed HWP angle induced by the retarded response of the detectors, encoded in the time constants, arises as a polarization angle error.

Subsequently correcting for detector time constants, the correlation between the measured polarization angle and the precipitable water vapor (PWV) measured at the close-by Atacama Pathfinder Experiment[1] (APEX) location was found to be insignificant. If such time constant deconvolution is not performed, a correlation induced by the dependence of the time constants on the atmospheric loading and hence on the local PWV is found. The demodulated polarization data stream explained in Section 4.3.1 is modeled as polarization map convolved with a beam of Tau extracted from a observation performed with the IRAM 30 m telescope [98]. The fluctuations of detector polarization angles between seasons was found to be insignificant. The discrepancies in the measured polarization angle between detectors in a pair are measured as $90^\circ.5 \pm 1^\circ.2$, compatible with the designed target of 90°. The simulated systematic error cause by the detector polarization angle error was found to be statistically subdominant.

The estimated polarized flux extracted from these observations is employed to measure the polarization efficiency of the telescope and receiver. The polarization efficiency estimation is worsened in four manners: the non-ideality of the cold HWP (explained in [17, 23]), the non-ideality of the rotating HWP, the breaking of the Mizuguchi–Dragone (MD) condition [99, 100], and nonvanishing bolometer time constants. The first three are characterized by polarization efficiency terms that are inherent to the detectors and telescope geometry and are corrected by rescaling the data stream and noise weights with the predicted values from coherent source lab measurements and design detector bandpasses [90] and physical optics simulation [101]. The detector time constant behaves low-pass filter on the time domain

[1] `http://www.apex-telescope.org/`

of the data stream, with a response below unity at the polarization modulation frequency. Its polarization efficiency is related with the numerical value of the time constant, which at the same time relies on the detector bias point and optical loading. In consequence, this polarization efficiency term is corrected by deconvolving the estimated time constant from the chopped thermal calibration source before and after every block of four CESs. The mean contributions to the overall polarization efficiency from the four ways are, in the same order as mentioned above, $\varepsilon \approx 0.98, 0.98, 0.93$ and 0.98. The values extracted from the TauA calibration are found to be compatible with the predictions, though showing a larger statistical uncertainty, as we would expect.

The overall polarization angle is self-calibrated by requiring $C_\ell^{EB} = 0$ as dictated in [102]. There is a degeneracy between the overall polarization efficiency and the absolute gain of the polarization maps, and the overall polarization angle is fixed by making coincident the Polarbear E-mode spectrum to the Planck 143 GHz E-mode spectrum on the Polarbear wide patch.

4.3 Analysis of Data

The framework and processing steps used to convert the raw detector data stream into polarization maps, that will be used in this work as inputs for the power spectrum estimator (the focus of this work) will be reviewed in this section.

4.3.1 Processing of Data Stream

This stage uses a pre-processing and demodulation steps akin to those in [93,103]. The terms corresponding to detector nonlinearity and instrumental polarization are not considered in this review for clarity. The model for the raw detector data stream with respect to instrument coordinates can be expressed as

$$d_m(t) = I(t) + \varepsilon \mathfrak{Re}\{[Q(t) + iU(t)]e^{-i(4\chi + 2\theta_{det})}\} + A(\chi, t) + \mathcal{N}_m \tag{4.1}$$

with $\chi \approx \omega t$ as the HWP angle, $m(\chi) \equiv e^{-i4\chi}$ characterizing the polarization modulation of the HWP, ε as the polarization efficiency, θ_{det} as the detector angle in the telescope frame, $\mathcal{N}_m$ as the detector white noise, and $A(\chi, t)$ as a slow pace fluctuating HWP-synchronous structure in the data stream.

Before demodulate the data stream, HWP-synchronous structure $A(\chi, t)$ is subtracted by an iterative method akin to [104]. The HWP angle is reproduced from the encoder. The HWP synchronous structure is obtained according to [92] and is separated into harmonics. Discontinuities in the data stream are substituted with the HWP synchronous structure. The data stream is bandpass filtered for each harmonic $n \in \{1, 2, ...7\}$ with a frequency width of 1 Hz and demodulated to generate a time-dependent amplitude for the corresponding harmonic of the HWP synchronous structure. The amplitude of each harmonic is modeled as a linear trend. The sum of these n fits is subtracted from every data stream, and the procedure

is repeated. Subsequently of the HWP structure subtraction, the polarization emission is recovered by multiplying the data stream by two times the conjugate of the modulation function $2m^*(\chi)$ and is low pass filtered to reconstruct the polarization emission,

$$d_d(t) = \varepsilon[Q(t) + iU(t)]e^{-2i\theta_{det}} + \mathcal{N}_d \tag{4.2}$$

The remaining analysis steps will use the data stream saved at an 8 Hz frequency resolution. This is because the elevated frequency resolution of the raw bolometer data stream and the amount of Fourier Transform operations, such as the demodulation step in the essential simulations would be extremely resource intensive. The window function corresponding to the 8 Hz frequency resolution is negligible for our multipole domain. The detector time constant is deconvolved from the data stream after the demodulation of the data stream polarization.

It is imperative to remark that the noise in the data stream after demodulation, $\mathcal{N}_d$, is complex and both the real and imaginary parts have two times the variance of the bolometer white noise before demodulation $\mathcal{N}_m$ because of the need to consider twice the overall processed data stream to properly reconstruct the stokes parameters Q and U. The polarization precision obtained in this way has not an inherent discrepancy with the one obtained by differencing the bolometer data streams within a pair. The noise $\mathcal{N}_d$ can be well characterized as a noise floor plus a unique red noise component shared by all the bolometers. The demodulation procedure supposes a proper isolation of temperature and polarization signals in time domain frequency, that is, the HWP frequency is well above the numerical value of the scan speed over the beam width. The effect of an improper isolation of both temperature and polarization signals are quantified in real data and the impact was found to be statistically subdominant. These demodulated data streams are fed to the following data characterization and mapmaking steps.

The low-pass filtered HWP synchronous structure subtracted data stream (the 0f or temperature component) and the demodulated data stream at two times the HWP frequency (the 2f component) are subsequently considered for data characterization and selection.

4.3.2 Data Selection and Characterization

The data selection procedure performed in this pipeline is composed of several iterations of progressively discriminatory data quality standards to describe red noise and suppress potential effects of systematic error. The rounds can be summarized in succinct words as rejecting glitches and time well-defined singular events, rejecting data depending on the individual detector noise attributes during the transit of an observation, rejecting data depending on array noise attributes, and rejecting data depending on map domain noise.

For the purpose of every round, the elemental constituent of data treated is the bolometer subscan. The data corresponding to the intervals when the telescope is accelerating (called turnarounds) are totally cut. In Table 4.2, the efficiencies corresponding to the different stages of data selection are shown and I refer the reader to [6, 18] for a better description of

them. The main inputs to the end-to-end efficiency are the portion of time the observation region is accessible to be scanned, incurred hardware pauses by maintenance and weather conditions, and total focal plane yield generated by burned out bolometers and glitch rejections. An overall of 2985 CES observations are fed to the subsequent mapmaking pipeline from the entire observation campaign ranging from July 25, 2014 to December 30, 2016.

Category	Stage of Data Selection	Efficiency
Operations and yield	Time spent observing patch	36.8%
	Focal plane yield	50.7%
Data Selection	Glitch cuts and off bolometers	29.2%
	Individual bolometer PSDs	76.6%
	Common mode PSD and maps	79.6%
	Overall data selection	17.8%

Table 4.2: Operations and data selection efficiency for this study. In total 2985 CESs of one-hour extension have any portion of data fed in the final science pipeline. The focal plane yield is normalized to the originally intended number of active optical detectors, that is 1274. The overall data selection efficiency is the multiplicative result of the three rows above it. Table from [6]. ©AAS. Reproduced with permission.

As a first task in my participation at the Polarbear Project, I was assigned to conduct a glitch flagging statistics study of at that moment available data selection database. This comprised a cross check of the main data selection efforts and did not arise any significant finding. It was in line with the flagging statistics expectation and did not play any role in the final data selection used in [6]. Furthermore, is not considered the main goal of this work and so a deeper description of it is out of the scope of this thesis. Nevertheless, I briefly summarize it here for completeness and documentation of my efforts devoted to the experiment.

There were roughly 600 active bolometers in the focal plane taking TOD of the intensity or polarization. Each CES is associated with a set of parameters, for example, the elevation angle and azimuth range (Fig. 4.4 shows the distribution of the database), time range, etc., and a flag array generated by the, at that moment, available pipeline containing a number of elements corresponding to the number of subscans times the number of bolometers, representing each element a bolometer subscan, which is a subscan for a certain bolometer. It encodes unsigned 129-bit integers. Each bit of the flag set corresponds to a specific cut. If one is active, the corresponding subscan is discarded for the respective bolometer. There are different kinds of cuts associated with different sources of problems: inadequate scan parameters, presence of glitches in the TOD, rejection of the gain calibration or Power Spectral Density (PSD), etc. With this database was possible to check some glitch statistics correlated with others.

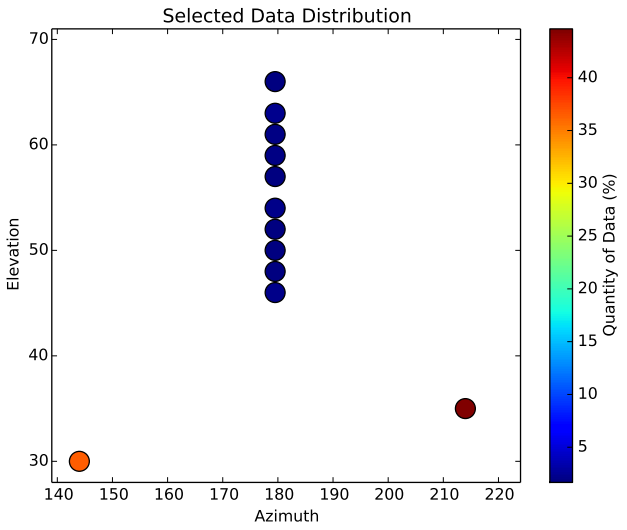

Figure 4.4: Distribution of the data chosen for the performed glitch flagging statistics study in the azimuth-elevation plane.

Histograms of the different kinds of flagging criteria with the mentioned database were generated and the fraction of glitchy data as a function of elevation angle and azimuth was analyzed. Potential problematic elevations were considered. David Boettger took data with accelerometers installed in the telescope and dedicated scans using them were performed to check for elevation anomalies in the behavior of the telescope. I implemented a code to analyze the accelerometer measurements of the telescope. With this was possible to check the vibrational level for a given elevation. An example of an output of this script is shown in Fig. 4.5. At higher elevation I found a higher vibrational response with respect to lower elevations, as expected, but no significant pathological behavior was discovered.

4.3.3 Red Noise Model

Two noise models are considered for the simulation pipeline with a verified overall compatibility. The red noise component in the time domain of the data can be characterized by a unique common mode $1/f^{\alpha}$ term, implying that modes of higher order in the data stream covariance are unimportant. The analysis pipeline is run from the beginning up to the end in two arrangements: one where a data stream noise model is considered and other where random sign coaddition of single CES maps are used to produce "signflip" noise realizations.

Referring to the data stream noise model, white noise is produced for each detector based on the supposition of lack of correlations between detectors and the noise weights obtained in the steps involved in Section 4.3.2. The common mode red noise is generated in the telescope frame for the stokes parameters Q and U independently and is made to be coincident with the amplitude and exponent power-law α fixed by the real data. Then, this noise mode is rotated into the polarization angle of every detector and combined with the white noise that is not correlated.

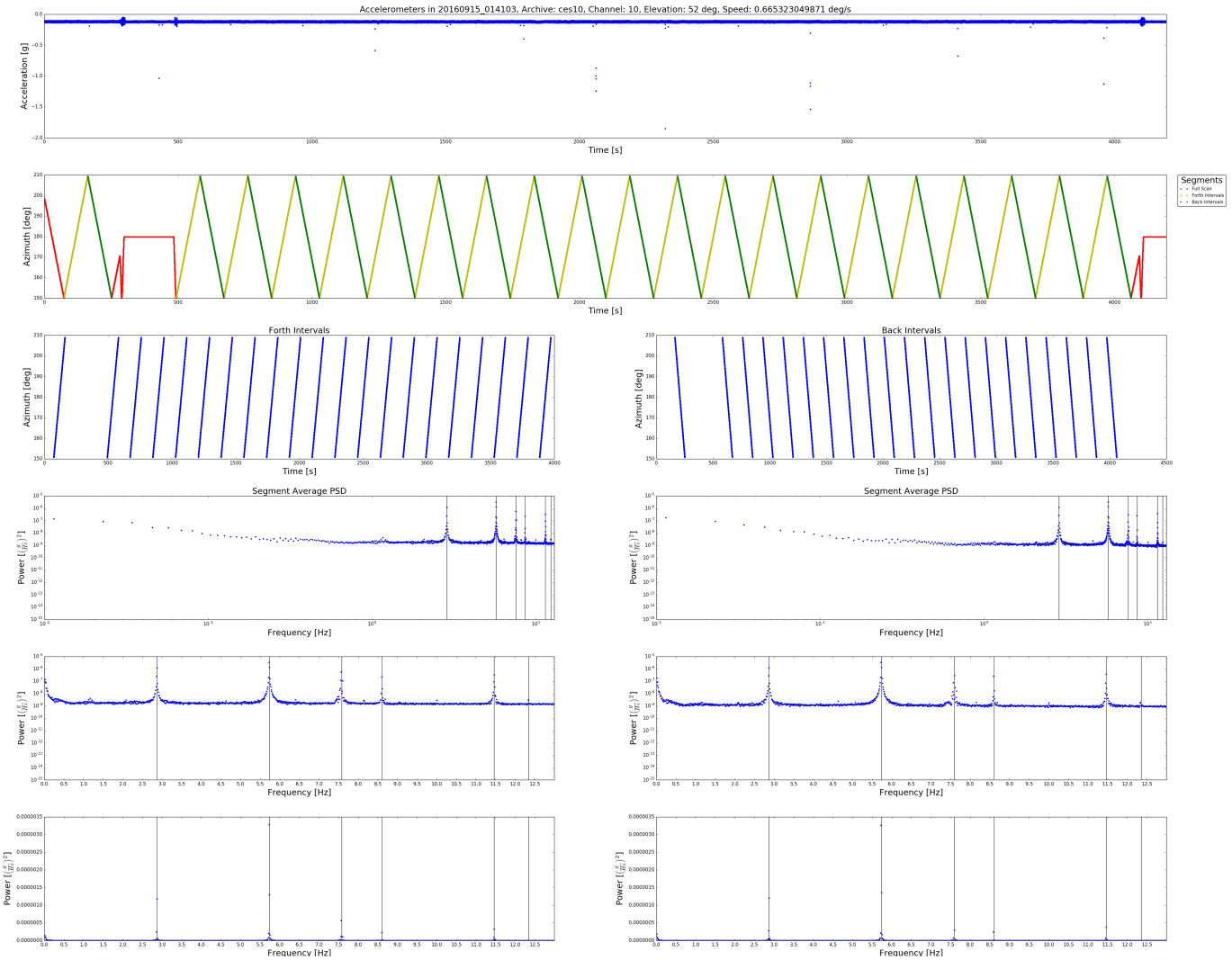

Figure 4.5: An example of output generated by the code implemented to check the vibrational level for a given elevation. In this case, $El = 52°$. The vibrational response is represented as the power of the measurements and the peaks were identified with vertical lines. Subsequent analysis considered the distribution of peaks per elevation.

In the "signflip" pipeline, the noise realizations are produced by randomly giving a $+1$ or -1 factor to every map at the time of the coaddition of the CESs. This generates noise realizations that match the power spectrum and correlation pattern of the real data, with the supposition of lack of correlation between CESs noise fluctuations. This supposition does not hold if coherent drift in the amplitude of the ground synchronous structure is present. The impact of this effect is not relevant for the error budget.

A good compatibility between the "signflip" and the data stream noise realizations is found using the cross-spectrum estimator presented in Section 5.1. In Fig. 4.6 the noise bias extracted from both configurations is plotted. The full coadd and every null test split that are mentioned in Section 6.4 coincide satisfactorily, apart from one null split. In the "top versus bottom detectors" splits that separates paired bolometers, an extra variance and anticorrelation is measured in map space between the two splits that is not possible to be

replicated by the data stream noise model. Intensity noise aliasing into the polarization frequencies in the data stream can reproduce a noise anticorrelation pattern in agreement with the one mentioned above. This can be easily reproduced with the "signflip" noise realizations.

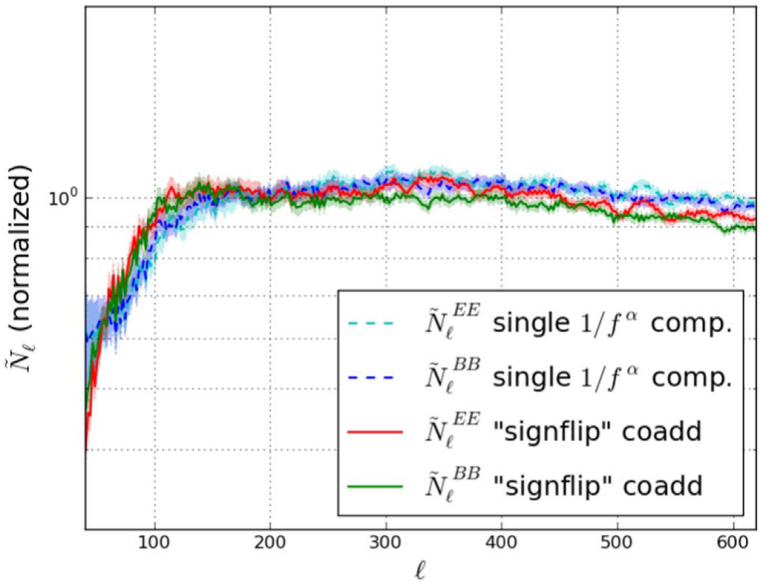

Figure 4.6: A comparison for the noise bias estimation for the all the observation set between the data stream noise model and the "signflip" coaddition configuration is shown. An overall agreement between the two configurations is patent. The fiducial power spectrum pipeline uses the "signflip" noise model as one of the inputs. These spectra are not corrected by the filter transfer or beam window functions presented in Section 5.1. The shaded area illustrates the standard deviation of the reproduced noise bias. Figure from [6]. ©AAS. Reproduced with permission.

The random sign coaddition configuration is adopted to produce the noise realizations fed in the fiducial null tests and error bar estimation.

4.3.4 Mapmaking Pipeline

In this pipeline stage, the MASTER mapmaker [105] is adopted where the data stream is filtered to mitigate spurious red noise and mapped in the sky by an inverse variance noise weighting.

The mapmaker is fed with the demodulated data streams explained in Section 4.3.1 which undergone another pile of time domain filters. The order configuration of the filtering steps is determined to prevent bias in the estimated coefficients of intensity leakage by artificial modes in the intensity and polarization data stream.

The beginning filter step is performed in Fourier space and the demodulated data stream is low pass filtered for frequencies higher than 1.2 Hz. A collection of notch filters is administered to Fourier space glitches marked in the data selection stage. For each detector on the

focal plane a notch width of 10 mHz is applied if an evident glitch is detected in a number above fifty bolometers for a specific hour-long CES. The same collection of notch filters is administered to simulations.

The next filter step subtracts a second-order polynomial from every detector data stream for the entire hour-long CES. Thermal variations of the focal plane and cryogenics are predicted to drive this mode.

The subsequent filter step removes a ground-fixed template in the measured Stokes parameters I, Q, and U. The filter is generated by averaging the data stream in telescope coordinates using $14'.4$ azimuth bins and removing the constructed template from the data stream. Every detector undergone this process individually. Both back and forth subscans are processed by an identical template. The ground synchronous structure is believed to be sourced by far-sidelobe response of the nearby ground emission. For a conservative removal, it is assumed that hour long CESs are not correlated between them, and a single ground-fixed template is removed for every hour long CES although typically a steady ground-fixed emission from one hour long CESs to others is measured. A maximum estimated for the contribution in the error budget induced by potential time fluctuations of this signal during every hour-long CES is estimated. The final estimated power spectrum undergone negligible variations if the bin size is changed or a template that has been previously smoothed is removed.

After the subtraction of these spurious modes, intensity-to polarization leakage produced by bolometer nonlinearities and instrumental polarization generated from the off-axis telescope architecture are subtracted out with the use of a PCA akin to that in [93]. The intensity leakage coefficients are observed to slightly depend on frequency when it is lower than the scan frequency of the telescope, and glitches in the data stream Fourier space are measured at frequencies well above. The leakage coefficients are then predicted from a duplication of the data stream that has been low pass filtered at 300 mHz and a first-order polynomial has been removed from every subscan of it. Subsequently, from the data stream a three-dimensional covariance square matrix linking the I, Q, and U Stokes parameters is estimated and averaged over the subscans. The covariance matrix is then employed to compute the leakage coefficients according to [93]. A steady behavior of the predicted leakage coefficients is observed during the scans. The initial polarization data stream is then subjected to the removal of the intensity leakage not considering the subscan polynomial and low-pass filtering. The simulated error in the B-mode angular power spectrum generated by multiplicative detector nonlinearity is estimated to be subdominant in the final error budget. It is worthy to note that this PCA operation and leakage terms are not considered in the final simulation pipeline, i.e., only are used for the real data pipeline.

Consecutively, red noise suppression is tackled by removing a first-order polynomial from the data stream Stokes parameters Q and U for every subscan. As I have mentioned before, the temperature data does not undergo any additional treatment because it is not required

in the following steps of the pipeline. Moreover, is not part of the data products of the final analysis.

The final step consists in the mitigation of the low frequency mode measured across all the bolometers by a filtering operation. Every detector data stream in the telescope coordinates has the low pass filtered representation of the Q and U array common mode removed out from them. The low-pass filter is characterized by a spectral representation equivalent to the reciprocal of the fit PSD of the stacked timestream extracted in the data selection stage. Simulations undergo the same filtering. There is not an appreciable red noise contribution after the unique focal plane common mode considered here, as noted in Section 4.3.3.

After all these operations, the data stream is mapped into $8'$ pixels on the celestial sphere by a Lambert Cylindrical equal area projection. Fig. 4.7 shows real data and a sample noise realization converted into final maps. Corrections to account for the effect of the beam window function and the filter operations of the data stream lead to an effective map depth of 32 μK-arcmin.

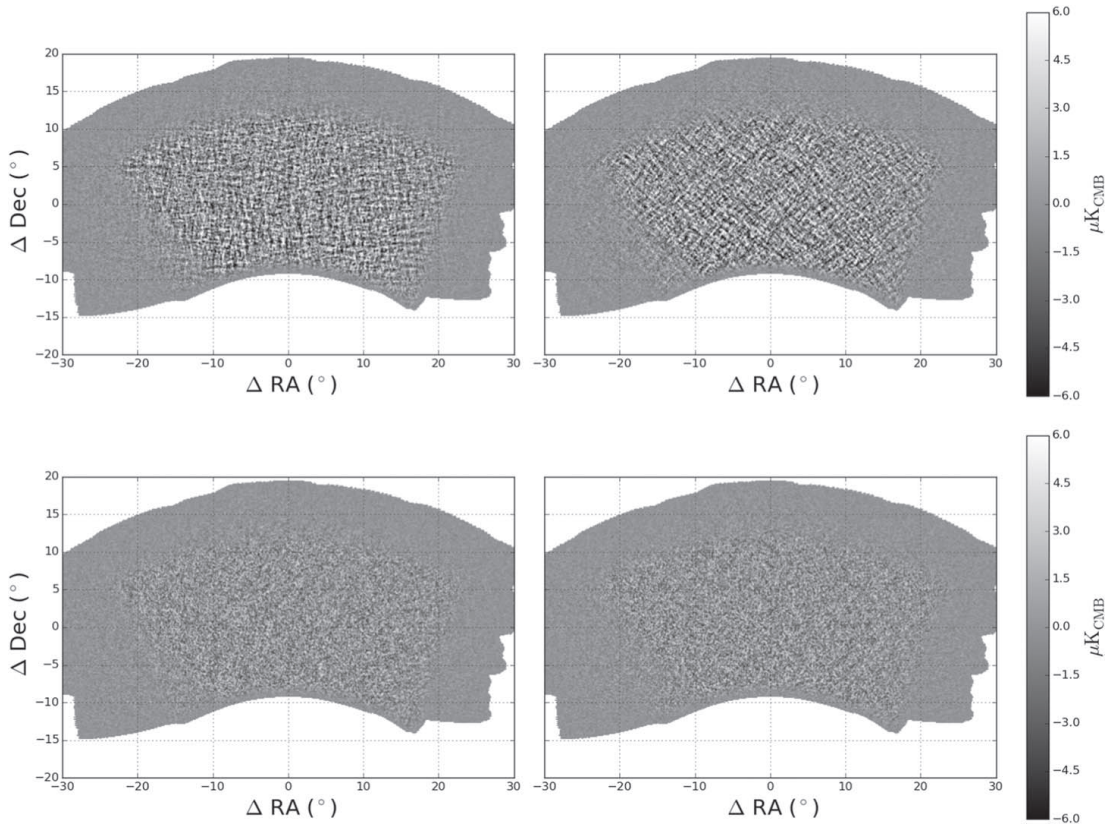

Figure 4.7: Polarization maps corresponding to the Stokes parameters Q and U of the real data (upper panel) and a sample noise realization generated by the "signflip" coaddition noise model configuration (lower panel) are shown for Polarbear. The E-mode polarization imprint of the CMB signal is appreciable in the real maps in the shape of a checkerboard structure for both Q and U Stokes parameters. Figure from [6]. ©AAS. Reproduced with permission.

Chapter 5

Power Spectrum Estimator

The focus of this thesis are the modifications implemented in the B-mode pseudospectrum stage of the power spectrum estimator. In Section 5.1, a description of the different stages of the estimator, that was previously used in the context of the small patch analysis, is provided. In Section 5.2, a pair of analyses evidencing potential problems with this estimator when applied to our wide patch analysis configuration are discussed, serving as motivation for the work described in this thesis. Finally, in section 5.3, I describe my efforts performing exploratory analyses of possible solutions or mitigations of such problems.

Section 5.1 is mainly based on [8, 106]. Section 5.2.1 takes from [107] and Section 5.2.2 takes from [108].

5.1 Background

The power spectrum estimator is mainly based on the previous work developed in the context of the small patch analyses ([23] and "Pipeline A" in [17]), that was followed by several small corrections implemented to mitigate numerical inaccuracies at large scales (low multipole moments), that constitutes the hearth of this work. Nevertheless, I start giving an overview of the preceding estimator that was used in the framework of the small patch analysis, before the changes of this work (and other contributions developed in parallel) were implemented in the context of the wide patch analysis, to understand the motivations and achievements generated by these efforts.

The relevant aspects of this C_{BB} estimation pipeline are summarized here, that are mainly based on the Monte Carlo Apodized Spherical Transform Estimator (MASTER) method described in [105]. The estimator is somewhat changed to employ cross-spectra between maps observed in different days, as outlined in [109, 110].

The MASTER method is essentially employed to consider that although power spectra that represents the entire sky is intended to be characterized, we only have access to a partial coverage of it. Also, the method considers the anisotropy in the maps produced by the filter

operations applied to the TOD and the beam finite angular resolution. Considering a specific full sky spectrum characterized by its ensemble average $\langle C_\ell \rangle$, where the mean is computed over a large number of sky realizations, the method models the measurements as

$$\begin{aligned} \langle \tilde{D}_\ell \rangle &= \sum_{\ell'} K_{\ell\ell'} \langle D_{\ell'} \rangle + \langle \tilde{N}_\ell \rangle \\ K_{\ell\ell'} &= M_{\ell\ell'} F_{\ell'} B^2_{\ell'} \end{aligned} \tag{5.1}$$

Where we have used the rescaled spectrum $\langle D_\ell \rangle$ of $\langle C_\ell \rangle$ using the definition Eq.(3.59), and the same for $\langle \tilde{D}_\ell \rangle$ with $\langle \tilde{C}_\ell \rangle$. $\langle \tilde{D}_\ell \rangle$ denotes the rescaled pseudo-spectrum that is effectively measured at first instance in the partial observed sky maps, $M_{\ell\ell'}$ denotes the mode coupling matrix, F_ℓ denotes the filter transfer function and B_ℓ is the instrument beam spectrum, which measurement for the wide patch case is explained in Section 4.2.3, and $\langle \tilde{N}_\ell \rangle$ represents the noise bias. The apodization produced by the partial patch coverage, along with the edge taper applied to every map during the map preparation described in Section 5.1.1, correlates different Fourier modes from the whole sky, that is modeled by the mode coupling matrix. The filter transfer function F_ℓ models the reduction in power of the Fourier modes induced by the filter operations applied to the TOD. The filtering can be understood as removing out signal and noise in modes with exceptionally poor signal-to-noise ratio. This is equivalent to down-weigh the modes that have been filtered, and the filter transfer function guarantees the proper normalization of the total average.

Polarbear employs exclusively cross-spectra for the estimation of $\langle \tilde{C}_\ell \rangle$. The advantage of a cross-spectrum estimator is that it is unbiased in a way that the value expected for the estimator is the signal $\langle \tilde{C}_\ell \rangle$ [109], allowing to assume $\langle \tilde{N}_\ell \rangle = 0$. In the other hand, considering "auto-spectra" contributions using maps from individual days that are cross-correlated with themselves, as is customary in other procedures such as the original outline of the MASTER method, induces a noise bias that must be accounted by simulations and removed. The exclusive consideration of cross-spectra averts this additional problem with the side effect that the signal contained in the cross correlations of the same day is lost.

5.1.1 Preparation of Maps

The abovementioned same-day maps are fed to the power spectrum estimator. Apodization must be applied to the maps before the Fourier transform of them are used to compute the power spectra. This is done by the down-weighting of pixels with high levels of noise located at the boundaries of the map, and the masking of point sources. The maps of temperature are apodized using a cutoff of the inverse noise variance at the boundaries of the map, and with a uniform function where the CMB anisotropies are detected with a high signal-to-noise ratio. The maps of the Stokes parameters Q and U are apodized in the same way to each other using a cutoff on an estimate of the highest noise level between the maps of Q or U. Pixels of the map with an apodization function numerical value lower than 0.01 of the maximum value of the apodization window are set to zero. There is also a masking of the point sources in the map. The mitigation of the $E \to B$ leakage is performed by the change of the apodization boundaries according to the method outlined in [111]. For each pixel in the map, its inverse variance noise estimates are multiplied by the apodization mask. The estimation for the

inverse variance noise associated with each pixel in the map is multiplied by the apodization mask and integrated over the whole map to generate an individual numerical weighting value associated with each map ω_k^X, where k denotes the observation day that corresponds to that map and $X \in [T, E, B]$.

5.1.2 Estimation of Pseudo-spectra

The measured CMB anisotropy can be expressed as a superposition of Fourier modes with wavenumber $\vec{\ell}$, as outlined in Section 3.7. Two dimensional Fourier transforms associated with the temperature, E-mode and B-mode anisotropies achieve this decomposition [112],

$$\begin{aligned} \hat{T}_k(\vec{\ell}) &= \int d^2\vec{x} W_k^T(\vec{x}) I_k(\vec{x}) e^{-i\vec{\ell}\cdot\vec{x}} \\ [\hat{E} \pm i\hat{B}]_k(\vec{\ell}) &= -\int d^2\vec{x} W_k^P(\vec{x}) [Q \pm iU]_k(\vec{x}) e^{\mp 2i\phi_\ell} e^{-i\vec{\ell}\cdot\vec{x}} \end{aligned} \tag{5.2}$$

where k is the single day map index, ϕ_ℓ is the multipole moment angle, and the apodization window functions for the maps of temperature and polarization are denoted by $W_k^T(\vec{x})$ and $W_k^P(\vec{x})$, respectively. Nevertheless, there is a mixing of E-modes and B-modes induced by the gradient of the apodization window function, $W_k^P(\vec{x})$, in Eq.(5.2). To mitigate this source of contamination for B-modes, the pure-estimators are used [19]. The Fourier B-mode signal is defined considering the flat-sky approximation as,

$$\begin{aligned} \hat{B}_k(\vec{\ell}) = &- \sin 2\phi_\ell \mathcal{F}\left[W_k^P Q\right](\vec{\ell}) + \cos 2\phi_\ell \mathcal{F}\left[W_k^P U\right](\vec{\ell}) \\ &- \frac{2i}{\ell}\left(\sin\phi_\ell \mathcal{F}\left[W_{k;x}^P Q + W_{k;y}^P U\right](\vec{\ell}) + \cos\phi_\ell \mathcal{F}\left[W_{k;y}^P Q - W_{k;x}^P U\right](\vec{\ell})\right) \\ &+ \frac{1}{\ell^2}\mathcal{F}\left[2W_{k;xy}^P Q + \left(W_{k;yy}^P - W_{k;xx}^P\right) U\right](\vec{\ell}) \end{aligned} \tag{5.3}$$

Where we have defined the Fourier transform operator as

$$\mathcal{F}[A](\vec{\ell}) = \int d\vec{n} A(\vec{n}) e^{-i\vec{\ell}\cdot\vec{n}} \tag{5.4}$$

And the semicolons in the apodization window functions of Eq.(5.3) are followed by subscripts that denotes partial derivatives of the corresponding window function. However, the E-mode is not modified by this new definition in this pipeline because contaminations from B-modes is imperceptible when contrasted to the original E-mode signal. Furthermore, this would make the performance of the EE power spectrum estimator worse by rejecting ambiguous modes that are helpful to determine the power of the E-modes [19]. We recall that the TOD filtering and apodization of the maps changes the original Fourier modes and therefore from these we will form pseudo-spectrum estimators and not spectrum-estimators. The outcome of this step will be the Fourier transforms of the single day maps $\tilde{m}_k^A$, where k denotes the number of map and $A \in [T, E, B]$.

5.1.3 Power Pseudo-spectra

Solely the correlations that are from the same day are considered for the estimation of the power pseudo-spectrum $\tilde{D}_\ell$. This is done by average weighting the map products where each map in the product comes from a different day. The estimator then is expressed as,

$$\tilde{C}_{\vec{\ell}}^{XY} = \frac{1}{\sum_{i\neq j}\omega_i\omega_j}\sum_{i\neq j}\omega_i\tilde{m}_i^X\omega_j\tilde{m}_j^{Y*} \tag{5.5}$$

where $X, Y \in [T, E, B]$ and i and j corresponds to the map index and it ranges every day where maps are available for each patch of the sky. An estimation of 2D Fourier pseudo-spectra, purposely discarding the products where $i = j$ that are equivalent to the auto-spectra of single day maps, is obtained.

For each patch of the sky, two dimensional estimations of TT, EE, TE, TB, EB, and BB are computed using Eq.(5.5). Subsequently, one dimensional pseudo-spectra of high-resolution are obtained when these estimations are averaged across bins in the radial direction of size $\Delta\ell = 40$. The fine size of the bins and the patch of the sky signify a large correlation between the signals of bins that are neighbors meaning that they are measurements that cannot be considered as independent.

5.1.4 Power Spectra

The estimations of the underlying power spectra $\tilde{D}_\ell^{AB}$ now can be derived from the estimations of D_ℓ^{AB}. This can be done by the formation of $K_{\ell\ell'} = M_{\ell\ell'}F_{\ell'}B_{\ell'}^2$. The estimation of B_ℓ in the context of the wide patch is already discussed in Section 4.2.3. The mode coupling matrix $M_{\ell\ell'}$ is computed in an analytical way using the apodization masks computed for the maps co-added across the full observation campaign [113] at the pseudo-spectra resolution, i.e., $\Delta\ell = 40$.

The filter transfer function F_ℓ is obtained from the Monte Carlo method. A set of hundreds of random CMB map Gaussian realizations of one arcminute resolution using as input cosmology the WMAP-9 best fit ΛCDM angular power spectra [114] are created. Then, observations and analysis are simulated for each map without the presence of noise, and finally the output angular power-spectrum obtained from these simulations is contrasted with the initial input cosmology to obtain F_ℓ. The value of this estimation does not depend heavily on the input cosmology. In addition, $E \to B$ leakage can be induced by the filtering of the ground template and polynomial component. The mitigation of this leakage is performed using realizations of maps with solely TT and EE or TT and BB and removal of the leakage is performed at the level of the pseudo-spectra,

$$\tilde{D}_\ell^{BB(sub)} = \tilde{D}_\ell^{BB} - \frac{F_{\ell'}^{E\to B}}{F_{\ell'}^{E\to E}}\tilde{D}_\ell^{EE} \tag{5.6}$$

$M_{\ell\ell'}$, F_ℓ, and B_ℓ are computed with bins of high-resolution ($\Delta\ell = 40$). The narrowness and large correlations of the bins computed in the pseudo-spectra stage makes singular, at the

chosen resolution, the mode coupling matrix $M_{\ell\ell'}$. This prevent us to make the inversion of $K_{\ell\ell'}$ and directly use Eq.(5.1) to find the underlying D_ℓ for a measured $\tilde{D}_\ell$.

In consequence, $\tilde{D}_\ell$ and $K_{\ell\ell'}$ are binned into larger bins and $\tilde{D}_b$ and $K_{bb'}$ are obtained, respectively. The benefit to choose bins with high-resolution at the beginning of the power spectrum estimator pipeline is that the expensive steps in terms of computational resources has to be done only for one time, and the choice of other bin widths can performed at the end of this pipeline with little cost. The choice of four even spaced bins between $500 < \ell < 2100$ implemented in this analysis leads to $\Delta\ell = 400$. This has two advantages: the correlation reduction that are estimated between the bins and the error shrinkage on each bin. This binning is expressed as,

$$\langle \tilde{D}_b \rangle = \sum_{b'} K_{bb'} \langle D_{b'} \rangle \tag{5.7}$$

An unbiased estimation in each bin b of the band power D_b can be solved from Eq.(5.7) as,

$$D_b = \sum_{b'} K^{-1}_{bb'} \tilde{D}_b \tag{5.8}$$

Considering this binning resolution, the correlation between bins is small enough to make feasible the inversion of $K_{bb'}$ to derive $K^{-1}_{bb'}$ needed for Eq.(5.8).

5.2 Previous Studies and Motivation

The primary goal of these efforts was the validation of the power spectrum estimator described in Section 5.1 to be implemented in the context of the wide patch configuration, at that point validated only for the small patch configuration. Previous studies carried by members of the collaboration, first by Satoru Takakura [108], and later replicated by David Boettger [107], seemed to shed lights on possible problems that were affecting the behavior of the BB power spectrum estimator. An excess of the expected power at low multipole moments (large scales) was the first indication. In this section I describe these studies to better understand the motivations and possible solutions that I was assigned to study and finally implement to mitigate them.

5.2.1 Boettger's Study

David Boettger replicated previous Takakura's work showing that there is a detectable bias in our implementation of the MASTER algorithm that shows up at low multipole moments, or large scales, when using a wide patch configuration [107]. The idea was to run the full pipeline for a set of simulations drawn from a given cosmology and compare it with the final power spectrum estimation. A set of 48 maps characterized by a two arcminute resolution and a 79° apodization mask size using Gaussian realizations of the power spectra plotted with dashed lines in Fig. 5.1 were generated. The mode coupling matrix $M_{\ell\ell'}$ is computed at an initial resolution $\Delta\ell = 20$, same resolution chosen for the output power spectra.

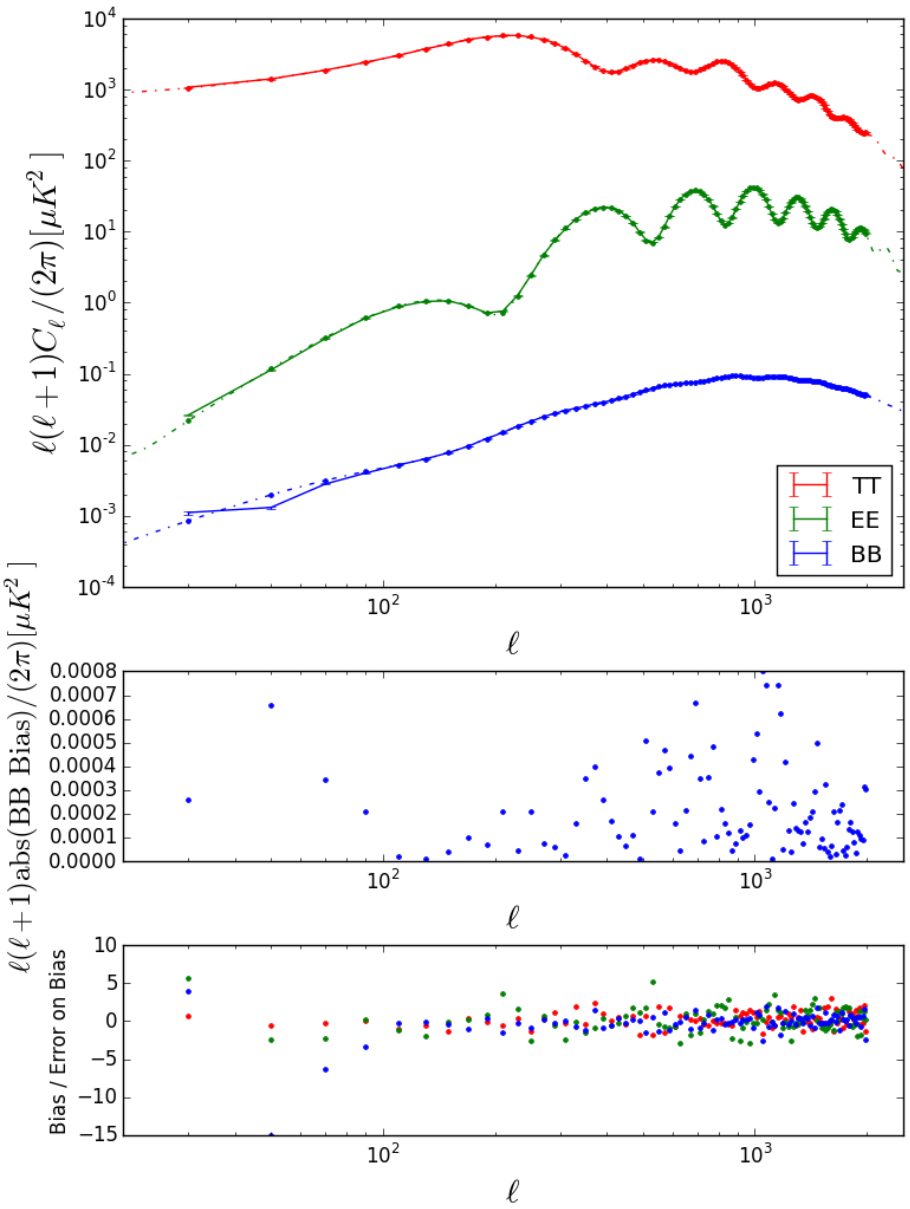

Figure 5.1: Power spectra estimation output for set of 48 maps characterized by a two arcminute resolution and a 79° apodization mask size using Gaussian realizations. Top panel: Angular power spectrum. Shown in dashed lines, the input cosmology for the simulations. In solid lines, the estimated values obtained from the power spectra estimator are shown. Middle panel: BB absolute bias defined as the absolute value of the discrepancy between the input and output BB power spectrum shown in the top panel. Bottom panel: The bias as a fraction of the error on the bias. The error on the bias is computed as the standard deviation of all the simulations divided by the square-root of the number of simulations. Courtesy of D. Boettger.

From Fig. 5.1, it is worthy to emphasize that the highest BB bias is not at low multipole moments, though as a fraction of the error it does increase more at low multipole moments. Nevertheless, the lowest multipole moment bin does not have the highest relative bias, hence the picture is potentially more complicated than just a low multipole moment problem. The distribution of the error relative bias in Fig. 5.2 looks Gaussian, apart from evident outliers

which are clearly the highest on the BB spectrum.

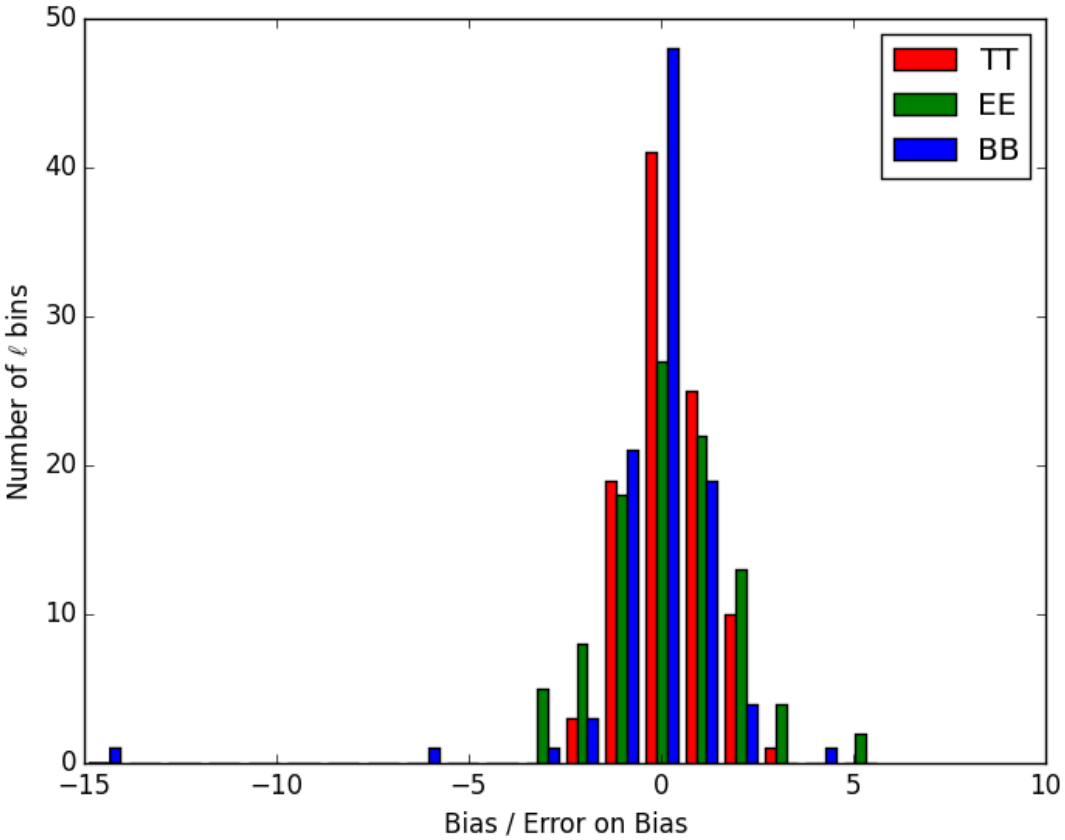

Figure 5.2: The distribution of the error relative bias shown in Fig. 5.1. Courtesy of D. Boettger.

The BB estimator and pure-B counter terms as implemented in Eq.(5.3) are expanded in ℓ around $\ell \to \infty$ so that the terms in Eq.(25) of [19] are approximated as $N'_{ell} = 2/\sqrt{(\ell-1)(\ell+2)} \approx 2/\ell$ and $N_{ell} = 1/\sqrt{(\ell-1)\ell(\ell+1)(\ell+2)} \approx 1/\ell^2$. Although this should not actually bias the spectrum because it will be corrected by the filter transfer function, Boettger tried adding the terms back into the estimator without these approximations to see if it would affect the results, with the quantified modifications of Eq.(5.3) shown in Fig. 5.3. He confirmed that adding this modification into the estimator does not modify the level of bias observed in the output. Anyway, it slightly rises the scatter in the simulations.

The behavior of the $BB \to BB$ filter transfer function at low multipole moment is greatly different than $EE \to EE$ or $TT \to TT$ due to its fast change. The power spectrum estimator implementation smooths the computed filter transfer function by the convolution of a kernel with it. This does not impose problems where the transfer filter function is changing slowly, but the rapid changes in the $BB \to BB$ filter transfer function at low multipole moment are smoothed away by this process and leads to a roughly 30% discrepancies between the unsmoothed and smoothed F_ℓ, as shown in Fig. 5.4.

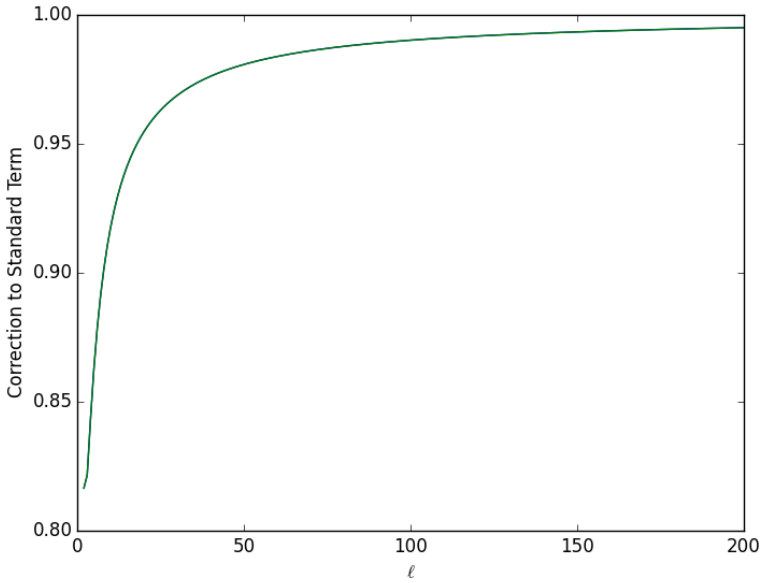

Figure 5.3: Fractional correction to the standard term of Eq.(5.3) if $N'_{ell} = 2/\sqrt{(\ell-1)(\ell+2)}$ and $N_{ell} = 1/\sqrt{(\ell-1)\ell(\ell+1)(\ell+2)}$ in Eq.(25) of [19] are not approximated for $\ell \to \infty$ in the implementation of our power spectrum estimator. Courtesy of D. Boettger.

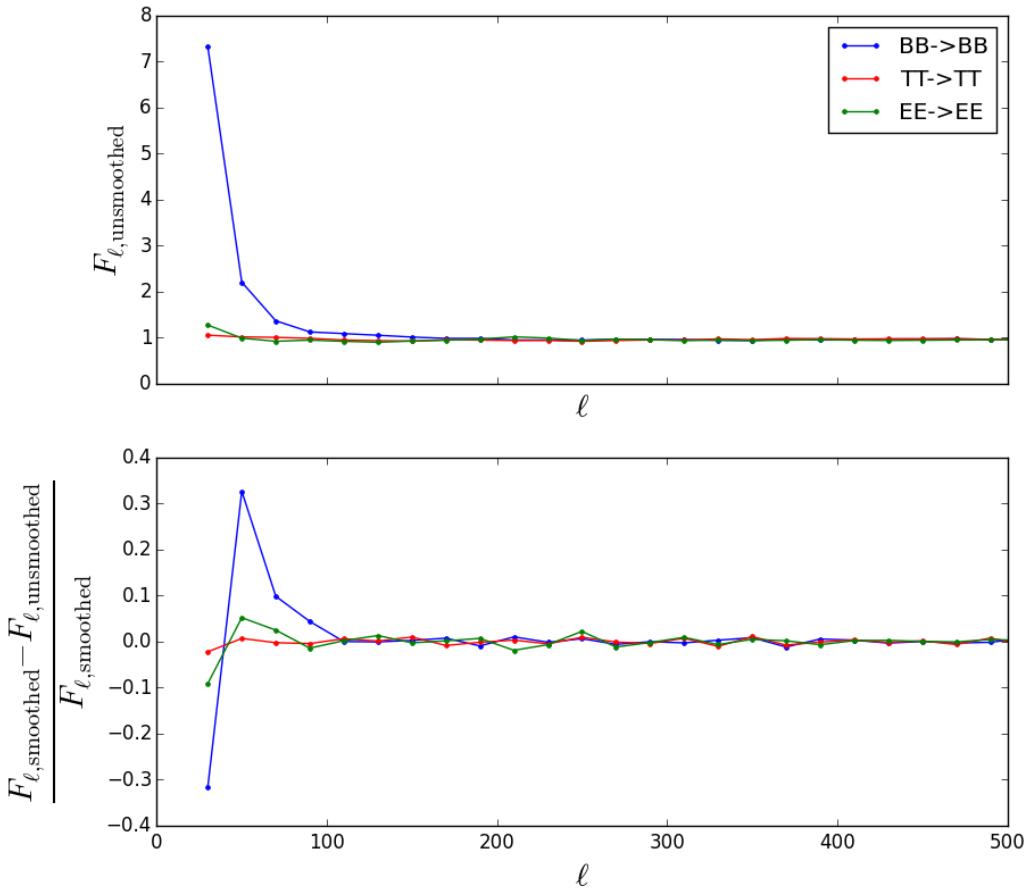

Figure 5.4: Top panel: Smoothed version of the filter transfer function implemented in our estimator. Bottom panel: Fractional difference of the smoothed version of the filter transfer function with one where the smoothing is not applied. Courtesy of D. Boettger.

These significant discrepancies between the smoothed and unsmoothed versions of the filter transfer function directly bias the BB spectrum at low multipole moments. If the smoothing is disabled in the simulations used for the power spectrum estimator output shown in Fig. 5.1, the BB bias at low multipole moments is reduced by more than an order of magnitude, while the TT and EE bias are still present at a similar (slightly reduced) level as compared to before and shown in Fig. 5.5.

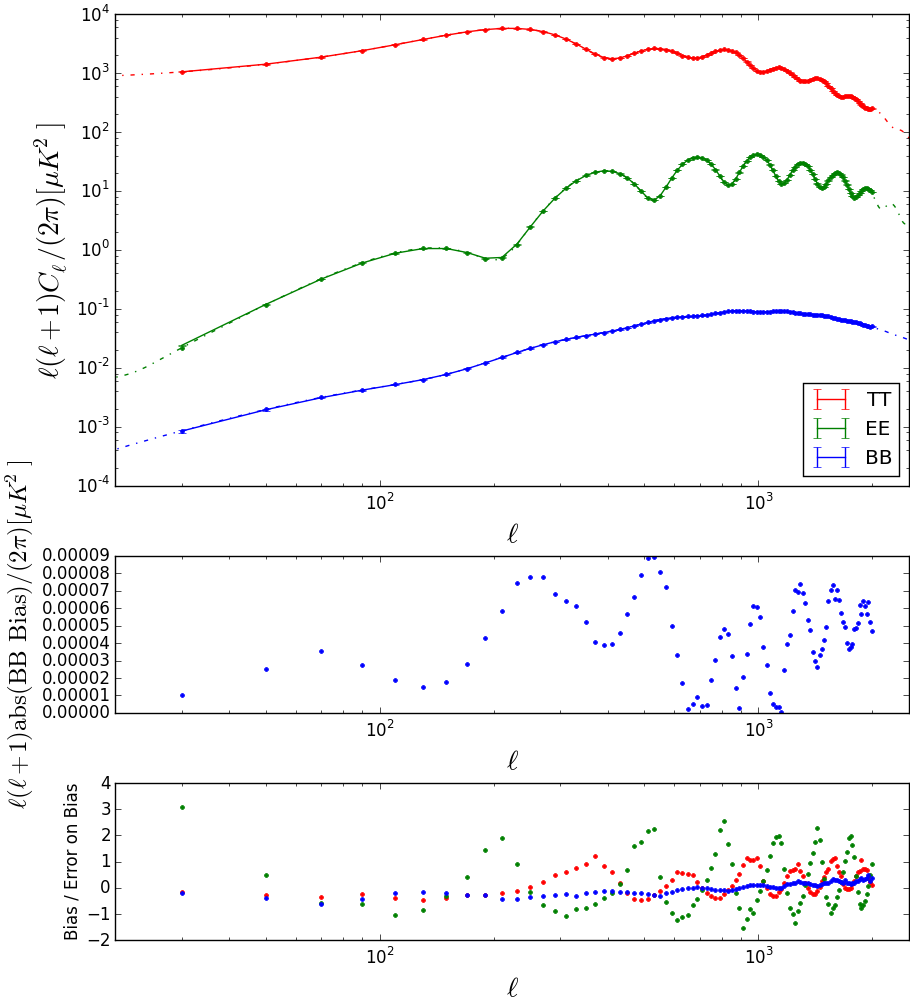

Figure 5.5: Same as Fig. 5.1, but without the application of the smoothing in the filter transfer function. Courtesy of D. Boettger.

Boettger mentioned that simply removing the convolution may not be the correct way to solve this problem, as the reason of why the smoothing was implemented in the first place was not well documented. The behavior of the $BB \rightarrow BB$ filter transfer function was clearly anomalous, exceeding the unity at low multipole moments what would mean an excess of power at the pseudo spectrum level for those multipole moments, instead of the loss of power expected by the TOD filtering and processing that motivates the implementation of such operation. The reason of this behavior was unclear. Boettger concluded that if there is a resolvable problem with the BB behavior that keeps the filter transfer function smooth, it seemed it would also fix the low ℓ bias problem. The application or not of the leakage subtraction expressed in Eq.(5.6) did not make a significant difference in the abovementioned

conclusions. The $BBBB$ mode coupling matrix exhibited the same anomalous behavior as the filter transfer function at low multipole moments, as plotted in Fig. 5.6.

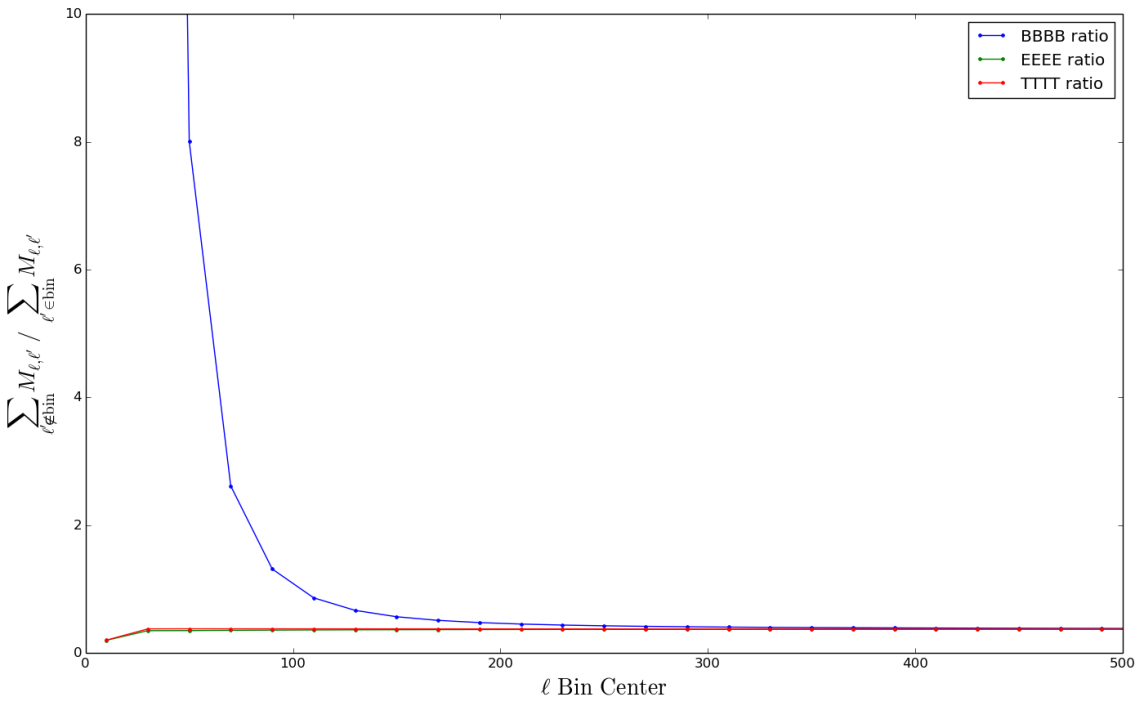

Figure 5.6: For the mode coupling matrices involved in the power spectrum estimation shown in Fig. 5.1, the total contribution of the mode couplings with every other multipole moments for a given multipole moment ℓ as a fraction of the total mode coupling contributions for that multipole moment, including the mode coupling from the same multipole moment, is shown. Courtesy of D. Boettger.

The detected problem is that the mode coupling matrix $M_{\ell\ell'}$ as computed either analytically (as described in 5.1.4) or using Monte Carlo simulations showed strong coupling between sky power (ℓ') at almost any multipole moment into observed pseudo-power at low multipole moment (ℓ). This excess of power is only present when the counter terms in Eq.(5.3), that correct for $E \rightarrow B$ leakage produced by the presence of the apodization window function, are used. It is worthy to mention that both the analytic expression for the mode mixing and the Monte Carlo simulations use the same expression for the counter terms.

Using the Monte Carlo (MC) implementation instead of the analytic one for the calculation of the mode coupling matrix makes it easier to explicitly test these effects term by term. The MC code works by generating a map of Q and U with pure B-mode power in a given band of multipole moments, passing it through the chosen apodization window functions, and measuring the resulting B-mode power including the counter term corrections.

In Fig. 5.7 there is a demonstration of this, where the two-dimensional spectrum output is plotted after injecting Gaussian pure B-mode power into a multipole moment ring $400 < \ell < 420$. The left plot shows the result without applying the counter terms, and the right shows the counter terms applied. It can be noted for the corrected case that the

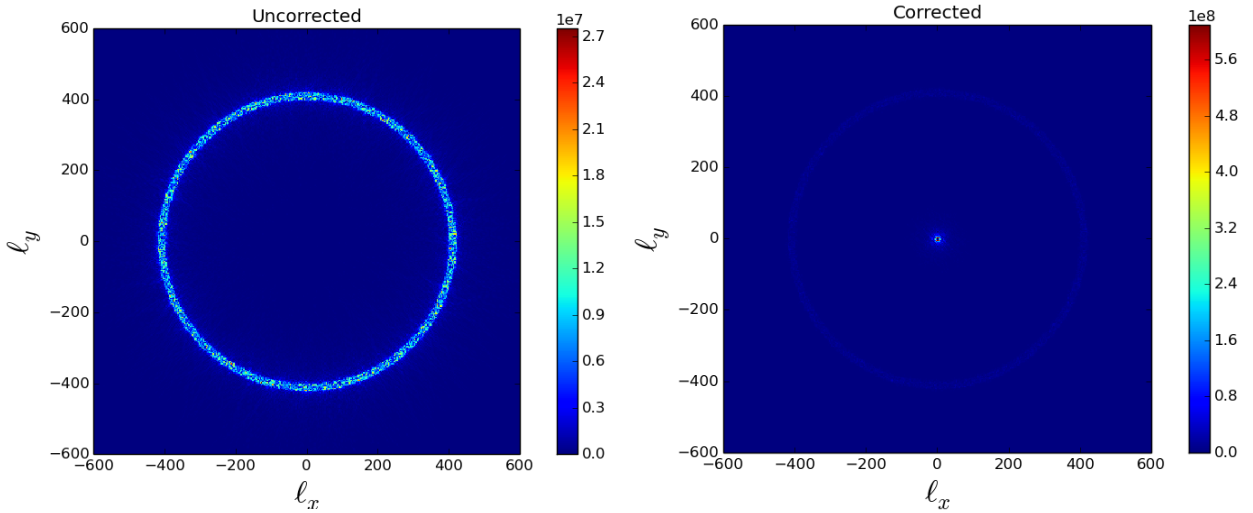

Figure 5.7: A two-dimensional power spectrum estimation output is shown after injecting Gaussian pure B-mode power into a multipole moment ring $400 < \ell < 420$. Left panel: without the application of the counter terms in Eq.(5.3). Right panel: with the application of the counter terms in Eq.(5.3). Courtesy of D. Boettger.

magnitude of power measured in the multipolar ring is effectively unchanged; the counter terms just add extra power into the center at low multipole moments, implying that the total power is not correctly restored at the end of this process. Simulations injecting normalized power at $\ell = 410$ as before, but with varying mask size and taper are shown in Fig. 5.8. Also, the power in the $\ell = 410$ bin and few adjacent bins is plotted in Fig. 5.9 to check if it sums to one, independent of the kernel size. This demonstrates that the counter terms are producing the low multipole moment power and not mixing it from somewhere else in multipole moment space.

The final conclusion posed by Boettger is that, although using pure B-modes reduces the $E \to B$ leakage produced by the presence of the apodization window functions, it induces a new source for $B \to B$ mixing that should be corrected. Pure B-modes would be not orthogonal and not normalized. Independent computations carried by Boettger and me to obtain Eq.(5.3) from [19] under the flat sky approximation using the basis identification $Y_{\ell m} \to e^{i\ell m}$, leads to Eq.(5.3) multiplied by a ℓ^2 factor. A normalization $1/\ell^2$ to obtain Eq.(3.14) in the case of full sky ($W(\vec{x}) = 1$ and so no counter terms) seems to be applied, but this should not be the case for the partial sky coverage. The idea to redefine this normalization is proposed.

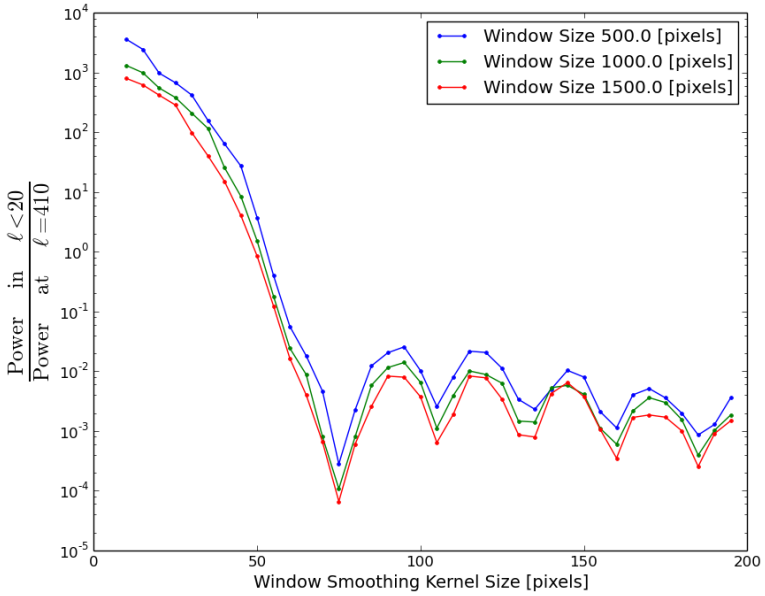

Figure 5.8: The resulting two-dimensional spectra for simulations injecting normalized power at $\ell = 410$ is collapsed into the normalized one-dimensional spectra, and the ratio of power at low multipole moment (below $\ell = 20$) to the power in the $\ell = 410$ bin is shown. Since power is only injected into the simulations at $400 < \ell < 420$, this ratio should be as low as possible. The different curves are using circular window functions convolved with kernels labeled by their sizes. Each point on the plot represents the average of 20 realizations. Courtesy of D. Boettger.

5.2.2 Takakura's Study

On a parallel study conducted by Satoru Takakura [108] and based on [19, 112, 115], he considered the definition of the *mixed estimator* (in the sense that is not a pure estimator):

$$[\hat{E} \pm i\hat{B}]^{mixed}(\vec{\ell}) = -\int \frac{d^2\vec{x}}{2\pi}[Q \pm iU](\vec{x})W(\vec{x})\bar{\partial}^{\mp 2}\left[e^{-i\vec{\ell}\cdot\vec{x}}\right] \tag{5.9}$$

And the *pure estimator*:

$$\begin{aligned}[\hat{E} \pm i\hat{B}]^{pure}(\vec{\ell}) &= \int \frac{d^2\vec{x}}{2\pi}[Q \pm iU](\vec{x})\bar{\partial}^{\mp 2}w(\vec{x}) \\ &= -\int \frac{d^2\vec{x}}{2\pi}[Q \pm iU](\vec{x})\bar{\partial}^{\mp 2}\left[W(\vec{x})e^{-i\vec{\ell}\cdot\vec{x}}\right]\end{aligned} \tag{5.10}$$

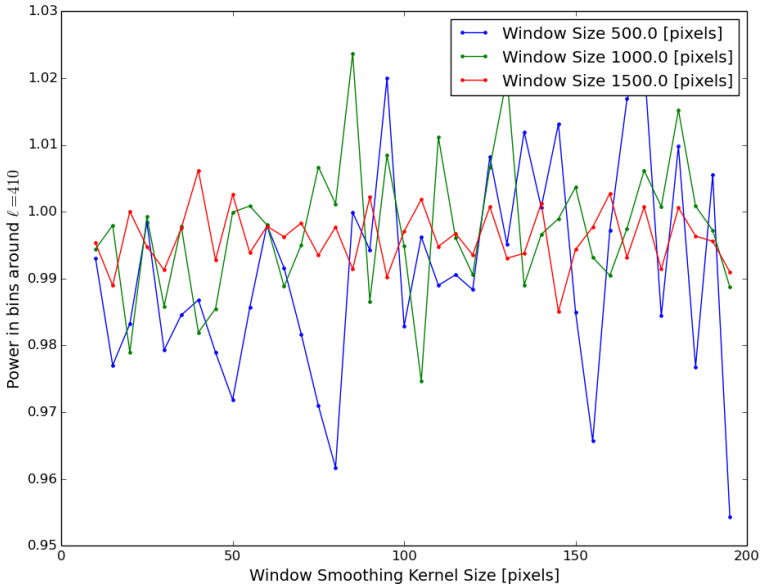

Figure 5.9: The resulting power spectrum estimation in the $\ell = 410$ bin and few adjacent bins for simulations injecting normalized power at $\ell = 410$ is shown for the same configuration illustrated in Fig. 5.8. Courtesy of D. Boettger.

Where we have defined a differential operator applied on a function $f(\mathbf{x})$ as:

$$\bar{\partial}^{\mp 1}\left[f(\mathbf{x})\right] = \int \frac{d^2\vec{\ell}}{2\pi} f(\vec{\ell}) e^{\mp i\phi_{\vec{\ell}}} e^{i\vec{\ell}\vec{x}} \tag{5.11}$$

Where the function $f(\mathbf{x})$ can be expressed as:

$$f(\vec{x}) = \int \frac{d^2\vec{\ell}}{2\pi} f(\vec{\ell}) e^{i\vec{\ell}\vec{x}} \tag{5.12}$$

Takakura posed that, under the flat sky approximation, the operator $\bar{\partial}$ takes the following form:

$$\begin{aligned} \bar{\partial}^{\mp 1}\left[e^{i\vec{\ell}\cdot\vec{x}}\right] &= \frac{\partial_x \mp i\partial_y}{i\ell}\left[e^{i\vec{\ell}\cdot\vec{x}}\right] \\ &= \frac{\ell_x \mp i\ell_y}{\ell} e^{i\vec{\ell}\cdot\vec{x}} \\ &= e^{\mp i\phi_{\vec{\ell}}} e^{i\vec{\ell}\vec{x}} \end{aligned} \tag{5.13}$$

If we naively expand the operator $\bar{\partial}$ following the same rule as in the first line of Eq.(5.13) but considering the function $W(\vec{x})e^{-i\vec{\ell}\cdot\vec{x}}$ instead of $e^{i\vec{\ell}\cdot\vec{x}}$ in Eq.(5.10), it becomes,

$$\begin{aligned} [\hat{E} \pm i\hat{B}]^{pure}(\vec{\ell}) \approx -\int \frac{d^2\vec{x}}{2\pi} [Q \pm iU](\vec{x}) e^{-i\vec{\ell}\cdot\vec{x}} \\ \left[e^{\mp 2i\phi_{\vec{\ell}}} W(\vec{x}) + \frac{2i}{\ell} e^{\mp i\phi_\ell} \left[\partial_x \mp i\partial_y\right] W(\vec{x}) - \frac{1}{\ell^2} e^{\mp i\phi_\ell} \left[\partial_x \mp i\partial_y\right]^2 W(\vec{x}) \right] \end{aligned} \tag{5.14}$$

The first term in Eq.(5.14) is the usual expression that we obtain from Eq.(5.9), that we

denote as the *mixed term* and from where the first term in Eq.(5.3) comes, and the second and third term in Eq.(5.14) correspond to the first and second counter terms in Eq.(5.3), and therefore this derivation corresponds to the estimator implemented in our pipeline, Eq.(5.3). Nevertheless, Takakura claimed that there is a second approximation apart from the flat sky assumption in Eq.(5.14) and hence Eq.(5.14) is already an approximation of the expression that we would obtain only using the flat sky formalism. This follows from considering Eqs.(5.12) and (5.13) in the operator evaluated in Eq.(5.3),

$$\begin{aligned}\bar{\partial}^{\mp 1}\left[W(\vec{x})e^{-i\vec{\ell}\cdot\vec{x}}\right] &= \bar{\partial}^{\mp 1}\left[\int \frac{d^2\vec{\ell}'}{2\pi}W(\vec{\ell}')e^{i(\vec{\ell}'-\vec{\ell})\vec{x}}\right] \\ &= \int \frac{d^2\vec{\ell}'}{2\pi}W(\vec{\ell}')\frac{\partial_x \mp i\partial_y}{i|\vec{\ell}'-\vec{\ell}|}\left[e^{i\vec{\ell}\cdot\vec{x}}\right]\end{aligned} \tag{5.15}$$

If we assume that the apodization window function lacks of small scale structure, that would be the case, for example, of well enough smoothed window functions, then we can adopt the approximation $\ell \gg \ell'$:

$$\begin{aligned}\bar{\partial}^{\mp 1}\left[W(\vec{x})e^{-i\vec{\ell}\cdot\vec{x}}\right] &= \int \frac{d^2\vec{\ell}'}{2\pi}W(\vec{\ell}')\frac{\partial_x \mp i\partial_y}{i\ell}\left[e^{i\vec{\ell}\cdot\vec{x}}\right] \\ &= \frac{\partial_x \mp i\partial_y}{i\ell}\left[W(\vec{x})e^{-i\vec{\ell}\cdot\vec{x}}\right]\end{aligned} \tag{5.16}$$

And then we have shown that the expression used in Eq.(5.14) is another approximation under the flat sky assumption. Nevertheless, it is important to note that Eq.(5.13) is not an approximation, as for such case, we can evaluate $W(\vec{x}) = 1$, meaning $W(\vec{\ell}) = \delta(\ell)$ in Eq.(5.15) and the first line of Eq.(5.13) is obtained consistently without any further use of approximations. A precise expansion of $\bar{\partial}^{\mp 2}\left[W(\vec{x})e^{-i\vec{\ell}\cdot\vec{x}}\right]$ in Eq.(5.10) can be obtained is we use (5.11) instead:

$$\begin{aligned}\bar{\partial}^{\mp 2}\left[W(\vec{x})e^{-i\vec{\ell}\cdot\vec{x}}\right] &= \int \frac{d^2\vec{\ell}'}{2\pi}W(\vec{\ell}')e^{\mp 2i\phi_{\vec{\ell}'-\vec{\ell}}}e^{i(\vec{\ell}'-\vec{\ell})\vec{x}} \\ &= e^{\mp 2i\phi_{\vec{\ell}}}e^{-i\vec{\ell}\vec{x}}\int \frac{d^2\vec{\ell}'}{2\pi}W(\vec{\ell}')e^{\mp 2i(\phi_{\vec{\ell}'-\vec{\ell}}-\phi_{-\vec{\ell}})}e^{i\vec{\ell}'\vec{x}}\end{aligned} \tag{5.17}$$

Where we can expand

$$\begin{aligned}\phi_{\vec{\ell}'-\vec{\ell}} - \phi_{-\vec{\ell}} &= \arctan\left[\frac{\ell'\sin\Delta\phi}{\ell-\ell'\cos\Delta\phi}\right] \\ &= \sum_{n=0}^{\infty}\frac{1}{n}\left(\frac{\ell'}{\ell}\right)^n\sin(n\Delta\phi)\end{aligned} \tag{5.18}$$

Where we have defined $\Delta\phi \equiv \phi_{-\vec{\ell}} - \phi_{-\vec{\ell}'}$. Hence, terms with $n > 2$ are needed to improve the accuracy of Eq.(5.14). Takakura concluded that the strange behavior observed in Fig. 5.7 could be caused in the cases when $\ell \sim \ell'$ allowed by the mode contributions from the apodization window function.

5.3 Possible solutions

Considering the studies described in Section 5.2, the collaboration considered the evaluation of the following mitigations for the problems found [116]:

(A) Compute $\bar{\partial}^{\mp 2}\left[W(\vec{x})e^{-i\vec{\ell}\cdot\vec{x}}\right]$ directly.

(B) Raise order of the Taylor expansion in Eq.(5.18).

(C) Smooth the apodization window function to only allow contributions from ℓ' small in Eq.(5.15).

(D) Mask lowest multipole moment bin properly.

(E) Change the $1/\ell^2$ normalization used in Eq.(5.10) as suggested in Section 5.2.1.

An even more general solution that one can propose to solve all this sort of problems is to consider a curved sky implementation of the whole pipeline and abandon the flat-sky framework. Nevertheless, at this stage of development of the pipeline, and considering the extension of the flat-sky consideration through all the stages of the pipeline, including the ones mentioned in Chapter 4, it is not convenient at this point to focus our efforts in that direction without a considerably delay in the analysis timeline and a substantial deviation of human resources from other parallel projects that are much promising in the long term by the development of state of the art instrumentation. Instead, a mitigation of such effects is preferred for a timely accomplishment of this project and build on these results and experience for the most exciting long-term projects such as Simons Array or Simons Observatory.

I was assigned to study and possibly implement one of the options between (A) and (E), where (A) is a generalization of the possible solution (B). Mitigation (C) was later implemented by the member of the collaboration Neil Goeckner-Wald [18], and regarding (D) the code masks all the terms with $\ell, \ell' < 10$ in Eq.(5.1). Here I give a description of the exploratory studies evaluating the behavior of both (A) and (E) proposed solutions that I performed.

5.3.1 Direct computation of $\bar{\partial}^{\mp 2}\left[W(\vec{x})e^{-i\vec{\ell}\cdot\vec{x}}\right]$

Considering the pure B-mode presented in Section 5.2.2, from Eq.(5.10) the pure B-mode can be expressed as,

$$\begin{aligned}\hat{B}^{pure}(\vec{\ell}) &= \int \frac{d^2\vec{x}}{2\pi}\left[Q(\vec{x})\frac{1}{2i}\left(\bar{\partial}^{+2}-\bar{\partial}^{-2}\right) - U(\vec{x})\frac{1}{2}\left(\bar{\partial}^{+2}+\bar{\partial}^{-2}\right)\right]\left[W(\vec{x})e^{-i\vec{\ell}\cdot\vec{x}}\right] \\ &= \int \frac{d^2\vec{x}}{2\pi}\left[Q(\vec{x})Q_B^P(\vec{x},\vec{\ell}) + U(\vec{x})U_B^P(\vec{x},\vec{\ell})\right]\end{aligned} \tag{5.19}$$

Where I have defined,

$$
\begin{aligned}
Q_B^P(\vec{x},\vec{\ell}) &\equiv \frac{1}{2i}\left(\bar{\partial}^{+2}-\bar{\partial}^{-2}\right)\left[W(\vec{x})e^{-i\vec{\ell}\cdot\vec{x}}\right] \\
U_B^P(\vec{x},\vec{\ell}) &\equiv -\frac{1}{2}\left(\bar{\partial}^{+2}+\bar{\partial}^{-2}\right)\left[W(\vec{x})e^{-i\vec{\ell}\cdot\vec{x}}\right]
\end{aligned}
\tag{5.20}
$$

So that the proposed pure multipole $\hat{B}^{pure}(\vec{\ell})$ is defined as the sum of the overlap integrals between the Stokes maps $Q(\vec{x})$ and $U(\vec{x})$ with the "Stokes pure B-modes" $Q_B^P(\vec{x},\vec{\ell})$ and $U_B^P(\vec{x},\vec{\ell})$, respectively. In the same way, we can define these "Stokes pure B-modes" $Q_B^I(\vec{x},\vec{\ell})$ and $U_B^I(\vec{x},\vec{\ell})$ corresponding to the existing pipeline implementation from Eq.(5.3) as

$$
\begin{aligned}
Q_B^I(\vec{x},\vec{\ell}) &\equiv 2\frac{e^{i\vec{\ell}\cdot\vec{x}}}{\ell^2}\left[\frac{\partial^2 W}{\partial x\partial y}(\vec{x}) - i\ell\sin(\phi_\ell)\frac{\partial W}{\partial x}(\vec{x}) - i\ell\cos(\phi_\ell)\frac{\partial W}{\partial y}(\vec{x}) - \frac{\ell^2}{2}\sin(2\phi_\ell)W(\vec{x})\right] \\
U_B^I(\vec{x},\vec{\ell}) &\equiv \frac{e^{i\vec{\ell}\cdot\vec{x}}}{\ell^2}\left[\frac{\partial^2 W}{\partial^2 y}(\vec{x}) - \frac{\partial^2 W}{\partial^2 x}(\vec{x}) + 2i\ell\cos(\phi_\ell)\frac{\partial W}{\partial x}(\vec{x}) - 2i\ell\sin(\phi_\ell)\frac{\partial W}{\partial y}(\vec{x}) + \ell^2\cos(2\phi_\ell)W(\vec{x})\right]
\end{aligned}
\tag{5.21}
$$

These definitions will be useful in the following analysis discussed in Section 5.3.2. The idea is to compare in real space the behavior of both estimators. To make this comparison more illustrative, let us consider the toy model example used, for example, in the tests performed in [19], of a cosine apodization window function

$$
W(\theta,\varphi) = \begin{cases} 1 & \text{for } \theta \leq r - r_* \\ \frac{1}{2} - \frac{1}{2}\cos\left(\pi\frac{r-\theta}{r_*}\right) & \text{for } r - r_* \leq \theta \leq r \\ 0 & \text{for } \theta \geq r \end{cases}
\tag{5.22}
$$

The parameter r is the window size, and tha parameter r_* is the apodization length. For this comparison, we will choose $r = 15°$ and $r_* = 5°$, also tested in [19], with other parameters akin to our final wide patch configuration. The apodization window function for this configuration is shown in Fig. 5.10.

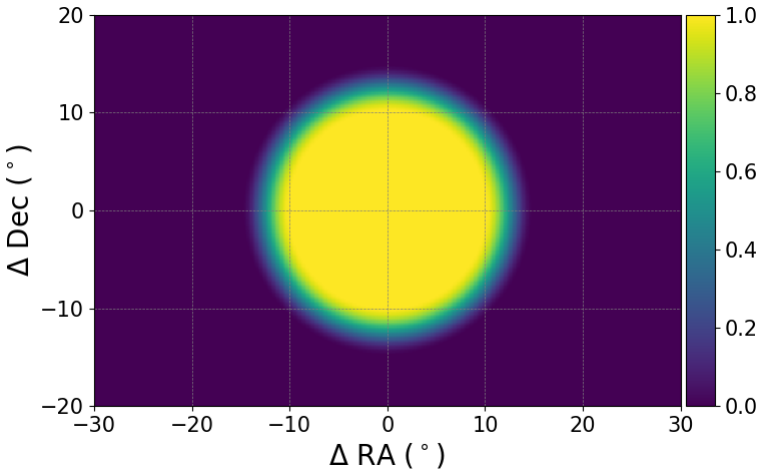

Figure 5.10: The cosine apodization window function defined in Eq.(5.22), for $r = 15°$ and $r_* = 5°$ centered in a $30° \times 30°$ sky patch, with a 8' pixel size.

We can evaluate these "Stokes pure B-modes" given this apodization window function. The resulting real space patterns are shown in Figs. 5.11 and 5.12, for $\ell = 30$ and $\ell = 60$, respectively. As we expect from a pure pseudo-C_ℓ estimator behavior, in both cases the counter terms are effectively smeared over an area close to the edges of the apodization window function [19]. Nevertheless, it is evident that the proposed modes $Q_B^P(\vec{x}, \vec{\ell})$ and $U_B^P(\vec{x}, \vec{\ell})$ spill an appreciable amount of power outside the boundary of the apodization window function, as compared with the current implemented modes $Q_B^I(\vec{x}, \vec{\ell})$ and $U_B^I(\vec{x}, \vec{\ell})$. The phenomenon is more patent at low multipole moments, comparing Figs. 5.11 and 5.12. This means that directions in the sky from the $Q(\vec{x})$ and $U(\vec{x})$ maps already masked out by the apodization window function, would be introduced in the analysis anyway in Eq.(5.19). The sky patch coverage is optimized to reduce the polarized foreground contamination to the measured B-modes [117]. The behavior of the proposed estimator can introduce contamination from polarized diffuse Galactic synchrotron and thermal dust emissions, or from unexpected, polarized point sources, located outside of our targeted sky patch, to our measurements. This deformation of the effective mask, in the sense of the final spatial contributions injected from the $Q(\vec{x})$ and $U(\vec{x})$ maps to our analysis, was considered unacceptable and so no further studies were considered in this direction. This also affects the consideration of the solution (B), as the analyzed solution in this section is a generalization of it. Furthermore, for the solution analyzed in this study, the number of Fourier transform operations involved per multipole moment makes this estimator computationally expensive for our current analysis pipeline.

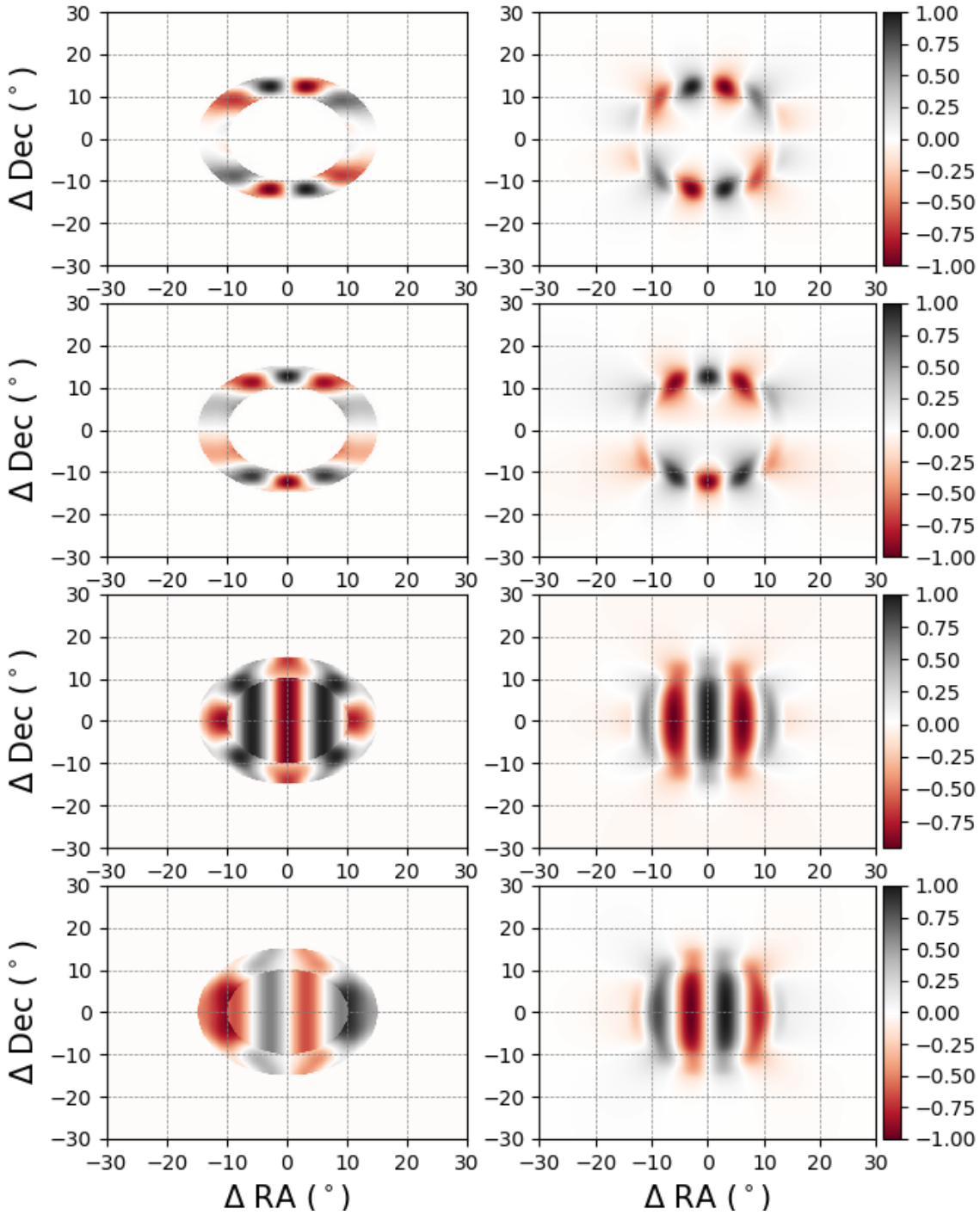

Figure 5.11: The $\ell = 30$ and $\phi_{\vec{\ell}} = 0$ peak-normalized "Stokes pure B-mode" $Q_B^X(\vec{x}, \vec{\ell})$ and $U_B^X(\vec{x}, \vec{\ell})$ patterns as defined in Eqs.(5.20) and (5.21), for $X \in \{P, I\}$ respectively, given the cosine apodization window function shown in Fig. 5.10. Left panels are for $X = I$ and right panels are for $X = P$. From top to bottom panels, the real component of $Q_B^X(\vec{x}, \vec{\ell})$, the imaginary component of $Q_B^X(\vec{x}, \vec{\ell})$, the real component of $U_B^X(\vec{x}, \vec{\ell})$ and the imaginary component of $U_B^X(\vec{x}, \vec{\ell})$.

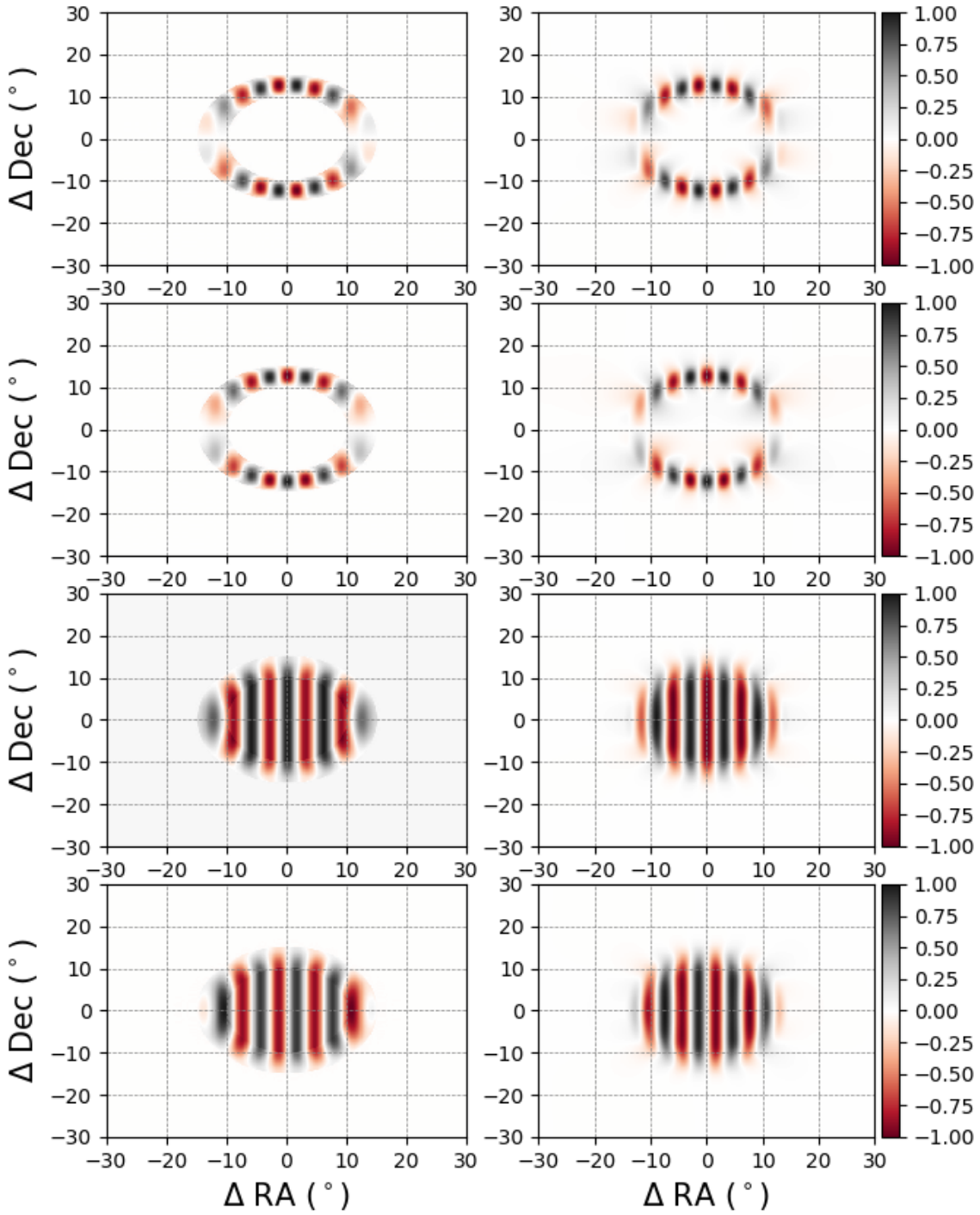

Figure 5.12: The $\ell = 60$ and $\phi_{\vec{\ell}} = 0$ peak-normalized "Stokes pure B-mode" $Q_B^X(\vec{x}, \vec{\ell})$ and $U_B^X(\vec{x}, \vec{\ell})$ patterns as defined in Eqs.(5.20) and (5.21), for $X \in \{P, I\}$ respectively, given the cosine apodization window function shown in Fig. 5.10. Left panels are for $X = I$ and right panels are for $X = P$. From top to bottom panels, the real component of $Q_B^X(\vec{x}, \vec{\ell})$, the imaginary component of $Q_B^X(\vec{x}, \vec{\ell})$, the real component of $U_B^X(\vec{x}, \vec{\ell})$ and the imaginary component of $U_B^X(\vec{x}, \vec{\ell})$.

5.3.2 Change of Normalization

There are two independent problems that conspire to make the situation difficult to be solved using a single method. The partial-sky coverage, in one side, induces an $E \to B$ leakage and also a $B \to B$ mode mixing at low multipole moments induced by the loss of orthogonality of the B-modes that motivates the introduction of the pure-B power spectrum estimator. On the other hand, the use of this estimator under the flat sky approximation induces an excess of BB power in the reconstructed power spectrum. The truncation of the low multipole moments in Eq.(5.1), as finally implemented for $\ell < 10$, sounds a very tempting solution to be extended to higher multipole moments to recover, for example, the $50 < \ell < 100$ bin. Actually, the low $\ell < 10$ truncation already bias the very low ℓ power spectrum, as the loss of orthogonal modes induced by partial sky coverage also spreads to neighboring multipole moments the information contained in the low multipole moments, and the direct masking of a portion of the low multipole moment range will also produce a loss of information on the higher modes, including the ones in the $50 < \ell < 100$ bin if this truncation cutoff is naively raised, producing another source of biasing. In the other way, if we just let the things as they are, we will have the spurious excess of BB power already mentioned. In this section, an intermediate solution is proposed.

The choice of a set of pure modes $w = \ell^{-2} W e^{-i\vec{\ell}\cdot\vec{x}}$ in Eq.(5.10) is suggested to be faster but a suboptimal solution for the problem of the $E \to B$ leakage [112]. Instead, motivated by the conclusions of Section 5.2.1, and as already stated in item (E), we define the "unnormalized Stokes pure B-modes", using Eq.(5.21) as:

$$\begin{aligned} Q_B(\vec{x},\vec{\ell}) \equiv \ell^2 Q_B^I(\vec{x},\vec{\ell}) &= 2e^{i\vec{\ell}\cdot\vec{x}}\left[\frac{\partial^2 W}{\partial x \partial y} - i\ell\sin(\phi_\ell)\frac{\partial W}{\partial x} - i\ell\cos(\phi_\ell)\frac{\partial W}{\partial y} - \frac{\ell^2}{2}\sin(2\phi_\ell)W\right](\vec{x}) \\ U_B(\vec{x},\vec{\ell}) \equiv \ell^2 U_B^I(\vec{x},\vec{\ell}) &= e^{i\vec{\ell}\cdot\vec{x}}\left[\frac{\partial^2 W}{\partial^2 y} - \frac{\partial^2 W}{\partial^2 x} + 2i\ell\cos(\phi_\ell)\frac{\partial W}{\partial x} - 2i\ell\sin(\phi_\ell)\frac{\partial W}{\partial y} + \ell^2\cos(2\phi_\ell)W\right](\vec{x}) \end{aligned} \tag{5.23}$$

Then, using this modes we redefined Eq.(5.19) for "unnormalized pure B-modes",

$$\hat{B}^{up}(\vec{\ell}) \equiv \int \frac{d^2\vec{x}}{2\pi}\left[Q(\vec{x})Q_B(\vec{x},\vec{\ell}) + U(\vec{x})U_B(\vec{x},\vec{\ell})\right] \tag{5.24}$$

We can evaluate this expression injecting an unnormalized pure $\vec{\ell}'$ B-mode,

$$\hat{B}^{up}_{\vec{\ell}'}(\vec{\ell}) \equiv \int \frac{d^2\vec{x}}{2\pi}\left[Q_B^*(\vec{x},\vec{\ell}')Q_B(\vec{x},\vec{\ell}) + U_B^*(\vec{x},\vec{\ell}')U_B(\vec{x},\vec{\ell})\right] \tag{5.25}$$

This is analogous to the case for some subset Ω of the sky for polarization fields lying in it that defines a normed vector space with the inner product,

$$\int_\Omega (QQ' + UU')d\Omega \tag{5.26}$$

That is presented on [115], for the polarization fields $P(\hat{\mathbf{n}}) = (Q + iU)(\hat{\mathbf{n}})$ and $P'(\hat{\mathbf{n}}) =$

$(Q' + iU')(\hat{\mathbf{n}})$, Eq.(3.7). And it is assumed that these two fields are orthogonal if their inner product is zero. In such case, Q, Q', U and U' correspond to the usual Stokes parameters that are real by definition. In this case, we are dealing with Stokes modes and so we take the complex conjugate of those parameters. This allow us to define a new normalization,

$$\mathcal{N}(\vec{\ell}) = \mathcal{N}(\ell, \phi_{\vec{\ell}}) \equiv \left[\sum_{\vec{\ell}'} \hat{B}^{up}_{\vec{\ell}'}(\vec{\ell}) \hat{B}^{up^*}_{\vec{\ell}'}(\vec{\ell}) \right]^{-\frac{1}{4}} \tag{5.27}$$

This expression can be evaluated numerically. Nevertheless, it is computationally expensive considering that the pipeline should be run for a large number of simulations. Instead, an analytic expression can be obtained,

$$\mathcal{N}(\vec{\ell}) = \left[\sum_{\vec{\ell}'} A(\vec{\ell}, \vec{\ell}') + B(\vec{\ell}, \vec{\ell}') - B(\vec{\ell}', \vec{\ell}) + C(\vec{\ell}) + C(\vec{\ell}') + D(\vec{\ell}, \vec{\ell}') + E(\vec{\ell}) - E(\vec{\ell}') + F \right]^{-\frac{1}{4}} \tag{5.28}$$

Where, for simplicity, I have omitted the dependence on the apodization window function $W(\vec{x})$, its derivatives and $\Delta\vec{\ell} = \vec{\ell} - \vec{\ell}'$ that are present in the following definitions

$$\begin{aligned}
A(\vec{\ell}, \vec{\ell}') &= \ell^2 \ell'^2 \cos\left[2\left(\phi_{\vec{\ell}} - \phi_{\vec{\ell}'}\right)\right] \mathcal{F}\left[W^2\right](\Delta\vec{\ell}) \\
B(\vec{\ell}, \vec{\ell}') &= -2i\ell^2\ell' \left\{ \cos\left(2\phi_{\vec{\ell}} - \phi_{\vec{\ell}'}\right) \mathcal{F}\left[W\frac{\partial W}{\partial x}\right](\Delta\vec{\ell}) + \sin\left(2\phi_{\vec{\ell}} - \phi_{\vec{\ell}'}\right) \mathcal{F}\left[W\frac{\partial W}{\partial y}\right](\Delta\vec{\ell}) \right\} \\
C(\vec{\ell}) &= -\ell^2 \left\{ \cos\left(2\phi_{\vec{\ell}}\right) \mathcal{F}\left[W\left(\frac{\partial^2 W}{\partial^2 x} - \frac{\partial^2 W}{\partial^2 y}\right)\right]\left(\Delta\vec{\ell}\right) + 2\sin\left(2\phi_{\vec{\ell}}\right) \mathcal{F}\left[W\frac{\partial^2 W}{\partial x \partial y}\right](\Delta\vec{\ell}) \right\} \\
D(\vec{\ell}, \vec{\ell}') &= 4\ell\ell' \cos\left(\phi_{\vec{\ell}} - \phi_{\vec{\ell}'}\right) \mathcal{F}\left[\left(\frac{\partial W}{\partial x}\right)^2 + \left(\frac{\partial W}{\partial y}\right)^2\right](\Delta\vec{\ell}) \\
E(\vec{\ell}) &= -2i\ell \Bigg\{ \cos\left(\phi_{\vec{\ell}}\right) \mathcal{F}\left[\frac{\partial W}{\partial x}\left(\frac{\partial^2 W}{\partial^2 x} - \frac{\partial^2 W}{\partial^2 y}\right) + 2\frac{\partial W}{\partial y}\frac{\partial^2 W}{\partial x \partial y}\right](\Delta\vec{\ell}) \\
&\quad + \sin\left(\phi_{\vec{\ell}}\right) \mathcal{F}\left[2\frac{\partial W}{\partial x}\frac{\partial^2 W}{\partial x \partial y} - \frac{\partial W}{\partial y}\left(\frac{\partial^2 W}{\partial^2 x} - \frac{\partial^2 W}{\partial^2 y}\right)\right](\Delta\vec{\ell}) \Bigg\} \\
F &= \mathcal{F}\left[\left(\frac{\partial^2 W}{\partial^2 x} - \frac{\partial^2 W}{\partial^2 y}\right)^2 + 4\left(\frac{\partial^2 W}{\partial x \partial y}\right)^2\right](\Delta\vec{\ell})
\end{aligned} \tag{5.29}$$

For the full sky case, Eq.(5.27) for both the numerical and analytical computations reduces to the standard $1/\ell^2$, up to a numerical error. We are interested in a modification of the behavior of such normalization at low multipole moments, so that it does not blow up when the flat sky approximation breaks at $\ell \to 0$ creating spurious B-mode power that can couple to high multipole moments even after mode-coupling corrections. Let us start evaluating both implementations for the case presented in Section 5.3.1, the cosine apodization window function, and $phi_{\vec{\ell}} = 0$. These are shown in Fig. 5.13. We can appreciate that both expressions behave $\propto 1/\ell^2$ for $\ell \gtrsim 75$, up to an imperceptible positive offset due to the loss of power induced by the small scale features of the apodization window function, being the analytical expression closer than the numerical implementation to desired behavior at

high multipole moments. Despite several checks, the source of this discrepancy between both implementations has not been found in either the implementation of the numerical normalization nor the computation of the analytical normalization, but it is limited to a percent fractional error level in the worst case, being in some cases orders of magnitude below this, as shown in the bottom panel of Fig. 5.13. At low multipole moments, the normalization does not explode, as desired.

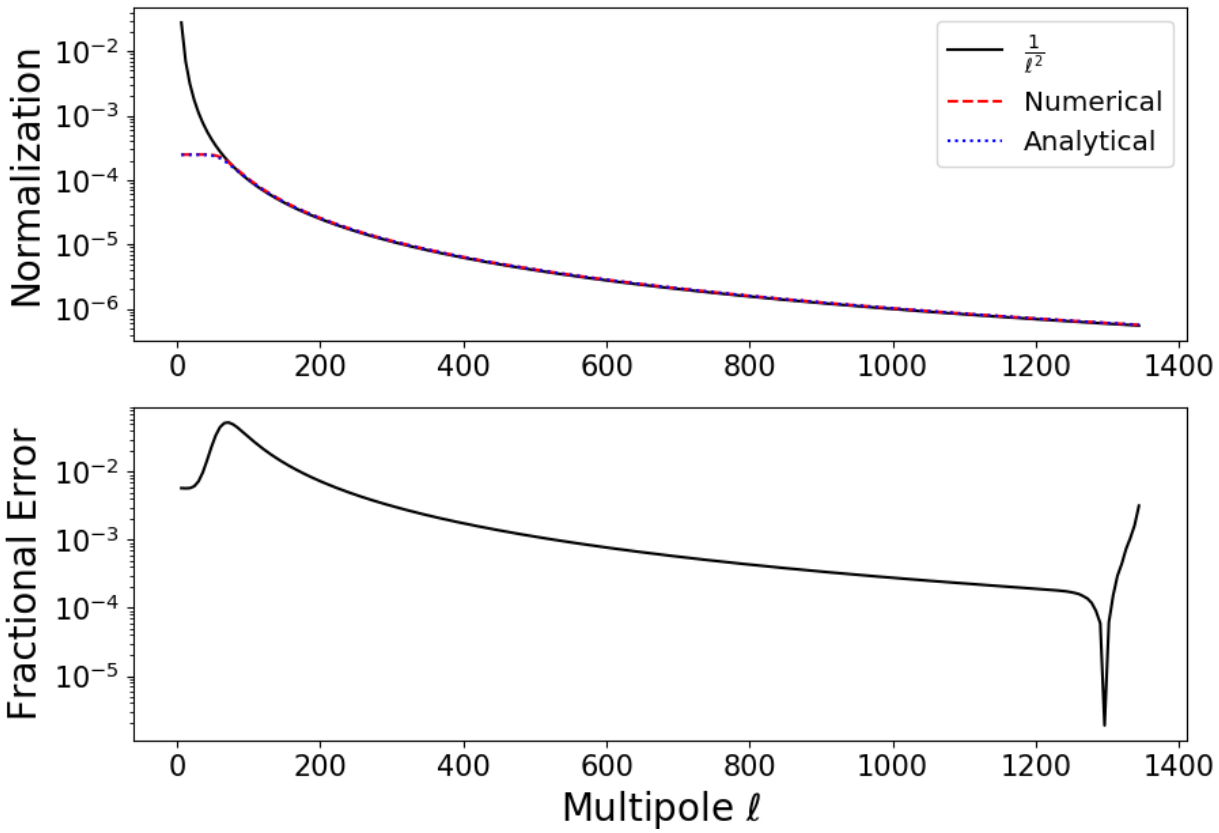

Figure 5.13: The normalization $\mathcal{N}(\ell, \phi_{\vec{\ell}} = 0°)$ for the apodization window function presented in Section 5.3.1. Top panel: The standard $1/\ell^2$, the numerical as defined in Eq.(5.27) and the analytical as defined in Eq.(5.28) normalizations are shown as a function of multipole moment. Bottom panel: The absolute value of the fractional error between the numerical and analytical normalizations for the same multipole moment range.

We can now do the same analysis considering a more realistic case, such as the final apodization window function used for the wide patch analysis, implemented by Goeckner-Wald [18], that is described and shown in Fig. 5.14 and will be adopted for the rest of the analysis considered in this thesis. We can evaluate again the normalizations for $\phi_{\vec{\ell}} = 0°$ in Fig. 5.15 and we arrive to the same conclusion as with Fig. 5.13, with the positive offset more evident. Nevertheless, we realize that there is also a multipole moment angle dependence $\phi_{\vec{\ell}}$, and so I show this dependence for two fixed ℓ corresponding to the multipole moment region of interest for possible modifications: $\ell = 50$ in Fig. 5.16 and $\ell = 100$ in Fig. 5.17. There are three important observations regarding these two cases. First, the shape of the normalization and fractional error for both cases seems to be similar. Second, in both cases the previous observation regarding the percent level upper bound of the fractional error between the two implementations of the normalization still applies. Extrapolating from these

two cases it is easy to convince ourselves that the highest fractional error in this multipole moment range is in the vicinity of $\phi_{\vec{\ell}} = 90°$. We plot the normalization for this case in 5.18 and we verified our previous conclusions without further corrections. Third, we also notice that the fractional change of both normalizations as a function of multipole moment angle $\phi_{\vec{\ell}}$ is within the percent level.

We are interested in reduce the number of operations for computationally efficiency, and given that the fractional error between the two implementations is already within this range, we decide to fix the multipole moment angle to $\phi_{\vec{\ell}} = 0$, that is in the range of lowest fractional discrepancies between the two implementations, as inferred from Figs. 5.16 and 5.17, that also can be seen as a trade-off decision between the normalization uncertainty in the definition and the fluctuations of them as a function of multipole moment angle. For the same reasons, the analytical implementation is adopted in the subsequent analysis. The impact of this multipole moment angle fixing within the context of the analytical implementation will be assessed in Section 6.2 and assumed for the rest of this chapter.

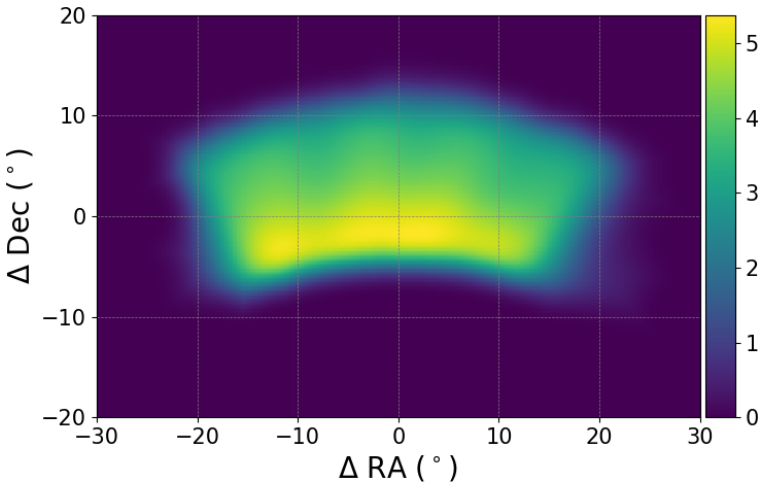

Figure 5.14: The final apodization window function used in the pseudo spectrum stage of the wide patch analysis with an 8'-pixel size. The smoothing employed with this mask is considerably more aggressive than the small patch analysis. To fulfill the pure-B mode estimator requirements regarding the vanishing of both the apodization window function and its derivatives on the sky patch edge [19], a 8° cosine square edge taper is applied, along with a 8° Hamming window to the map of pixel weights. Point sources are not masked in the power spectrum estimation to avert sharp features in the apodization window function or an important sky area reduction [18].

As in Section 5.2.1, another test that we can perform is inject Gaussian pure B-mode power into a multipole moment ring $400 < \ell < 420$. The two-dimensional pseudo spectrum outputs are shown in Fig. 5.19. There, we can see that the spurious B-mode power introduced in the low multipole moments for the standard pure estimator is removed with the use of the analytical normalization. Furthermore, we can check if the goal of the pure estimator, that is the mitigation of the $E \to B$ leakage induced by the gradient of the apodization window function, is still achieved with the introduction of this new normalization. A Gaussian E-mode power is injected into a multipole moment ring $400 < \ell < 420$. The two-dimensional

pseudo spectrum outputs are shown in Fig. 5.20. We confirm that the good behavior of the pure estimator is conserved when using the proposed normalization. Furthermore, a low multipole moment leakage still present in the standard pure estimator is again removed by the substitution of the standard normalization.

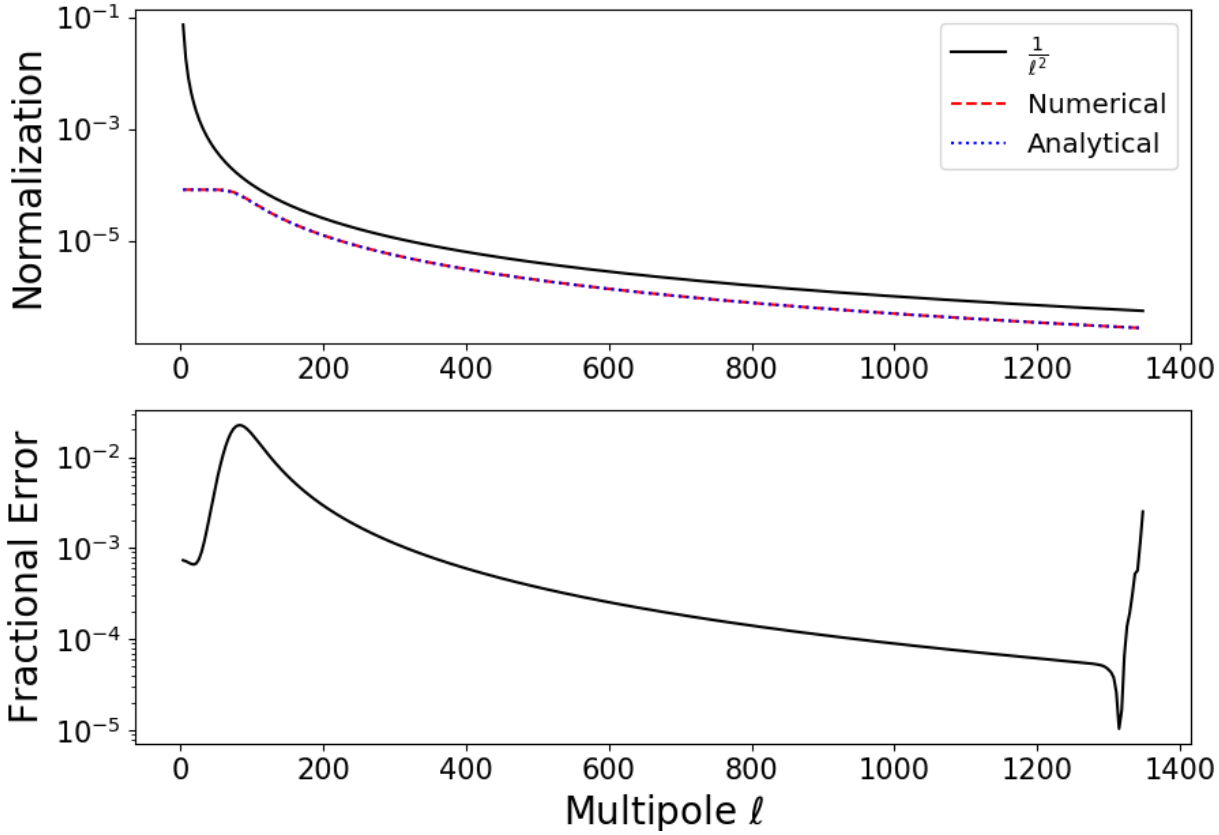

Figure 5.15: The normalization $\mathcal{N}(\ell, \phi_{\vec{\ell}} = 0°)$ for the apodization window function presented in Fig. 5.14. Top panel: The standard $1/\ell^2$, the numerical as defined in Eq.(5.27) and the analytical as defined in Eq.(5.28) normalizations are shown as a function of multipole moment. Bottom panel: The absolute value of the fractional error between the numerical and analytical normalizations for the same multipole moment range.

Nevertheless, this is a very specific choice of multipole moments to have a broad view of the performance of this normalization. For a more general view of the spurious B-mode contamination at low multipole moments and the $E \to B$ leakage, the mode mixing matrix $M_{\ell\ell'}$ is useful. We use the Monte Carlo (MC) implementation described in Section 5.2.1, where n_{MC} noise realizations are used to compute their pseudo spectrum using fine multipole moment bins to estimate the mode-coupling. For realistic performance evaluation, we use the final desired configuration of the pipeline, bins of width $\Delta\ell = 2$ and $n_{MC} = 10$.

The outputs for the $BBBB$ term, and the $EEBB$ component that represents the $E \to B$ leakage, are shown in Fig. 5.21. In the case of the mixed estimator, the $BBBB$ matrix is diagonal. A clearly non vanishing and diagonal $EEBB$ component is observed. In the case of the pure estimator, the $BBBB$ shows a large correlation of low multipole moments of the spectrum with all multipole moments of the pseudo-spectrum, but the $EEBB$ component

is substantially reduced. This "low ell foot" structure allows the mitigation of the E-to-B leakage [20], but the use of the implemented analytical normalization reduces the off-diagonal feature in the mode coupling matrix, improving at some level the numerical stability of the estimator [18]. There is a slight rise in the $EEBB$ contribution, but still far below the levels of the mixed estimator. Furthermore, the observed off-diagonal structure in the case of the $BBBB$ component for the standard pure estimator is also observed in the $EEBB$ term at some level and is consequently removed with the use of the proposed normalization, helping with the numerical stability of the estimator as well.

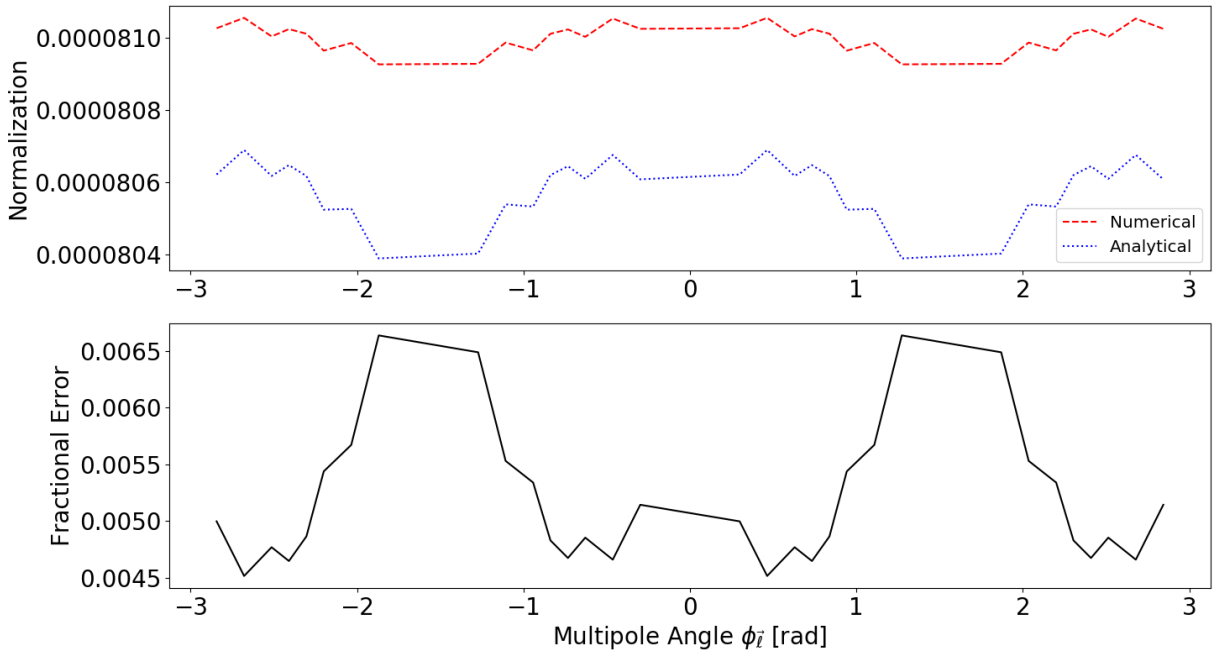

Figure 5.16: The normalization $\mathcal{N}(\ell = 50, \phi_{\vec{\ell}})$ for the apodization window function presented in Fig. 5.14. Top panel: The standard $1/\ell^2$, the numerical as defined in Eq.(5.27) and the analytical as defined in Eq.(5.28) normalizations are shown as a function of multipole moment angle. Bottom panel: The absolute value of the fractional error between the numerical and analytical normalizations for the same multipole moment angle range.

The outcomes of these exploratory tests are promising but need to be verified in the context of a more realistic application of these modifications, mimicking the treatment that real data would undergone to produce science results. End-to-end pipeline executions, from simulated observations of mock maps generated with an input cosmology to estimated spectra, are used in Chapter 6 to validate the performance of these pseudo-spectrum modifications.

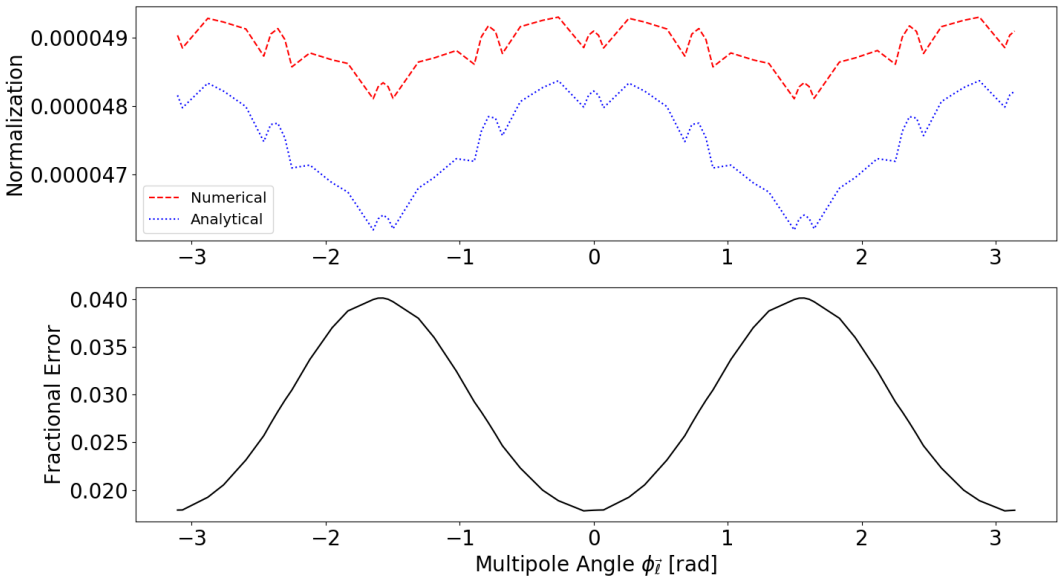

Figure 5.17: The normalization $\mathcal{N}(\ell = 100, \phi_{\vec{\ell}})$ for the apodization window function presented in Fig. 5.14. Top panel: The standard $1/\ell^2$, the numerical as defined in Eq.(5.27) and the analytical as defined in Eq.(5.28) normalizations are shown as a function of multipole moment angle. Bottom panel: The absolute value of the fractional error between the numerical and analytical normalizations for the same multipole moment angle range.

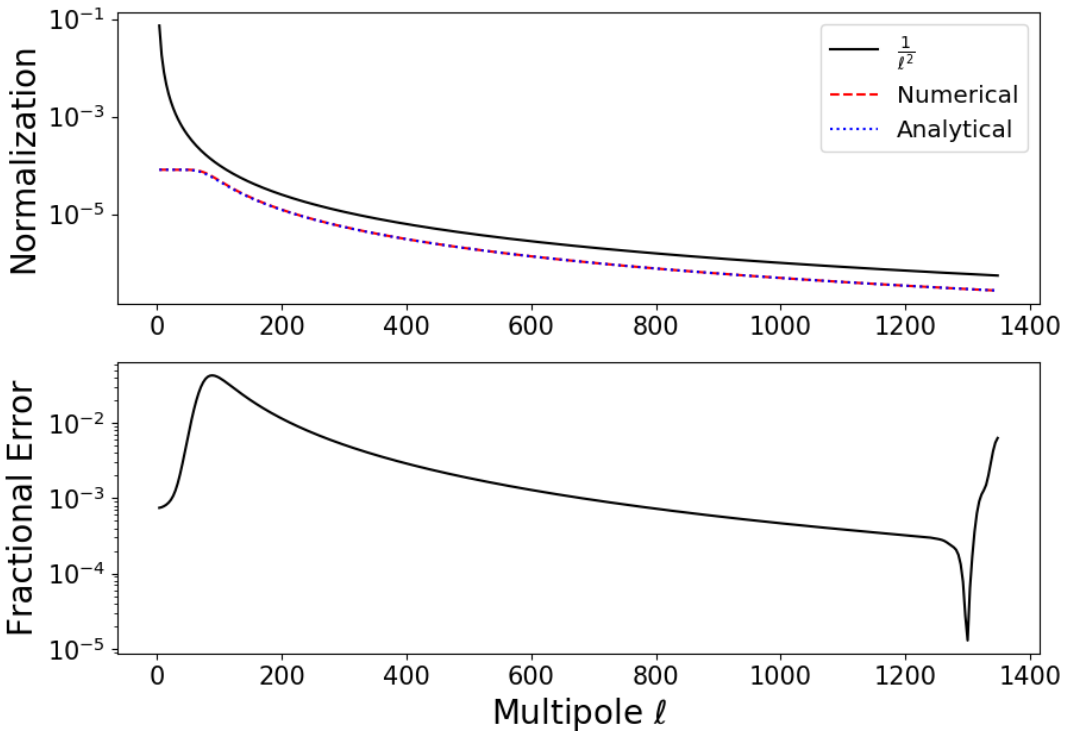

Figure 5.18: The normalization $\mathcal{N}(\ell, \phi_{\vec{\ell}} = 90°)$ for the apodization window function presented in Fig. 5.14. Top panel: The standard $1/\ell^2$, the numerical as defined in Eq.(5.27) and the analytical as defined in Eq.(5.28) normalizations are shown as a function of multipole moment. Bottom panel: The absolute value of the fractional error between the numerical and analytical normalizations for the same multipole moment range.

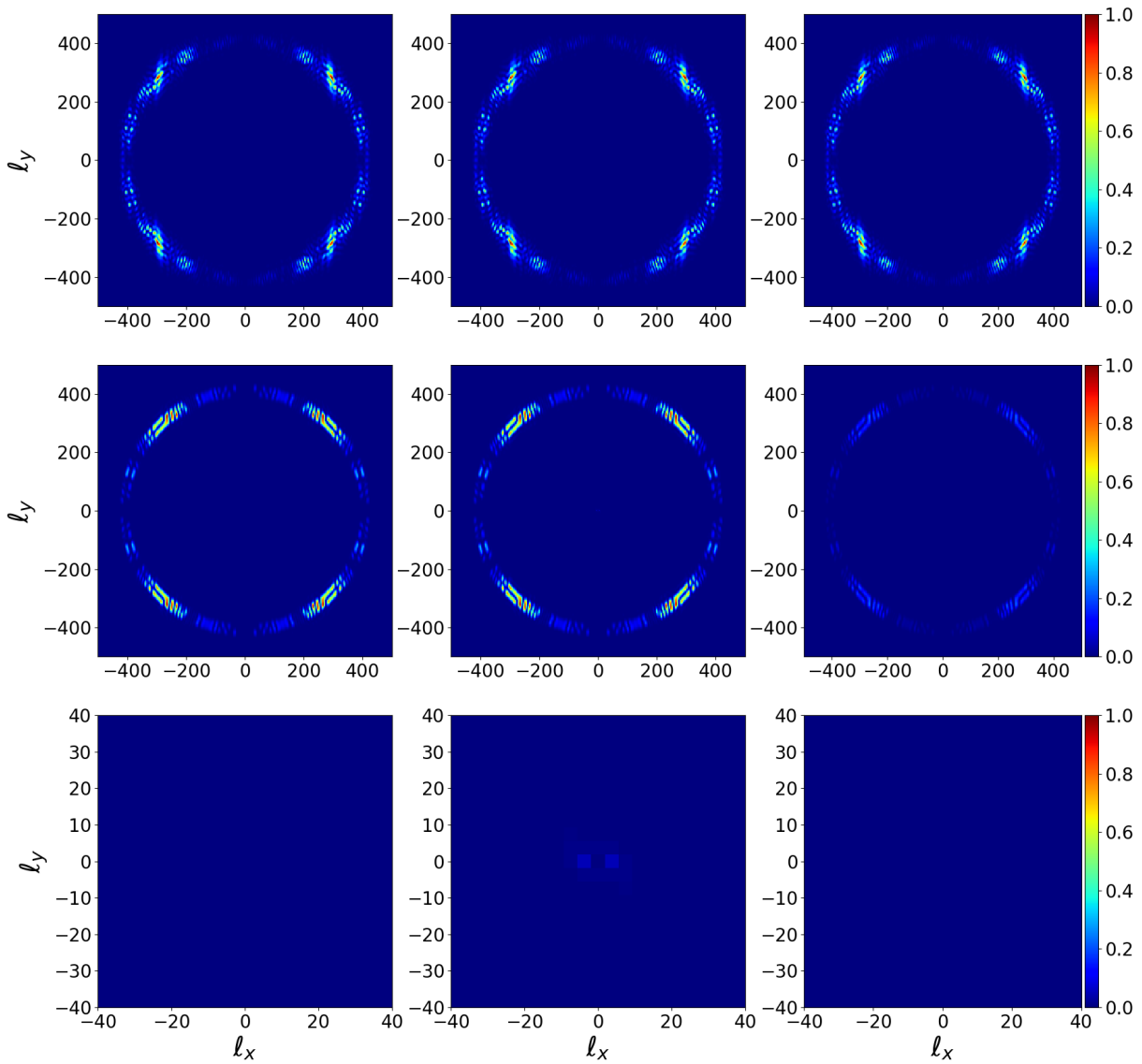

Figure 5.19: A two-dimensional pseudo spectrum output is shown after injecting Gaussian pure B-mode power into a multipole moment ring $400 < \ell < 420$. The upper panels are the E-modes. The second row are the B-modes and the bottom panels are the same as the second row but zoomed in the low multipole moment range. The left panels show the result with the use of mixed estimator with the standard $1/\ell^2$ normalization, the middle panels show the use of the pure estimator with the standard $1/\ell^2$ normalization and the right panels show the use of the pure estimator with the analytical normalization Eq.(5.28) for $\phi_{\vec{\ell}} = 0°$.

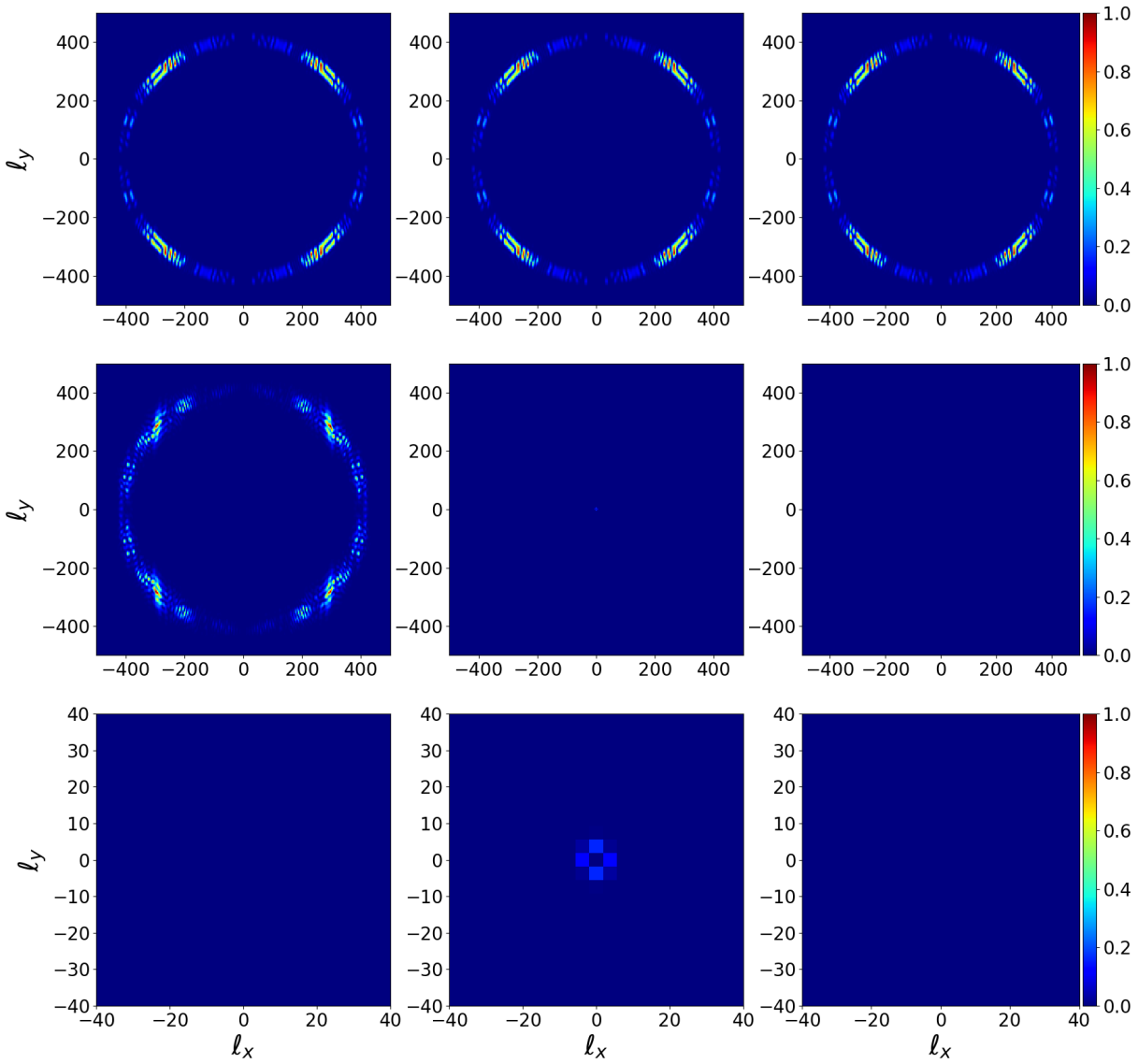

Figure 5.20: A two-dimensional pseudo spectrum output is shown after injecting Gaussian E-mode power into a multipole moment ring $400 < \ell < 420$. The upper panels are the E-modes. The second row are the B-modes and the bottom panels are the same as the second row but zoomed in the low multipole moment range. The left panels show the result with the use of mixed estimator with the standard $1/\ell^2$ normalization, the middle panels show the use of the pure estimator with the standard $1/\ell^2$ normalization and the right panels show the use of the pure estimator with the analytical normalization Eq.(5.28) for $\phi_{\vec{\ell}} = 0°$.

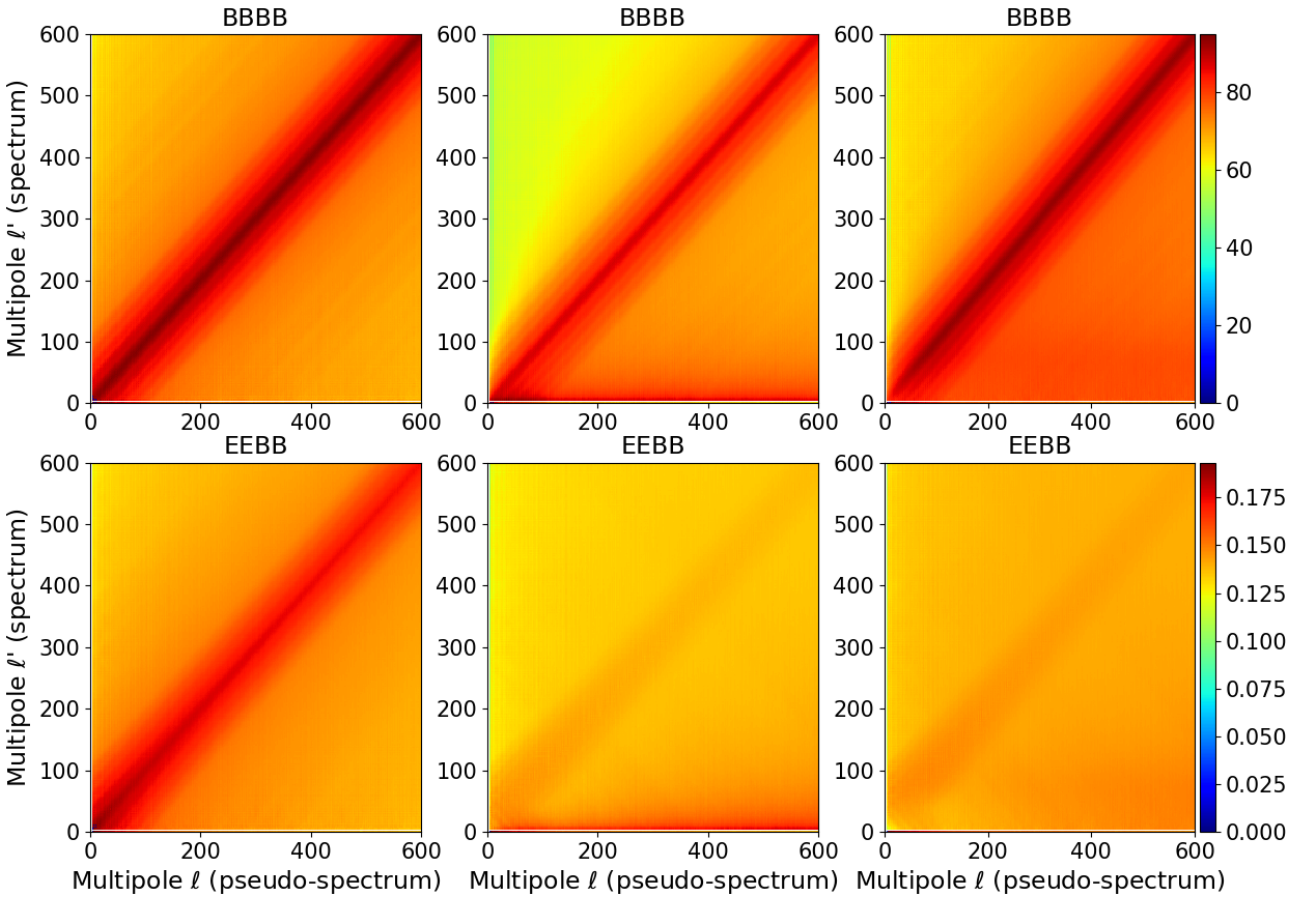

Figure 5.21: Mode-mode mixing matrices $\log_{10} M_{\ell\ell'}$ with multipole moment bins of size $\Delta\ell = 2$ for the wide patch window apodization function shown in Fig. 5.14 for the cases of the mixed estimator (left panels), the pure estimator with the standard $1/\ell^2$ normalization (middle panels), and the pure estimator with the analytical normalization (right panels). The first row shows the $BBBB$ term, and the second row shows the cross component $EEBB$ that represents the $E \to B$ leakage. In the case of the mixed estimator, the $BBBB$ matrix is diagonal along with the $EEBB$ component. In the case of the pure estimator, the BBBB case shows a large correlation of low multipole moments of the spectrum (horizontal ℓ') with all multipole moments of the pseudo-spectrum (vertical ℓ), but the $EEBB$ component is substantially reduced. This structure allows the minimization of the $E \to B$ leakage [20]. The introduction of the implemented analytical normalization removes most of the off-diagonal structure that can cause problems to the numerical stability of the estimator [18], at the price of a slightly increased $EEBB$ component, but still far below the levels of the mixed estimator.

Chapter 6

Evaluations of the Modifications to the B-Mode Pseudo-Spectrum

The purpose of this chapter is to assess the performance of the implemented modifications that I have introduced to the B-mode pseudo-spectrum related with the change of the normalization explained in Section 5.3.2 and the parameters chosen for its implementation using simulations fed to end-to-end runs of the analysis pipeline. In Section 6.2 I evaluate the impact of the use of the multipole angle choice in the proposed normalization with both the use of a multipole angle dependent normalization and the standard $1/\ell^2$ normalization. In Section 6.3 I explain the tests that I performed to prove the resilience of my proposed modifications to input spectrum variations. Finally, in Section 6.4 I describe the efforts performed by the collaboration in the introduction of these modifications to the main data analysis pipeline in the context of the null tests and final cross checks of the impact of this plugging, along with the final validation of the fiducial data analysis pipeline including these modifications. My prime efforts are focused on Sections 6.2 and 6.3, while Section 6.4 describe the efforts performed primarily by the member of the collaboration Neil Goeckner-Wald with minor inputs from my side.

Section 6.1 takes from [18] and Section 6.4 is chiefly based on [6].

6.1 Final Pipeline Configuration

In this section I describe aspects of the power spectrum estimator configuration used for both the end-to-end pipeline tests employed to evaluate the performance of the proposed modifications, as well as for the data analysis presented in [6], that has not been mentioned previously in this manuscript. The structure of the estimator greatly follows the one outlined in Section 5.1, with minor modifications implemented to mitigate numerical inaccuracies at large scales (low multipoles). I will highlight these modifications, along with the configuration choices not mentioned in Section 5.3.2, emphasizing the aspects relevant to the changes here evaluated. A deeper review of the final configuration used for the power spectrum estimator employed for science results can be found in [6, 18].

The observations are arranged into 38 stacks of roughly same weight and coverage of the sky. These stacks are generated from the sequence of ten days caused by the strategy of observation. During the post-processing steps several sequences of ten days are merged owing to an uneven sky coverage or poor weighting. To reduce the bias produced by noise, the computation of cross spectra between these stacks using Eq.(5.5) is performed. The pseudo spectrum is binned with bins of width $\Delta\ell = 2$. The window apodization function and the computation of the mode coupling matrix $M_{\ell\ell'}$ considered in this analysis display the same configuration described in Section 5.3.2. The filter transfer function is obtained using an iterative process,

$$F_\ell^n = F_\ell^{n-1} + \frac{\tilde{C}_\ell - \sum_{\ell'} M_{\ell\ell'} F_{\ell'}^{n-1} C_{\ell'} B_{\ell'}^2}{C_\ell B_\ell^2} \text{ and } F_\ell^0 = 1. \tag{6.1}$$

During this analysis, I pointed out the existence of negative values in the implemented filter transfer functions for BB and EE at low multipoles. This issue was later investigated by Goeckner-Wald who attributed these findings to fluctuations in the iterative procedure defined in Eq.(6.1) induced by the overfitting in the pseudo spectra of simulations. To avoid this issue, the iterative procedure is stopped at $n = 3$. This numerical instability is produced when the not well conditioned mode mixing matrix $M_{\ell\ell'}$ is inverted to solve F_ℓ from Eq.(5.1). An appreciable but not significant bias is introduced in the lowest multipole bin of the estimated power spectrum when this cutoff in the iteration process is adopted. As realized in Section 5.2.1, previous configuration of the pipeline had adopted a direct smoothing of the filter transfer function F_ℓ. Nevertheless, as we have detected in Section 5.2.1, a consequence of this is a more patent bias found in the low multipole bins where the filter transfer function is fast decreasing. Simulated sky maps of 1' pixels generated from EE-only and BB-only Planck 2018 best fit ΛCDM [3] input power spectra are used to compute the filter transfer function.

One difference with the previous configuration of the small patch analysis outlined in Section 5.1 is the use bins of width $\Delta\ell = 50$ instead of $\Delta\ell = 400$ for the estimation of the power spectra. Their statistical error is represented by the standard error of the Monte Carlo (MC) simulations.

With the introduction of the changes to the B-mode pseudospectrum normalization proposed in Section 5.3.2, Goeckner-Wald noticed that the code was considerably slower than without these changes, even with the fixing of the multipole angle $\phi_{\vec{\ell}} = 0°$ in Eq.(5.28). To achieve a reasonable computation time and considering that we are interested only in a modification of the estimator behavior at low multipoles, the new normalization for $\ell < 100$ is computed using my implementation and Goeckner-Wald rescaled it to merge the new calculation smoothly with the $1/\ell^2$ standard normalization for $\ell > 100$ using a simple splicing. This is done for every purpose of the pipeline runs, including the fiducial power spectrum pipeline for science results.

For the purposes of the tests here described, one year of simulated observations from

October 06, 2015 to October 06, 2016, are used, in contrast with the two years of data used for the fiducial power spectrum pipeline. The filter transfer function and mode mixing matrix are estimated from simulated 8 $TT + EE$ and 8 $TT + BB$ signal-only Planck 2018 ΛCDM input sky maps for each test. For the reconstructed spectra, 16 $TT + EE + BB$ signal-only simulations are used per test, using the same input cosmology as the filter transfer function and mode mixing matrix. Any other configuration or input needed for these tests can be found described in Chapters 4 and 5, or in [6,18], as these tests try to replicate the conditions of the fiducial power spectrum pipeline at a smaller computational scale due to computational cost.

6.2 Multipolar angle dependence

In this section I compare the behavior of the power spectrum estimator using the proposed normalization defined in Eq.5.28 as implemented in the data analysis pipeline and described in Section 6.1, i.e, with $\phi_{\vec{\ell}} = 0°$ and the standard normalization for $\ell > 100$, with the cases where the standard $1/\ell^2$ normalization is used for every multipole, and where more angles are evaluated in Eq.5.28 for the implemented normalization. More concretely, all the angles for $\ell < 110$ are evaluated and then the same stitching with the standard $1/\ell^2$ normalization is applied for $\ell > 110$. A full evaluation of the multipolar angle dependence for a larger multipolar region is not feasible computationally for the configuration outlined in Section 6.1, even for a one time execution.

The BB pseudo-spectrum output for the three cases is shown in Fig. 6.1. We realize that the spurious excess of power at low ℓ as compared with the BB input cosmology represented with the black dashed line in Fig. 6.4, emerges when the standard normalization is used. Furthermore, this is not present when both modified normalizations are used. These two modified normalizations act as an effective low ℓ pass filter for $\ell < 50$. Our lowest science multipolar spectrum bin is $50 < \ell < 100$, so this can be understood as a partial masking of multipoles lower than our target multipolar bands reducing the possibilities that those multipoles contaminate our results by mode-mode mixing, that is in fact what happens when spurious power is present in those multipoles, as found when the standard normalization is used. For $\ell > 110$, the three cases are coincident, as expected by construction. Finally, both modified normalizations are mostly compatible for all the multipole range, confirming our early conjectures from Section 5.3.2.

Regarding the mode-coupling matrices corresponding to this test, these are shown in Fig. 6.2 for $BBBB$ and $EEBB$, in the same way as in Fig. 5.21. The difference of its structure when the standard or the implemented normalization without multipolar angle dependence are used is consistent with our previous discussion in Section 5.3.2 regarding Fig. 5.21. Additionally, now we can confirm that the multipolar angle-dependent case exhibits the same behavior as the fixed multipolar angle case, as expected.

Considering the filter transfer functions corresponding to this test, these are shown in

Fig. 6.3 for $BB \to BB$ and $EE \to BB$. For $BB \to BB$ case, we can see that both modified versions reduce somewhat the rapid fall of the filter transfer function at low ℓ when the standard normalization is used. Also, from the $EE \to BB$ case we noticed a clear reduction of the $E \to B$ leakage present in the pseudo-spectra at low ℓ, that helps in the lessening of the leakage propagation and its variance through further stages of the pipeline when both modified estimators are used. Finally, the use of both modified normalizations leads to a similar behavior, as intended.

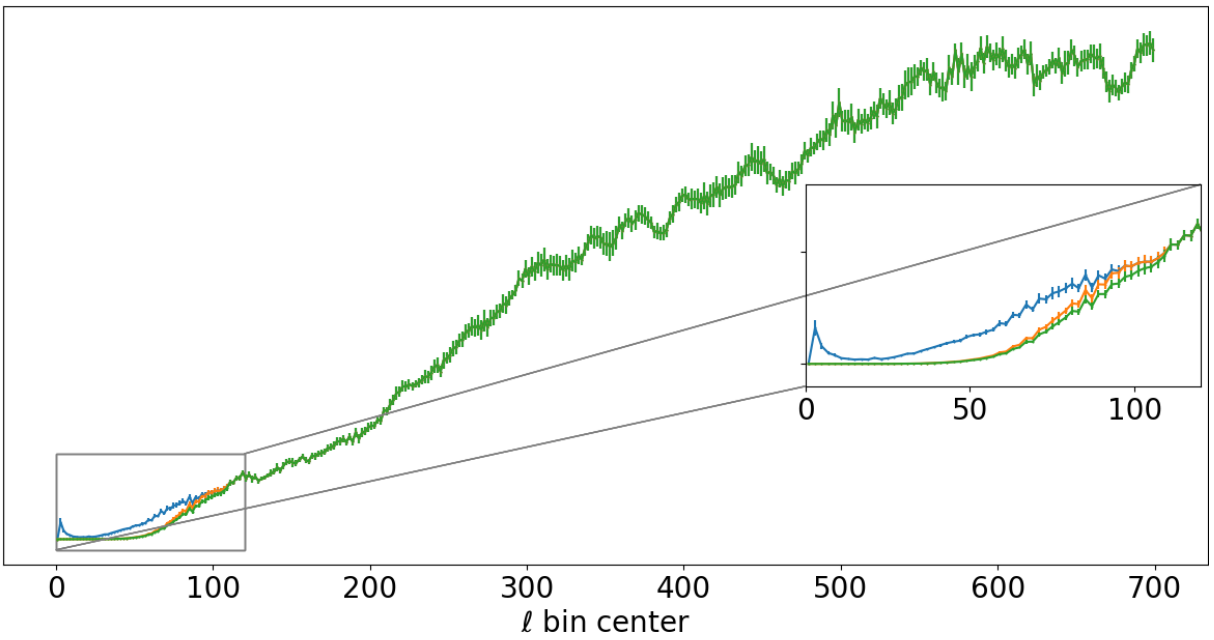

Figure 6.1: The uncalibrated BB pseudo-spectrum output with $\Delta\ell = 2$. The curves are shown for the pure estimator when the standard $1/\ell^2$ normalization is used (blue line), when the proposed normalization as described in Section 6.1 is employed (orange line) and when this proposed normalization is modified with a full evaluation of the multipolar angle dependence in Eq.5.28 for $\ell < 110$ and the standard normalization for $\ell > 110$ is used (green line). The error bars are obtained from the standard error of the Monte Carlo (MC) simulations.

Finally, we can analyze the estimated spectra of this test, that, at the end, are the goal of any power spectrum estimator. We present the two most important cases, BB is shown in Fig. 6.4, and EB is shown in Fig. 6.5, for our science multipole bins. There, we define the significance as,

$$t = \frac{|\bar{D}_b - D_b^{theory}|}{\bar{\sigma}_b} \tag{6.2}$$

Where $\bar{D}_b$ is the average binned rescaled spectrum outputs Eq.3.59 of the simulations, D_b^{theory} is the binned rescaled spectrum input from where the simulations are drawn and $\sigma_{\bar{b}}$ is the standard error of the binned rescaled spectrum outputs.

For the case of the estimated spectrum for BB, we see an overall slightly better performance of the implemented normalization with $\phi_{\vec{\ell}} = 0°$ over the other two implementations of the normalization. This is because for most of the bins the three implementations behave

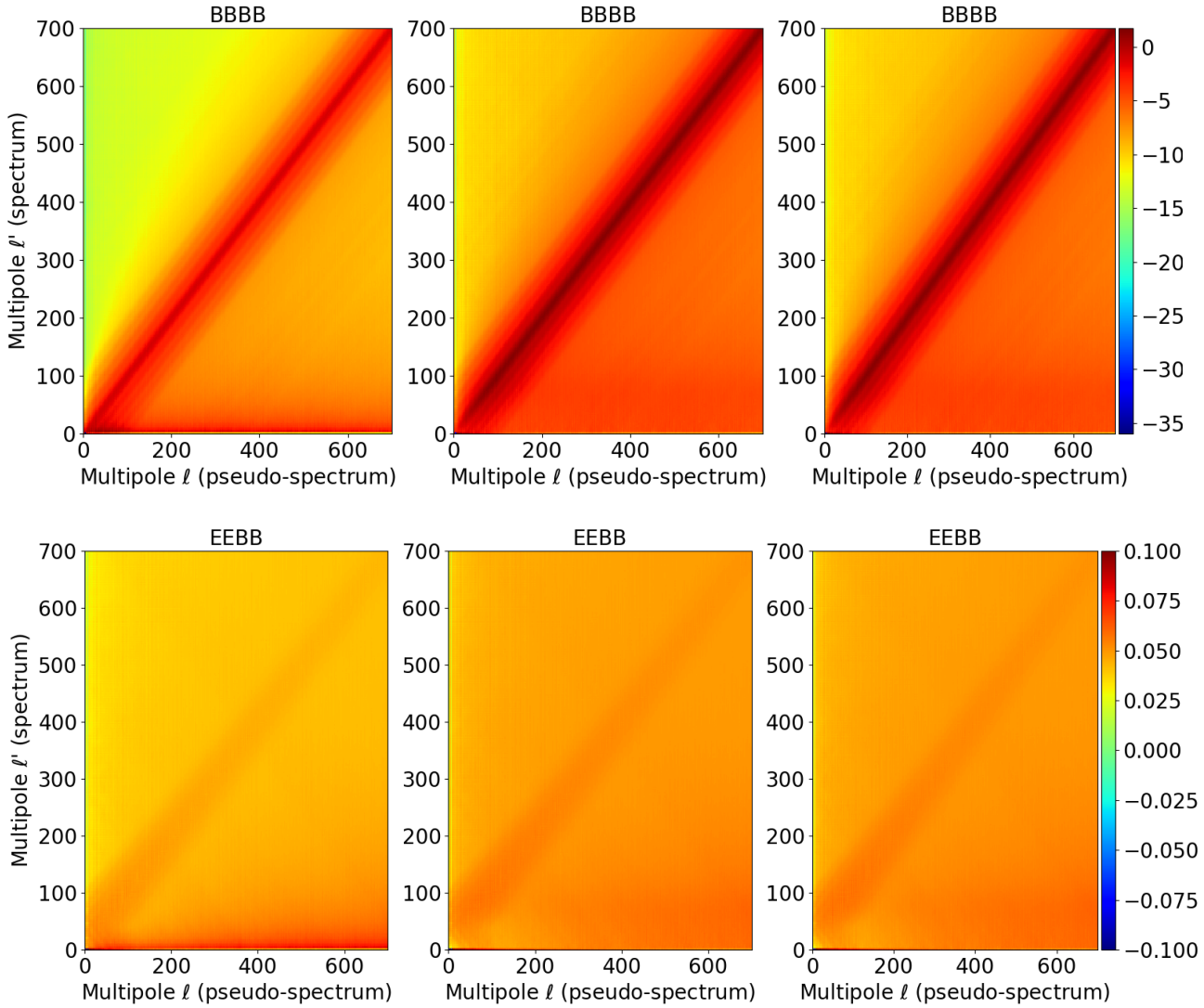

Figure 6.2: Mode-mode mixing matrix $\log_{10} M_{\ell\ell'}$ outputs with multipole bins of size $\Delta\ell = 2$, for the cases of the pure estimator when the standard $1/\ell^2$ normalization is used (left panel), when the proposed normalization as described in Section 6.1 is employed (middle panel) and when this proposed normalization is modified with a full evaluation of the multipolar angle dependence in Eq.5.28 for $\ell < 110$ and the standard normalization for $\ell > 110$ is used (right panel). The first row shows the $BBBB$ term, and the second row shows the cross component $EEBB$ that represents the $E \to B$ leakage.

similarly, but the differences are concentrated in the lowest bin, where the mentioned normalization is more than 2σ closer to the underlying spectrum than the standard normalization, and surprisingly more than 1σ closer than the multipolar angle dependent normalization. This is of extremely importance, as most of our bias problems where focused in the lowest bin, and in terms of science goals, this represents the most unexplored and challenging bin, where the recombination bump is expected at $\ell \sim 100$.

Finally, for the case of the estimated power spectrum for EB, we see an overall slightly better performance for both proposed normalizations over the standard normalization. Again, this is because for most of the bins the three implementations behave similarly, but the differences are concentrated in the lowest multipole bin, where the modified normalizations are roughly 0.3σ closer to the underlying spectrum than the standard normalization. Although the difference is not of remarkably significance, as they are below the statistical error, they help somewhat with the reduction of the $E \to B$ leakage and the introduction of variance into the B-mode estimator, as can be noted above. The modified normalizations exhibit totally compatible performances for this case. We conclude that the fixing choice of $\phi_{\vec{\ell}} = 0^\circ$ does not have a negative impact in the goal of our modifications when compared to a more extended evaluation of the multipolar angle and, even more, it could have a better performance in the measurements of the underlying B-modes. Also, we observe a better performance of the proposed modifications of the estimator when compared with the standard normalization, but we need to confirm these results for a more realistic scenario, when the underlying cosmology is not totally known beforehand, i.e., when perturbed input spectra are fed into the estimator.

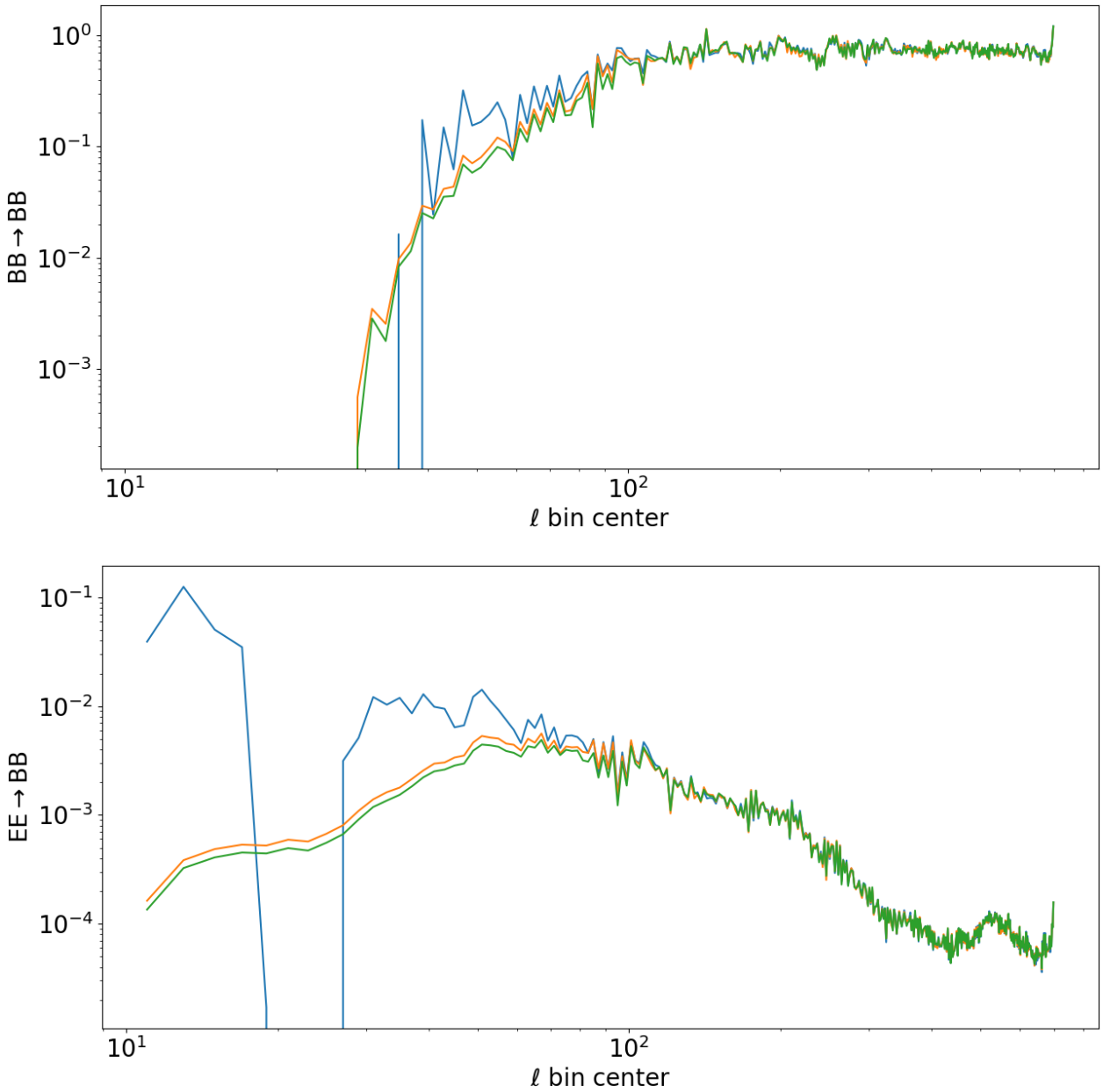

Figure 6.3: Filter transfer function outputs for the cases of the pure estimator when the standard $1/\ell^2$ normalization is used (blue line), when the proposed normalization as described in Section 6.1 is employed (orange line) and when this proposed normalization is modified with a full evaluation of the multipolar angle dependence in Eq.5.28 for $\ell < 110$ and the standard normalization for $\ell > 110$ is used (green line). The first row shows the $BB \to BB$ term, and the second row shows the cross component $EE \to BB$ that represents the $E \to B$ leakage.

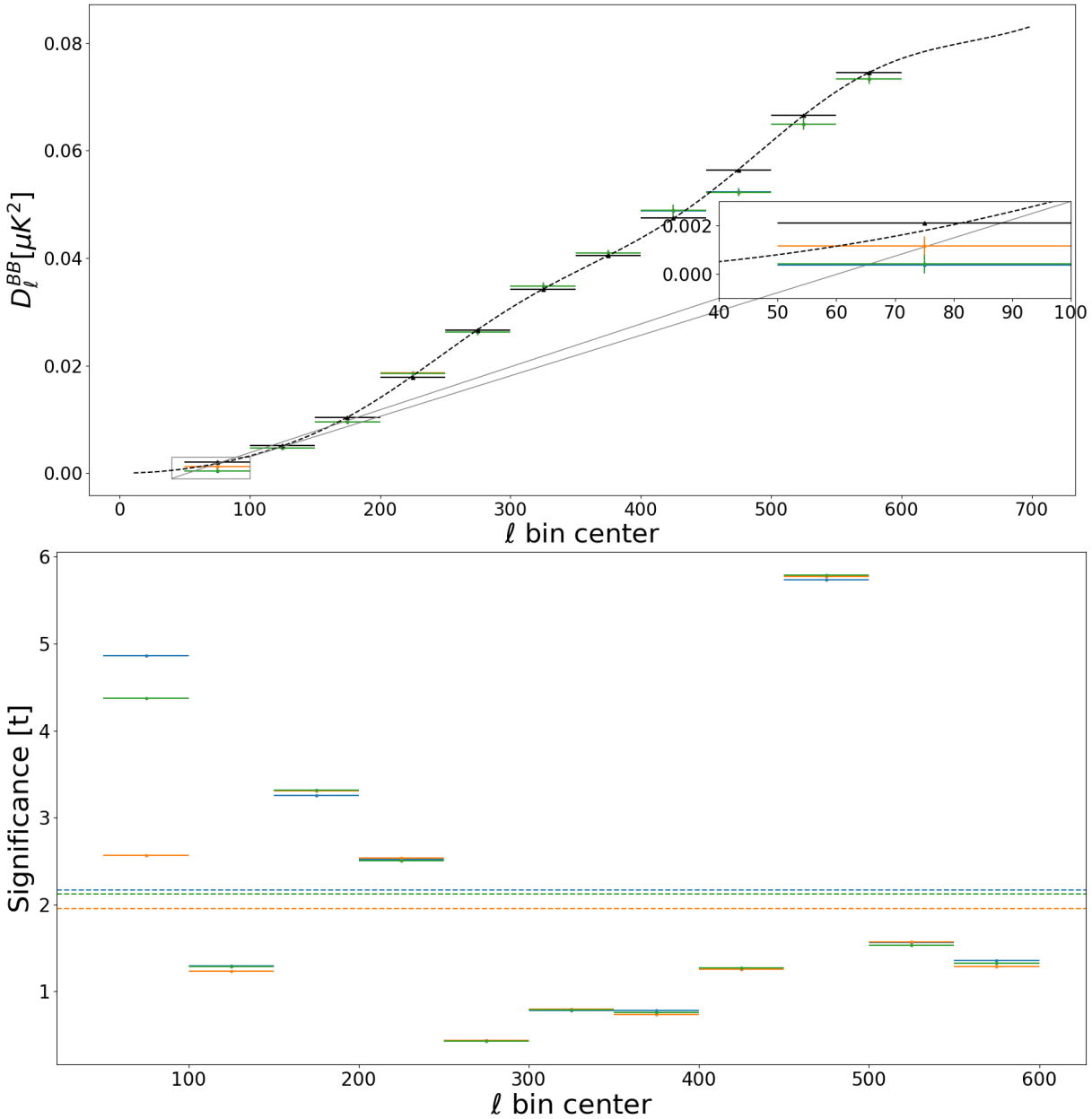

Figure 6.4: BB estimated power spectrum outputs for the cases of the pure estimator when the standard $1/\ell^2$ normalization is used (blue line), when the proposed normalization as described in Section 6.1 is employed (orange line) and when this proposed normalization is modified with a full evaluation of the multipolar angle dependence in Eq.5.28 for $\ell < 110$ and the standard normalization for $\ell > 110$ is used (green line). Top panel: The binned power spectrum is shown as points with their error bars. The dashed black line corresponds to the underlying input power spectrum. The black points and their error bars correspond to their binned version. Bottom panel: The significance of the discrepancy of the three estimated power spectra with respect to the binned theory as defined in Eq.6.2. The dashed lines correspond to the average significance over all the multipole range. The multipole bin width is $\Delta\ell = 50$ and the multipole centers are $\ell = [75, 125, 175, 225, 275, 325, 375, 425, 475, 525, 575]$. The vertical error bars are obtained from the standard error of the Monte Carlo (MC) simulations and the horizontal bars are defined by the bin width.

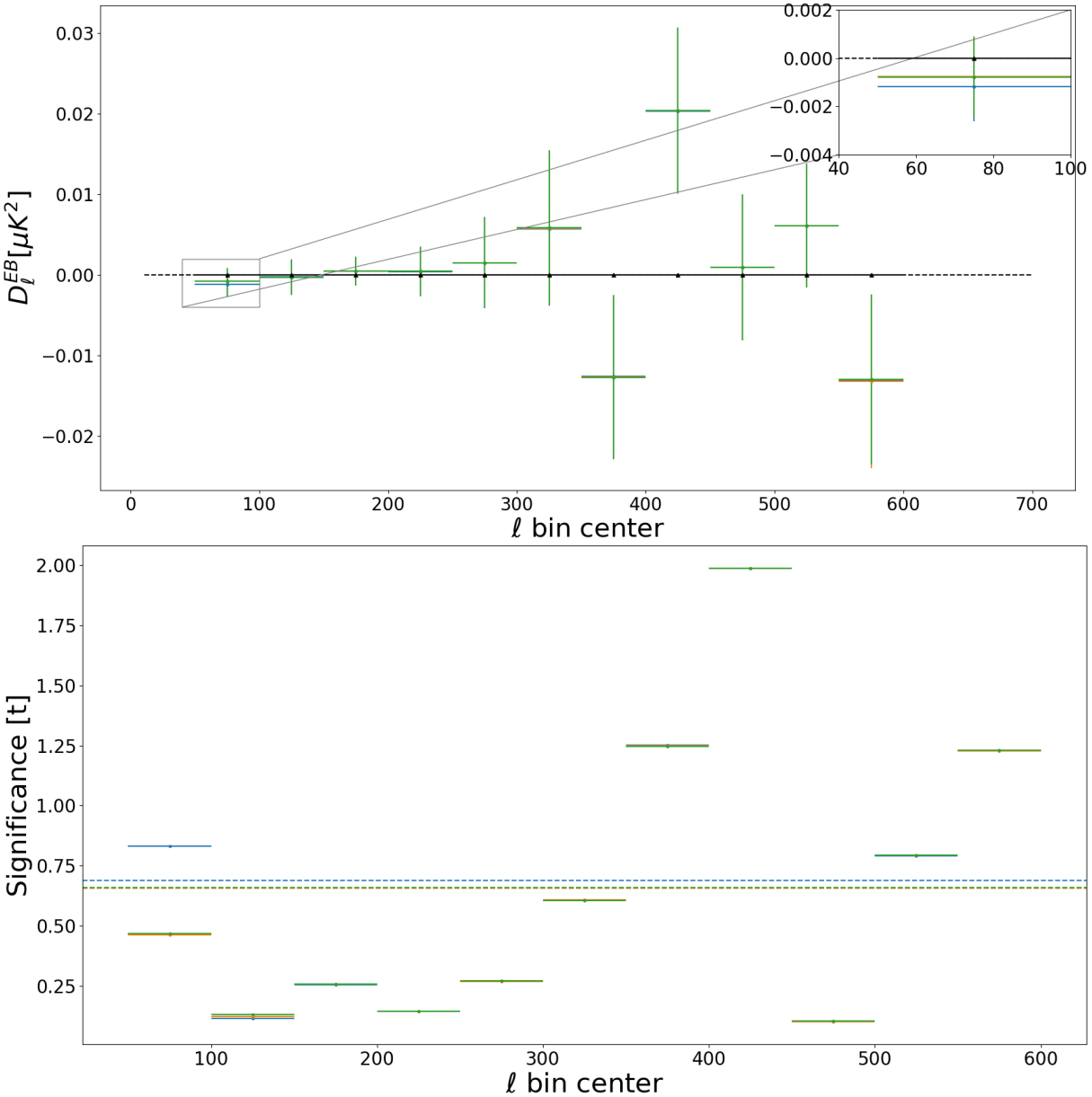

Figure 6.5: EB estimated power spectrum outputs for the cases of the pure estimator when the standard $1/\ell^2$ normalization is used (blue line), when the proposed normalization as described in Section 6.1 is employed (orange line) and when this proposed normalization is modified with a full evaluation of the multipolar angle dependence in Eq.5.28 for $\ell < 110$ and the standard normalization for $\ell > 110$ is used (green line). Top panel: The binned power spectrum is shown as points with their error bars. The dashed black line corresponds to the underlying input power spectrum. The black points and their error bars correspond to their binned version. Bottom panel: The significance of the discrepancy of the three estimated power spectra with respect to the binned theory as defined in Eq.6.2. The dashed lines correspond to the average significance over all the multipole range. The multipole bin width is $\Delta\ell = 50$ and the multipole centers are $\ell = [75, 125, 175, 225, 275, 325, 375, 425, 475, 525, 575]$. The vertical error bars are obtained from the standard error of the Monte Carlo (MC) simulations and the horizontal bars are defined by the bin width.

6.3 Robustness to spectrum variation

As part of the validation of the implementation of the proposed normalization, I perform a sequence of tests that uses simulations with changing BB input spectrum comparing the case where the implemented pure spectrum estimator makes use of the proposed normalization and when the standard normalization is used in its place. Basically, I was interested to see if the normalization makes the estimator more resilient to input spectra changes than just allowing the transfer function to fix the problem on its own. To do that, I make a slight modification to the pipeline configuration outlined in Section 6.1. As implied here, instead of using the exact fiducial power spectra mentioned in Section 6.1 and used for Section 6.2 and for most of the applications of the fiducial pipeline to feed the simulation inputs, their BB component is perturbed before. The input spectrum is varied introducing Gaussian noise with a multipolar semi-dependent level on each multipole ℓ. More precisely, I consider the following perturbation,

$$\delta C_\ell = \begin{cases} \mathcal{N}\left(\frac{(N-\ell)}{5N}\sigma_n, \frac{\ell^2}{N^2}\sigma_n^2\right) & \text{for } \ell < N \\ \mathcal{N}\left(0, \sigma_n^2\right) & \text{for } \ell \geq N \end{cases} \tag{6.3}$$

Where $\mathcal{N}(\mu, \sigma^2)$ is the normal distribution with mean μ and variance σ^2, and should not be confused with the normalization introduced in Section 5.3.2. The multipole cutoff is set to $N = 150$, and σ_n is related with the level of Gaussian noise introduced in each test and multipole ℓ. The perturbation is modeled in this way for many reasons. First, to make it independent of any preconceived cosmology. Second, it allows slightly increased level of non-triviality for the perturbation at low multipoles, where we are more interested to challenge our modifications. This is done with an increasing variance and a positive decreasing offset from the lowest multipoles up to $\ell = N$, where the offset is set to zero and the variance is kept constant for higher multipoles. Finally, this form of the perturbation and the parameter values considered for these tests avoid the presence of negative input spectrum values at low multipoles for the results shown here. We considered five different variations, from $\sigma_n = 1.0 \cdot 10^{-3}\mu K^2$ to $\sigma_n = 1.4 \cdot 10^{-3}\mu K^2$ with increments of $10^{-4}\mu K^2$.

The filter transfer function for the two normalization cases is fixed to the fiducial input cosmology described in Section 6.1 (indeed, they are the same used for Section 6.2), and hence are not re-computed for each perturbed input spectrum test, in line with the goal of this procedure. The rest of the configuration follows the one delineated in Section 6.1.

The results for the BB output spectra are shown in Fig. 6.6. There is a slightly better overall performance of the use of the proposed normalization over the use of the standard normalization in 4 of the 5 cases exposed here. Furthermore, in all of the variations, the lowest bin spectrum is much better reconstructed with the use of the proposed normalization, with 4 out of 5 of them with a significant difference between 3σ and 4σ with respect to the standard normalization scenario. We verify the improved resilience in the use of the proposed normalization by the pure B-mode spectrum estimator over the use of the standard normalization under variations of the BB input spectrum for the estimation of the lowest multipole spectrum bin.

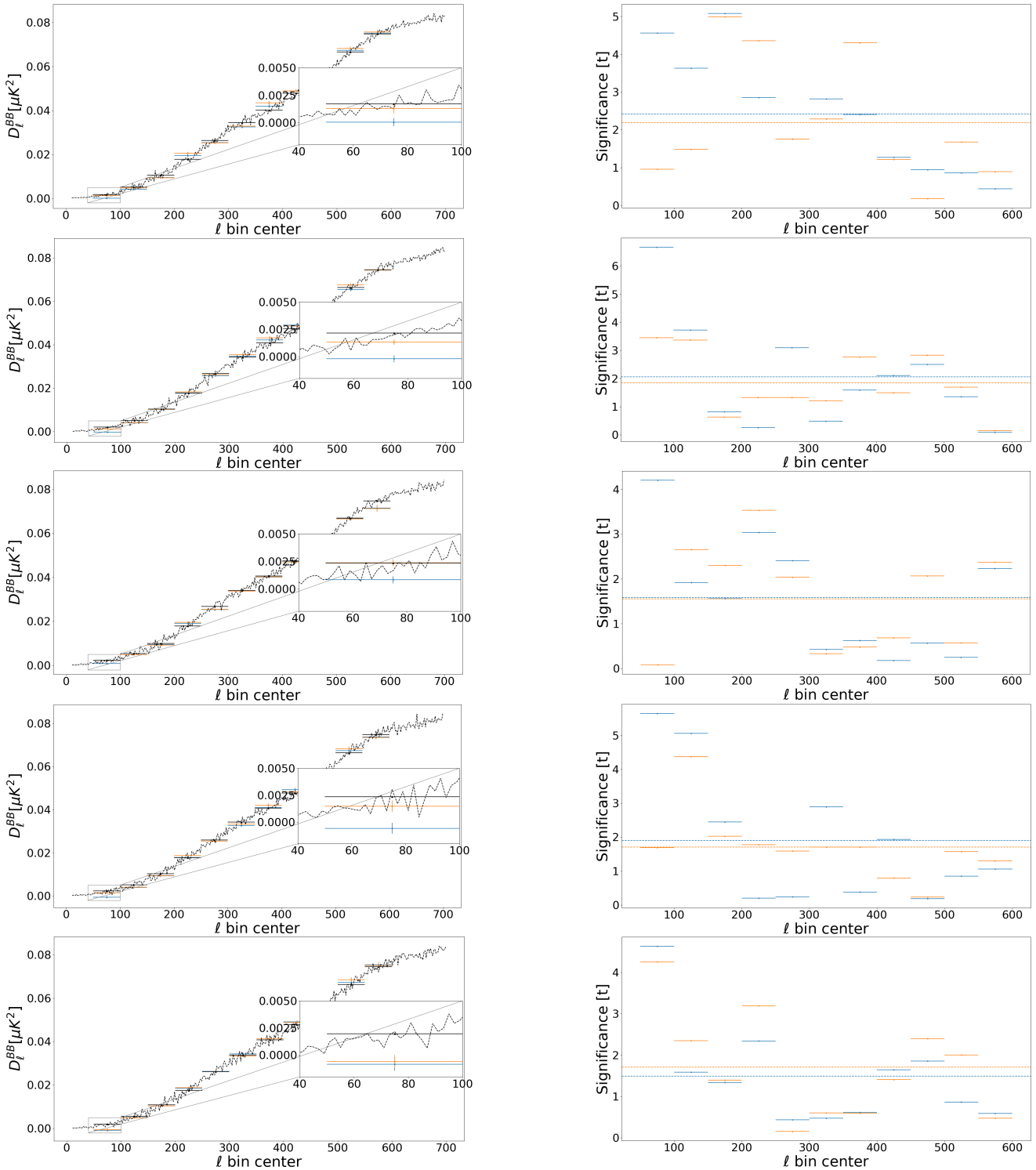

Figure 6.6: Same as Fig. 6.4 for the tests described in Section 6.3. Left panels: Same as top panel of Fig. 6.4 . Right panels: Same as bottom panel of Fig. 6.4. From top to bottom panels, the Gaussian noise levels are associated with $\sigma_n = [1.0 \cdot 10^{-3}, 1.1 \cdot 10^{-3}, 1.2 \cdot 10^{-3}, 1.3 \cdot 10^{-3}, 1.4 \cdot 10^{-3}]\mu K^2$.

6.4 Null Tests and Power Spectrum Validation

A map split null test framework has been implemented to check for internal consistency of our data to understand the noise properties, and to find overlooked systematic contamination in the angular power spectrum. Normally, the map pair differences contain traces of the signal owing to the effects caused by the filter process and the anisotropic scan pattern, that is more patent at large scales. Hence, the method at first implemented in the context of the QUIET experiment [118], and later employed in previous analyses of Polarbear, is adopted for our main analysis. In the definition of the null spectrum, the mode-coupling and filtering are considered,

$$\hat{C}_\ell^{null} = \hat{C}_\ell^A + \hat{C}_\ell^B - 2\hat{C}_\ell^{AB} \tag{6.4}$$

where we have introduced $\hat{C}_\ell^A$ and $\hat{C}_\ell^B$ to denote the estimated auto spectrum corresponding to each map split half. In the same manner, we denote $\hat{C}_\ell^{AB}$ as the cross spectrum between the map halves. The spectra is estimated from the same procedure outlined in Section 5.1.

The computation of the mode-mixing matrix and filter transfer function is performed in the same manner used in the fiducial angular power spectrum pipeline, where 92 EE-only and 92 BB-only Planck 2018 ΛCDM simulated input maps are used in each test. The directions in the sky present in both halves of the map splits are the only ones considered to generate the mode-coupling matrix and pseudo-spectrum. The multipole binning is the same mentioned in Section 6.1. The EE, EB, and BB real data null spectra are contrasted to 192 simulations with $EE + BB$ signal and noise. This number of simulations is enough to achieve a percent-level precision on the filter transfer functions and the PTE values of the null spectrum in our targeted ℓ range.

Noise simulations produced by the "signflip" pipeline mentioned in Section 4.3.3 are used for the fiducial null test statistics, that is not significantly discrepant from the PTE values extracted with the data stream noise model also discussed in Section 4.3.3, except for the "top versus bottom detectors" null splits that directly divides detector pairs,. This is caused by the existence of an extra anticorrelated noise component that shows up when detector pairs are put apart that is not considered in the data stream noise model presented in Section 4.3.3.

The final null test configuration separates the data in 18 mostly uncorrelated split types aimed to test an ample variety of possible sources of systematic biases. The data set is separated into halves of the same weight when it is feasible. The statistic $\chi_{null} \equiv \hat{C}_b^{null}/\sigma(\hat{C}_b^{null})$ is calculated for every bin and null spectrum, where the standard deviation of the MC null spectra is denoted as $\sigma(\hat{C}_b^{null})$. χ_{null} is used due to its sensitivity to systematic contamination and χ^2_{null} is also used to find outliers. To check for systematic biases and congruence of the noise model, five statistics are calculated using the χ_{null} values. These statistics were defined before real data was used to estimate the power spectra. For each statistic, a PTE value is calculated contrasting the real data to the same statistic calculated from the MC simulations.

A direct comparison between data and realizations takes for any correlations that shows up between multipole bins and split types in the calculation of the PTE values. An extra statistic P_{low} corresponding to the lowest of the five PTE values is considered. The PTE of P_{low} must be above 5% for a given test to be considered as passed. Also, a Kolmogorov–Smirnov (KS) test is used to prove that the PTE values of the χ^2_{null} values by test, by bin, and overall correspond to a uniform distribution and discard any systematic discrepancy between the simulated and real uncertainties. All these performed tests were considered successful. For a specification of the 18 null test axes, the statistics used and the quantitative results obtained from these tests I refer the reader to [6, 18].

Regarding the relationship with the evaluation of the performance of the proposed modifications presented in this work, the process to arrive to the final null test framework configuration described above is more relevant than the outcomes. The null test campaign was mainly lead by the member of the collaboration Goeckner-Wald. It consisted of ten consecutive and evolutive rounds before the final version was used to evaluate the internal consistency of the real data. During the progression of the rounds, the configuration of the null test framework was improved to better reflect the possibilities to catch systematic sources of contamination (such as the definition of the split null tests, the statistics or the choice of the noise model pipeline), the changes and updates of the fiducial data analysis pipeline were progressively introduced, artificial biasing introduced by the data analysis and not present in the real data was removed or mitigated and the whole code was debugged.

Particularly relevant for us consists the ninth round, where the proposed changes in the B-mode pseudo-spectrum described in this work were formally introduced in the main pipeline, along with other changes such as the introduction of new gain templates and Fourier Fast Transform notch filtering. A cross-check execution with and without the use of the proposed normalization was performed, as we have done in Sections 6.2 and 6.3. The pseudo-spectrum code was found to run slightly slower with the changes than with the standard pure B-estimator implementation, but not in a way to become a rate limiting step. The most evident power spectrum estimation issues were declared solved [119]. The introduction of these changes did not introduce significant systematic contamination related with any of the null test splits or amplified some existing ones. Since then, all the rest of the road until the publication of the results [6] included the use of the modifications proposed and implemented in the context of this thesis.

Finally, the end-to-end data analysis pipeline including the mentioned modifications were validated with both HEALPix [120] curved sky and flat sky inputs [18].

Chapter 7

Polarbear BB Power Spectrum Results

In this section, based on [6, 18], I briefly describe the main results of the experiment's wide patch analysis, where the modifications presented in the context of this manuscript are used. Fig. 7.1 illustrates the reconstructed B-mode angular power spectrum of the real data. A moderate surplus of power above the predictions from the ΛCDM lensing model in the lowest two multipole binds is measured. This remarks the importance of the high accuracy needed for the lowest bin that we have promoted in the context of this work. Current measurements of the B-mode angular power spectrum such as the ones shown in Fig. 3.14 along with the one reported in this work are summarized in Fig. 7.2.

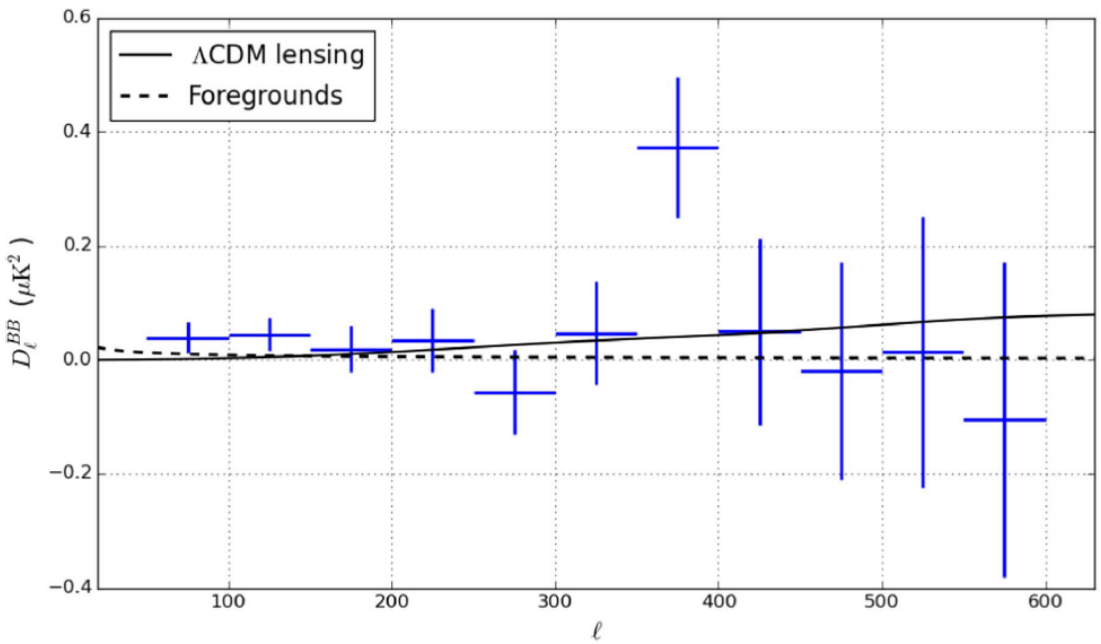

Figure 7.1: The result of the B-mode angular power spectrum measurement using the fiducial cross-spectrum pipeline described in Section 6.4. The error bars are only from the statistical uncertainties. The dashed line is obtained from foreground best-fit dust power at 150 GHz described in [6]. The outlier measurement present at $\ell = 375$ has a PTE of 9% as described in [6], meaning that this deviation is not significant. Figure from [6]. ©AAS. Reproduced with permission.

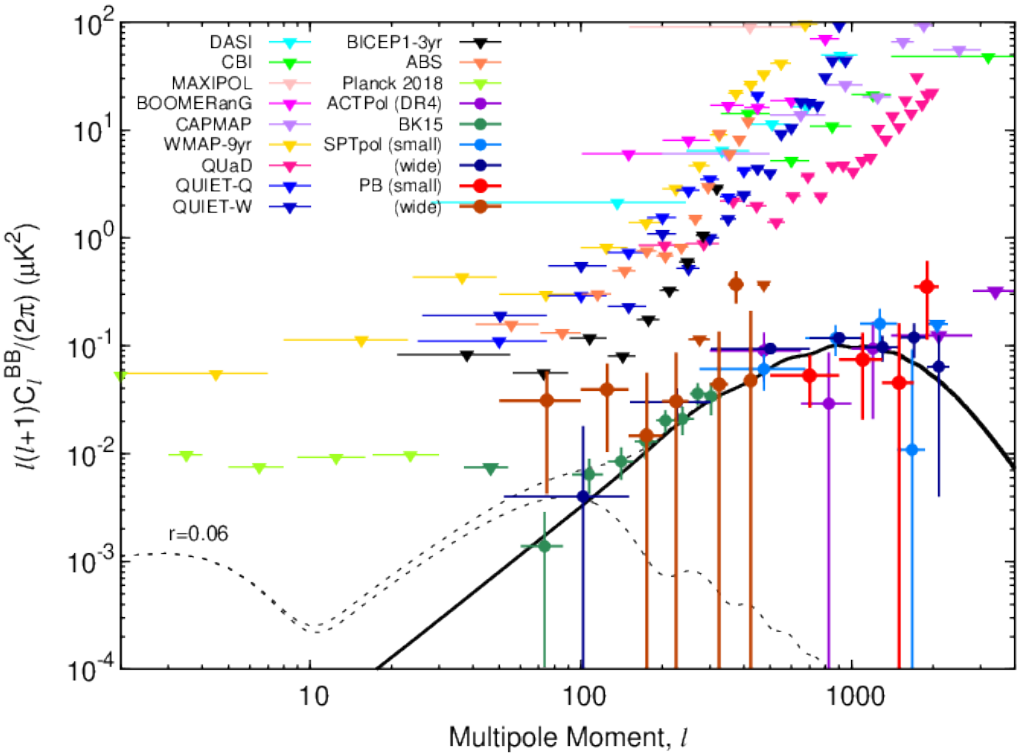

Figure 7.2: Current measurements of the B-mode angular power spectrum, where the measurements reported in Fig. 7.1 are labeled as "PB (wide)". Courtesy of Y. Chinone.

An estimation of the total amplitude of the measured B-mode signal compared to earlier measurements is calculated. For this estimation, it is assumed a sky with an underlying foreground contribution that follows a power law $D_{\ell,dust} = 9 \times 10^{-3}(\ell/80)^{-0.6}\mu K^2$ extracted from the BICEP2 and Keck Array spectral decomposition at 150GHz measured from the same sky region [88] and an underlying lensing CMB contribution matching the Planck 2018 ΛCDM lensing B-mode angular power spectrum. A reduced $\chi^2 = 11.6/11$ relative to this model is estimated showing a good consistency. If we naively fit a total B-mode amplitude to rescale this template, then $A_{BB} = 1.8 \pm 0.8$ is obtained, dismissing the null BB hypothesis at 2.2σ. This estimation ignores the small non-Gaussianity of the band power distributions shape. Nevertheless, this is considered in a subsequent cosmological parameter constraints analysis described in [6]. Finally, a naive uncertainty on r from realizations of ΛCDM with only lensing ($r = 0$) is calculated, finding a $\sigma(r) = 0.34$, ignoring the non-Gaussianity of the likelihood shape.

I have given this final description for completeness, but more about other results, such as cross-correlation analysis with Planck maps, contamination from polarized point sources and parameter constraints, that are beyond the scope of this work, can be found in [6]. Additionally, other intermediate steps of the wide patch analysis campaign not mentioned here such as the quantification of the low-ℓ statistical performance, the map level calibration or the simulation of systematic uncertainties can be found there and in [18].

Chapter 8

Conclusions, Discussions, and Overview

In the first three chapters, I give a non-specialized review starting from the basics of the early universe science to methodically introduce the reader to the motivations, first, of the whole experiment where this thesis is framed, and then, to the specific goals of my efforts described in this work. Due to the wide spectrum of areas involved in these collaborative projects, from experimental physics to data analysis to theoretical physics, it is important to keep in mind that most of the readers will have more expertise in some aspects of the experiment than in others, motivating me to don't be a miser of words for those chapters.

In Chapter 4, I describe the Polarbear experiment and the early stages of the analysis that the data must undergone to be converted from raw data streams measured by the detectors, to polarization sky maps.

In Chapter 5, a description of the power spectrum estimator, that was previously used in the context of the small patch analysis, that greatly follows the MASTER pipeline, is provided. Due to the $E \to B$ leakage induced by the partial sky coverage of the experiment, the pseudo-spectrum of this estimator, called here the mixed estimator, is modified to be a pure B-mode estimator, in the sense that the estimator vanishes for a realization of the CMB without noise which is comprised of only E-modes [19]. Previous studies [107, 108] of the viability of the application of this estimator to the new analysis involved in this work, that comprises a wider patch of the sky than in the previous analyses, shown an excess of reconstructed BB power spectrum, along with an abrupt change of the filter transfer function, at low multipole moments. I show that the mode-mixing matrix of the estimator also exhibits a remarkable off-diagonal structure associated with the pseudo-spectrum low multipole moments, that allows the mitigation of the $E \to B$ leakage [20] but can affect the numerical stability of the estimator [18]. These studies also show that the smoothing of the filter transfer function to reduce artificially its pathological structure only worsen the low ℓ BB bias of the reconstructed power spectrum.

An exploratory study of potential solutions is performed. A direct computation of a

non-expanded version of the ladder operator used to obtain the pure B-modes in the power spectrum estimator Eq.(5.10) is evaluated. A deformation of the effective window apodization function, in the sense of the pixels finally considered for the analysis and their relative weights, is found. The polarization mask is optimized in order to reduce the polarized foreground contamination to the measured B-modes [117], and so this alteration was considered unacceptable.

There are two independent problems that conspire to make the situation difficult to be solved using a single method. The partial-sky coverage, in one side, creates an $E \to B$ leakage and also a $B \to B$ mode mixing at low multipole moments induced by the loss of orthogonality of the B-modes that motivates the introduction of the pure-B power spectrum estimator. In the other hand, the use of this estimator under the flat sky approximation induces an excess of BB power in the reconstructed power spectrum. An increase of the cutoff for the truncation of the low multipole moments in the power spectrum estimation Eq.(5.1) can bias the reconstructed spectrum in the lowest ℓ bins, ruling out this as an alternative solution.

Another option initially considered was a phenomenological change of the $1/\ell^2$ normalization in the pure B-modes pseudo spectrum Eq.(5.3) to avoid the pathological excess of power at very low ℓ due to the breaking of the flat-sky approximation. Both a numerical Eq.(5.27) and analytical Eq.(5.28) expression are obtained, with a discrepancy between them corresponding at most to a percent fractional error level in the $50 < \ell < 100$ multipole moment region, without a known cause. Nevertheless, this level of discrepancy is considered acceptable and the analytical expression is contemplated for further evaluations given its reduced computational costs relative to the numerical implementation. At high ℓ, both expressions are found to behave as the standard $1/\ell^2$ normalization. At high ℓ, a flattener normalization when compare with the $1/\ell^2$ normalization is obtained.

Using the window apodization function used for our main analysis, the variations of the normalization $\mathcal{N}(\ell, \phi_{\vec{\ell}})$ when $\phi_{\vec{\ell}}$ is varied for a fixed ℓ are found to be at the percent fractional error level for the ℓ region of interest. Hence, this dependence is fixed at $\phi_{\vec{\ell}} = 0$, that is in the vicinity of minimum fractional error discrepancy between the numerical and analytical normalizations, for any subsequent use of this implementation justified by computational reasons. Qualitatively, for the pure B-mode pseudo spectrum it is found a reduction of the spurious excess of power at low ℓ when relative high ℓ power is injected, either from B-modes or E-modes, when comparing the proposed $\mathcal{N}(\ell, \phi_{\vec{\ell}} = 0^\circ)$ normalization with the standard $1/\ell^2$ normalization. Furthermore, for the implementation of this proposed normalization, we do not observe a noticeable growth of the $E \to B$ leakage, that is the primarily reason to use the pure-B estimator. Finally, it is observed an important reduction of the off-diagonal feature in the mode coupling matrix $M_{\ell\ell'}$ for $BBBB$ and $EEBB$, when the modified normalization is used. This somewhat improves the numerical stability of the estimator, with a slight increment in the $E \to B$ leakage as compared with the standard normalization, but still well below the levels of the mixed estimator.

In Chapter 6, more strict and quantitative tests are performed to evaluate the performance of the implemented modifications introduced to the B-mode pseudo-spectrum and the parameters chosen for its implementation by the use of simulated observations fed to end-to-end runs of the analysis pipeline. In Section 6.2, the impact of the use of the multipole angle choice in the proposed normalization is tested, which discrepancy is not significant with respect to a dependent multipole angle normalization at the pseudo spectrum level. Nevertheless, at the level of the reconstructed spectra, the proposed normalization is more than 2σ closer to the underlying spectrum than the standard normalization, and surprisingly more than 1σ than the multipolar angle dependent normalization. This is of extremely importance, as most of our bias problems where focused in the lowest bin, and in terms of science goals, this represents the most unexplored and challenging bin, where the recombination bump is expected at $\ell \sim 100$.

We conclude that the fixing choice of $\phi_{\vec{\ell}} = 0°$ does not have a negative impact in the goal of our modifications when compared to a more extended evaluation of the multipolar angle and, even more, it could have a better performance in the measurements of the underlying B-modes. Also, we observe a better performance of the proposed modifications of the estimator when compared with the standard normalization for the unperturbed input spectra case.

In Section 6.3, a sequence of tests that uses simulations with changing BB input spectrum comparing the case where the implemented pure spectrum estimator makes use of the proposed normalization and when the standard normalization is used in its place is carried. The goal was to prove if the normalization makes the estimator more resilient to input spectra changes than just allowing the transfer function to fix the problem on its own. The filter transfer function for the two normalization cases were fixed to the fiducial Planck 2018 ΛCDM input cosmology. The input spectrum variations shown that the lowest bin spectrum is much better reconstructed with the use of the proposed normalization, with 80% of the tests in the perturbation regime presented in this work with a significant difference between 3σ and 4σ when comparing to the standard normalization case. An improved resilience under variations of the BB input spectrum for the estimation of the lowest multipole spectrum bin when comparing the use of the implemented modifications in the power spectrum estimator with the case where these changes are not applied is obtained.

In Section 6.3, these conclusions are reinforced by noticing that the overall end-to-end data analysis pipeline including the mentioned modifications were validated with both HEALPix curved sky and flat sky inputs.

Finally, in Chapter 7, the final measured B-mode angular power spectrum of the Polarbear data obtained with the estimator changes discussed in this work shows a moderate excess of power above the predictions from the ΛCDM lensing model in the lowest two multipole bin. This remarks the importance of the high accuracy needed for the lowest bin that

we have pushed in the context of this work.

Despite the success in the mitigation of the power spectrum estimator problems that motivated the realization of the presented work, the implementation employed here should not be considered as a rule of thumb solution to any low ℓ BB bias emerged in the context of a flat sky approximation implementation of the pure-B estimator. Instead, this should be regarded as an ad hoc mitigation for the wide sky patch configuration of the Polarbear data analysis. An alternate use of this implementation should consider an acute evaluation of its performance applied to the specific experiment configuration, including, for example, the sky patch size, the pseudo-spectrum and spectrum bin sizes $\Delta\ell$, or the methods used for the computations of the mode mixing matrices $M_{\ell\ell'}$.

Other approaches emerged in the context of this work that are suggested to deal with potential power spectrum low ℓ BB biases while using a pure-B estimator are, first, the consideration of a sky coordinate system that closely represents the actual curved geometry. If this is not possible, and the flat sky formalism is employed, then a direct computation of a non-expanded version of the ladder operator used to obtain the pure B-modes should be evaluated. This would be the case if the potential foreground contamination introduced by the alteration of the effective window apodization functions in polarization are found to be subdominant relative to the reduction of the flat-sky induced BB bias, and the computational costs are considered affordable.

Bibliography

[1] S. Perlmutter, G. Aldering, G. Goldhaber, R. A. Knop, P. Nugent, P. G. Castro, S. Deustua, S. Fabbro, A. Goobar, D. E. Groom, I. M. Hook, A. G. Kim, M. Y. Kim, J. C. Lee, N. J. Nunes, R. Pain, C. R. Pennypacker, R. Quimby, C. Lidman, R. S. Ellis, M. Irwin, R. G. McMahon, P. Ruiz-Lapuente, N. Walton, B. Schaefer, B. J. Boyle, A. V. Filippenko, T. Matheson, A. S. Fruchter, N. Panagia, H. J. M. Newberg, W. J. Couch, and T. S. C. Project, "Measurements of Ω and Λ from 42 High-Redshift Supernovae," *The Astrophysical Journal*, vol. 517, no. 2, pp. 565–586, Jun 1999. [Online]. Available: https://doi.org/10.1086%2F307221

[2] Planck Collaboration, Aghanim, N., Akrami, Y., Arroja, F., Ashdown, M., Aumont, J., Baccigalupi, C., Ballardini, M., Banday, A. J., Barreiro, R. B., Bartolo, N., Basak, S., Battye, R., Benabed, K., Bernard, J.-P., Bersanelli, M., Bielewicz, P., Bock, J. J., Bond, J. R., Borrill, J., Bouchet, F. R., Boulanger, F., Bucher, M., Burigana, C., Butler, R. C., Calabrese, E., Cardoso, J.-F., Carron, J., Casaponsa, B., Challinor, A., Chiang, H. C., Colombo, L. P. L., Combet, C., Contreras, D., Crill, B. P., Cuttaia, F., de Bernardis, P., de Zotti, G., Delabrouille, J., Delouis, J.-M., Désert, F.-X., Di Valentino, E., Dickinson, C., Diego, J. M., Donzelli, S., Doré, O., Douspis, M., Ducout, A., Dupac, X., Efstathiou, G., Elsner, F., Enßlin, T. A., Eriksen, H. K., Falgarone, E., Fantaye, Y., Fergusson, J., Fernandez-Cobos, R., Finelli, F., Forastieri, F., Frailis, M., Franceschi, E., Frolov, A., Galeotta, S., Galli, S., Ganga, K., Génova-Santos, R. T., Gerbino, M., Ghosh, T., González-Nuevo, J., Górski, K. M., Gratton, S., Gruppuso, A., Gudmundsson, J. E., Hamann, J., Handley, W., Hansen, F. K., Helou, G., Herranz, D., Hildebrandt, S. R., Hivon, E., Huang, Z., Jaffe, A. H., Jones, W. C., Karakci, A., Keihänen, E., Keskitalo, R., Kiiveri, K., Kim, J., Kisner, T. S., Knox, L., Krachmalnicoff, N., Kunz, M., Kurki-Suonio, H., Lagache, G., Lamarre, J.-M., Langer, M., Lasenby, A., Lattanzi, M., Lawrence, C. R., Le Jeune, M., Leahy, J. P., Lesgourgues, J., Levrier, F., Lewis, A., Liguori, M., Lilje, P. B., Lilley, M., Lindholm, V., López-Caniego, M., Lubin, P. M., Ma, Y.-Z., Macías-Pérez, J. F., Maggio, G., Maino, D., Mandolesi, N., Mangilli, A., Marcos-Caballero, A., Maris, M., Martin, P. G., Martinelli, M., Martínez-González, E., Matarrese, S., Mauri, N., McEwen, J. D., Meerburg, P. D., Meinhold, P. R., Melchiorri, A., Mennella, A., Migliaccio, M., Millea, M., Mitra, S., Miville-Deschênes, M.-A., Molinari, D., Moneti, A., Montier, L., Morgante, G., Moss, A., Mottet, S., Münchmeyer, M., Natoli, P., Nørgaard-Nielsen, H. U., Oxborrow, C. A., Pagano, L., Paoletti, D., Partridge, B., Patanchon, G., Pearson, T. J., Peel, M., Peiris, H. V., Perrotta, F., Pettorino, V., Piacentini, F., Polastri, L., Polenta, G., Puget, J.-L., Rachen, J. P., Reinecke, M., Remazeilles, M., Renault, C., Renzi, A., Rocha, G., Rosset, C., Roudier, G., Rubiño-Martín, J. A., Ruiz-Granados, B., Salvati, L., Sandri, M., Savelainen, M., Scott, D., Shellard, E. P. S., Shiraishi, M.,

Sirignano, C., Sirri, G., Spencer, L. D., Sunyaev, R., Suur-Uski, A.-S., Tauber, J. A., Tavagnacco, D., Tenti, M., Terenzi, L., Toffolatti, L., Tomasi, M., Trombetti, T., Valiviita, J., Van Tent, B., Vibert, L., Vielva, P., Villa, F., Vittorio, N., Wandelt, B. D., Wehus, I. K., White, M., White, S. D. M., Zacchei, A., and Zonca, A., "Planck 2018 results - I. Overview and the cosmological legacy of Planck," *A&A*, vol. 641, p. A1, 2020. [Online]. Available: https://doi.org/10.1051/0004-6361/201833880

[3] Planck Collaboration, Aghanim, N., Akrami, Y., Ashdown, M., Aumont, J., Baccigalupi, C., Ballardini, M., Banday, A. J., Barreiro, R. B., Bartolo, N., Basak, S., Battye, R., Benabed, K., Bernard, J.-P., Bersanelli, M., Bielewicz, P., Bock, J. J., Bond, J. R., Borrill, J., Bouchet, F. R., Boulanger, F., Bucher, M., Burigana, C., Butler, R. C., Calabrese, E., Cardoso, J.-F., Carron, J., Challinor, A., Chiang, H. C., Chluba, J., Colombo, L. P. L., Combet, C., Contreras, D., Crill, B. P., Cuttaia, F., de Bernardis, P., de Zotti, G., Delabrouille, J., Delouis, J.-M., Di Valentino, E., Diego, J. M., Doré, O., Douspis, M., Ducout, A., Dupac, X., Dusini, S., Efstathiou, G., Elsner, F., Enßlin, T. A., Eriksen, H. K., Fantaye, Y., Farhang, M., Fergusson, J., Fernandez-Cobos, R., Finelli, F., Forastieri, F., Frailis, M., Fraisse, A. A., Franceschi, E., Frolov, A., Galeotta, S., Galli, S., Ganga, K., Génova-Santos, R. T., Gerbino, M., Ghosh, T., González-Nuevo, J., Górski, K. M., Gratton, S., Gruppuso, A., Gudmundsson, J. E., Hamann, J., Handley, W., Hansen, F. K., Herranz, D., Hildebrandt, S. R., Hivon, E., Huang, Z., Jaffe, A. H., Jones, W. C., Karakci, A., Keihänen, E., Keskitalo, R., Kiiveri, K., Kim, J., Kisner, T. S., Knox, L., Krachmalnicoff, N., Kunz, M., Kurki-Suonio, H., Lagache, G., Lamarre, J.-M., Lasenby, A., Lattanzi, M., Lawrence, C. R., Le Jeune, M., Lemos, P., Lesgourgues, J., Levrier, F., Lewis, A., Liguori, M., Lilje, P. B., Lilley, M., Lindholm, V., López-Caniego, M., Lubin, P. M., Ma, Y.-Z., Macías-Pérez, J. F., Maggio, G., Maino, D., Mandolesi, N., Mangilli, A., Marcos-Caballero, A., Maris, M., Martin, P. G., Martinelli, M., Martínez-González, E., Matarrese, S., Mauri, N., McEwen, J. D., Meinhold, P. R., Melchiorri, A., Mennella, A., Migliaccio, M., Millea, M., Mitra, S., Miville-Deschênes, M.-A., Molinari, D., Montier, L., Morgante, G., Moss, A., Natoli, P., Nørgaard-Nielsen, H. U., Pagano, L., Paoletti, D., Partridge, B., Patanchon, G., Peiris, H. V., Perrotta, F., Pettorino, V., Piacentini, F., Polastri, L., Polenta, G., Puget, J.-L., Rachen, J. P., Reinecke, M., Remazeilles, M., Renzi, A., Rocha, G., Rosset, C., Roudier, G., Rubiño-Martín, J. A., Ruiz-Granados, B., Salvati, L., Sandri, M., Savelainen, M., Scott, D., Shellard, E. P. S., Sirignano, C., Sirri, G., Spencer, L. D., Sunyaev, R., Suur-Uski, A.-S., Tauber, J. A., Tavagnacco, D., Tenti, M., Toffolatti, L., Tomasi, M., Trombetti, T., Valenziano, L., Valiviita, J., Van Tent, B., Vibert, L., Vielva, P., Villa, F., Vittorio, N., Wandelt, B. D., Wehus, I. K., White, M., White, S. D. M., Zacchei, A., and Zonca, A., "Planck 2018 results - VI. Cosmological parameters," *A&A*, vol. 641, p. A6, 2020. [Online]. Available: https://doi.org/10.1051/0004-6361/201833910

[4] S. Dodelson and F. Schmidt, *Modern Cosmology*, Second ed., S. Dodelson and F. Schmidt, Eds. Academic Press: An imprint of Elsevier, 2021. [Online]. Available: https://doi.org/10.1016/c2017-0-01943-2

[5] W. Hu and M. White, "A CMB polarization primer," *New Astronomy*, vol. 2, no. 4, pp. 323 – 344, 1997. [Online]. Available: http://www.sciencedirect.com/science/

article/pii/S1384107697000225

[6] S. Adachi, M. A. O. Aguilar Faúndez, K. Arnold, C. Baccigalupi, D. Barron, D. Beck, S. Beckman, F. Bianchini, D. Boettger, J. Borrill, J. Carron, S. Chapman, K. Cheung, Y. Chinone, K. Crowley, A. Cukierman, M. Dobbs, H. E. Bouhargani, T. Elleflot, J. Errard, G. Fabbian, C. Feng, T. Fujino, N. Galitzki, N. Goeckner-Wald, J. Groh, G. Hall, N. Halverson, T. Hamada, M. Hasegawa, M. Hazumi, C. A. Hill, L. Howe, Y. Inoue, G. Jaehnig, O. Jeong, D. Kaneko, N. Katayama, B. Keating, R. Keskitalo, S. Kikuchi, T. Kisner, N. Krachmalnicoff, A. Kusaka, A. T. Lee, D. Leon, E. Linder, L. N. Lowry, A. Mangu, F. Matsuda, Y. Minami, M. Navaroli, H. Nishino, A. T. P. Pham, D. Poletti, G. Puglisi, C. L. Reichardt, Y. Segawa, M. Silva-Feaver, P. Siritanasak, N. Stebor, R. Stompor, A. Suzuki, O. Tajima, S. Takakura, S. Takatori, D. Tanabe, G. P. Teply, C. Tsai, C. Verges, B. Westbrook, and Y. Zhou, "A Measurement of the Degree-scale CMB B-mode Angular Power Spectrum with Polarbear," *The Astrophysical Journal*, vol. 897, no. 1, p. 55, Jul 2020. [Online]. Available: https://doi.org/10.3847%2F1538-4357%2Fab8f24

[7] K. N. Abazajian, P. Adshead, Z. Ahmed, S. W. Allen, D. Alonso, K. S. Arnold, C. Baccigalupi, J. G. Bartlett, N. Battaglia, B. A. Benson, C. A. Bischoff, J. Borrill, V. Buza, E. Calabrese, R. Caldwell, J. E. Carlstrom, C. L. Chang, T. M. Crawford, F.-Y. Cyr-Racine, F. De Bernardis, T. de Haan, S. di Serego Alighieri, J. Dunkley, C. Dvorkin, J. Errard, G. Fabbian, S. Feeney, S. Ferraro, J. P. Filippini, R. Flauger, G. M. Fuller, V. Gluscevic, D. Green, D. Grin, E. Grohs, J. W. Henning, J. C. Hill, R. Hlozek, G. Holder, W. Holzapfel, W. Hu, K. M. Huffenberger, R. Keskitalo, L. Knox, A. Kosowsky, J. Kovac, E. D. Kovetz, C.-L. Kuo, A. Kusaka, M. Le Jeune, A. T. Lee, M. Lilley, M. Loverde, M. S. Madhavacheril, A. Mantz, D. J. E. Marsh, J. McMahon, P. D. Meerburg, J. Meyers, A. D. Miller, J. B. Munoz, H. N. Nguyen, M. D. Niemack, M. Peloso, J. Peloton, L. Pogosian, C. Pryke, M. Raveri, C. L. Reichardt, G. Rocha, A. Rotti, E. Schaan, M. M. Schmittfull, D. Scott, N. Sehgal, S. Shandera, B. D. Sherwin, T. L. Smith, L. Sorbo, G. D. Starkman, K. T. Story, A. van Engelen, J. D. Vieira, S. Watson, N. Whitehorn, and W. L. Kimmy Wu, "CMB-S4 Science Book, First Edition," *arXiv e-prints*, p. arXiv:1610.02743, Oct. 2016.

[8] D. Boettger, "CMB Polarization Measurements with the Polarbear Experiment," Ph.D. dissertation, UC San Diego, 2014.

[9] S. Aiola, E. Calabrese, L. Maurin, S. Naess, B. L. Schmitt, M. H. Abitbol, G. E. Addison, P. A. R. Ade, D. Alonso, M. Amiri, S. Amodeo, E. Angile, J. E. Austermann, T. Baildon, N. Battaglia, J. A. Beall, R. Bean, D. T. Becker, J. R. Bond, S. M. Bruno, V. Calafut, L. E. Campusano, F. Carrero, G. E. Chesmore, H.-m. Cho., S. K. Choi, S. E. Clark, N. F. Cothard, D. Crichton, K. T. Crowley, O. Darwish, R. Datta, E. V. Denison, M. J. Devlin, C. J. Duell, S. M. Duff, A. J. Duivenvoorden, J. Dunkley, R. o. Dünner, T. Essinger-Hileman, M. Fankhanel, S. Ferraro, A. E. Fox, B. Fuzia, P. A. Gallardo, V. Gluscevic, J. E. Golec, E. Grace, M. Gralla, Y. Guan, K. Hall, M. Halpern, D. Han, P. Hargrave, M. Hasselfield, J. M. Helton, S. Henderson, B. Hensley, J. C. Hill, G. C. Hilton, M. Hilton, A. D. Hincks, R. Hložek, S.-P. P. Ho, J. Hubmayr, K. M. Huffenberger, J. P. Hughes, L. Infante, K. Irwin, R. Jackson, J. Klein, K. Knowles, B. Koopman, A. Kosowsky, V. Lakey, D. Li, Y. Li, Z. Li, M. Lokken, T. Louis,

M. Lungu, A. MacInnis, M. Madhavacheril, F. Maldonado, M. Mallaby-Kay, D. Marsden, J. McMahon, F. Menanteau, K. Moodley, T. Morton, T. Namikawa, F. Nati, L. Newburgh, J. P. Nibarger, A. Nicola, M. D. Niemack, M. R. Nolta, J. Orlowski-Sherer, L. A. Page, C. G. Pappas, B. Partridge, P. Phakathi, H. Prince, R. Puddu, F. J. Qu, J. Rivera, N. Robertson, F. Rojas, M. Salatino, E. Schaan, A. Schillaci, N. Sehgal, B. D. Sherwin, C. Sierra, J. Sievers, C. Sifon, P. Sikhosana, S. Simon, D. N. Spergel, S. T. Staggs, J. Stevens, E. Storer, D. D. Sunder, E. R. Switzer, B. Thorne, R. Thornton, H. Trac, J. Treu, C. Tucker, L. R. Vale, A. Van Engelen, J. Van Lanen, E. M. Vavagiakis, K. Wagoner, Y. Wang, J. T. Ward, E. J. Wollack, Z. Xu, F. Zago, and N. Zhu, "The Atacama Cosmology Telescope: DR4 Maps and Cosmological Parameters," *arXiv e-prints*, p. arXiv:2007.07288, Jul. 2020.

[10] J. W. Henning, J. T. Sayre, C. L. Reichardt, P. A. R. Ade, A. J. Anderson, J. E. Austermann, J. A. Beall, A. N. Bender, B. A. Benson, L. E. Bleem, J. E. Carlstrom, C. L. Chang, H. C. Chiang, H.-M. Cho, R. Citron, C. C. Moran, T. M. Crawford, A. T. Crites, T. de Haan, M. A. Dobbs, W. Everett, J. Gallicchio, E. M. George, A. Gilbert, N. W. Halverson, N. Harrington, G. C. Hilton, G. P. Holder, W. L. Holzapfel, S. Hoover, Z. Hou, J. D. Hrubes, N. Huang, J. Hubmayr, K. D. Irwin, R. Keisler, L. Knox, A. T. Lee, E. M. Leitch, D. Li, A. Lowitz, A. Manzotti, J. J. McMahon, S. S. Meyer, L. Mocanu, J. Montgomery, A. Nadolski, T. Natoli, J. P. Nibarger, V. Novosad, S. Padin, C. Pryke, J. E. Ruhl, B. R. Saliwanchik, K. K. Schaffer, C. Sievers, G. Smecher, A. A. Stark, K. T. Story, C. Tucker, K. Vanderlinde, T. Veach, J. D. Vieira, G. Wang, N. Whitehorn, W. L. K. Wu, and V. Yefremenko, "Measurements of the Temperature and E-mode Polarization of the CMB from 500 Square Degrees of SPTpol Data," *The Astrophysical Journal*, vol. 852, no. 2, p. 97, Jan 2018. [Online]. Available: https://doi.org/10.3847%2F1538-4357%2Faa9ff4

[11] J. T. Sayre, C. L. Reichardt, J. W. Henning, P. A. R. Ade, A. J. Anderson, J. E. Austermann, J. S. Avva, J. A. Beall, A. N. Bender, B. A. Benson, F. Bianchini, L. E. Bleem, J. E. Carlstrom, C. L. Chang, P. Chaubal, H. C. Chiang, R. Citron, C. Corbett Moran, T. M. Crawford, A. T. Crites, T. de Haan, M. A. Dobbs, W. Everett, J. Gallicchio, E. M. George, A. Gilbert, N. Gupta, N. W. Halverson, N. Harrington, G. C. Hilton, G. P. Holder, W. L. Holzapfel, J. D. Hrubes, N. Huang, J. Hubmayr, K. D. Irwin, L. Knox, A. T. Lee, D. Li, A. Lowitz, J. J. McMahon, S. S. Meyer, L. M. Mocanu, J. Montgomery, A. Nadolski, T. Natoli, J. P. Nibarger, G. Noble, V. Novosad, S. Padin, S. Patil, C. Pryke, J. E. Ruhl, B. R. Saliwanchik, K. K. Schaffer, C. Sievers, G. Smecher, A. A. Stark, C. Tucker, K. Vanderlinde, T. Veach, J. D. Vieira, G. Wang, N. Whitehorn, W. L. K. Wu, and V. Yefremenko, "Measurements of B-mode polarization of the cosmic microwave background from 500 square degrees of SPTpol data," *Phys. Rev. D*, vol. 101, p. 122003, Jun 2020. [Online]. Available: https://link.aps.org/doi/10.1103/PhysRevD.101.122003

[12] E. M. George, C. L. Reichardt, K. A. Aird, B. A. Benson, L. E. Bleem, J. E. Carlstrom, C. L. Chang, H.-M. Cho, T. M. Crawford, A. T. Crites, T. de Haan, M. A. Dobbs, J. Dudley, N. W. Halverson, N. L. Harrington, G. P. Holder, W. L. Holzapfel, Z. Hou, J. D. Hrubes, R. Keisler, L. Knox, A. T. Lee, E. M. Leitch, M. Lueker, D. Luong-Van, J. J. McMahon, J. Mehl, S. S. Meyer, M. Millea, L. M. Mocanu, J. J. Mohr, T. E. Montroy, S. Padin, T. Plagge, C. Pryke, J. E. Ruhl, K. K. Schaffer,

L. Shaw, E. Shirokoff, H. G. Spieler, Z. Staniszewski, A. A. Stark, K. T. Story, A. van Engelen, K. Vanderlinde, J. D. Vieira, R. Williamson, and O. Zahn, "A measurement of secondary cosmic microwave background anisotropies from the 2500-square-degree SPT-SZ survey," *The Astrophysical Journal*, vol. 799, no. 2, p. 177, Jan 2015. [Online]. Available: https://doi.org/10.1088%2F0004-637x%2F799%2F2%2F177

[13] C. L. Reichardt, S. Patil, P. A. R. Ade, A. J. Anderson, J. E. Austermann, J. S. Avva, E. Baxter, J. A. Beall, A. N. Bender, B. A. Benson, F. Bianchini, L. E. Bleem, J. E. Carlstrom, C. L. Chang, P. Chaubal, H. C. Chiang, T. L. Chou, R. Citron, C. Corbett Moran, T. M. Crawford, A. T. Crites, T. de Haan, M. A. Dobbs, W. Everett, J. Gallicchio, E. M. George, A. Gilbert, N. Gupta, N. W. Halverson, N. Harrington, J. W. Henning, G. C. Hilton, G. P. Holder, W. L. Holzapfel, J. D. Hrubes, N. Huang, J. Hubmayr, K. D. Irwin, L. Knox, A. T. Lee, D. Li, A. Lowitz, D. Luong-Van, J. J. McMahon, J. Mehl, S. S. Meyer, M. Millea, L. M. Mocanu, J. J. Mohr, J. Montgomery, A. Nadolski, T. Natoli, J. P. Nibarger, G. Noble, V. Novosad, Y. Omori, S. Padin, C. Pryke, J. E. Ruhl, B. R. Saliwanchik, J. T. Sayre, K. K. Schaffer, E. Shirokoff, C. Sievers, G. Smecher, H. G. Spieler, Z. Staniszewski, A. A. Stark, C. Tucker, K. Vand erlinde, T. Veach, J. D. Vieira, G. Wang, N. Whitehorn, R. Williamson, W. L. K. Wu, and V. Yefremenko, "An Improved Measurement of the Secondary Cosmic Microwave Background Anisotropies from the SPT-SZ + SPTpol Surveys," *arXiv e-prints*, p. arXiv:2002.06197, Feb. 2020.

[14] P. A. R. Ade, Z. Ahmed, R. W. Aikin, K. D. Alexander, D. Barkats, S. J. Benton, C. A. Bischoff, J. J. Bock, R. Bowens-Rubin, J. A. Brevik, I. Buder, E. Bullock, V. Buza, J. Connors, J. Cornelison, B. P. Crill, M. Crumrine, M. Dierickx, L. Duband, C. Dvorkin, J. P. Filippini, S. Fliescher, J. Grayson, G. Hall, M. Halpern, S. Harrison, S. R. Hildebrandt, G. C. Hilton, H. Hui, K. D. Irwin, J. Kang, K. S. Karkare, E. Karpel, J. P. Kaufman, B. G. Keating, S. Kefeli, S. A. Kernasovskiy, J. M. Kovac, C. L. Kuo, N. A. Larsen, K. Lau, E. M. Leitch, M. Lueker, K. G. Megerian, L. Moncelsi, T. Namikawa, C. B. Netterfield, H. T. Nguyen, R. O'Brient, R. W. Ogburn, S. Palladino, C. Pryke, B. Racine, S. Richter, A. Schillaci, R. Schwarz, C. D. Sheehy, A. Soliman, T. St. Germaine, Z. K. Staniszewski, B. Steinbach, R. V. Sudiwala, G. P. Teply, K. L. Thompson, J. E. Tolan, C. Tucker, A. D. Turner, C. Umiltà, A. G. Vieregg, A. Wandui, A. C. Weber, D. V. Wiebe, J. Willmert, C. L. Wong, W. L. K. Wu, H. Yang, K. W. Yoon, and C. Zhang, "Constraints on Primordial Gravitational Waves Using *Planck*, WMAP, and New BICEP2/*Keck* Observations through the 2015 Season," *Phys. Rev. Lett.*, vol. 121, p. 221301, Nov 2018. [Online]. Available: https://link.aps.org/doi/10.1103/PhysRevLett.121.221301

[15] S. K. Choi, M. Hasselfield, S.-P. P. Ho, B. Koopman, M. Lungu, M. H. Abitbol, G. E. Addison, P. A. R. Ade, S. Aiola, D. Alonso, M. Amiri, S. Amodeo, E. Angile, J. E. Austermann, T. Baildon, N. Battaglia, J. A. Beall, R. Bean, D. T. Becker, J. R. Bond, S. M. Bruno, E. Calabrese, V. Calafut, L. E. Campusano, F. Carrero, G. E. Chesmore, H.-m. Cho., S. E. Clark, N. F. Cothard, D. Crichton, K. T. Crowley, O. Darwish, R. Datta, E. V. Denison, M. J. Devlin, C. J. Duell, S. M. Duff, A. J. Duivenvoorden, J. Dunkley, R. Dünner, T. Essinger-Hileman, M. Fankhanel, S. Ferraro, A. E. Fox, B. Fuzia, P. A. Gallardo, V. Gluscevic, J. E. Golec, E. Grace, M. Gralla, Y. Guan, K. Hall, M. Halpern, D. Han, P. Hargrave, S. Henderson, B. Hensley, J. C. Hill, G. C.

Hilton, M. Hilton, A. D. Hincks, R. Hložek, J. Hubmayr, K. M. Huffenberger, J. P. Hughes, L. Infante, K. Irwin, R. Jackson, J. Klein, K. Knowles, A. Kosowsky, V. Lakey, D. Li, Y. Li, Z. Li, M. Lokken, T. Louis, A. MacInnis, M. Madhavacheril, F. Maldonado, M. Mallaby-Kay, D. Marsden, L. Maurin, J. McMahon, F. Menanteau, K. Moodley, T. Morton, S. Naess, T. Namikawa, F. Nati, L. Newburgh, J. P. Nibarger, A. Nicola, M. D. Niemack, M. R. Nolta, J. Orlowski-Sherer, L. A. Page, C. G. Pappas, B. Partridge, P. Phakathi, H. Prince, R. Puddu, F. J. Qu, J. Rivera, N. Robertson, F. Rojas, M. Salatino, E. Schaan, A. Schillaci, B. L. Schmitt, N. Sehgal, B. D. Sherwin, C. Sierra, J. Sievers, C. Sifon, P. Sikhosana, S. Simon, D. N. Spergel, S. T. Staggs, J. Stevens, E. Storer, D. D. Sunder, E. R. Switzer, B. Thorne, R. Thornton, H. Trac, J. Treu, C. Tucker, L. R. Vale, A. Van Engelen, J. Van Lanen, E. M. Vavagiakis, K. Wagoner, Y. Wang, J. T. Ward, E. J. Wollack, Z. Xu, F. Zago, and N. Zhu, "The Atacama Cosmology Telescope: A Measurement of the Cosmic Microwave Background Power Spectra at 98 and 150 GHz," *arXiv e-prints*, p. arXiv:2007.07289, Jul. 2020.

[16] S. Adachi, M. A. O. A. Faúndez, K. Arnold, C. Baccigalupi, D. Barron, D. Beck, F. Bianchini, S. Chapman, K. Cheung, Y. Chinone, K. Crowley, M. Dobbs, H. E. Bouhargani, T. Elleflot, J. Errard, G. Fabbian, C. Feng, T. Fujino, N. Galitzki, N. Goeckner-Wald, J. Groh, G. Hall, M. Hasegawa, M. Hazumi, H. Hirose, A. H. Jaffe, O. Jeong, D. Kaneko, N. Katayama, B. Keating, S. Kikuchi, T. Kisner, A. Kusaka, A. T. Lee, D. Leon, E. Linder, L. N. Lowry, F. Matsuda, T. Matsumura, Y. Minami, M. Navaroli, H. Nishino, A. T. P. Pham, D. Poletti, C. L. Reichardt, Y. Segawa, P. Siritanasak, O. Tajima, S. Takakura, S. Takatori, D. Tanabe, G. P. Teply, C. Tsai, C. Vergès, B. Westbrook, and Y. Z. and, "A Measurement of the CMB E-mode Angular Power Spectrum at Subdegree Scales from 670 Square Degrees of POLARBEAR Data," *The Astrophysical Journal*, vol. 904, no. 1, p. 65, nov 2020. [Online]. Available: https://doi.org/10.3847%2F1538-4357%2Fabbacd

[17] P. A. R. Ade, M. Aguilar, Y. Akiba, K. Arnold, C. Baccigalupi, D. Barron, D. Beck, F. Bianchini, D. Boettger, J. Borrill, S. Chapman, Y. Chinone, K. Crowley, A. Cukierman, R. Dünner, M. Dobbs, A. Ducout, T. Elleflot, J. Errard, G. Fabbian, S. M. Feeney, C. Feng, T. Fujino, N. Galitzki, A. Gilbert, N. Goeckner-Wald, J. C. Groh, G. Hall, N. Halverson, T. Hamada, M. Hasegawa, M. Hazumi, C. A. Hill, L. Howe, Y. Inoue, G. Jaehnig, A. H. Jaffe, O. Jeong, D. Kaneko, N. Katayama, B. Keating, R. Keskitalo, T. Kisner, N. Krachmalnicoff, A. Kusaka, M. L. Jeune, A. T. Lee, E. M. Leitch, D. Leon, E. Linder, L. Lowry, F. Matsuda, T. Matsumura, Y. Minami, J. Montgomery, M. Navaroli, H. Nishino, H. Paar, J. Peloton, A. T. P. Pham, D. Poletti, G. Puglisi, C. L. Reichardt, P. L. Richards, C. Ross, Y. Segawa, B. D. Sherwin, M. Silva-Feaver, P. Siritanasak, N. Stebor, R. Stompor, A. Suzuki, O. Tajima, S. Takakura, S. Takatori, D. Tanabe, G. P. Teply, T. Tomaru, C. Tucker, N. Whitehorn, and A. Zahn, "A Measurement of the Cosmic Microwave Background B-mode Polarization Power Spectrum at Subdegree Scales from Two Years of polarbear Data," *The Astrophysical Journal*, vol. 848, no. 2, p. 121, Oct 2017. [Online]. Available: https://doi.org/10.3847%2F1538-4357%2Faa8e9f

[18] N. Goeckner-Wald, "A Measurement of the Degree Scale B-mode CMB Angular Power Spectrum from the Polarbear Experiment," Ph.D. dissertation, University of California, Berkeley, 2019.

[19] K. M. Smith, "Pseudo-C_ℓ estimators which do not mix E and B modes," *Phys. Rev. D*, vol. 74, p. 083002, Oct 2006. [Online]. Available: https://link.aps.org/doi/10.1103/PhysRevD.74.083002

[20] J. Peloton, "Data analysis and scientific exploitation of the CMB B-modes experiment, POLARBEAR," Theses, Universite Paris Diderot-Paris VII ; Laboratoire AstroParticule & Cosmologie , Sep. 2015. [Online]. Available: https://tel.archives-ouvertes.fr/tel-01257383

[21] D. Baumann. Cosmology. Part III Mathematical Tripos. [Online]. Available: http://theory.uchicago.edu/~liantaow/my-teaching/dark-matter-472/lectures.pdf

[22] D. Baumann, "TASI Lectures on Inflation," *arXiv e-prints*, p. arXiv:0907.5424, Jul. 2009.

[23] P. A. R. Ade, Y. Akiba, A. E. Anthony, K. Arnold, M. Atlas, D. Barron, D. Boettger, J. Borrill, C. Borys, S. Chapman, Y. Chinone, M. Dobbs, T. Elleflot, J. Errard, G. Fabbian, C. Feng, D. Flanigan, A. Gilbert, W. Grainger, N. W. Halverson, M. Hasegawa, K. Hattori, M. Hazumi, W. L. Holzapfel, Y. Hori, J. Howard, P. Hyland, Y. Inoue, G. C. Jaehnig, A. Jaffe, B. Keating, Z. Kermish, R. Keskitalo, T. Kisner, M. Le Jeune, A. T. Lee, E. M. Leitch, E. Linder, M. Lungu, F. Matsuda, T. Matsumura, X. Meng, N. J. Miller, H. Morii, S. Moyerman, M. J. Myers, M. Navaroli, H. Nishino, H. Paar, J. Peloton, D. Poletti, E. Quealy, G. Rebeiz, C. L. Reichardt, P. L. Richards, C. Ross, K. Rotermund, I. Schanning, D. E. Schenck, B. D. Sherwin, A. Shimizu, C. Shimmin, M. Shimon, P. Siritanasak, G. Smecher, H. Spieler, N. Stebor, B. Steinbach, R. Stompor, A. Suzuki, S. Takakura, A. Tikhomirov, T. Tomaru, B. Wilson, A. Yadav, and O. Zahn, "Evidence for Gravitational Lensing of the Cosmic Microwave Background Polarization from Cross-Correlation with the Cosmic Infrared Background," *Phys. Rev. Lett.*, vol. 112, p. 131302, Apr 2014. [Online]. Available: https://link.aps.org/doi/10.1103/PhysRevLett.112.131302

[24] A. Einstein, "Die Feldgleichungen der Gravitation," *Sitzungsberichte der Königlich Preußischen Akademie der Wissenschaften (Berlin)*, pp. 844–847, 1915.

[25] E. Hubble, "A relation between distance and radial velocity among extra-galactic nebulae," *Proceedings of the National Academy of Sciences*, vol. 15, no. 3, pp. 168–173, 1929. [Online]. Available: https://www.pnas.org/content/15/3/168

[26] G. Gamow, "The Origin of Elements and the Separation of Galaxies," *Phys. Rev.*, vol. 74, pp. 505–506, Aug 1948. [Online]. Available: https://link.aps.org/doi/10.1103/PhysRev.74.505.2

[27] Gamow, G., "The Evolution of the Universe," *Nature*, vol. 162, no. 4122, pp. 680–682, 1948. [Online]. Available: https://doi.org/10.1038/162680a0

[28] R. A. Alpher, "A Neutron-Capture Theory of the Formation and Relative Abundance of the Elements," *Phys. Rev.*, vol. 74, pp. 1577–1589, Dec 1948. [Online]. Available: https://link.aps.org/doi/10.1103/PhysRev.74.1577

[29] R. A. Alpher and R. Herman, "Evolution of the Universe," *Nature*, vol. 162, no. 4124, pp. 774–775, 1948. [Online]. Available: https://doi.org/10.1038/162774b0

[30] A. A. Penzias, "The Origin of the Elements," *Science*, vol. 205, no. 4406, pp. 549–554, 1979. [Online]. Available: https://science.sciencemag.org/content/205/4406/549

[31] A. G. Doroshkevich and I. D. Novikov, "Mean density of radiation in the Metagalaxy and certain problems in relativistic cosmology," *Soviet Physics Doklady*, vol. 9, p. 111, Aug 1964.

[32] A. A. Penzias and R. W. Wilson, "A Measurement of excess antenna temperature at 4080 Mc/s," *Astrophys. J.*, vol. 142, pp. 419–421, 1965.

[33] R. Dicke, P. Peebles, P. Roll, and D. Wilkinson, "Cosmic Black-Body Radiation," *Astrophys. J.*, vol. 142, pp. 414–419, 1965.

[34] R. B. Partridge and D. T. Wilkinson, "Isotropy and Homogeneity of the Universe from Measurements of the Cosmic Microwave Background," *Phys. Rev. Lett.*, vol. 18, pp. 557–559, Apr 1967. [Online]. Available: https://link.aps.org/doi/10.1103/PhysRevLett.18.557

[35] J. C. Mather *et al.*, "Measurement of the Cosmic Microwave Background spectrum by the COBE FIRAS instrument," *Astrophys. J.*, vol. 420, pp. 439–444, 1994.

[36] D. J. Fixsen, E. S. Cheng, J. M. Gales, J. C. Mather, R. A. Shafer, and E. L. Wright, "The Cosmic Microwave Background Spectrum from the Full COBE FIRAS data set," *The Astrophysical Journal*, vol. 473, no. 2, pp. 576–587, Dec 1996. [Online]. Available: https://doi.org/10.1086%2F178173

[37] G. F. Smoot *et al.*, "Structure in the COBE differential microwave radiometer first year maps," *Astrophys. J. Lett.*, vol. 396, pp. L1–L5, 1992.

[38] E. Torbet, M. J. Devlin, W. B. Dorwart, T. Herbig, A. D. Miller, M. R. Nolta, L. Page, J. Puchalla, and H. T. Tran, "A Measurement of the Angular Power Spectrum of the Microwave Background Made from the High Chilean Andes," *The Astrophysical Journal*, vol. 521, no. 2, pp. L79–L82, Aug 1999. [Online]. Available: https://doi.org/10.1086%2F312197

[39] P. de Bernardis, P. A. R. Ade, J. J. Bock, J. R. Bond, J. Borrill, A. Boscaleri, K. Coble, B. P. Crill, G. De Gasperis, G. De Troia, P. C. Farese, P. G. Ferreira, K. Ganga, M. Giacometti, E. Hivon, V. V. Hristov, A. Iacoangeli, A. H. Jaffe, A. E. Lange, L. Martinis, S. Masi, P. Mason, P. D. Mauskopf, A. Melchiorri, L. Miglio, T. Montroy, C. B. Netterfield, E. Pascale, F. Piacentini, D. Pogosyan, F. Pongetti, S. Prunet, S. Rao, G. Romeo, J. E. Ruhl, F. Scaramuzzi, D. Sforna, and N. Vittorio, "First results from the BOOMERanG experiment," *AIP Conference Proceedings*, vol. 555, no. 1, pp. 85–94, 2001. [Online]. Available: https://aip.scitation.org/doi/abs/10.1063/1.1363510

[40] S. Hanany, P. Ade, A. Balbi, J. Bock, J. Borrill, A. Boscaleri, P. de Bernardis, P. G. Ferreira, V. V. Hristov, A. H. Jaffe, A. E. Lange, A. T. Lee, P. D. Mauskopf, C. B. Netterfield, S. Oh, E. Pascale, B. Rabii, P. L. Richards, G. F. Smoot, R. Stompor, C. D. Winant, and J. H. P. Wu, "MAXIMA-1: A Measurement of the Cosmic Microwave Background Anisotropy on Angular Scales of 10[arcmin] to 5°," *The Astrophysical Journal*, vol. 545, no. 1, pp. L5–L9, Dec 2000. [Online]. Available: https://doi.org/10.1086%2F317322

[41] J. Bond *et al.*, "CMB analysis of Boomerang & Maxima & the cosmic parameters $\{\Omega_{tot}$, $\Omega_b h^2$, $\Omega_{cdm} h^2$, Ω_Λ, $n_s\}$," in *IAU Symposium 201: New Cosmological Data and the Value of the Fundamental Parameters*, Nov 2000.

[42] E. Komatsu, K. M. Smith, J. Dunkley, C. L. Bennett, B. Gold, G. Hinshaw, N. Jarosik, D. Larson, M. R. Nolta, L. Page, D. N. Spergel, M. Halpern, R. S. Hill, A. Kogut, M. Limon, S. S. Meyer, N. Odegard, G. S. Tucker, J. L. Weiland, E. Wollack, and E. L. Wright, "Seven-Year Wilkinson Microwave Anisotropy Probe (WMAP) Observations: Cosmological Interpretation," *The Astrophysical Journal Supplement Series*, vol. 192, no. 2, p. 18, Jan 2011. [Online]. Available: https://doi.org/10.1088%2F0067-0049%2F192%2F2%2F18

[43] A. G. Riess, A. V. Filippenko, P. Challis, A. Clocchiatti, A. Diercks, P. M. Garnavich, R. L. Gilliland, C. J. Hogan, S. Jha, R. P. Kirshner, B. Leibundgut, M. M. Phillips, D. Reiss, B. P. Schmidt, R. A. Schommer, R. C. Smith, J. Spyromilio, C. Stubbs, N. B. Suntzeff, and J. Tonry, "Observational Evidence from Supernovae for an Accelerating Universe and a Cosmological Constant," *The Astronomical Journal*, vol. 116, no. 3, pp. 1009–1038, Sep 1998. [Online]. Available: https://doi.org/10.1086%2F300499

[44] A. H. Guth, "Inflationary universe: A possible solution to the horizon and flatness problems," *Phys. Rev. D*, vol. 23, pp. 347–356, Jan 1981. [Online]. Available: https://link.aps.org/doi/10.1103/PhysRevD.23.347

[45] K. Sato, "First-order phase transition of a vacuum and the expansion of the Universe," *Monthly Notices of the Royal Astronomical Society*, vol. 195, no. 3, pp. 467–479, Jul 1981. [Online]. Available: https://doi.org/10.1093/mnras/195.3.467

[46] A. Linde, "A new inflationary universe scenario: A possible solution of the horizon, flatness, homogeneity, isotropy and primordial monopole problems," *Physics Letters B*, vol. 108, no. 6, pp. 389–393, Feb 1982. [Online]. Available: https://doi.org/10.1016%2F0370-2693%2882%2991219-9

[47] A. Starobinsky, "Dynamics of phase transition in the new inflationary universe scenario and generation of perturbations," *Physics Letters B*, vol. 117, no. 3, pp. 175 – 178, 1982. [Online]. Available: http://www.sciencedirect.com/science/article/pii/037026938290541X

[48] A. Albrecht and P. J. Steinhardt, "Cosmology for grand unified theories with radiatively induced symmetry breaking," *Phys. Rev. Lett.*, vol. 48, pp. 1220–1223, Apr 1982. [Online]. Available: https://link.aps.org/doi/10.1103/PhysRevLett.48.1220

[49] A. Riess, S. Casertano, W. Yuan, L. Macri, and D. Scolnic, "Large Magellanic Cloud Cepheid Standards Provide a 1% Foundation for the Determination of the Hubble Constant and Stronger Evidence for Physics beyond ΛCDM," *The Astrophysical Journal*, vol. 876, p. 85, 05 2019.

[50] Millon, M., Galan, A., Courbin, F., Treu, T., Suyu, S. H., Ding, X., Birrer, S., Chen, G. C.-F., Shajib, A. J., Sluse, D., Wong, K. C., Agnello, A., Auger, M. W., Buckley-Geer, E. J., Chan, J. H. H., Collett, T., Fassnacht, C. D., Hilbert, S., Koopmans, L. V. E., Motta, V., Mukherjee, S., Rusu, C. E., Sonnenfeld, A.,

Spiniello, C., and Van de Vyvere, L., "TDCOSMO - I. An exploration of systematic uncertainties in the inference of H0 from time-delay cosmography," *A&A*, vol. 639, p. A101, 2020. [Online]. Available: https://doi.org/10.1051/0004-6361/201937351

[51] S. Pandey, M. Raveri, and B. Jain, "Model independent comparison of supernova and strong lensing cosmography: Implications for the hubble constant tension," *Phys. Rev. D*, vol. 102, p. 023505, Jul 2020. [Online]. Available: https://link.aps.org/doi/10.1103/PhysRevD.102.023505

[52] G. E. Addison, D. J. Watts, C. L. Bennett, M. Halpern, G. Hinshaw, and J. L. Weiland, "Elucidating ΛCDM: Impact of Baryon Acoustic Oscillation Measurements on the Hubble Constant Discrepancy," *The Astrophysical Journal*, vol. 853, no. 2, p. 119, jan 2018. [Online]. Available: https://doi.org/10.3847/1538-4357/aaa1ed

[53] A. Coc, E. Vangioni-Flam, P. Descouvemont, A. Adahchour, and C. Angulo, "Updated Big Bang Nucleosynthesis Compared with Wilkinson Microwave Anisotropy Probe Observations and the Abundance of Light Elements," *The Astrophysical Journal*, vol. 600, no. 2, pp. 544–552, Jan 2004. [Online]. Available: https://doi.org/10.1086%2F380121

[54] L. Sbordone *et al.*, "The metal-poor end of the Spite plateau. 1: Stellar parameters, metallicities and lithium abundances," *Astron. Astrophys.*, vol. 522, p. A26, 2010.

[55] B. Ryden, *Introduction to cosmology*, Second ed. Cambridge University Press, Nov 2016.

[56] A. Liddle, *An Introduction to Modern Cosmology*, Second ed. Wiley-VCH, May 2003.

[57] V. Mukhanov, *Physical Foundations of Cosmology*. Cambridge University Press, 2005.

[58] S. Weinberg, *Cosmology*. Oxford University Press, Sep 2008.

[59] G. Fuller, "Lectures."

[60] C. W. Misner, K. Thorne, and J. Wheeler, *Gravitation*, 1973.

[61] D. H. Lyth and A. R. Liddle, *The Primordial Density Perturbation: Cosmology, Inflation and the Origin of Structure*. Cambridge University Press, 2009.

[62] Z. Xu, M. K. Brewer, P. F. Rojas, Y. Li, K. Osumi, B. Pradenas, A. Ali, J. W. Appel, C. L. Bennett, R. Bustos, M. Chan, D. T. Chuss, J. Cleary, J. D. Couto, S. Dahal, R. Datta, K. L. Denis, R. Dünner, J. R. Eimer, T. Essinger-Hileman, D. Gothe, K. Harrington, J. Iuliano, J. Karakla, T. A. Marriage, N. J. Miller, C. Núñez, I. L. Padilla, L. Parker, M. A. Petroff, R. Reeves, K. Rostem, D. A. N. Valle, D. J. Watts, J. L. Weiland, and E. J. W. and, "Two-year Cosmology Large Angular Scale Surveyor (CLASS) Observations: 40 GHz Telescope Pointing, Beam Profile, Window Function, and Polarization Performance," *The Astrophysical Journal*, vol. 891, no. 2, p. 134, Mar 2020. [Online]. Available: https://doi.org/10.3847%2F1538-4357%2Fab76c2

[63] B. P. Crill, P. A. R. Ade, E. S. Battistelli, S. Benton, R. Bihary, J. J. Bock, J. R. Bond, J. Brevik, S. Bryan, C. R. Contaldi, O. Doré, M. Farhang, L. Fissel, S. R. Golwala, M. Halpern, G. Hilton, W. Holmes, V. V. Hristov, K. Irwin, W. C. Jones, C. L. Kuo, A. E. Lange, C. Lawrie, C. J. MacTavish, T. G. Martin, P. Mason, T. E. Montroy, C. B. Netterfield, E. Pascale, D. Riley, J. E. Ruhl, M. C. Runyan, A. Trangsrud, C. Tucker, A. Turner, M. Viero, and D. Wiebe, "SPIDER: a balloon-borne large-scale CMB polarimeter," in *Space Telescopes and Instrumentation 2008: Optical, Infrared, and Millimeter*, J. M. O. Jr., M. W. M. de Graauw, and H. A. MacEwen, Eds., vol. 7010, International Society for Optics and Photonics. SPIE, 2008, pp. 800 – 811. [Online]. Available: https://doi.org/10.1117/12.787446

[64] J. A. Rubiño-Martín, R. Rebolo, M. Aguiar, R. Génova-Santos, F. Gómez-Reñasco, J. M. Herreros, R. J. Hoyland, C. López-Caraballo, A. E. P. Santos, V. S. de la Rosa, A. Vega-Moreno, T. Viera-Curbelo, E. Martínez-Gonzalez, R. B. Barreiro, F. J. Casas, J. M. Diego, R. Fernández-Cobos, D. Herranz, M. López-Caniego, D. Ortiz, P. Vielva, E. Artal, B. Aja, J. Cagigas, J. L. Cano, L. de la Fuente, A. Mediavilla, J. V. Terán, E. Villa, L. Piccirillo, R. Battye, E. Blackhurst, M. Brown, R. D. Davies, R. J. Davis, C. Dickinson, S. Harper, B. Maffei, M. McCulloch, S. Melhuish, G. Pisano, R. A. Watson, M. Hobson, K. Grainge, A. Lasenby, R. Saunders, and P. Scott, "The QUIJOTE-CMB experiment: studying the polarisation of the galactic and cosmological microwave emissions," in *Ground-based and Airborne Telescopes IV*, L. M. Stepp, R. Gilmozzi, and H. J. Hall, Eds., vol. 8444, International Society for Optics and Photonics. SPIE, 2012, pp. 987 – 997. [Online]. Available: https://doi.org/10.1117/12.926581

[65] P. Ade, J. Aguirre, Z. Ahmed, S. Aiola, A. Ali, D. Alonso, M. A. Alvarez, K. Arnold, P. Ashton, J. Austermann, H. Awan, C. Baccigalupi, T. Baildon, D. Barron, N. Battaglia, R. Battye, E. Baxter, A. Bazarko, J. A. Beall, R. Bean, D. Beck, S. Beckman, B. Beringue, F. Bianchini, S. Boada, D. Boettger, J. R. Bond, J. Borrill, M. L. Brown, S. M. Bruno, S. Bryan, E. Calabrese, V. Calafut, P. Calisse, J. Carron, A. Challinor, G. Chesmore, Y. Chinone, J. Chluba, H.-M. S. Cho, S. Choi, G. Coppi, N. F. Cothard, K. Coughlin, D. Crichton, K. D. Crowley, K. T. Crowley, A. Cukierman, J. M. D'Ewart, R. Dünner, T. de Haan, M. Devlin, S. Dicker, J. Didier, M. Dobbs, B. Dober, C. J. Duell, S. Duff, A. Duivenvoorden, J. Dunkley, J. Dusatko, J. Errard, G. Fabbian, S. Feeney, S. Ferraro, P. Fluxà, K. Freese, J. C. Frisch, A. Frolov, G. Fuller, B. Fuzia, N. Galitzki, P. A. Gallardo, J. T. G. Ghersi, J. Gao, E. Gawiser, M. Gerbino, V. Gluscevic, N. Goeckner-Wald, J. Golec, S. Gordon, M. Gralla, D. Green, A. Grigorian, J. Groh, C. Groppi, Y. Guan, J. E. Gudmundsson, D. Han, P. Hargrave, M. Hasegawa, M. Hasselfield, M. Hattori, V. Haynes, M. Hazumi, Y. He, E. Healy, S. W. Henderson, C. Hervias-Caimapo, C. A. Hill, J. C. Hill, G. Hilton, M. Hilton, A. D. Hincks, G. Hinshaw, R. Hložek, S. Ho, S.-P. P. Ho, L. Howe, Z. Huang, J. Hubmayr, K. Huffenberger, J. P. Hughes, A. Ijjas, M. Ikape, K. Irwin, A. H. Jaffe, B. Jain, O. Jeong, D. Kaneko, E. D. Karpel, N. Katayama, B. Keating, S. S. Kernasovskiy, R. Keskitalo, T. Kisner, K. Kiuchi, J. Klein, K. Knowles, B. Koopman, A. Kosowsky, N. Krachmalnicoff, S. E. Kuenstner, C.-L. Kuo, A. Kusaka, J. Lashner, A. Lee, E. Lee, D. Leon, J. S.-Y. Leung, A. Lewis, Y. Li, Z. Li, M. Limon, E. Linder, C. Lopez-Caraballo, T. Louis, L. Lowry,

M. Lungu, M. Madhavacheril, D. Mak, F. Maldonado, H. Mani, B. Mates, F. Matsuda, L. Maurin, P. Mauskopf, A. May, N. McCallum, C. McKenney, J. McMahon, P. D. Meerburg, J. Meyers, A. Miller, M. Mirmelstein, K. Moodley, M. Munchmeyer, C. Munson, S. Naess, F. Nati, M. Navaroli, L. Newburgh, H. N. Nguyen, M. Niemack, H. Nishino, J. Orlowski-Scherer, L. Page, B. Partridge, J. Peloton, F. Perrotta, L. Piccirillo, G. Pisano, D. Poletti, R. Puddu, G. Puglisi, C. Raum, C. L. Reichardt, M. Remazeilles, Y. Rephaeli, D. Riechers, F. Rojas, A. Roy, S. Sadeh, Y. Sakurai, M. Salatino, M. S. Rao, E. Schaan, M. Schmittfull, N. Sehgal, J. Seibert, U. Seljak, B. Sherwin, M. Shimon, C. Sierra, J. Sievers, P. Sikhosana, M. Silva-Feaver, S. M. Simon, A. Sinclair, P. Siritanasak, K. Smith, S. R. Smith, D. Spergel, S. T. Staggs, G. Stein, J. R. Stevens, R. Stompor, A. Suzuki, O. Tajima, S. Takakura, G. Teply, D. B. Thomas, B. Thorne, R. Thornton, H. Trac, C. Tsai, C. Tucker, J. Ullom, S. Vagnozzi, A. van Engelen, J. V. Lanen, D. D. V. Winkle, E. M. Vavagiakis, C. Vergès, M. Vissers, K. Wagoner, S. Walker, J. Ward, B. Westbrook, N. Whitehorn, J. Williams, J. Williams, E. J. Wollack, Z. Xu, B. Yu, C. Yu, F. Zago, H. Zhang, and N. Z. and, "The Simons Observatory: science goals and forecasts," *Journal of Cosmology and Astroparticle Physics*, vol. 2019, no. 02, pp. 056–056, Feb 2019. [Online]. Available: https://doi.org/10.1088%2F1475-7516%2F2019%2F02%2F056

[66] H. Sugai, P. A. R. Ade, Y. Akiba, D. Alonso, K. Arnold, J. Aumont, J. Austermann, C. Baccigalupi, A. J. Banday, R. Banerji, R. B. Barreiro, S. Basak, J. Beall, S. Beckman, M. Bersanelli, J. Borrill, F. Boulanger, M. L. Brown, M. Bucher, A. Buzzelli, E. Calabrese, F. J. Casas, A. Challinor, V. Chan, Y. Chinone, J. F. Cliche, F. Columbro, A. Cukierman, D. Curtis, P. Danto, P. de Bernardis, T. de Haan, M. De Petris, C. Dickinson, M. Dobbs, T. Dotani, L. Duband, A. Ducout, S. Duff, A. Duivenvoorden, J. M. Duval, K. Ebisawa, T. Elleflot, H. Enokida, H. K. Eriksen, J. Errard, T. Essinger-Hileman, F. Finelli, R. Flauger, C. Franceschet, U. Fuskeland, K. Ganga, J. R. Gao, R. Génova-Santos, T. Ghigna, A. Gomez, M. L. Gradziel, J. Grain, F. Grupp, A. Gruppuso, J. E. Gudmundsson, N. W. Halverson, P. Hargrave, T. Hasebe, M. Hasegawa, M. Hattori, M. Hazumi, S. Henrot-Versille, D. Herranz, C. Hill, G. Hilton, Y. Hirota, E. Hivon, R. Hlozek, D. T. Hoang, J. Hubmayr, K. Ichiki, T. Iida, H. Imada, K. Ishimura, H. Ishino, G. C. Jaehnig, M. Jones, T. Kaga, S. Kashima, Y. Kataoka, N. Katayama, T. Kawasaki, R. Keskitalo, A. Kibayashi, T. Kikuchi, K. Kimura, T. Kisner, Y. Kobayashi, N. Kogiso, A. Kogut, K. Kohri, E. Komatsu, K. Komatsu, K. Konishi, N. Krachmalnicoff, C. L. Kuo, N. Kurinsky, A. Kushino, M. Kuwata-Gonokami, L. Lamagna, M. Lattanzi, A. T. Lee, E. Linder, B. Maffei, D. Maino, M. Maki, A. Mangilli, E. Martínez-González, S. Masi, R. Mathon, T. Matsumura, A. Mennella, M. Migliaccio, Y. Minami, K. Mistuda, D. Molinari, L. Montier, G. Morgante, B. Mot, Y. Murata, J. A. Murphy, M. Nagai, R. Nagata, S. Nakamura, T. Namikawa, P. Natoli, S. Nerval, T. Nishibori, H. Nishino, Y. Nomura, F. Noviello, C. O'Sullivan, H. Ochi, H. Ogawa, H. Ogawa, H. Ohsaki, I. Ohta, N. Okada, N. Okada, L. Pagano, A. Paiella, D. Paoletti, G. Patanchon, F. Piacentini, G. Pisano, G. Polenta, D. Poletti, T. Prouvé, G. Puglisi, D. Rambaud, C. Raum, S. Realini, M. Remazeilles, G. Roudil, J. A. Rubiño-Martín, M. Russell, H. Sakurai, Y. Sakurai, M. Sandri, G. Savini, D. Scott, Y. Sekimoto, B. D. Sherwin, K. Shinozaki, M. Shiraishi, P. Shirron, G. Signorelli, G. Smecher, P. Spizzi, S. L. Stever, R. Stompor, S. Sugiyama, A. Suzuki, J. Suzuki, E. Switzer, R. Takaku,

H. Takakura, S. Takakura, Y. Takeda, A. Taylor, E. Taylor, Y. Terao, K. L. Thompson, B. Thorne, M. Tomasi, H. Tomida, N. Trappe, M. Tristram, M. Tsuji, M. Tsujimoto, C. Tucker, J. Ullom, S. Uozumi, S. Utsunomiya, J. Van Lanen, G. Vermeulen, P. Vielva, F. Villa, M. Vissers, N. Vittorio, F. Voisin, I. Walker, N. Watanabe, I. Wehus, J. Weller, B. Westbrook, B. Winter, E. Wollack, R. Yamamoto, N. Y. Yamasaki, M. Yanagisawa, T. Yoshida, J. Yumoto, M. Zannoni, and A. Zonca, "Updated Design of the CMB Polarization Experiment Satellite LiteBIRD," *Journal of Low Temperature Physics*, vol. 199, no. 3, pp. 1107–1117, 2020. [Online]. Available: https://doi.org/10.1007/s10909-019-02329-w

[67] N. Gandilo, P. Ade, D. Benford, C. Bennett, D. Chuss, R. Datta, J. Dotson, T. Essinger-Hileman, D. Fixsen, M. Halpern, G. Hilton, G. Hinshaw, K. Irwin, C. Jhabvala, M. Kimball, A. Kogut, L. Lowe, J. McMahon, T. Miller, P. Mirel, S. H. Moseley, S. Pawlyk, S. Rodriguez, E. Sharp, P. Shirron, J. G. Staguhn, D. Sullivan, E. Switzer, P. Taraschi, C. Tucker, A. Walts, and E. Wollack, "The Primordial Inflation Polarization ExploreR (PIPER)," in *American Astronomical Society Meeting Abstracts #231*, ser. American Astronomical Society Meeting Abstracts, vol. 231, Jan. 2018, p. 314.05.

[68] A. A. Starobinsky, "A New Type of Isotropic Cosmological Models Without Singularity," *Adv. Ser. Astrophys. Cosmol.*, vol. 3, pp. 130–133, 1987.

[69] B. Pradenas Márquez, "Theoretical and observational characterization of primordial scales and symmetries," Master's thesis, Universidad de Chile, 2019.

[70] S. M. Céspedes Castillo, "Cosmic inflation in a landscape of heavy fields," Master's thesis, Universidad de Chile, 2013.

[71] B. P. Abbott, R. Abbott, T. D. Abbott, M. R. Abernathy, F. Acernese, K. Ackley, C. Adams, T. Adams, P. Addesso, R. X. Adhikari, V. B. Adya, C. Affeldt, M. Agathos, K. Agatsuma, N. Aggarwal, O. D. Aguiar, L. Aiello, A. Ain, P. Ajith, B. Allen, A. Allocca, P. A. Altin, S. B. Anderson, W. G. Anderson, K. Arai, M. A. Arain, M. C. Araya, C. C. Arceneaux, J. S. Areeda, N. Arnaud, K. G. Arun, S. Ascenzi, G. Ashton, M. Ast, S. M. Aston, P. Astone, P. Aufmuth, C. Aulbert, S. Babak, P. Bacon, M. K. M. Bader, P. T. Baker, F. Baldaccini, G. Ballardin, S. W. Ballmer, J. C. Barayoga, S. E. Barclay, B. C. Barish, D. Barker, F. Barone, B. Barr, L. Barsotti, M. Barsuglia, D. Barta, J. Bartlett, M. A. Barton, I. Bartos, R. Bassiri, A. Basti, J. C. Batch, C. Baune, V. Bavigadda, M. Bazzan, B. Behnke, M. Bejger, C. Belczynski, A. S. Bell, C. J. Bell, B. K. Berger, J. Bergman, G. Bergmann, C. P. L. Berry, D. Bersanetti, A. Bertolini, J. Betzwieser, S. Bhagwat, R. Bhandare, I. A. Bilenko, G. Billingsley, J. Birch, R. Birney, O. Birnholtz, S. Biscans, A. Bisht, M. Bitossi, C. Biwer, M. A. Bizouard, J. K. Blackburn, C. D. Blair, D. G. Blair, R. M. Blair, S. Bloemen, O. Bock, T. P. Bodiya, M. Boer, G. Bogaert, C. Bogan, A. Bohe, P. Bojtos, C. Bond, F. Bondu, R. Bonnand, B. A. Boom, R. Bork, V. Boschi, S. Bose, Y. Bouffanais, A. Bozzi, C. Bradaschia, P. R. Brady, V. B. Braginsky, M. Branchesi, J. E. Brau, T. Briant, A. Brillet, M. Brinkmann, V. Brisson, P. Brockill, A. F. Brooks, D. A. Brown, D. D. Brown, N. M. Brown, C. C. Buchanan, A. Buikema, T. Bulik, H. J. Bulten, A. Buonanno, D. Buskulic, C. Buy, R. L. Byer, M. Cabero, L. Cadonati, G. Cagnoli, C. Cahillane, J. C. Bustillo, T. Callister, E. Calloni, J. B. Camp, K. C.

Cannon, J. Cao, C. D. Capano, E. Capocasa, F. Carbognani, S. Caride, J. C. Diaz, C. Casentini, S. Caudill, M. Cavaglià, F. Cavalier, R. Cavalieri, G. Cella, C. B. Cepeda, L. C. Baiardi, G. Cerretani, E. Cesarini, R. Chakraborty, T. Chalermsongsak, S. J. Chamberlin, M. Chan, S. Chao, P. Charlton, E. Chassande-Mottin, H. Y. Chen, Y. Chen, C. Cheng, A. Chincarini, A. Chiummo, H. S. Cho, M. Cho, J. H. Chow, N. Christensen, Q. Chu, S. Chua, S. Chung, G. Ciani, F. Clara, J. A. Clark, F. Cleva, E. Coccia, P.-F. Cohadon, A. Colla, C. G. Collette, L. Cominsky, M. Constancio, A. Conte, L. Conti, D. Cook, T. R. Corbitt, N. Cornish, A. Corsi, S. Cortese, C. A. Costa, M. W. Coughlin, S. B. Coughlin, J.-P. Coulon, S. T. Countryman, P. Couvares, E. E. Cowan, D. M. Coward, M. J. Cowart, D. C. Coyne, R. Coyne, K. Craig, J. D. E. Creighton, T. D. Creighton, J. Cripe, S. G. Crowder, A. M. Cruise, A. Cumming, L. Cunningham, E. Cuoco, T. D. Canton, S. L. Danilishin, S. D'Antonio, K. Danzmann, N. S. Darman, C. F. Da Silva Costa, V. Dattilo, I. Dave, H. P. Daveloza, M. Davier, G. S. Davies, E. J. Daw, R. Day, S. De, D. DeBra, G. Debreczeni, J. Degallaix, M. De Laurentis, S. Deléglise, W. Del Pozzo, T. Denker, T. Dent, H. Dereli, V. Dergachev, R. T. DeRosa, R. De Rosa, R. DeSalvo, S. Dhurandhar, M. C. Díaz, L. Di Fiore, M. Di Giovanni, A. Di Lieto, S. Di Pace, I. Di Palma, A. Di Virgilio, G. Dojcinoski, V. Dolique, F. Donovan, K. L. Dooley, S. Doravari, R. Douglas, T. P. Downes, M. Drago, R. W. P. Drever, J. C. Driggers, Z. Du, M. Ducrot, S. E. Dwyer, T. B. Edo, M. C. Edwards, A. Effler, H.-B. Eggenstein, P. Ehrens, J. Eichholz, S. S. Eikenberry, W. Engels, R. C. Essick, T. Etzel, M. Evans, T. M. Evans, R. Everett, M. Factourovich, V. Fafone, H. Fair, S. Fairhurst, X. Fan, Q. Fang, S. Farinon, B. Farr, W. M. Farr, M. Favata, M. Fays, H. Fehrmann, M. M. Fejer, D. Feldbaum, I. Ferrante, E. C. Ferreira, F. Ferrini, F. Fidecaro, L. S. Finn, I. Fiori, D. Fiorucci, R. P. Fisher, R. Flaminio, M. Fletcher, H. Fong, J.-D. Fournier, S. Franco, S. Frasca, F. Frasconi, M. Frede, Z. Frei, A. Freise, R. Frey, V. Frey, T. T. Fricke, P. Fritschel, V. V. Frolov, P. Fulda, M. Fyffe, H. A. G. Gabbard, J. R. Gair, L. Gammaitoni, S. G. Gaonkar, F. Garufi, A. Gatto, G. Gaur, N. Gehrels, G. Gemme, B. Gendre, E. Genin, A. Gennai, J. George, L. Gergely, V. Germain, A. Ghosh, A. Ghosh, S. Ghosh, J. A. Giaime, K. D. Giardina, A. Giazotto, K. Gill, A. Glaefke, J. R. Gleason, E. Goetz, R. Goetz, L. Gondan, G. González, J. M. G. Castro, A. Gopakumar, N. A. Gordon, M. L. Gorodetsky, S. E. Gossan, M. Gosselin, R. Gouaty, C. Graef, P. B. Graff, M. Granata, A. Grant, S. Gras, C. Gray, G. Greco, A. C. Green, R. J. S. Greenhalgh, P. Groot, H. Grote, S. Grunewald, G. M. Guidi, X. Guo, A. Gupta, M. K. Gupta, K. E. Gushwa, E. K. Gustafson, R. Gustafson, J. J. Hacker, B. R. Hall, E. D. Hall, G. Hammond, M. Haney, M. M. Hanke, J. Hanks, C. Hanna, M. D. Hannam, J. Hanson, T. Hardwick, J. Harms, G. M. Harry, I. W. Harry, M. J. Hart, M. T. Hartman, C.-J. Haster, K. Haughian, J. Healy, J. Heefner, A. Heidmann, M. C. Heintze, G. Heinzel, H. Heitmann, P. Hello, G. Hemming, M. Hendry, I. S. Heng, J. Hennig, A. W. Heptonstall, M. Heurs, S. Hild, D. Hoak, K. A. Hodge, D. Hofman, S. E. Hollitt, K. Holt, D. E. Holz, P. Hopkins, D. J. Hosken, J. Hough, E. A. Houston, E. J. Howell, Y. M. Hu, S. Huang, E. A. Huerta, D. Huet, B. Hughey, S. Husa, S. H. Huttner, T. Huynh-Dinh, A. Idrisy, N. Indik, D. R. Ingram, R. Inta, H. N. Isa, J.-M. Isac, M. Isi, G. Islas, T. Isogai, B. R. Iyer, K. Izumi, M. B. Jacobson, T. Jacqmin, H. Jang, K. Jani, P. Jaranowski, S. Jawahar, F. Jiménez-Forteza, W. W. Johnson, N. K. Johnson-McDaniel, D. I. Jones, R. Jones, R. J. G. Jonker, L. Ju, K. Haris, C. V. Kalaghatgi, V. Kalogera, S. Kandhasamy, G. Kang, J. B. Kanner, S. Karki,

M. Kasprzack, E. Katsavounidis, W. Katzman, S. Kaufer, T. Kaur, K. Kawabe, F. Kawazoe, F. Kéfélian, M. S. Kehl, D. Keitel, D. B. Kelley, W. Kells, R. Kennedy, D. G. Keppel, J. S. Key, A. Khalaidovski, F. Y. Khalili, I. Khan, S. Khan, Z. Khan, E. A. Khazanov, N. Kijbunchoo, C. Kim, J. Kim, K. Kim, N.-G. Kim, N. Kim, Y.-M. Kim, E. J. King, P. J. King, D. L. Kinzel, J. S. Kissel, L. Kleybolte, S. Klimenko, S. M. Koehlenbeck, K. Kokeyama, S. Koley, V. Kondrashov, A. Kontos, S. Koranda, M. Korobko, W. Z. Korth, I. Kowalska, D. B. Kozak, V. Kringel, B. Krishnan, A. Królak, C. Krueger, G. Kuehn, P. Kumar, R. Kumar, L. Kuo, A. Kutynia, P. Kwee, B. D. Lackey, M. Landry, J. Lange, B. Lantz, P. D. Lasky, A. Lazzarini, C. Lazzaro, P. Leaci, S. Leavey, E. O. Lebigot, C. H. Lee, H. K. Lee, H. M. Lee, K. Lee, A. Lenon, M. Leonardi, J. R. Leong, N. Leroy, N. Letendre, Y. Levin, B. M. Levine, T. G. F. Li, A. Libson, T. B. Littenberg, N. A. Lockerbie, J. Logue, A. L. Lombardi, L. T. London, J. E. Lord, M. Lorenzini, V. Loriette, M. Lormand, G. Losurdo, J. D. Lough, C. O. Lousto, G. Lovelace, H. Lück, A. P. Lundgren, J. Luo, R. Lynch, Y. Ma, T. MacDonald, B. Machenschalk, M. MacInnis, D. M. Macleod, F. Magaña Sandoval, R. M. Magee, M. Mageswaran, E. Majorana, I. Maksimovic, V. Malvezzi, N. Man, I. Mandel, V. Mandic, V. Mangano, G. L. Mansell, M. Manske, M. Mantovani, F. Marchesoni, F. Marion, S. Márka, Z. Márka, A. S. Markosyan, E. Maros, F. Martelli, L. Martellini, I. W. Martin, R. M. Martin, D. V. Martynov, J. N. Marx, K. Mason, A. Masserot, T. J. Massinger, M. Masso-Reid, F. Matichard, L. Matone, N. Mavalvala, N. Mazumder, G. Mazzolo, R. McCarthy, D. E. McClelland, S. McCormick, S. C. McGuire, G. McIntyre, J. McIver, D. J. McManus, S. T. McWilliams, D. Meacher, G. D. Meadors, J. Meidam, A. Melatos, G. Mendell, D. Mendoza-Gandara, R. A. Mercer, E. Merilh, M. Merzougui, S. Meshkov, C. Messenger, C. Messick, P. M. Meyers, F. Mezzani, H. Miao, C. Michel, H. Middleton, E. E. Mikhailov, L. Milano, J. Miller, M. Millhouse, Y. Minenkov, J. Ming, S. Mirshekari, C. Mishra, S. Mitra, V. P. Mitrofanov, G. Mitselmakher, R. Mittleman, A. Moggi, M. Mohan, S. R. P. Mohapatra, M. Montani, B. C. Moore, C. J. Moore, D. Moraru, G. Moreno, S. R. Morriss, K. Mossavi, B. Mours, C. M. Mow-Lowry, C. L. Mueller, G. Mueller, A. W. Muir, A. Mukherjee, D. Mukherjee, S. Mukherjee, N. Mukund, A. Mullavey, J. Munch, D. J. Murphy, P. G. Murray, A. Mytidis, I. Nardecchia, L. Naticchioni, R. K. Nayak, V. Necula, K. Nedkova, G. Nelemans, M. Neri, A. Neunzert, G. Newton, T. T. Nguyen, A. B. Nielsen, S. Nissanke, A. Nitz, F. Nocera, D. Nolting, M. E. N. Normandin, L. K. Nuttall, J. Oberling, E. Ochsner, J. O'Dell, E. Oelker, G. H. Ogin, J. J. Oh, S. H. Oh, F. Ohme, M. Oliver, P. Oppermann, R. J. Oram, B. O'Reilly, R. O'Shaughnessy, C. D. Ott, D. J. Ottaway, R. S. Ottens, H. Overmier, B. J. Owen, A. Pai, S. A. Pai, J. R. Palamos, O. Palashov, C. Palomba, A. Pal-Singh, H. Pan, Y. Pan, C. Pankow, F. Pannarale, B. C. Pant, F. Paoletti, A. Paoli, M. A. Papa, H. R. Paris, W. Parker, D. Pascucci, A. Pasqualetti, R. Passaquieti, D. Passuello, B. Patricelli, Z. Patrick, B. L. Pearlstone, M. Pedraza, R. Pedurand, L. Pekowsky, A. Pele, S. Penn, A. Perreca, H. P. Pfeiffer, M. Phelps, O. Piccinni, M. Pichot, M. Pickenpack, F. Piergiovanni, V. Pierro, G. Pillant, L. Pinard, I. M. Pinto, M. Pitkin, J. H. Poeld, R. Poggiani, P. Popolizio, A. Post, J. Powell, J. Prasad, V. Predoi, S. S. Premachandra, T. Prestegard, L. R. Price, M. Prijatelj, M. Principe, S. Privitera, R. Prix, G. A. Prodi, L. Prokhorov, O. Puncken, M. Punturo, P. Puppo, M. Pürrer, H. Qi, J. Qin, V. Quetschke, E. A. Quintero, R. Quitzow-James, F. J. Raab, D. S. Rabeling, H. Radkins, P. Raffai, S. Raja, M. Rakhmanov, C. R.

Ramet, P. Rapagnani, V. Raymond, M. Razzano, V. Re, J. Read, C. M. Reed, T. Regimbau, L. Rei, S. Reid, D. H. Reitze, H. Rew, S. D. Reyes, F. Ricci, K. Riles, N. A. Robertson, R. Robie, F. Robinet, A. Rocchi, L. Rolland, J. G. Rollins, V. J. Roma, J. D. Romano, R. Romano, G. Romanov, J. H. Romie, D. Rosińska, S. Rowan, A. Rüdiger, P. Ruggi, K. Ryan, S. Sachdev, T. Sadecki, L. Sadeghian, L. Salconi, M. Saleem, F. Salemi, A. Samajdar, L. Sammut, L. M. Sampson, E. J. Sanchez, V. Sandberg, B. Sandeen, G. H. Sanders, J. R. Sanders, B. Sassolas, B. S. Sathyaprakash, P. R. Saulson, O. Sauter, R. L. Savage, A. Sawadsky, P. Schale, R. Schilling, J. Schmidt, P. Schmidt, R. Schnabel, R. M. S. Schofield, A. Schönbeck, E. Schreiber, D. Schuette, B. F. Schutz, J. Scott, S. M. Scott, D. Sellers, A. S. Sengupta, D. Sentenac, V. Sequino, A. Sergeev, G. Serna, Y. Setyawati, A. Sevigny, D. A. Shaddock, T. Shaffer, S. Shah, M. S. Shahriar, M. Shaltev, Z. Shao, B. Shapiro, P. Shawhan, A. Sheperd, D. H. Shoemaker, D. M. Shoemaker, K. Siellez, X. Siemens, D. Sigg, A. D. Silva, D. Simakov, A. Singer, L. P. Singer, A. Singh, R. Singh, A. Singhal, A. M. Sintes, B. J. J. Slagmolen, J. R. Smith, M. R. Smith, N. D. Smith, R. J. E. Smith, E. J. Son, B. Sorazu, F. Sorrentino, T. Souradeep, A. K. Srivastava, A. Staley, M. Steinke, J. Steinlechner, S. Steinlechner, D. Steinmeyer, B. C. Stephens, S. P. Stevenson, R. Stone, K. A. Strain, N. Straniero, G. Stratta, N. A. Strauss, S. Strigin, R. Sturani, A. L. Stuver, T. Z. Summerscales, L. Sun, P. J. Sutton, B. L. Swinkels, M. J. Szczepańczyk, M. Tacca, D. Talukder, D. B. Tanner, M. Tápai, S. P. Tarabrin, A. Taracchini, R. Taylor, T. Theeg, M. P. Thirugnanasambandam, E. G. Thomas, M. Thomas, P. Thomas, K. A. Thorne, K. S. Thorne, E. Thrane, S. Tiwari, V. Tiwari, K. V. Tokmakov, C. Tomlinson, M. Tonelli, C. V. Torres, C. I. Torrie, D. Töyrä, F. Travasso, G. Traylor, D. Trifirò, M. C. Tringali, L. Trozzo, M. Tse, M. Turconi, D. Tuyenbayev, D. Ugolini, C. S. Unnikrishnan, A. L. Urban, S. A. Usman, H. Vahlbruch, G. Vajente, G. Valdes, M. Vallisneri, N. van Bakel, M. van Beuzekom, J. F. J. van den Brand, C. Van Den Broeck, D. C. Vander-Hyde, L. van der Schaaf, J. V. van Heijningen, A. A. van Veggel, M. Vardaro, S. Vass, M. Vasúth, R. Vaulin, A. Vecchio, G. Vedovato, J. Veitch, P. J. Veitch, K. Venkateswara, D. Verkindt, F. Vetrano, A. Viceré, S. Vinciguerra, D. J. Vine, J.-Y. Vinet, S. Vitale, T. Vo, H. Vocca, C. Vorvick, D. Voss, W. D. Vousden, S. P. Vyatchanin, A. R. Wade, L. E. Wade, M. Wade, S. J. Waldman, M. Walker, L. Wallace, S. Walsh, G. Wang, H. Wang, M. Wang, X. Wang, Y. Wang, H. Ward, R. L. Ward, J. Warner, M. Was, B. Weaver, L.-W. Wei, M. Weinert, A. J. Weinstein, R. Weiss, T. Welborn, L. Wen, P. Weßels, T. Westphal, K. Wette, J. T. Whelan, S. E. Whitcomb, D. J. White, B. F. Whiting, K. Wiesner, C. Wilkinson, P. A. Willems, L. Williams, R. D. Williams, A. R. Williamson, J. L. Willis, B. Willke, M. H. Wimmer, L. Winkelmann, W. Winkler, C. C. Wipf, A. G. Wiseman, H. Wittel, G. Woan, J. Worden, J. L. Wright, G. Wu, J. Yablon, I. Yakushin, W. Yam, H. Yamamoto, C. C. Yancey, M. J. Yap, H. Yu, M. Yvert, A. Zadrożny, L. Zangrando, M. Zanolin, J.-P. Zendri, M. Zevin, F. Zhang, L. Zhang, M. Zhang, Y. Zhang, C. Zhao, M. Zhou, Z. Zhou, X. J. Zhu, M. E. Zucker, S. E. Zuraw, and J. Zweizig, "Observation of Gravitational Waves from a Binary Black Hole Merger," *Phys. Rev. Lett.*, vol. 116, p. 061102, Feb 2016. [Online]. Available: https://link.aps.org/doi/10.1103/PhysRevLett.116.061102

[72] M. Zaldarriaga, "Nature of the $E-B$ decomposition of CMB polarization," *Phys. Rev. D*, vol. 64, p. 103001, Oct 2001. [Online]. Available: https:

//link.aps.org/doi/10.1103/PhysRevD.64.103001

[73] J. R. Bond and G. Efstathiou, "The statistics of cosmic background radiation fluctuations," *Monthly Notices of the Royal Astronomical Society*, vol. 226, no. 3, pp. 655–687, June 1987. [Online]. Available: https://doi.org/10.1093/mnras/226.3.655

[74] S. Dodelson, "Coherent phase argument for inflation," *AIP Conference Proceedings*, vol. 689, no. 1, pp. 184–196, 2003. [Online]. Available: https://aip.scitation.org/doi/abs/10.1063/1.1627736

[75] M. Kamionkowski, A. Kosowsky, and A. Stebbins, "A Probe of Primordial Gravity Waves and Vorticity," *Phys. Rev. Lett.*, vol. 78, pp. 2058–2061, Mar 1997. [Online]. Available: https://link.aps.org/doi/10.1103/PhysRevLett.78.2058

[76] U. Seljak and M. Zaldarriaga, "Signature of Gravity Waves in the Polarization of the Microwave Background," *Phys. Rev. Lett.*, vol. 78, pp. 2054–2057, Mar 1997. [Online]. Available: https://link.aps.org/doi/10.1103/PhysRevLett.78.2054

[77] M. Zaldarriaga and U. Seljak, "Gravitational lensing effect on cosmic microwave background polarization," *Phys. Rev. D*, vol. 58, p. 023003, Jun 1998. [Online]. Available: https://link.aps.org/doi/10.1103/PhysRevD.58.023003

[78] W. Hu and T. Okamoto, "Mass Reconstruction with Cosmic Microwave Background Polarization," *The Astrophysical Journal*, vol. 574, no. 2, pp. 566–574, Aug 2002. [Online]. Available: https://doi.org/10.1086%2F341110

[79] M. Zaldarriaga and U. Seljak, "All-sky analysis of polarization in the microwave background," *Phys. Rev. D*, vol. 55, pp. 1830–1840, Feb 1997. [Online]. Available: https://link.aps.org/doi/10.1103/PhysRevD.55.1830

[80] M. Kamionkowski and E. D. Kovetz, "The Quest for B Modes from Inflationary Gravitational Waves," *Annual Review of Astronomy and Astrophysics*, vol. 54, no. 1, pp. 227–269, 2016. [Online]. Available: https://doi.org/10.1146/annurev-astro-081915-023433

[81] W. Hu, "Weak lensing of the CMB: A harmonic approach," *Phys. Rev. D*, vol. 62, p. 043007, Jul 2000. [Online]. Available: https://link.aps.org/doi/10.1103/PhysRevD.62.043007

[82] A. Challinor and A. Lewis, "Lensed CMB power spectra from all-sky correlation functions," *Phys. Rev. D*, vol. 71, p. 103010, May 2005. [Online]. Available: https://link.aps.org/doi/10.1103/PhysRevD.71.103010

[83] K. Abazajian, K. Arnold, J. Austermann, B. Benson, C. Bischoff, J. Bock, J. Bond, J. Borrill, E. Calabrese, J. Carlstrom, C. Carvalho, C. Chang, H. Chiang, S. Church, A. Cooray, T. Crawford, K. Dawson, S. Das, M. Devlin, M. Dobbs, S. Dodelson, O. Doré, J. Dunkley, J. Errard, A. Fraisse, J. Gallicchio, N. Halverson, S. Hanany, S. Hildebrandt, A. Hincks, R. Hlozek, G. Holder, W. Holzapfel, K. Honscheid, W. Hu, J. Hubmayr, K. Irwin, W. Jones, M. Kamionkowski, B. Keating, R. Keisler, L. Knox, E. Komatsu, J. Kovac, C.-L. Kuo, C. Lawrence, A. Lee, E. Leitch, E. Linder, P. Lubin, J. McMahon, A. Miller, L. Newburgh, M. Niemack, H. Nguyen, H. Nguyen, L. Page,

C. Pryke, C. Reichardt, J. Ruhl, N. Sehgal, U. Seljak, J. Sievers, E. Silverstein, A. Slosar, K. Smith, D. Spergel, S. Staggs, A. Stark, R. Stompor, A. Vieregg, G. Wang, S. Watson, E. Wollack, W. Wu, K. Yoon, and O. Zahn, "Neutrino physics from the cosmic microwave background and large scale structure," *Astroparticle Physics*, vol. 63, pp. 66 – 80, 2015, dark Energy and CMB. [Online]. Available: http://www.sciencedirect.com/science/article/pii/S092765051400084X

[84] J. M. Kovac, E. M. Leitch, C. Pryke, J. E. Carlstrom, N. W. Halverson, and W. L. Holzapfel, "Detection of polarization in the cosmic microwave background using DASI," *Nature*, vol. 420, no. 6917, pp. 772–787, 2002. [Online]. Available: https://doi.org/10.1038/nature01269

[85] D. Hanson, S. Hoover, A. Crites, P. A. R. Ade, K. A. Aird, J. E. Austermann, J. A. Beall, A. N. Bender, B. A. Benson, L. E. Bleem, J. J. Bock, J. E. Carlstrom, C. L. Chang, H. C. Chiang, H.-M. Cho, A. Conley, T. M. Crawford, T. de Haan, M. A. Dobbs, W. Everett, J. Gallicchio, J. Gao, E. M. George, N. W. Halverson, N. Harrington, J. W. Henning, G. C. Hilton, G. P. Holder, W. L. Holzapfel, J. D. Hrubes, N. Huang, J. Hubmayr, K. D. Irwin, R. Keisler, L. Knox, A. T. Lee, E. Leitch, D. Li, C. Liang, D. Luong-Van, G. Marsden, J. J. McMahon, J. Mehl, S. S. Meyer, L. Mocanu, T. E. Montroy, T. Natoli, J. P. Nibarger, V. Novosad, S. Padin, C. Pryke, C. L. Reichardt, J. E. Ruhl, B. R. Saliwanchik, J. T. Sayre, K. K. Schaffer, B. Schulz, G. Smecher, A. A. Stark, K. T. Story, C. Tucker, K. Vanderlinde, J. D. Vieira, M. P. Viero, G. Wang, V. Yefremenko, O. Zahn, and M. Zemcov, "Detection of B-Mode Polarization in the Cosmic Microwave Background with Data from the South Pole Telescope," *Phys. Rev. Lett.*, vol. 111, p. 141301, Sep 2013. [Online]. Available: https://link.aps.org/doi/10.1103/PhysRevLett.111.141301

[86] P. A. R. Ade, R. W. Aikin, D. Barkats, S. J. Benton, C. A. Bischoff, J. J. Bock, J. A. Brevik, I. Buder, E. Bullock, C. D. Dowell, L. Duband, J. P. Filippini, S. Fliescher, S. R. Golwala, M. Halpern, M. Hasselfield, S. R. Hildebrandt, G. C. Hilton, V. V. Hristov, K. D. Irwin, K. S. Karkare, J. P. Kaufman, B. G. Keating, S. A. Kernasovskiy, J. M. Kovac, C. L. Kuo, E. M. Leitch, M. Lueker, P. Mason, C. B. Netterfield, H. T. Nguyen, R. O'Brient, R. W. Ogburn, A. Orlando, C. Pryke, C. D. Reintsema, S. Richter, R. Schwarz, C. D. Sheehy, Z. K. Staniszewski, R. V. Sudiwala, G. P. Teply, J. E. Tolan, A. D. Turner, A. G. Vieregg, C. L. Wong, and K. W. Yoon, "Detection of B-Mode Polarization at Degree Angular Scales by BICEP2," *Phys. Rev. Lett.*, vol. 112, p. 241101, Jun 2014. [Online]. Available: https://link.aps.org/doi/10.1103/PhysRevLett.112.241101

[87] P. A. R. Ade, Z. Ahmed, R. W. Aikin, K. D. Alexander, D. Barkats, S. J. Benton, C. A. Bischoff, J. J. Bock, J. A. Brevik, I. Buder, E. Bullock, V. Buza, J. Connors, B. P. Crill, C. D. Dowell, C. Dvorkin, L. Duband, J. P. Filippini, S. Fliescher, S. R. Golwala, M. Halpern, S. Harrison, M. Hasselfield, S. R. Hildebrandt, G. C. Hilton, V. V. Hristov, H. Hui, K. D. Irwin, K. S. Karkare, J. P. Kaufman, B. G. Keating, S. Kefeli, S. A. Kernasovskiy, J. M. Kovac, C. L. Kuo, E. M. Leitch, M. Lueker, P. Mason, K. G. Megerian, C. B. Netterfield, H. T. Nguyen, R. O'Brient, R. W. O. IV, A. Orlando, C. Pryke, C. D. Reintsema, S. Richter, R. Schwarz, C. D. Sheehy, Z. K. Staniszewski, R. V. Sudiwala, G. P. Teply, K. L. Thompson, J. E. Tolan, A. D. Turner,

A. G. Vieregg, A. C. Weber, J. Willmert, C. L. Wong, and K. W. Y. and, "BICEP2 / Keck Array V: Measurements of B-mode Polarization at Degree Angular Scales and 150 GHz by the Keck Array," *The Astrophysical Journal*, vol. 811, no. 2, p. 126, Sep 2015. [Online]. Available: https://doi.org/10.1088%2F0004-637x%2F811%2F2%2F126

[88] P. A. R. Ade, N. Aghanim, Z. Ahmed, R. W. Aikin, K. D. Alexander, M. Arnaud, J. Aumont, C. Baccigalupi, A. J. Banday, D. Barkats, R. B. Barreiro, J. G. Bartlett, N. Bartolo, E. Battaner, K. Benabed, A. Benoît, A. Benoit-Lévy, S. J. Benton, J.-P. Bernard, M. Bersanelli, P. Bielewicz, C. A. Bischoff, J. J. Bock, A. Bonaldi, L. Bonavera, J. R. Bond, J. Borrill, F. R. Bouchet, F. Boulanger, J. A. Brevik, M. Bucher, I. Buder, E. Bullock, C. Burigana, R. C. Butler, V. Buza, E. Calabrese, J.-F. Cardoso, A. Catalano, A. Challinor, R.-R. Chary, H. C. Chiang, P. R. Christensen, L. P. L. Colombo, C. Combet, J. Connors, F. Couchot, A. Coulais, B. P. Crill, A. Curto, F. Cuttaia, L. Danese, R. D. Davies, R. J. Davis, P. de Bernardis, A. de Rosa, G. de Zotti, J. Delabrouille, J.-M. Delouis, F.-X. Désert, C. Dickinson, J. M. Diego, H. Dole, S. Donzelli, O. Doré, M. Douspis, C. D. Dowell, L. Duband, A. Ducout, J. Dunkley, X. Dupac, C. Dvorkin, G. Efstathiou, F. Elsner, T. A. Enßlin, H. K. Eriksen, E. Falgarone, J. P. Filippini, F. Finelli, S. Fliescher, O. Forni, M. Frailis, A. A. Fraisse, E. Franceschi, A. Frejsel, S. Galeotta, S. Galli, K. Ganga, T. Ghosh, M. Giard, E. Gjerløw, S. R. Golwala, J. González-Nuevo, K. M. Górski, S. Gratton, A. Gregorio, A. Gruppuso, J. E. Gudmundsson, M. Halpern, F. K. Hansen, D. Hanson, D. L. Harrison, M. Hasselfield, G. Helou, S. Henrot-Versillé, D. Herranz, S. R. Hildebrandt, G. C. Hilton, E. Hivon, M. Hobson, W. A. Holmes, W. Hovest, V. V. Hristov, K. M. Huffenberger, H. Hui, G. Hurier, K. D. Irwin, A. H. Jaffe, T. R. Jaffe, J. Jewell, W. C. Jones, M. Juvela, A. Karakci, K. S. Karkare, J. P. Kaufman, B. G. Keating, S. Kefeli, E. Keihänen, S. A. Kernasovskiy, R. Keskitalo, T. S. Kisner, R. Kneissl, J. Knoche, L. Knox, J. M. Kovac, N. Krachmalnicoff, M. Kunz, C. L. Kuo, H. Kurki-Suonio, G. Lagache, A. Lähteenmäki, J.-M. Lamarre, A. Lasenby, M. Lattanzi, C. R. Lawrence, E. M. Leitch, R. Leonardi, F. Levrier, A. Lewis, M. Liguori, P. B. Lilje, M. Linden-Vørnle, M. López-Caniego, P. M. Lubin, M. Lueker, J. F. Macías-Pérez, B. Maffei, D. Maino, N. Mandolesi, A. Mangilli, M. Maris, P. G. Martin, E. Martínez-González, S. Masi, P. Mason, S. Matarrese, K. G. Megerian, P. R. Meinhold, A. Melchiorri, L. Mendes, A. Mennella, M. Migliaccio, S. Mitra, M.-A. Miville-Deschênes, A. Moneti, L. Montier, G. Morgante, D. Mortlock, A. Moss, D. Munshi, J. A. Murphy, P. Naselsky, F. Nati, P. Natoli, C. B. Netterfield, H. T. Nguyen, H. U. Nørgaard-Nielsen, F. Noviello, D. Novikov, I. Novikov, R. O'Brient, R. W. Ogburn, A. Orlando, L. Pagano, F. Pajot, R. Paladini, D. Paoletti, B. Partridge, F. Pasian, G. Patanchon, T. J. Pearson, O. Perdereau, L. Perotto, V. Pettorino, F. Piacentini, M. Piat, D. Pietrobon, S. Plaszczynski, E. Pointecouteau, G. Polenta, N. Ponthieu, G. W. Pratt, S. Prunet, C. Pryke, J.-L. Puget, J. P. Rachen, W. T. Reach, R. Rebolo, M. Reinecke, M. Remazeilles, C. Renault, A. Renzi, S. Richter, I. Ristorcelli, G. Rocha, M. Rossetti, G. Roudier, M. Rowan-Robinson, J. A. Rubiño Martín, B. Rusholme, M. Sandri, D. Santos, M. Savelainen, G. Savini, R. Schwarz, D. Scott, M. D. Seiffert, C. D. Sheehy, L. D. Spencer, Z. K. Staniszewski, V. Stolyarov, R. Sudiwala, R. Sunyaev, D. Sutton, A.-S. Suur-Uski, J.-F. Sygnet, J. A. Tauber, G. P. Teply, L. Terenzi, K. L. Thompson, L. Toffolatti, J. E. Tolan, M. Tomasi, M. Tristram, M. Tucci, A. D. Turner, L. Valenziano, J. Valiviita,

B. Van Tent, L. Vibert, P. Vielva, A. G. Vieregg, F. Villa, L. A. Wade, B. D. Wandelt, R. Watson, A. C. Weber, I. K. Wehus, M. White, S. D. M. White, J. Willmert, C. L. Wong, K. W. Yoon, D. Yvon, A. Zacchei, and A. Zonca, "Joint Analysis of BICEP2/Keck Array and Planck Data," *Phys. Rev. Lett.*, vol. 114, p. 101301, Mar 2015. [Online]. Available: https://link.aps.org/doi/10.1103/PhysRevLett.114.101301

[89] A. Kusaka, J. Appel, T. Essinger-Hileman, J. Beall, L. Campusano, H.-M. Cho, S. Choi, K. Crowley, J. Fowler, P. Gallardo, M. Hasselfield, G. Hilton, S.-P. Ho, K. Irwin, N. Jarosik, M. Niemack, G. Nixon, M. Nolta, J. Page, and K.-W. Yoon, "Results from the Atacama B-mode Search (ABS) Experiment," *Journal of Cosmology and Astroparticle Physics*, vol. 2018, Jan 2018.

[90] K. Arnold, P. A. R. Ade, A. E. Anthony, D. Barron, D. Boettger, J. Borrill, S. Chapman, Y. Chinone, M. A. Dobbs, J. Errard, G. Fabbian, D. Flanigan, G. Fuller, A. Ghribi, W. Grainger, N. Halverson, M. Hasegawa, K. Hattori, M. Hazumi, W. L. Holzapfel, J. Howard, P. Hyland, A. Jaffe, B. Keating, Z. Kermish, T. Kisner, M. L. Jeune, A. T. Lee, E. Linder, M. Lungu, F. Matsuda, T. Matsumura, N. J. Miller, X. Meng, H. Morii, S. Moyerman, M. J. Myers, H. Nishino, H. Paar, E. Quealy, C. Reichardt, P. L. Richards, C. Ross, A. Shimizu, C. Shimmin, M. Shimon, M. Sholl, P. Siritanasak, H. Spieler, N. Stebor, B. Steinbach, R. Stompor, A. Suzuki, T. Tomaru, C. Tucker, and O. Zahn, "The bolometric focal plane array of the POLARBEAR CMB experiment," in *Millimeter, Submillimeter, and Far-Infrared Detectors and Instrumentation for Astronomy VI*, W. S. Holland, Ed., vol. 8452, International Society for Optics and Photonics. SPIE, 2012, pp. 381 – 392. [Online]. Available: https://doi.org/10.1117/12.927057

[91] Z. D. Kermish, P. Ade, A. Anthony, K. Arnold, D. Barron, D. Boettger, J. Borrill, S. Chapman, Y. Chinone, M. A. Dobbs, J. Errard, G. Fabbian, D. Flanigan, G. Fuller, A. Ghribi, W. Grainger, N. Halverson, M. Hasegawa, K. Hattori, M. Hazumi, W. L. Holzapfel, J. Howard, P. Hyland, A. Jaffe, B. Keating, T. Kisner, A. T. Lee, M. L. Jeune, E. Linder, M. Lungu, F. Matsuda, T. Matsumura, X. Meng, N. J. Miller, H. Morii, S. Moyerman, M. J. Myers, H. Nishino, H. Paar, E. Quealy, C. L. Reichardt, P. L. Richards, C. Ross, A. Shimizu, M. Shimon, C. Shimmin, M. Sholl, P. Siritanasak, H. Spieler, N. Stebor, B. Steinbach, R. Stompor, A. Suzuki, T. Tomaru, C. Tucker, and O. Zahn, "The POLARBEAR experiment," in *Millimeter, Submillimeter, and Far-Infrared Detectors and Instrumentation for Astronomy VI*, W. S. Holland, Ed., vol. 8452, International Society for Optics and Photonics. SPIE, 2012, pp. 366 – 380. [Online]. Available: https://doi.org/10.1117/12.926354

[92] A. Kusaka, T. Essinger-Hileman, J. W. Appel, P. Gallardo, K. D. Irwin, N. Jarosik, M. R. Nolta, L. A. Page, L. P. Parker, S. Raghunathan, J. L. Sievers, S. M. Simon, S. T. Staggs, and K. Visnjic, "Modulation of cosmic microwave background polarization with a warm rapidly rotating half-wave plate on the Atacama B-Mode Search instrument," *Review of Scientific Instruments*, vol. 85, no. 2, p. 024501, 2014. [Online]. Available: https://doi.org/10.1063/1.4862058

[93] S. Takakura, M. Aguilar, Y. Akiba, K. Arnold, C. Baccigalupi, D. Barron, S. Beckman, D. Boettger, J. Borrill, S. Chapman, Y. Chinone, A. Cukierman, A. Ducout, T. Elleflot,

J. Errard, G. Fabbian, T. Fujino, N. Galitzki, N. Goeckner-Wald, N. W. Halverson, M. Hasegawa, K. Hattori, M. Hazumi, C. Hill, L. Howe, Y. Inoue, A. H. Jaffe, O. Jeong, D. Kaneko, N. Katayama, B. Keating, R. Keskitalo, T. Kisner, N. Krachmalnicoff, A. Kusaka, A. T. Lee, D. Leon, L. Lowry, F. Matsuda, T. Matsumura, M. Navaroli, H. Nishino, H. Paar, J. Peloton, D. Poletti, G. Puglisi, C. L. Reichardt, C. Ross, P. Siritanasak, A. Suzuki, O. Tajima, S. Takatori, and G. Teply, "Performance of a continuously rotating half-wave plate on the POLARBEAR telescope," *Journal of Cosmology and Astroparticle Physics*, vol. 2017, no. 05, pp. 008–008, May 2017. [Online]. Available: https://doi.org/10.1088%2F1475-7516%2F2017%2F05%2F008

[94] Planck Collaboration, Ade, P. A. R., Aghanim, N., Argüeso, F., Armitage-Caplan, C., Arnaud, M., Ashdown, M., Atrio-Barandela, F., Aumont, J., Baccigalupi, C., Banday, A. J., Barreiro, R. B., Bartlett, J. G., Battaner, E., Beelen, A., Benabed, K., Benoît, A., Benoit-Lévy, A., Bernard, J.-P., Bersanelli, M., Bielewicz, P., Bobin, J., Bock, J. J., Bonaldi, A., Bonavera, L., Bond, J. R., Borrill, J., Bouchet, F. R., Bridges, M., Bucher, M., Burigana, C., Butler, R. C., Cardoso, J.-F., Carvalho, P., Catalano, A., Challinor, A., Chamballu, A., Chen, X., Chiang, H. C., Chiang, L.-Y, Christensen, P. R., Church, S., Clemens, M., Clements, D. L., Colombi, S., Colombo, L. P. L., Couchot, F., Coulais, A., Crill, B. P., Curto, A., Cuttaia, F., Danese, L., Davies, R. D., Davis, R. J., de Bernardis, P., de Rosa, A., de Zotti, G., Delabrouille, J., Delouis, J.-M., Désert, F.-X., Dickinson, C., Diego, J. M., Dole, H., Donzelli, S., Doré, O., Douspis, M., Dupac, X., Efstathiou, G., Enßlin, T. A., Eriksen, H. K., Finelli, F., Forni, O., Frailis, M., Franceschi, E., Galeotta, S., Ganga, K., Giard, M., Giardino, G., Giraud-Héraud, Y., González-Nuevo, J., Górski, K. M., Gratton, S., Gregorio, A., Gruppuso, A., Hansen, F. K., Hanson, D., Harrison, D. L., Henrot-Versillé, S., Hernández-Monteagudo, C., Herranz, D., Hildebrandt, S. R., Hivon, E., Hobson, M., Holmes, W. A., Hornstrup, A., Hovest, W., Huffenberger, K. M., Jaffe, A. H., Jaffe, T. R., Jones, W. C., Juvela, M., Keihänen, E., Keskitalo, R., Kisner, T. S., Kneissl, R., Knoche, J., Knox, L., Kunz, M., Kurki-Suonio, H., Lagache, G., Lähteenmäki, A., Lamarre, J.-M., Lasenby, A., Laureijs, R. J., Lawrence, C. R., Leahy, J. P., Leonardi, R., León-Tavares, J., Leroy, C., Lesgourgues, J., Liguori, M., Lilje, P. B., Linden-Vørnle, M., López-Caniego, M., Lubin, P. M., Macías-Pérez, J. F., Maffei, B., Maino, D., Mandolesi, N., Maris, M., Marshall, D. J., Martin, P. G., Martínez-González, E., Masi, S., Massardi, M., Matarrese, S., Matthai, F., Mazzotta, P., McGehee, P., Meinhold, P. R., Melchiorri, A., Mendes, L., Mennella, A., Migliaccio, M., Mitra, S., Miville-Deschênes, M.-A., Moneti, A., Montier, L., Morgante, G., Mortlock, D., Munshi, D., Murphy, J. A., Naselsky, P., Nati, F., Natoli, P., Negrello, M., Netterfield, C. B., Nørgaard-Nielsen, H. U., Noviello, F., Novikov, D., Novikov, I., O´Dwyer, I. J., Osborne, S., Oxborrow, C. A., Paci, F., Pagano, L., Pajot, F., Paladini, R., Paoletti, D., Partridge, B., Pasian, F., Patanchon, G., Pearson, T. J., Perdereau, O., Perotto, L., Perrotta, F., Piacentini, F., Piat, M., Pierpaoli, E., Pietrobon, D., Plaszczynski, S., Pointecouteau, E., Polenta, G., Ponthieu, N., Popa, L., Poutanen, T., Pratt, G. W., Prézeau, G., Prunet, S., Puget, J.-L., Rachen, J. P., Reach, W. T., Rebolo, R., Reinecke, M., Remazeilles, M., Renault, C., Ricciardi, S., Riller, T., Ristorcelli, I., Rocha, G., Rosset, C., Roudier, G., Rowan-Robinson, M., Rubiño-Martín, J. A., Rusholme, B., Sandri, M., Santos, D., Savini, G., Scott, D., Seiffert, M. D., Shellard, E. P. S., Spencer, L. D., Starck, J.-L., Stolyarov, V.,

Stompor, R., Sudiwala, R., Sunyaev, R., Sureau, F., Sutton, D., Suur-Uski, A.-S., Sygnet, J.-F., Tauber, J. A., Tavagnacco, D., Terenzi, L., Toffolatti, L., Tomasi, M., Tristram, M., Tucci, M., Tuovinen, J., Türler, M., Umana, G., Valenziano, L., Valiviita, J., Van Tent, B., Varis, J., Vielva, P., Villa, F., Vittorio, N., Wade, L. A., Walter, B., Wandelt, B. D., Yvon, D., Zacchei, A., and Zonca, A., "Planck 2013 results. XXVIII. The Planck Catalogue of Compact Sources," *A&A*, vol. 571, p. A28, 2014. [Online]. Available: https://doi.org/10.1051/0004-6361/201321524

[95] T. Murphy, E. M. Sadler, R. D. Ekers, M. Massardi, P. J. Hancock, E. Mahony, R. Ricci, S. Burke-Spolaor, M. Calabretta, R. Chhetri, G. De Zotti, P. G. Edwards, J. A. Ekers, C. A. Jackson, M. J. Kesteven, E. Lindley, K. Newton-McGee, C. Phillips, P. Roberts, R. J. Sault, L. Staveley-Smith, R. Subrahmanyan, M. A. Walker, and W. E. Wilson, "The Australia Telescope 20 GHz Survey: the source catalogue," *Monthly Notices of the Royal Astronomical Society*, vol. 402, no. 4, pp. 2403–2423, Mar 2010. [Online]. Available: https://doi.org/10.1111/j.1365-2966.2009.15961.x

[96] F. T. Matsuda, "Cosmic Microwave Background Polarization Science and Optical Design of the POLARBEAR and Simons Array Experiments," Ph.D. dissertation, University of California, San Diego, 2017.

[97] K. T. Crowley, S. M. Simon, M. Silva-Feaver, N. Goeckner-Wald, A. Ali, J. Austermann, M. L. Brown, Y. Chinone, A. Cukierman, B. Dober, S. M. Duff, J. Dunkley, J. Errard, G. Fabbian, P. A. Gallardo, S.-P. P. Ho, J. Hubmayr, B. Keating, A. Kusaka, N. McCallum, J. McMahon, F. Nati, M. D. Niemack, G. Puglisi, M. S. Rao, C. L. Reichardt, M. Salatino, P. Siritanasak, S. Staggs, A. Suzuki, G. Teply, D. B. Thomas, J. N. Ullom, C. Vergès, M. R. Vissers, B. Westbrook, E. J. Wollack, Z. Xu, and N. Zhu, "Studies of systematic uncertainties for Simons Observatory: detector array effects," in *Millimeter, Submillimeter, and Far-Infrared Detectors and Instrumentation for Astronomy IX*, J. Zmuidzinas and J.-R. Gao, Eds., vol. 10708, International Society for Optics and Photonics. SPIE, 2018, pp. 658 – 684. [Online]. Available: https://doi.org/10.1117/12.2313414

[98] Aumont, J., Conversi, L., Thum, C., Wiesemeyer, H., Falgarone, E., Macías-Pérez, J. F., Piacentini, F., Pointecouteau, E., Ponthieu, N., Puget, J. L., Rosset, C., Tauber, J. A., and Tristram, M., "Measurement of the Crab nebula polarization at 90 GHz as a calibrator for CMB experiments," *A&A*, vol. 514, p. A70, 2010. [Online]. Available: https://doi.org/10.1051/0004-6361/200913834

[99] Y. Mizugutch, M. Akagawa, and H. Yokoi, "Offset Dual Reflector Antenna," in *IEEE International Symposium on Antennas and Propagation Digest*, Jan. 1976, pp. 2–5.

[100] C. Dragone, "Offset multireflector antennas with perfect pattern symmetry and polarization discrimination," *AT T Technical Journal*, vol. 57, pp. 2663–2684, Sep. 1978.

[101] F. T. Matsuda, S. Takakura, K. Arnold, D. Boettger, Y. Chinone, M. Hazumi, B. Keating, A. Kusaka, and A. T. Lee, "Cross-polarization systematics due to Mizuguchi-Dragone condition breaking by a continuously rotating half-wave plate at prime focus in the Huan Tran telescope," in *Millimeter, Submillimeter, and Far-Infrared Detectors and Instrumentation for Astronomy IX*, J. Zmuidzinas and

J.-R. Gao, Eds., vol. 10708, International Society for Optics and Photonics. SPIE, 2018, pp. 769 – 786. [Online]. Available: https://doi.org/10.1117/12.2313177

[102] B. G. Keating, M. Shimon, and A. P. S. Yadav, "Self-calibration of Cosmic Microwave Background Polarization Experiments," *The Astrophysical Journal*, vol. 762, no. 2, p. L23, Dec 2012. [Online]. Available: https://doi.org/10.1088%2F2041-8205%2F762%2F2%2Fl23

[103] S. Takakura, M. A. O. Aguilar-Faúndez, Y. Akiba, K. Arnold, C. Baccigalupi, D. Barron, D. Beck, F. Bianchini, D. Boettger, J. Borrill, K. Cheung, Y. Chinone, T. Elleflot, J. Errard, G. Fabbian, C. Feng, N. Goeckner-Wald, T. Hamada, M. Hasegawa, M. Hazumi, L. Howe, D. Kaneko, N. Katayama, B. Keating, R. Keskitalo, T. Kisner, N. Krachmalnicoff, A. Kusaka, A. T. Lee, L. N. Lowry, F. T. Matsuda, A. J. May, Y. Minami, M. Navaroli, H. Nishino, L. Piccirillo, D. Poletti, G. Puglisi, C. L. Reichardt, Y. Segawa, M. Silva-Feaver, P. Siritanasak, A. Suzuki, O. Tajima, S. Takatori, D. Tanabe, G. P. Teply, and C. Tsai, "Measurements of Tropospheric Ice Clouds with a Ground-based CMB Polarization Experiment, POLARBEAR," *The Astrophysical Journal*, vol. 870, no. 2, p. 102, Jan 2019. [Online]. Available: https://doi.org/10.3847%2F1538-4357%2Faaf381

[104] B. R. Johnson, J. Collins, M. E. Abroe, P. A. R. Ade, J. Bock, J. Borrill, A. Boscaleri, P. de Bernardis, S. Hanany, A. H. Jaffe, T. Jones, A. T. Lee, L. Levinson, T. Matsumura, B. Rabii, T. Renbarger, P. L. Richards, G. F. Smoot, R. Stompor, H. T. Tran, C. D. Winant, J. H. P. Wu, and J. Zuntz, "MAXIPOL: Cosmic Microwave Background Polarimetry Using a Rotating Half-Wave Plate," *The Astrophysical Journal*, vol. 665, no. 1, pp. 42–54, Aug 2007. [Online]. Available: https://doi.org/10.1086%2F518105

[105] E. Hivon, K. M. Gorski, C. B. Netterfield, B. P. Crill, S. Prunet, and F. Hansen, "MASTER of the Cosmic Microwave Background Anisotropy Power Spectrum: A Fast Method for Statistical Analysis of Large and Complex Cosmic Microwave Background Data Sets," *The Astrophysical Journal*, vol. 567, no. 1, pp. 2–17, Mar 2002. [Online]. Available: https://doi.org/10.1086%2F338126

[106] S. Takakura, "Characterization of a continuous polarization modulator using a half-wave plate for measurements of degree-scale cosmic microwave background with the POLARBEAR experiment," Ph.D. dissertation, Osaka University, Jun 2017.

[107] D. Boettger, "Pure E/B Estimator," Jun 2017, Polarbear internal presentation; unpublished.

[108] S. Takakura, "Problem in expansion of pure EB estimator," Jun 2017, Polarbear internal presentation; unpublished.

[109] G. Hinshaw, D. N. Spergel, L. Verde, R. S. Hill, S. S. Meyer, C. Barnes, C. L. Bennett, M. Halpern, N. Jarosik, A. Kogut, E. Komatsu, M. Limon, L. Page, G. S. Tucker, J. L. Weiland, E. Wollack, and E. L. Wright, "First-Year Wilkinson Microwave Anisotropy Probe (WMAP) Observations: The Angular Power Spectrum," *The Astrophysical Journal Supplement Series*, vol. 148, no. 1, pp. 135–159, Sep 2003. [Online]. Available: https://doi.org/10.1086%2F377225

[110] C. Bischoff, A. Brizius, I. Buder, Y. Chinone, K. Cleary, R. N. Dumoulin, A. Kusaka, R. Monsalve, S. K. Næss, L. B. Newburgh, R. Reeves, K. M. Smith, I. K. Wehus, J. A. Zuntz, J. T. L. Zwart, L. Bronfman, R. Bustos, S. E. Church, C. Dickinson, H. K. Eriksen, P. G. Ferreira, T. Gaier, J. O. Gundersen, M. Hasegawa, M. Hazumi, K. M. Huffenberger, M. E. Jones, P. Kangaslahti, D. J. Kapner, C. R. Lawrence, M. Limon, J. May, J. J. McMahon, A. D. Miller, H. Nguyen, G. W. Nixon, T. J. Pearson, L. Piccirillo, S. J. E. Radford, A. C. S. Readhead, J. L. Richards, D. Samtleben, M. Seiffert, M. C. Shepherd, S. T. Staggs, O. Tajima, K. L. Thompson, K. Vanderlinde, R. Williamson, and B. Winstein, "First Season QUIET Observations: Measurements of Cosmic Microwave Background Polarization Power Spectra at 43 GHz in the Multipole Range $25 \leqslant \ell \leqslant 475$," *The Astrophysical Journal*, vol. 741, no. 2, p. 111, Oct 2011. [Online]. Available: https://doi.org/10.1088%2F0004-637x%2F741%2F2%2F111

[111] J. Grain, M. Tristram, and R. Stompor, "Polarized CMB power spectrum estimation using the pure pseudo-cross-spectrum approach," *Phys. Rev. D*, vol. 79, p. 123515, Jun 2009. [Online]. Available: https://link.aps.org/doi/10.1103/PhysRevD.79.123515

[112] R. Pearson, B. Sherwin, and A. Lewis, "CMB lensing reconstruction using cut sky polarization maps and pure B modes," *Phys. Rev. D*, vol. 90, p. 023539, Jul 2014. [Online]. Available: https://link.aps.org/doi/10.1103/PhysRevD.90.023539

[113] T. Louis, S. Næss, S. Das, J. Dunkley, and B. Sherwin, "Lensing simulation and power spectrum estimation for high-resolution CMB polarization maps," *Monthly Notices of the Royal Astronomical Society*, vol. 435, no. 3, pp. 2040–2047, Aug 2013. [Online]. Available: https://doi.org/10.1093/mnras/stt1421

[114] G. Hinshaw, D. Larson, E. Komatsu, D. N. Spergel, C. L. Bennett, J. Dunkley, M. R. Nolta, M. Halpern, R. S. Hill, N. Odegard, L. Page, K. M. Smith, J. L. Weiland, B. Gold, N. Jarosik, A. Kogut, M. Limon, S. S. Meyer, G. S. Tucker, E. Wollack, and E. L. Wright, "Nine-year Wilkinson Microwave Anisotropy Probe (WMAP) Observations: Cosmological Parameter Results," *The Astrophysical Journal Supplement Series*, vol. 208, no. 2, p. 19, Sep 2013. [Online]. Available: https://doi.org/10.1088%2F0067-0049%2F208%2F2%2F19

[115] K. M. Smith and M. Zaldarriaga, "General solution to the $E-B$ mixing problem," *Phys. Rev. D*, vol. 76, p. 043001, Aug 2007. [Online]. Available: https://link.aps.org/doi/10.1103/PhysRevD.76.043001

[116] S. Takakura and D. Boettger, "Power spectrum estimation for low ell," Jun 2017, Polarbear internal presentation; unpublished.

[117] Krachmalnicoff, N., Baccigalupi, C., Aumont, J., Bersanelli, M., and Mennella, A., "Characterization of foreground emission on degree angular scales for CMB B-mode observations - Thermal dust and synchrotron signal from Planck and WMAP data," *A&A*, vol. 588, p. A65, 2016. [Online]. Available: https://doi.org/10.1051/0004-6361/201527678

[118] C. A. Bischoff, "Observing the Cosmic Microwave Background polarization anisotropy at 40 GHz with QUIET," Ph.D. dissertation, Chicago U., 2010.

[119] N. Goeckner-Wald, M. Aguilar, and D. Boettger, "New pseudo-C_ℓ for the 9th round of null tests," Mar 2018, Polarbear internal presentation; unpublished.

[120] K. M. Gorski, E. Hivon, A. J. Banday, B. D. Wandelt, F. K. Hansen, M. Reinecke, and M. Bartelmann, "HEALPix: A Framework for High-Resolution Discretization and Fast Analysis of Data Distributed on the Sphere," *The Astrophysical Journal*, vol. 622, no. 2, pp. 759–771, Apr 2005. [Online]. Available: https://doi.org/10.1086%2F427976